University of Glasgow

Wang, Zhao (2026) *Flexible self-powered piezoelectric pressure sensors based on chitosan for wearable health monitoring.* PhD thesis.

https://theses.gla.ac.uk/86375/

Copyright and moral rights for this work are retained by the author

A copy can be downloaded for personal non-commercial research or study, without prior permission or charge

This work cannot be reproduced or quoted extensively from without first obtaining permission in writing from the author

The content must not be changed in any way or sold commercially in any format or medium without the formal permission of the author

When referring to this work, full bibliographic details including the author, title, awarding institution and date of the thesis must be given

Enlighten: Theses
https://theses.gla.ac.uk/
research-enlighten@glasgow.ac.uk

Flexible Self-Powered Piezoelectric Pressure Sensors Based on Chitosan for Wearable Health Monitoring



Zhao Wang

James Watt School of Engineering

University of Glasgow

This dissertation is submitted for the degree of

Doctor of Philosophy

July 2026

Declaration

I hereby declare that except where specific reference is made to the work of others, the contents of this dissertation are original and have not been submitted in whole or in part for consideration for any other degree or qualification in this, or any other university. This dissertation is my own work and contains nothing which is the outcome of work done in collaboration with others, except as specified in the text and Acknowledgements. The copyright of this thesis rests with the author. No quotation from it is permitted without full acknowledgement.

I declare that artificial intelligence tools were used to support language refinement, document restructuring and Microsoft Word formatting. All research questions, experimental work, data, scientific interpretation and final decisions remain my own, and all AI-assisted edits were reviewed against the underlying evidence and sources.

Zhao Wang

July 2026

Acknowledgements

Now it is eight o’clock in the evening, perhaps the most beautiful time of the day. It marks the quiet ending of the day, and the beginning of another kind of time: time that belongs entirely to oneself. It is a moment when work and study can be set aside, and one can simply return to oneself. At the final stage of writing this thesis, I would like to pause, put down my pen, and look back at the starting point of this journey and across the four years that have led me here. At that time, I could never have imagined that I would be able to persist until this point, meet so many outstanding and kind people, experience so many things I had never expected, and see many different sides of the world. I also never imagined that I would publish several papers along the way. Perhaps, to others, these achievements may not seem extraordinary, but to me, they mean more than enough.啊

At the very beginning, I simply followed my passion. I hoped that through my learning and research, I might be able to make a small contribution to society. Home-based wearable healthcare devices and remote health monitoring were not merely academic ideas to me. They came from a very personal wish: that one day, when I was working and could not always stay beside the elderly members of my family, I could use what I had learned to help them. I hoped that technology could, in some small way, accompany and care for them when I could not be there myself.

Yet life did not unfold as I had hoped. Before I was able to realise this dream, the person who meant the most to me left me. She had always been the driving force that kept me moving forward, and the person who supported and encouraged me without reservation. Sadly, she could not witness the moment when this journey reached its conclusion. She stopped there, and for a long time, I felt as though I had stopped too. I did not know what it meant, I only knew that everything that followed made it difficult for me to continue. Fortunately, I was surrounded by a group of warm and generous people. In the vast and seemingly endless sea, they lit one lighthouse after another for me, guiding me forward when I could no longer find the direction by myself.

Looking back on this journey, the people I most wish to thank are my parents, my supervisor Andrew, and Bhavani. I have never considered myself the most naturally gifted student, nor someone who could overcome every limitation through diligence alone. Yet they have always supported and encouraged me unconditionally. At no point did they give up on me. Instead, they guided me step by step, supported me quietly from behind, and helped me

continue moving forward. All the achievements I have made are inseparable from their support and encouragement.

When I first began my PhD, I was very introverted and often afraid to speak. In many conversations, I would react a little more slowly than others. Perhaps Andrew noticed this. After each discussion, he would thoughtfully send me a short message explaining what had just been discussed, what needed to be done, and reminding me that I could always contact him if I had any questions. Later, in every meeting, Andrew would notice and acknowledge my progress. He has always been someone who gave me encouragement and positive energy. Perhaps it was because of this affirmation that I gradually became more confident, progressing from someone who was afraid to speak in meetings to someone who could travel alone and present confidently at international conferences. Every small step of my growth was supported by the continuous energy and encouragement he gave me.

I am also deeply grateful to Hadi for the warmth and kindness he has shown throughout my PhD. At the end of a long working day, he would often take the time to visit the lab and check in on his students, always with a warm smile on his face. Whenever experiments did not go as planned and I felt discouraged, his smile and reassuring presence had a remarkable way of lifting my spirits and making difficulties seem much more manageable. His kindness and encouragement brought a great deal of warmth and motivation to my PhD journey. I am also very grateful for the generous support he gave me whenever I attended conferences, always encouraging me and offering help whenever needed. I feel truly fortunate to have met such a warm, kind and supportive supervisor during my PhD.

I would also like to express my deepest gratitude to Bhavani and his family. To me, Bhavani has been not only an academic mentor, but also a family member in a foreign country. I entered this field with enthusiasm, but there were many areas in which I was inexperienced and needed guidance. Bhavani patiently and meticulously guided me through experiments, taught me how to analyse results and how to write, and helped me build my own research system from the very beginning. Whenever I encountered difficulties, he would always tell me: “We are here, and you are also the best.” In life, his family, Ramani and Hemanth, have always treated me as one of their own. They told me that they were my family in the UK, and that no matter what happened, I would always be one of them.

I would also like to thank my parents. It is because of their selfless love, long-term support, and unwavering trust that I have been able to come this far, see a wider world, and become

a more complete version of myself. They are the quietest heroes of this journey, my strongest support, and the source of courage that has allowed me to keep moving forward. My gratitude to them can never be fully expressed in words.

Finally, I would like to thank every one of my friends, whether in the UK or in China. Because of them, my life has become richer, brighter, and more complete. I am grateful that they have studied with me, grown with me, helped me understand different versions of myself, and accompanied me in seeing many sides of the world. They have been with me through joy and sorrow, through difficult moments, and through the transformations of life. They have cared for me like family, especially when I was injured or ill. During those times, their attentive care made even the hardest moments feel warm. I am grateful for all the happiness and joy they have brought me, and for making me feel less alone in a foreign country.

This journey has been full of uncertainty. Yet because of all this love, support, trust, and companionship, I was able to move forward again and again, even at the moments when I most wanted to stop. I dedicate these words to everyone who has illuminated my path, lifted me up, and accompanied me to this point.

Abstract

With the rapid development of the Internet of Things, wearable electronics and smart medical technologies, flexible pressure sensors are evolving towards being lightweight, self-powered, biocompatible and environmentally sustainable. Piezoelectric pressure sensors can directly convert mechanical stimuli into electrical signals, enabling dynamic pressure sensing without the need for an external power source. As a result, they are widely used in fields such as electronic skin, health monitoring, human-machine interaction, and intelligent robotics. However, the piezoelectric materials currently in widespread use primarily rely on lead-containing piezoelectric ceramics or fluorinated polymers, which generally suffer from issues such as insufficient biocompatibility, lack of environmental degradability and limited flexibility. Meanwhile, although bio-based materials offer excellent sustainability, they are typically used only as flexible substrates or support layers, and their potential as active piezoelectric materials has not yet been fully explored. To address these issues, this thesis focuses on the bio-derived piezoelectric polymer chitosan and related polymer systems, systematically conducting research into the material design, performance optimisation and wearable applications of flexible, self-powered piezoelectric pressure sensors, with a particular emphasis on exploring the relationships between material composition, microstructure, piezoelectric properties and device functionality.

Firstly, using chitosan as the active piezoelectric material, flexible piezoelectric films were fabricated via a solution cast-filming method, and a sandwich-type piezoelectric pressure sensor was constructed. The study demonstrated that pure chitosan is capable of stable dynamic pressure sensing and exhibits good flexibility, bio-sourced properties and solubility. A 50 μm thick device achieved a pressure sensitivity of 32.25 mV/kPa and a frequency sensitivity of 316.79 mV/Hz, its dynamic response characteristics could mimic the rapid response of Pacinian corpuscles to pressure stimuli, thereby establishing a benchmark system for subsequent research into bio-based piezoelectric materials.

Subsequently, to enhance the piezoelectric properties of chitosan, organic-inorganic composite systems were developed using ZnO and $BaTiO_3$ nanoparticles, respectively. The ZnO composite significantly improved the piezoelectric coefficient and output performance, specifically, the 15 wt.% ZnO composite devices achieved a pressure sensitivity of 70.71 mV/kPa, a frequency sensitivity of 471.43 mV/Hz and a piezoelectric coefficient of 16 pC/N. A pressure sensor array was subsequently prepared, enabling target recognition, pressure

distribution detection, gesture recognition and wireless data transmission. In the $BaTiO_3$ system, lead-free ferroelectric nanoparticles further enhanced the electromechanical coupling capability, the 15 wt.% chitosan-$BaTiO_3$ composite achieved a pressure sensitivity of 276.07 mV/kPa, a frequency sensitivity of 2564.29 mV/Hz and an output of 24.9 V and was successfully integrated into a wireless smart insole to demonstrate a proof of concept for gait monitoring. Concurrently, the study systematically analysed the effects of nanoparticle dispersion, crystal structure and interfacial interactions on piezoelectric performance, revealing an intrinsic relationship between enhanced output performance and material flexibility.

Finally, to further explore the application of highly biocompatible polymers in piezoelectric sensing, Parylene C films of varying thicknesses were fabricated using chemical vapour deposition (CVD) and employed as an active piezoelectric layer in flexible pressure sensing. The study found that as the film thickness increased, its piezoelectric coefficient and output performance improved simultaneously. The 45 μm devices achieved a pressure sensitivity of 87.62 mV/kPa, a frequency sensitivity of 580.95 mV/Hz and a response time of 12 ms, whilst maintaining stable output over more than 1,200 cycles and during 10 consecutive days of testing. Furthermore, the Parylene C pressure sensor array was integrated into a wireless smart glove, enabling real-time monitoring of hand-object interactions and wireless data transmission.

In summary, this thesis has established a series of flexible, self-powered piezoelectric pressure-sensing material systems based on bio-derived polymers, validated the feasibility of chitosan and its composites as active piezoelectric layers, systematically revealed the influence of material composition, interface structure and microstructure on piezoelectric performance, and completed the validation of wearable systems such as wireless smart gloves, smart insoles and pressure-sensing arrays. These research findings not only enrich the design theory of bio-based flexible piezoelectric materials but also provide a new material system and technological foundation for the development of sustainable electronic skin, smart health monitoring, human-computer interaction and next-generation green wearable electronic devices

Table of Contents

Declaration ii

Acknowledgements iii

Abstract vi

Table of Contents viii

List of Figures xii

List of Tables ..... t

List of Abbreviations xxi

Chapter 1: Introduction 1

1.1 Research Background and Motivation 1

1.2 Structure of the Thesis 4

1.3 Main Contributions 7

1.4 List of Published Results 7

Chapter 2: Literature Review 9

2.1 Flexible Pressure Sensors 9

2.1.1 Background 9

2.1.2 Pressure Sensor Technologies 9

2.2 Piezoelectric Materials 13

2.2.1 Inorganic Materials 13

2.2.2 Organic Polymers 16

2.2.3 Composite Materials 18

2.2.4 Bio-Derived Piezoelectric Materials and Chitosan-Based Materials 18

2.3 Performance Characterization of Piezoelectric Pressure Sensors 24

2.3.1 Sensitivity and Linearity 24

2.3.2 Working Range 25

2.3.3 Stability and Durability 26

2.3.4 Response/Recovery Times and Hysteresis....27
2.3.5 Flexibility, Biocompatibility, and Degradability....28
2.4 Applications of the Piezoelectric Pressure Sensors....29
2.4.1 Health Surveillance and Biomedical Applications....30
2.4.2 Joint motion and pressure distribution monitoring....33
2.4.3 Human-Machine Interaction and Soft Robotics....34
2.5 Summary and Research Gaps....36
Chapter 3 Methodology....38
3.1 Materials....38
3.2 Method....40
3.2.1 Preparation of Piezoelectric Films....40
3.2.2 Fabrication of Pressure Sensor....41
3.3 Material Characterisation of Piezoelectric Films....41
3.3.1 Surface Characterisation of Piezoelectric Films....41
3.3.2 Microstructural and Crystalline Phase Structure of Piezoelectric Films....42
3.3.3 Mechanical Characterisation of Piezoelectric Films....43
3.3.4 Electrical Characterisation of Piezoelectric Films....44
Chapter 4: Pure Chitosan-Based Flexible Self-Powered Piezoelectric Pressure Sensor for Pacinian Corpuscle Mimicry....46
4.1 Introduction....46
4.2 Method....48
4.2.1 Preparation of Chitosan Films....48
4.2.2 Fabrication of Chitosan Sensor....49
4.3 Results and Discussion....50
4.3.1 Material Characterisation....50
4.3.2 Pressure Sensor Characterisation....53
4.3.3 Aqueous Dissolution....58

4.4 Summary 59

Chapter 5: Chitosan-ZnO Flexible Self-Powered Piezoelectric Pressure Sensor for Artificial Mechanoreceptor Applications.....60

5.1 Introduction 60

5.2 Methodology 62

5.2.1 Preparation of CS-ZnO Films 62

5.2.2 Fabrication of CS-ZnO Sensors 63

5.3 Results and Discussion.....63

5.3.1 Material Characterisation 63

5.3.2 Dielectric and Piezoelectric Properties 68

5.3.3 Pressure Sensor Characterisation 71

5.3.4 Aqueous Dissolution 78

5.4 Applications 79

5.4.1 Wireless Data Transmission 79

5.4.2 Sensor Array and Spatial Pressure Mapping.....80

5.4.3 Wearable Gesture Detection.....82

5.5 Summary 83

Chapter 6: Chitosan-$BaTiO_3$ Composite Flexible Self-Powered Pressure Sensor for a Wireless Gait-Monitoring Insole.....85

6.1 Introduction 85

6.2 Materials and Methods.....87

6.2.1 Preparation of CS-BTO Composite Films 87

6.2.2 Fabrication of the CS-BTO Sensor 88

6.2.3 Statistical Methods.....88

6.3 Results and Discussion.....89

6.3.1 Material Characterisation 89

6.3.2 Piezoelectric Coefficient (d_{33}).....93

6.3.3 Pressure Sensor Characterisation 94

6.3.4 Mechanical Properties 102
6.3.5 Application: Wireless Self-Powered Insole for Gait Monitoring 104
6.4 Summary 106
Chapter 7: Parylene C Flexible Self-Powered Pressure Sensors for Wearable Systems 107
7.1 Introduction 107
7.2 Method 109
7.2.1 Preparation of PAC Films 109
7.2.2 Fabrication of Pressure Sensors 110
7.3 Results and Discussion of PAC Sensor 111
7.3.1 Material Characterisation 111
7.3.2 Dielectric and Piezoelectric Properties 117
7.3.3 Pressure Sensor Characterisation 119
7.3.4 Stability 124
7.4 Applications 128
7.5 Summary 130
Chapter 8: Conclusions and Future Work 132
8.1 Conclusions 132
8.2 Future Work 136
8.2.1 Further Investigation of Chitosan-Parylene C Hybrid Films 136
8.2.2 Further Development of the Chitosan-Based Sensor Systems 139
Reference 142

List of Figures

Figure 1.1 Schematic illustration of the thesis structure. 6

Figure 2.1. Working principles of (a) piezoresistive, (b) capacitive, (c) piezoelectric and (d) triboelectric pressure sensors before and during force application [38]. 10

Figure 2.2 Historical development of piezoelectricity, piezoelectric materials and self-powered piezoelectric nanogenerators. 11

Figure 2.3 Schematic outlining the differences in the three polymorphs of chitin. The upper portion depicts how the chains are stacked via hydrogen-bonding interactions, while the lower portion illustrates how the direction of the chains changes as they are stacked [91].19

Figure 2.4 Preparation of chitosan from crustacean biowaste. (a) Conventional chemical extraction through sequential demineralisation, deproteinization and deacetylation. (b) Chemical structures showing deacetylation of chitin to chitosan, in which acetylamino groups are converted to amino groups. 20

Figure 2.5 Transient response and pressure hysteresis of an AlN piezoelectric sensor. (a) A filtered voltage waveform with a reported 10% to 90% rise time of approximately 35 ms. (b) Voltage readings during increasing and decreasing pressure, enlarged from the calibration inset. The measured curves show low hysteresis under the reported conditions [98]. 28

Figure 2.6 Physical and biological assessment of flexible materials. (a) A bent β-glycine/chitosan sensor [23]. (b)Viability of murine 3T3 embryonic fibroblasts after 24 and 72 h of exposure to chitosan and constituent materials of chitosan piezoelectric transducers [88]. (c) CS-ZnO 20:1 films before burial and after 4, 6 and 8 weeks in soil at room temperature. The 20:1 designation is the molar ratio of chitosan amino groups to zinc acetate precursor [100]. 29

Figure 2.7. Wearable piezoelectric blood pressure monitoring: (a) wrist attachment, (b) sensor structure and (c) conversion of sensor output to estimated blood pressure [104]. ...31

Figure 2.8. In vivo arterial monitoring: (a) the tissue adhesive sensor and reference system and (b) simultaneously recorded arterial pressure and piezoelectric output [106]. 33

Figure 2.9. Sensor locations and representative two channel outputs for multiaxial joint motion monitoring [109]. 34

Figure 2.10. Human machine interaction: (a) facial sensor placement, (b) the signal from left eye winking and (c) the signal from tongue movement [110]. 35

Figure 2.11. Electronic skin for robotic softness identification: (a) piezoelectric and liquid metal sensing mechanisms and (b) robotic manipulation and sorting [111]. 36

Figure 3.1 Schematic of the vibration test setup (TV 50018, TIRA GmbH), a tuneable pressure and frequency loading system used for pressure sensor characterisation. 45

Figure 4.1 Artificial Pacinian corpuscle mechanoreceptor emulating the human somatosensory system. The left panel shows the transmission of a pressure signal from a sensor on the fingertip through the peripheral nerves and spinal cord to the somatosensory and motor cortices. (a) The Pacinian corpuscle, a rapidly adapting (RA) mechanoreceptor located in the subcutaneous layer beneath the epidermis and dermis, responds to dynamic stimuli and produces a signal only when the stimulus changes. (b) The artificial mechanoreceptor, a sandwich-structured piezoelectric sensor comprising a piezoelectric layer between electrodes and insulation layers, generates a voltage output under dynamic compression that emulates the dynamic response of the Pacinian corpuscle. 48

Figure 4.2 Preparation of chitosan films and sensors. 49

Figure 4.3 SEM images of the chitosan films at 2 μm scale: (a) the thinner Chi-S1 and (b) the thicker Chi-S2. 50

Figure 4.4 XRD patterns of the chitosan films Chi-S1 and Chi-S2. 52

Figure 4.5 FTIR spectra of the chitosan films Chi-S1 and Chi-S2. 53

Figure 4.6 Plots of the output voltage of the chitosan sensors: (a) Chi-S1 and (b) Chi-S2 under different pressures from 20 to 80 kPa at a fixed frequency of 8 Hz, (c) Chi-S1 and (d) Chi-S2 under different frequencies from 2 to 8 Hz at a fixed pressure of 80 kPa. 54

Figure 4.7 Linear fits of the output voltage of the chitosan sensors: (a) Chi-S1 and (b) Chi-S2 against applied pressure, giving pressure sensitivities of 32.25 mV/kPa and 24.57 mV/kPa,

and (c) Chi-S1 and (d) Chi-S2 against loading frequency, giving frequency sensitivities of 316.79 mV/Hz and 228.57 mV/Hz. 55

Figure 4.8 Output voltage versus time of the chitosan sensors: (a) under stepwise increasing pressure from 20 kPa to 80 kPa at a fixed frequency of 8 Hz, (b) under stepwise increasing frequency from 2 Hz to 8 Hz at a fixed pressure of 80 kPa, and (c) cyclic stability over 1000 periodic compression cycles. 57

Figure 4.9 Dissolution of the chitosan film in deionised water (pH 6.5): (a) time-dependent dissolution of the chitosan film during immersion. 59

Figure 5.1 The human tactile sensing system, which functions as an array of receptors (a), and an equivalent artificial tactile sensory system (b), with the typical dynamic sensing signals (c) of a rapidly adapting (type-II) mechanoreceptor and an example wearable scenario on a runner (d).....62

Figure 5.2 Schematic representation of the process flow for the preparation of flexible CS-ZnO films. 63

Figure 5.3 SEM images for (a) pure ZnO film, (b) pure chitosan film, and (c) CS-ZnO film. 64

Figure 5.4 XRD patterns of the ZnO NPs, the pure chitosan film and the CS-ZnO composite film, showing the wurtzite ZnO reflections (indexed to JCPDS 36-1451) and the (020) and (200) reflections of chitosan, with both sets of reflections retained in the composite.....66

Figure 5.5. FTIR spectra of the pure chitosan film and the CS-ZnO composite film, showing the characteristic chitosan bands together with the Zn-O vibration of the added ZnO.....68

Figure 5.6 Impedance of the pure chitosan and CS-ZnO films as a function of frequency, from which the capacitance and permittivity were obtained. 69

Figure 5.7 piezoelectric coefficients of pure chitosan film, and composite films with 5 wt.%, 10 wt.%, and 15 wt.% of ZnO.....70

Figure 5.8. Pressure-sensing performance of the CS-ZnO sensors: output voltage of the pure chitosan film and the 5, 10 and 15 wt.% composites as a function of (a) applied pressure at 8 Hz and (b) loading frequency at 80 kPa.....72

Figure 5.9. Output-voltage response of the composites with (a)-(c) increasing applied pressure and (d)-(f) increasing loading frequency for the 5, 10 and 15 wt.% concentrations, respectively.....73

Figure 5.10 Linear fits of the output voltage used to obtain the sensitivities: output voltage against applied pressure for the composites with (a) 5, (b) 10 and (c) 15 wt.% ZnO, and output voltage against loading frequency for the composites with (d) 5, (e) 10 and (f) 15 wt.% ZnO, with the fitted line and the coefficient of determination shown in each panel. (g) Piezoelectric sensitivity value compares and for various sensors including bare chitosan with different thicknesses of 50 μm (Chi-S1) and 85 μm (Chi-S2), and CS-ZnO sensor doped with various concentrations of ZnO such as 5, 10, 15 wt.% under applied pressure and frequency and (h) the sensitivities' linear relationship. 76

Figure 5.11. Cyclic stability of the CS-ZnO composite sensor over 1000 compression cycles. 77

Figure 5.12. Dynamic response of the 15 wt.% CS-ZnO sensors to a randomly applied pressure, showing response and recovery times of approximately 12 ms each. 77

Figure 5.13. Photographs of the 15 wt.% CS-ZnO composite film in deionised water (pH 6.5-6.6) at regular time intervals, showing approximately complete dissolution within 2 h. 78

Figure 5.14. Wireless transmission of the CS–ZnO sensor array output through the nRF52840 BLE module: (a) system schematic; (b) photographs of a fabricated 5 × 5 sensor array and the corresponding wireless monitoring setup.....80

Figure 5.15 Outputs from the CS-ZnO sensor array: (a) the output-voltage map across the array, reproducing the contact pattern of a letter block, (b) a 2D pressure map of the letters 'UofG', and 3D pressure maps of (c) the letter 'C' and (d) the letters 'UofG', reproducing the contact shapes of the objects. 81

Figure 5.16. Detection of hand gestures using the wearable 15 wt.% CS-ZnO sensor, showing the output voltage responses for (a) flexion of a finger, (b) a scissor gesture, and (c) a curved-hand gesture. 83

Figure 6.1 Schematic illustration of a wearable wireless insole incorporating zero-bias piezoelectric sensing elements for gait monitoring. The insole integrates sensors at the heel, midfoot and forefoot, while an independently powered Bluetooth module (nRF52840 Feather) transmits the data to a mobile device. The insets show the structure of a CS-BTO pressure sensor, with potential applications highlighted, including human-machine interaction, telemedicine, sports monitoring, and personalised healthcare.....86

Figure 6.2 Schematic illustration of the fabrication process for CB composite films derived from marine bio-waste and subsequent assembly into a CB pressure sensor device.....88

Figure 6.3 SEM images and corresponding particle-size distribution histograms of the CS-BTO composite film at $BaTiO_3$ concentrations of (a) 5 wt.%, (b) 10 wt.% and (c) 15 wt.%. Scale bars, 5 μm. 90

Figure 6.4 XRD patterns of BTO powder, the CS-BTO composite films, the pure chitosan film and chitosan powder. 91

Figure 6.5 FTIR spectra of BTO powder, the CS-BTO composite films, and the pure chitosan films Chi-S1 and Chi-S2. 93

Figure 6.6 Piezoelectric coefficient d_{33} of the pure chitosan film and the 15 wt.% CS-BTO composites.....94

Figure 6.7 Output voltage of the CS-BTO sensors (a) under pressures from 20 to 80 kPa in 10 kPa increments at a fixed frequency of 8 Hz, and (b) under frequencies from 2 to 8 Hz in 1 Hz increments at a fixed pressure of 80 kPa. 95

Figure 6.8. Electrical output of the CS-BTO sensors at different BTO concentrations under a fixed excitation of 5 N at 5 Hz: (a) output voltage and (b) output current.....97

Figure 6.9 Linear fits of the piezoelectric response of the CS-BTO composites: (a)-(c) output voltage against applied pressure and (d)-(f) output voltage against frequency, for the 5, 10 and 15 wt.% composites.....98

Figure 6.10. Dynamic response of the 15 wt.% CS-BTO sensors: (a) transient response to a single pressure impulse, showing a response time of 0.24 ms and a recovery time of 0.64 ms,

(b) hysteresis under stepwise compressive loading and unloading between 20 and 80 kPa at a fixed frequency of 8 Hz. 100

Figure 6.11 (a) Long-term stability under continuous cyclic loading, illustrated over 1200s with sustained, repeatable applied pressure. Bending reliability tests of the CB sensor: (b) CB film under bending deformation and (c) output-voltage stability after 10^4 bending cycles for different BTO concentration (5, 10 and 15 wt.%). 101

Figure 6.12. Stress-strain analysis of CS-BTO (a) Instron test set-up with the film specimen mounted in the grips, and (b) tensile force-displacement curves of CB films with different BTO loadings (5, 10 and 15 wt.%). 103

Figure 6.13 shows the output-voltage distribution of the CS-BTO sensor array recorded from participants with different body weights: (a) Tester 1 (50 kg), (b) Tester 2 (70 kg), and (c) Tester 3 (75 kg). 105

Figure 7.1 Overview of the wireless, real-time health-monitoring concept based on flexible PAC piezoelectric pressure sensors, showing the wearable sensor, smart glove, real-time monitoring and data transmission to a mobile application through an Arduino with Bluetooth connectivity. 108

Figure 7.2 Schematic of the Chemical Vapor Deposition (CVD) process for PAC coating, showing vaporization, pyrolysis, and deposition onto a rotating substrate under low pressure (1.7 - 6.2 Pa). 109

Figure 7.3 Stepwise of the flexible PAC pressure sensor fabrication. 110

Figure 7.4 SEM images of PAC film surfaces with thicknesses of (a) 10 µm, (b) 25 µm, and (c) 45 µm (scale bar: 2 µm). 111

Figure 7.5 Corresponding AFM phase images (scan area: 5 µm × 5 µm) with thicknesses of (d) 10 µm, (e) 25 µm, and (f) 45 µm. 112

Figure 7.6 XRD patterns for PAC films (a) intensity and (b) normalised intensity. 114

Figure 7.7 FTIR spectra of the 10 and 45 µm PAC films. 115

Figure 7.8 Raman spectra of the PAC films. (a) full spectra of the 10, 25 and 45 μm films, and (b)-(e) enlarged views of the bands at approximately 690, 1007, 1339 and 2930 cm^{-1}. 117

Figure 7.9 Dielectric and piezoelectric characterisation of the PAC films. (a) electrical impedance against frequency, (b) capacitance against frequency and (c) relative permittivity against frequency for the 10 and 45 μm films, and (d) piezoelectric charge coefficient d_{33} for the 10, 25 and 45 μm films. 119

Figure 7.10 Changes in output voltage for PAC films under varying conditions, where (a) and (b) show the output voltage variations with respect to applied pressure and frequency, respectively for PAC films with different thicknesses; and output response voltages with increased (c) pressure and (d) frequency for PAC films with thicknesses of 10, 25, and 45 μm. 121

Figure 7.11 Stepwise output voltage of the 25 μm PAC sensor. (a) response to applied pressure increased in steps from 20 to 90 kPa at a fixed frequency, and (b) response to loading frequency increased in steps from 2 to 8 Hz at a fixed pressure. 123

Figure 7.12 Sensitivity plot for (a) pressure and (b) frequency with output voltage changes, showing linear increases in pressure and frequency respectively for PAC films with different thicknesses; (c) Comparison of pressure and frequency sensitivities for PAC sensors with different thicknesses. 124

Figure 7.13. Long-term stability tests of PAC piezoelectric pressure sensors with various thicknesses (10 μm, 25 μm, and 45 μm). (a) Daily average output voltage values recorded over a 10-day period under continuous fatigue tests (pressure: 90 kPa, frequency: 5 Hz, temperature: 20-25 °C, humidity: 30-35%). Corresponding detailed spiral plots illustrating real-time output voltage stability for sensors with thicknesses of (b) 10 μm, (c) 25 μm, and (d) 45 μm, respectively. 126

Figure 7.14. Response and recovery times of the PAC-based piezoelectric pressure sensor under instantaneous pressure loading and unloading conditions. 127

Figure 7.15 Smart glove demonstration with the PAC pressure sensor array. (a) the sensor array integrated into a textile glove, (b) the glove grasping a plastic cup at increasing grip

pressure, (c) the corresponding real-time output voltage, increasing from 0.2 V to 0.7 V as the grip tightened, and (d) schematic of the wireless system, in which the sensor signals are digitised and processed by a Nordic nRF52840 System-on-Chip and transmitted over Bluetooth Low Energy to a mobile application. 130

Figure 8.1 Schematic of the CS-PAC film preparation. (a) Preparation of the chitosan film, and (b) deposition of Parylene C onto the chitosan film by chemical vapour deposition to form the CS-PAC composite film. 137

Figure 8.2 SEM images of the CS-PAC films. (a)-(f) surface morphology of samples S1 to S6, showing an increasingly granular texture with increasing chitosan film thickness. 138

Figure 8.3 XRD patterns of the CS-PAC films, samples S1 to S6, with pristine chitosan and Parylene C included for reference. 139

Figure 8.4 FTIR spectra of the CS-PAC films, samples S1 to S6, with pristine chitosan and Parylene C included for reference. 139

List of Tables

Table 2.1 Comparison of the main pressure sensor technologies. 12

Table 3.1 Reagents and materials used in the experiment. 38

Table 3.2 Main instruments and equipment used in the experiment. 39

Table 8.1 Performance comparison of representative pressure sensors . 错误!未定义书签。

List of Abbreviations

ABBREVIATION	FULL NAME
2D	two-dimensional
3D	three-dimensional
ADC	analogue-to-digital converter
AF	agglomeration fraction
AFM	atomic force microscopy
AI	artificial intelligence
$BATIO_3$	barium titanate
BLE	Bluetooth Low Energy
BTO	barium titanate
CDS	cadmium sulfide
CHNCS	chitin nanocrystals
CNCS	cellulose nanocrystals
CNN	convolutional neural network
CNT	carbon nanotube
CS	chitosan
CS-BTO	chitosan-barium titanate composite

CS-ZNO	chitosan-zinc oxide composite
CVD	chemical vapour deposition
DDA	degree of deacetylation
DMHD	dimethylhexanediol
EDL	electric double layer
FE-SEM	field-emission scanning electron microscopy
FEP	fluoropolymer used with CSBT films
FPI	fluorinated polyimide
FTIR	Fourier transform infrared spectroscopy
FWHM	full width at half maximum
GAN	gallium nitride
GRU	gated recurrent unit
HMI	human-machine interface
HTN	arterial hypertension / hypertension
IOT	Internet of Things
IPA	isopropyl alcohol
KNN	potassium sodium niobate

LLO	laser lift-off
LSTM	long short-term memory
MFC	microfibrillated cellulose
MWCNT	multiwalled carbon nanotube
MXENE	MXene
NAOH	sodium hydroxide
NFC	near-field communication
NFES	near-field electrospinning
NHS	N-hydroxysuccinimide
NPS	nanoparticles
NTC	negative temperature coefficient
OFAT	one-factor-at-a-time
OSAS	Obstructive Sleep Apnea Syndrome
PAC	Parylene C
PAN	polyacrylonitrile
PBS	phosphate-buffered saline
PDMS	polydimethylsiloxane

PENG	piezoelectric nanogenerator
PET	polyethylene terephthalate
PI	polyimide
PLA	polylactic acid
PLGA	poly(lactic-co-glycolide)
PPS	piezoelectric pressure sensors
PTFE	polytetrafluoroethylene
PU	polyurethane
PVA	poly(vinyl alcohol)
PVC	poly(vinyl chloride)
PVD	physical vapour deposition
PVDF	polyvinylidene fluoride
PVDF-HFP	poly(vinylidene fluoride-co-hexafluoropropylene)
PVDF-TRFE	poly(vinylidene fluoride-trifluoroethylene)
PZT	lead zirconate titanate
ROI	region of interest
SEM	scanning electron microscopy

SICF	stretchable ionic capacitive fibre
SNS	SnS
SNS_2	SnS_2
SNSE	SnSe
SOC	System-on-Chip
T-NFES	triboelectric self-powered near-field electrospinning
TEM	transmission electron microscopy
TENG	triboelectric self-powered device / triboelectric nanogenerator
$TI_3C_2T_X$	$Ti_3C_2T_x$ MXene
TIO_2	TiO_2
TPU	thermoplastic polyurethane
WI-FI	Wi-Fi
XRD	X-ray diffraction
ZNO	zinc oxide

Chapter 1: Introduction

1.1 Research Background and Motivation

Flexible pressure sensors are central to wearable electronics, electronic skin, soft robotics, prosthetics and human-machine interfaces [1], [2], [3] They convert mechanical stimuli, including pressure, touch, vibration, bending and body motion, into electrical signals [4]. On-body and implantable sensors can capture movement, pressure distribution, gait, respiration, pulse and hand gestures. These measurements support health assessment, disease diagnosis and prosthetic control [5].

When integrated with wireless communication and artificial intelligence, wearable sensors can collect health-related data in home environments. Such systems may facilitate timely consultation for minor or early-stage health concerns and enable long-term monitoring of individuals who require continuous or frequent assessment. This capability is particularly relevant to older adults, people with chronic conditions and individuals undergoing rehabilitation. For these populations, frequent hospital visits may be inconvenient and may not capture daily variations in physical condition. Flexible pressure sensors are therefore becoming important components of home-based health-monitoring systems and may contribute to future healthcare delivery [4], [6].

Pressure sensors typically rely on piezoresistive, capacitive, optical, triboelectric or piezoelectric transduction mechanisms. Piezoresistive and capacitive sensors offer high sensitivity, simple device structures and compatibility with flexible substrates. However, they generally require an external power supply or bias voltage. In wearable systems, batteries and wired power-management modules can limit device miniaturisation, wearing comfort, operational lifetime and sustainability [7]. These limitations become more pronounced when sensors are distributed across the body, embedded in clothing, integrated into insoles or arranged in tactile arrays.

This challenge has driven the development of self-powered pressure sensors. Triboelectric and piezoelectric devices can convert mechanical energy from movement, vibration, tapping, pressing, bending or walking into electrical signals. Triboelectric devices can generate high voltages, but their performance depends on contact conditions, surface-charge behaviour and ambient humidity. Their high output impedance can also necessitate complex signal-

processing circuits. By contrast, piezoelectric pressure sensors generate electrical signals directly from mechanical deformation through the direct piezoelectric effect [8], [9]. Their self-powered operation, dynamic pressure response, compact form factor, high sensitivity and flexibility make them attractive for real-time wearable pressure monitoring. In this thesis, the term self-powered refers to the ability of the sensing element to convert the mechanical energy of an applied stimulus directly into a measurable electrical signal. Liu et al. distinguished sensors that generate their own electrical signals but require external power for subsequent data acquisition, processing and transmission from complete self-powered sensing systems in which these functions are also powered by harvested energy [7]. Under dynamic loading, the piezoelectric layer generates the sensing signal through the direct piezoelectric effect without an external bias voltage. In this work, the digital storage oscilloscope used for laboratory characterisation requires an independent power supply. The nRF52840-based wireless readout circuit used in the wearable demonstrations is also independently powered for signal acquisition, digitisation, processing and Bluetooth Low Energy (BLE) transmission. Accordingly, the term self-powered is used throughout this thesis specifically for signal generation at the sensing element level.

The practical application of flexible piezoelectric pressure sensors remains constrained by material selection. Materials for wearable and bio-integrated devices should ideally combine low weight, flexibility, stability, durability, a high piezoelectric coefficient, non-toxicity, biocompatibility and degradability. Traditional inorganic piezoelectric materials, such as lead zirconate titanate (PZT), exhibit high piezoelectric coefficients and strong electromechanical coupling. Nevertheless, their rigidity, brittleness, high density and lead toxicity limit their use in wearable and bio-integrated devices [10]. Lead-free materials, including zinc oxide (ZnO) and barium titanate ($BaTiO_3$), provide alternative piezoelectric functionality but remain mechanically rigid when used alone [11]. They therefore generally require integration into flexible material systems.

These limitations have stimulated interest in organic, polymeric and bio-based piezoelectric materials. Organic and polymeric materials offer greater flexibility, lower density and improved processability [12], [13]. Polyvinylidene fluoride (PVDF), poly (vinylidene fluoride-trifluoroethylene) (PVDF-TrFE), polylactic acid (PLA), fibronectin and gelatin have been investigated for flexible piezoelectric devices [12], [14], [15]. However, many polymeric piezoelectric materials exhibit lower piezoelectric coefficients than ceramic materials. Some also require additional processing, including poling, mechanical stretching,

heat treatment or phase and structural modulation, to achieve sufficient piezoelectric responses.

Sustainability and biocompatibility are particularly important for future wearable and biomedical pressure-monitoring applications. Many flexible sensors contain non-biodegradable synthetic polymers, metals and electronic components, which can contribute to electronic waste after disposal [16]. This issue is especially relevant to single-use or short-lifetime wearable devices. Bio-based materials could reduce environmental burdens while improving suitability for skin contact and biomedical applications[16], [17], [18]. However, many bio-based materials exhibit weak electrical responses. Further material and device engineering is therefore required to realise practical self-powered pressure sensors.

In this background, chitosan is a promising bio-based candidate material. Chitosan is a natural biopolymer obtained by deacetylation of chitin, which is widely found in the exoskeletons of crustaceans and other biological sources. Due to its solution processability, low cost, mechanical flexibility, documented biocompatibility, non-toxicity and material-level degradability, chitosan has attracted attention in the field of flexible electronics [18], [19]. Chitosan contains polar functional groups, including hydroxyl and amino groups, which can participate in polarisation behaviour under mechanical deformation. Consequently, chitosan is a potential candidate material for bio-based piezoelectric pressure sensors [24]. However, pure chitosan also has inherent limitations, including lower piezoelectric output and sensitivity compared to many inorganic piezoelectric materials. Its electromechanical response may also be influenced by factors such as film thickness, topography, molecular orientation, environmental conditions and device structure.

To address these limitations whilst retaining the advantages of flexible polymeric materials, this thesis investigates a series of chitosan-core, polymer-based piezoelectric pressure sensors. In this work, a detailed investigation on the feasibility of pure chitosan as a benchmark bio-sourced piezoelectric material towards the pressure sensors application. Subsequently, ZnO and $BaTiO_3$ are incorporated into chitosan to form chitosan-zinc oxide (CS-ZnO) and chitosan-barium titanate (CS-BTO) composite films, in which inorganic nanoparticles are used to enhance the electromechanical response, whilst chitosan provides flexibility and processability [21], [22], [23]. PAC is also investigated as a pressure-responsive piezoelectric polymer, rather than merely as a passive encapsulant or insulating material.

Consequently, the research motivation of this thesis can be summarised as a comprehensive problem spanning the material, device and application levels. At the material level, there is a need to develop flexible piezoelectric materials with biocompatibility that can generate measurable dynamic pressure responses without relying on rigid or toxic piezoelectric ceramics. At the device level, there is a need to construct simple sensor structures capable of operating in a self-powered mode under repetitive pressure and frequency loading. At the application level, demonstrate the potential that such sensors can be integrated into wearable configurations, including sensor arrays, smart gloves and smart insoles, for dynamic pressure monitoring and artificial tactile feedback.

Accordingly, this thesis focuses on the development and evaluation of flexible piezoelectric pressure sensors for wearable monitoring and artificial tactile sensing. The research compares pure chitosan, CS-ZnO, CS-BTO and PAC sensors to investigate how material composition and film thickness influence their piezoelectric properties and dynamic pressure and frequency responses. The specific research objectives are:

- To assess the suitability of flexible polymer films for piezoelectric pressure sensing under dynamic loading.
- To examine how material composition and film thickness affect the measured piezoelectric properties, mechanical behaviour and sensor response.
- To compare the pressure and frequency responses of the investigated sensors under defined loading conditions.
- To evaluate the response under repeated loading and demonstrate the integration of selected sensors into arrays and wearable devices with wireless readout.

1.2 Structure of the Thesis

This thesis is divided into eight chapters as illustrated in **Figure 1.1**.

Chapter 1 introduces the research background, motivation, main contributions, structure of the thesis, and previously published work relevant to this study. This chapter highlights the necessity of developing flexible, self-powered pressure sensors for wearable health monitoring and artificial tactile systems.

Chapter 2 reviews the literature related to flexible pressure sensors and self-powered piezoelectric pressure detection. This chapter first discusses the main pressure transduction

mechanisms, including piezoresistive, capacitive, triboelectric and piezoelectric sensors, and focuses on analysing their suitability for wearable and self-powered applications. Subsequently, the chapter reviews piezoelectric materials, including inorganic materials, organic polymer materials, organic-inorganic composites and bio-derived materials. The chapter further identifies key research gaps addressed in this thesis, including the demand for flexible, self-powered, biocompatible and more sustainable pressure sensing materials.

Chapter 3 introduces the generic materials, preparation methods, device structures, characterisation techniques and electromechanical testing procedures employed in this thesis. This chapter covers the preparation of chitosan films, composite films, PAC films and sandwich-structured pressure sensors, and introduces methods such as SEM, XRD, FTIR, Raman spectroscopy, atomic force microscopy, thickness measurement, d_{33} testing, dielectric characterisation, dynamic pressure testing and cyclic stability testing. This chapter provides the methodological foundation for the subsequent experimental chapters.

Chapter 4 investigates pure chitosan flexible self-powered pressure sensors. This chapter focuses on the preparation, morphology, crystal structure, chemical characteristics and dynamic pressure response behaviour of chitosan films and analyses the influence of film thickness on pressure and frequency responses. This chapter establishes pure chitosan as a reference material system and evaluates its relationship with the dynamic response inspired by Pacinian corpuscles.

Chapter 5 focuses on CS-ZnO pressure sensors for use in artificial mechanoreceptors. This chapter analyses how the introduction of ZnO nanoparticles alters the morphology, crystal structure, chemical interactions, dielectric behaviour, piezoelectric coefficient, pressure sensitivity, frequency sensitivity, stability and material-level solubility of chitosan-based films. The chapter also presents representative wearable and wireless pressure monitoring applications, including pressure distribution detection and dynamic motion detection based on sensor arrays.

Chapter 6 explores CS-BTO pressure sensors for wearable health monitoring and electronic skin applications. And evaluates the influence of $BaTiO_3$ concentration on nanoparticle distribution, agglomeration behaviour, crystalline characteristics, chemical interactions, piezoelectric coefficients, pressure sensitivity, frequency sensitivity, response behaviour and cycling stability. This chapter further demonstrates the application of CS-BTO sensors in

pressure distribution detection systems and smart insole configurations, highlighting their potential in gait-related monitoring and wearable health technologies.

Chapter 7 examines Parylene C (PAC) piezoelectric pressure sensors for wearable systems. It assesses the influence of PAC film thickness on morphology, crystallinity, chemical structure, dielectric and piezoelectric behaviour, dynamic pressure and frequency response, response and recovery time, and operational stability. The chapter then evaluates a PAC sensor array through smart-glove integration and wireless monitoring.

Chapter 8 summarises the main work of this thesis and discusses future research directions. This chapter compares the different material strategies investigated in this thesis, identifies their respective relative advantages and limitations, and discusses issues that still need to be addressed, including large-scale fabrication, long-term durability, flexible and stretchable electrodes, more realistic wearable testing, comprehensive device-level dissolution assessment, and further validation for biomedical or bio-integrated applications.

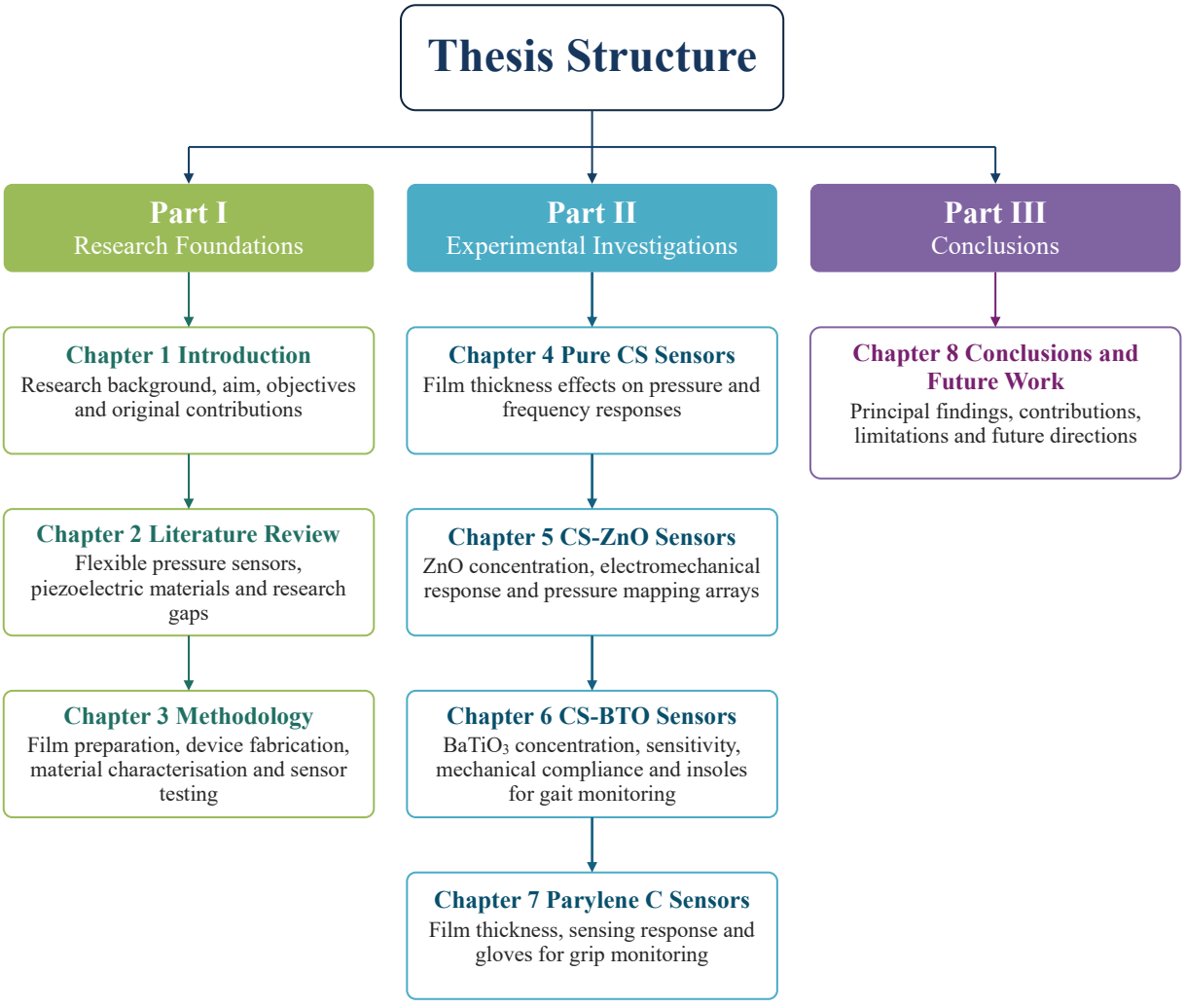


Figure 1.1 Schematic illustration of the thesis structure.

1.3 Main Contributions

- Developed and investigated CS-ZnO and CS-BTO composite pressure sensors with varying nanoparticle concentrations, using pure CS as a reference to evaluate changes in piezoelectric properties and dynamic sensing performance. The study also examined the associated changes in film stiffness for CS-BTO and the solubility of a selected CS-ZnO film.
- Systematically investigated the piezoelectric properties of Parylene C, examining the influence of film thickness on its structural characteristics, dielectric properties and dynamic sensing performance.
- Integrated the developed sensors into pressure mapping arrays, smart insoles and smart gloves for spatial pressure sensing, gesture detection, gait monitoring and grip monitoring, with wireless data transmission in selected demonstrations.
- Proposed a layered CS-PAC film architecture as an exploratory extension of the material systems developed in this thesis, supported by preliminary fabrication and material characterisation, with further systematic quantitative sensing evaluation reserved for future work.

1.4 List of Published Results

- **Published**

1. Wang Zhao, Yalagala Bhavani Prasad, Zhan Jungang, He Zixuan, Heidari Hadi and Feeney Andrew (2026) A hybrid chitosan-$BaTiO_3$ composite-based flexible and self-powered pressure sensor for wearable healthcare applications. ACS Applied Engineering Materials. Early Online Publication. doi: 10.1021/acsaenm.6c00330.
2. Wang Zhao, Yalagala Bhavani Prasad, Heidari Hadi and Feeney Andrew (2026) A hybrid Chitosan-Parylene C composite based piezoelectric pressure sensor for biomedical applications. Engineering Proceedings, 127(1), 17. doi: 10.3390/engproc2026127017.
3. Wang Zhao, Yalagala Bhavani Prasad, Heidari Hadi and Feeney Andrew (2025) Highly sensitive parylene C based flexible pressure sensors for wearable systems. Small Science, 5(7), 2500081. doi: 10.1002/smsc.202500081. PMID: 40666042; PMCID: PMC12257884.

4. Wang Zhao, Yalagala Bhavani Prasad, Zhang Jungang, Hafezi Mahshid, Heidari Hadi and Feeney Andrew (2025) Wireless and self-powered wearable pressure sensors based on chitosan for artificial mechanoreceptors. Advanced Materials Technologies, 10(11), 2401858. doi: 10.1002/admt.202401858.
5. Wang Zhao, Yalagala Bhavani Prasad, Heidari Hadi and Feeney Andrew (2024) A flexible and self-powered Chitosan-$BaTiO_3$ composite pressure sensor for e-skin applications. In: 2024 IEEE SENSORS, Kobe, Japan, 20-23 October 2024. ISBN 9798350363524. doi: 10.1109/SENSORS60989.2024.10785172.
6. Wang Zhao, Yalagala Bhavani Prasad, Hafezi Mahshid, Heidari Hadi and Feeney Andrew (2023) A bioprotein-based flexible and self-powered pressure sensor towards a biomimic of an artificial Pacinian corpuscle. In: IEEE 30th International Conference on Electronics, Circuits and Systems (ICECS), Istanbul, Turkey, 4-7 December 2023. ISBN 9798350326499. doi: 10.1109/ICECS58634.2023.10382948.

- **Manuscript to be submitted**

1. Yifei Wang, Elmergue Germano, Zhao Wang, Yankang Wang, Andrew Feeney, Kwok-Ho Lam and Sandy Cochran. “High-performance 15 MHz ultrasound imaging: synergising novel textured piezoceramics with coded excitation for deep-tissue imaging applications”

Chapter 2: Literature Review

This chapter reviews flexible pressure sensors by comparing piezoresistive, capacitive, triboelectric and piezoelectric pressure sensors according to their operating principles, structures, advantages and limitations. The discussion then focuses on piezoelectric materials used in flexible and wearable devices, with particular emphasis on chitosan as a bio-derived piezoelectric material. Finally, representative wearable applications are introduced, and the research gaps identified from the literature are summarized.

2.1 Flexible Pressure Sensors

2.1.1 Background

Flexible pressure sensors convert physical, chemical and bioelectrical signals from the body and translate them into information that can support health monitoring, rehabilitation assessment and human-machine interaction[24], [25]. Pressure is one of the most common physical signals, since touch, pulse, respiration, joint movement and plantar loading are all expressed through mechanical deformation[26]. A wearable pressure sensor thus needs to be flexible and lightweight, and it needs to remain in conformal contact with skin, joints or textiles during repeated movement. Flexible pressure sensors differ from rigid pressure sensors in this respect, as rigid devices cannot follow soft tissues or curved body surfaces without discomfort or mechanical mismatch. Wireless communication and data analysis further extend these sensors from single-point measurements to continuous personal health monitoring, provided that the sensing element can maintain stable output and low power demand[27].

2.1.2 Pressure Sensor Technologies

A pressure sensor converts pressure into a measurable and processable electrical signal. Depending on the sensing mechanism, flexible pressure sensors can be divided into piezoresistive, capacitive, piezoelectric and triboelectric types. Piezoresistive and capacitive pressure sensors were studied early and are widely used because their structures are relatively simple and their operating principles are clear. They detect pressure through changes in resistance or capacitance under an applied force, which allows them to respond to both static and dynamic pressure [28], [29]. However, these devices require an external power source to convert the resistance or capacitance change into an electrical signal.

Piezoelectric and triboelectric pressure sensors can generate voltage under mechanical deformation or contact-induced charge variation, so they can operate without an external power supply [30], [31]. This self-powered response is useful for dynamic pressure detection, where the signal is produced by a changing mechanical input[30], [31], [32]. The transduction mechanisms of piezoresistive, capacitive, piezoelectric and triboelectric devices are illustrated in **Figure 2.1**[33]**.**

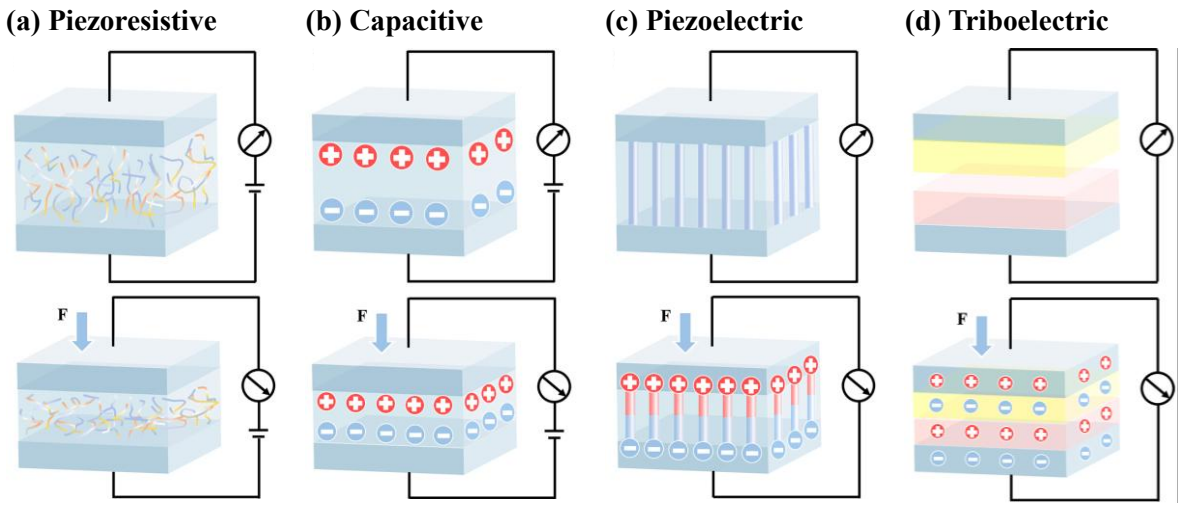


Figure 2.1. Working principles of (a) piezoresistive, (b) capacitive, (c) piezoelectric and (d) triboelectric pressure sensors before and during force application [38].

- **Piezoelectric Sensors**

In 1880, Jacques and Pierre Curie discovered that certain non-centrosymmetric dielectric crystals generate electric charges on their surfaces when subjected to mechanical stress, a phenomenon later known as the direct piezoelectric effect [34]. Under mechanical deformation, the centres of positive and negative charges within the material become displaced, producing a net polarisation, as a result, opposite charges appear on the two surfaces, and the material returns to its initial electrical state after the applied force is removed. Conversely, when an electric field is applied along the polarisation direction, the material undergoes mechanical deformation and recovers after the field is removed, which is referred to as the converse or inverse piezoelectric effect. Piezoelectric pressure sensors generate electrical charge directly from mechanical deformation through the direct piezoelectric effect, without any external power supply. An early approach to extracting electrical energy from a piezoelectric material involved dropping a steel ball onto a piezoelectric transducer [35] [36]. In 2006, Zhong Lin Wang first proposed the concept of the piezoelectric nanogenerator: using a Pt-coated atomic force microscopy (AFM) a-Si tip

to deflect a single zinc oxide (ZnO) nanowire, a piezoelectric signal of 8 mV was generated during compression of the ZnO, confirming the conversion of mechanical energy into electrical energy at the nanoscale [11]. In 2007, Xudong Wang used a ZnO nanowire array, rather than a single nanowire, to build a piezoelectric nanogenerator (PENG) that responded to ultrasonic energy; integrating more nanowires on a flexible substrate gave higher conversion efficiency and voltage [37]. In 2011, ZnO nanowire arrays containing thousands of nanowires were grown on a flexible substrate by a hydrothermal method, and the output voltage and current of a single layer reached 20 V and 6 μA, sufficient to power an electronic watch [38]. The key milestones in the development of piezoelectricity, piezoelectric materials and self-powered piezoelectric nanogenerators are summarised in **Figure 2.2**.

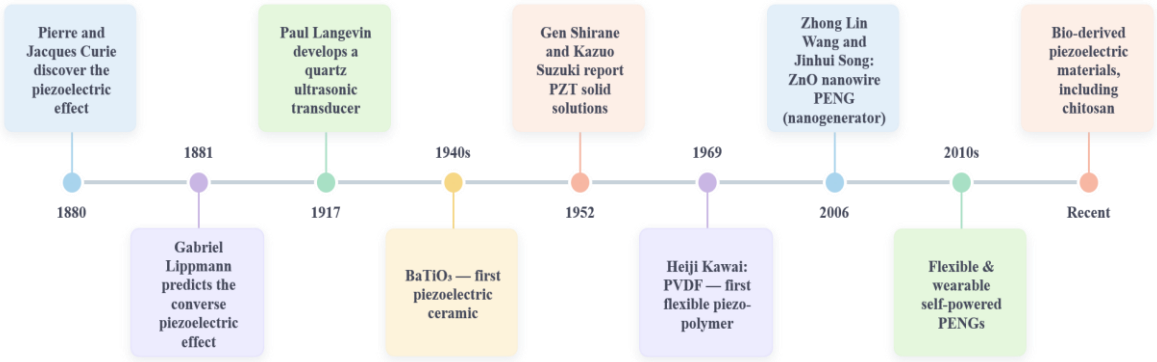


Figure 2.2 Historical development of piezoelectricity, piezoelectric materials and self-powered piezoelectric nanogenerators.

This progression reflects the expansion of piezoelectric research from conventional inorganic ceramics to flexible polymers, nanostructured generators and bio-derived materials suitable for wearable sensing. The voltage and current generated by a PENG arise from applied mechanical deformation. A PENG can thereby be used directly as a self-powered pressure sensor, with its electrical output serving as the sensing signal rather than solely as a power source. As the piezoelectric layer is deformed, the internal electric dipoles are displaced, and the resulting polarisation produces charges of opposite sign on the two surfaces, which drive a current through an external circuit. The device acts as a self-powered transducer that converts a mechanical input into a voltage or current output [35]. The self-powered operation removes the need for an external supply, while the direct coupling between deformation and charge gives high sensitivity, a short response time, simple signal conditioning, and good mechanical durability, since the charge is generated within the bulk of the material rather than at a contacting interface [32], [39]. The main limitation is that the response is predominantly dynamic. Charge flows only while the pressure is changing, so

static or slowly varying pressures produce little sustained signal, and the magnitude of the output depends strongly on the piezoelectric coefficient of the chosen material [40].

Among the four mechanisms, piezoresistive and capacitive sensors require an external power supply and are limited by the relatively long response times arising from the viscoelastic recovery of their flexible materials, which restricts their use in self-powered, dynamic, wearable scenarios [36]. Triboelectric and piezoelectric sensors are both self-powered and high sensitivity to dynamic stimuli, but triboelectric sensors suffer from wear at the contacting friction surfaces, more sensitivity to humidity, and low output current, and require complex high-impedance circuitry [41], [42]. Piezoelectric sensors, by contrast, convert dynamic mechanical deformation directly into charge through the bulk of the material rather than at a contacting interface, giving them better mechanical durability, higher output current, and simpler signal conditioning [32]. These technologies are compared in **Table 2.1**. For a self-powered, flexible, dynamic pressure sensor intended for continuous wearable health monitoring, the piezoelectric mechanism offers the most favourable overall balance, and the remainder of this chapter focuses on self-powered piezoelectric pressure sensors and the materials from which they are made.

Table 2.1 Comparison of the main pressure sensor technologies.

Classification	External power	Detectable pressure types	Advantages	Limitations
Piezoresistive	Required	Static and dynamic	Simple structure; Straightforward manufacturing process; Low power consumption; Wide measurement range	Susceptible to temperature fluctuations; Long response time; High hysteresis
Capacitive	Required	Static and dynamic	Low power consumption; Wide measurement range; High sensitivity; Insensitivity to temperature	Sensitive to parasitic capacitance and humidity; complex signal processing; bulky device configuration; long response/recovery time; poor linearity.

Triboelectric	Self-powered	Dynamic	Relatively high output voltage; Short response and recovery time; Low-frequency energy harvesting capability	Surface wear; High matched impedance; Low current; Environmentally sensitive; Requires complex circuits
Piezoelectric	Self-powered	Dynamic	High sensitivity and accuracy; Rapid response/recovery; Good power output; Light weight	Limited choice of materials; Poor temperature stability; Relatively low robustness

2.2 Piezoelectric Materials

Piezoelectric materials for wearable pressure sensors are required to meet both electrical and mechanical requirements. They need to generate measurable charge under deformation, while also being flexible, lightweight, stable, processable and compatible with the intended wearing conditions. Materials capable of producing electrical charge through mechanical stress are generally classified as inorganic materials, organic polymers, composite materials and bio-derived materials. Inorganic materials often provide strong electromechanical response but are usually rigid or brittle. Organic polymers offer flexibility and processability but generally produce lower output. Composite materials are used to combine these advantages, while bio-derived materials introduce biocompatibility, degradability and sustainability as additional design considerations [39] [43].

2.2.1 Inorganic Materials

Inorganic piezoelectric materials are widely used in sensors, actuators, and self-powered devices owing to their high piezoelectric constants, electromechanical coupling coefficients, mechanical strength, and stability[44], [45]. Based on their microstructure, they can be broadly classified into wurtzite-structured, perovskite-structured, and two-dimensional (2D) materials[46].

The wurtzite structure is a crystal structure in the hexagonal crystal system, with the AB-type chemical formula exhibiting polarisation along the c-axis, typical examples include zinc oxide (ZnO), gallium nitride (GaN), cadmium sulfide (CdS), and zinc sulfide (ZnS)[45], [47]. The earliest self-powered devices were fabricated using ZnO. Although its piezoelectric

constant d_{33} is only 10 to 12 pC/N, ZnO has attracted attention across various fields owing to its status as an important semiconductor material, its simple structure, high chemical stability, high transparency, high electrical conductivity, abundant raw materials, and suitability for fabricating various nanostructures. The crystal structure of ZnO features a hexagonal unit cell in which oxygen anions and zinc cations form a tetrahedral structure lacking central symmetry, when subjected to force along the polarisation direction, the cation and anion centres undergo relative displacement, exhibiting the piezoelectric effect[48]. Owing to its simple and diverse preparation methods, such as hydrothermal synthesis, pulsed laser deposition, and chemical synthesis, and its variety of structures, including nanowires, nanorods, and nanorings, ZnO has been extensively studied and applied in flexible pressure sensors[11], [49], [50].

The chemical formula for the perovskite structure is ABO_3, with a tetragonal/rhombohedral crystal structure, where a larger metal ion (A) sits at the corners, a smaller metal ion (B) at the centre, and oxygen anions at the faces of the unit cell. Owing to their excellent optoelectronic, ferroelectric, piezoelectric, and ionic-migration properties, this class of materials holds strong potential in self-powered pressure sensors and energy harvesting[44]. Common materials include lead zirconate titanate (PZT), $BaTiO_3$, potassium niobate ($KNbO_3$), and potassium sodium niobate (KNN). Lead zirconate titanate (PZT) has long been considered one of the most widely used materials in commercial applications, owing to its d_{33} value of 500-600 pC/N, high dielectric constant, Curie temperature of 350 °C, mechanical and chemical stability, low manufacturing cost, ease of controlling shape and dimensions, and the ability to be polarised in any direction, it has been widely used in transducers, imageing, and sensing [51]. However, PZT has a relatively high density and Young's modulus, meaning it is stiff, heavy, and has a high resonant frequency, which makes it unsuitable for flexible pressure sensors. Nevertheless, its high electromechanical coupling factor continues to motivate efforts to increase its flexibility and stretchability by fabricating nanometre-thick films or combining it with flexible substrates. For example, Kwi-Il Park used the laser lift-off (LLO) process to transfer a 2 μm PZT thin film onto a 125 μm flexible polyethylene terephthalate (PET) substrate and further encapsulated it to realise a thin-film self-powered device that generated a high output of 200 V and 150 $\mu A/cm^2$ in response to slight mechanical deformation [10]. However, the LLO method is expensive and difficult to scale, so chemical solution deposition has been used as an alternative to transfer the piezoelectric material to a polymer substrate [52]. In 2020, Shiyuan Liu further improved

the chemical deposition method, requiring no additional transfer processes or complicated coating and heating steps: fluorophlogopite mica was used to grow PZT thin films, and PZT-5H powder was added to the PZT solution to make a 2 μm-thick PZT film with only one cycle of coating and heat treatment, greatly simplifying the process, as 20 procedures are required to fabricate the same thickness using pure solution [53]. Flexibility can also be increased by structural modification of the inorganic piezoelectric generator, for example, forming nanoscale piezoelectric ribbons (5-10 μm wide and 250-500 nm thick) into a wavy structure on a soft silicone-rubber substrate enhanced the piezoelectric effect by 70% [51].

PZT contains lead (Pb), which raises environmental and biological concerns and limits its use in wearable devices. Research has consequently examined lead-free perovskite materials such as $BaTiO_3$. Although $BaTiO_3$ was initially limited by a lower piezoelectric coefficient and Curie temperature, composition modification using Ca^{2+} and Zr^{4+} has been reported to improve its piezoelectric response. Metal halide perovskites have also attracted interest because of their optoelectronic, ferroelectric and piezoelectric behaviour. For wearable pressure sensing, however, toxicity, stability and processing conditions remain central issues when these materials are considered for flexible devices [54] [55] [56].

Since the discovery of graphene by Novoselov et al in 2004, 2D materials with atomic-scale thickness have attracted attention, and 2D piezoelectric materials are no exception. When materials are exfoliated to the 2D scale, especially to an odd number of layers, their structure exhibits asymmetry and displays piezoelectric properties, such as MoS_2, $MoSe_2$, WS_2, WSe_2, In_2Se_3, GeSe, and SnS[57] [58], [59]. The properties of 2D piezoelectric materials are influenced by factors including bandgap, number of layers, and crystal orientation, and they are typically fabricated using mechanical exfoliation, chemical vapour deposition (CVD), physical vapour deposition (PVD), or solution-based methods [60]. The use of 2D piezoelectric materials is promising for achieving efficient and sensitive pressure feedback with minimal dimensions, owing to their nanoscale dimensions and tunable mechanical properties. Using a thermal-solvent etching method, Choi's team introduced sulfur-vacancy defects into 2D MoS_2, increasing the piezoelectric coefficient from 16.6 pC/N to 332 pC/N and the sensitivity from 7.72 mV/kPa to 262 mV/kPa [61]. Dai et al. transferred multilayer In_2Se_3 nanosheets onto a flexible PDMS substrate and, by aligning the polarisation directions of all layers, achieved an increase in electrical output as the number of layers increased, the output voltage of a 7-layer In_2Se_3 structure reached 363 mV, much higher than the 14 mV of

a single layer, and used this material to fabricate a self-powered pressure sensor for detecting human pulse and respiration [62].

Inorganic piezoelectric materials thus provide strong electromechanical output, but their rigidity, brittleness, high-temperature processing and, in some cases, toxicity do not match all requirements of soft wearable devices. This limitation explains why organic polymers, composite materials and bio-derived materials are also widely studied for flexible piezoelectric pressure sensors.

2.2.2 Organic Polymers

In recent years, challenges have arisen regarding the biocompatibility and degradability of traditional inorganic piezoelectric materials. Furthermore, the inherent brittleness and high stiffness of these materials are disadvantages for the fabrication of flexible sensors. More research is focused on organic polymer piezoelectric materials and their derived copolymers in self-powered wearable sensors, as they are chemically stable, flexible, lightweight, and impact-resistant, and have good moulding, processing, and manufacturing properties[14], [35], [63].

Piezoelectric polymers are classified as amorphous and semi-crystalline materials. Amorphous piezoelectric polymers are a sub-stable state of molecular-dipole freezing, with typical examples including polyacrylonitrile (PAN), polyphenylcyanoether, and vinylidene nitrile copolymers. Semi-crystalline polymers are obtained by dispersing microcrystalline regions in amorphous regions and display piezoelectric performance after polarisation by an external electric field or mechanical stretching, examples include polyvinylidene fluoride (PVDF), poly(D-lactic acid) (PDLA), polylactic acid (PLA), parylene C, poly(vinylidene fluoride-trifluoroethylene) (P(VDF-TrFE)), gelatin, and polyamides (PA) [15]. Their piezoelectric coupling coefficients are much lower than those of inorganic piezoelectric materials. For example, the piezoelectric coefficient (d_{33}) of the organic polymer PVDF is 30 pC/N, compared with 300 pC/N for the inorganic material PZT [64]. Accordingly, improving the piezoelectric coefficient is the primary route to making organic piezoelectric materials suitable for practical applications. Commonly adopted methods to change the composition of the materials, such as incorporating inorganic nanoparticles (e.g. $BaTiO_3$, ZnO) into organic polymers, structural design, such as constructing multilayered structures or composites, and material processing during or after fabrication to change the micro-

morphology, induce crystalline-phase transition, or improve the nanostructure and crystallinity, such as mechanical stretching, polarisation treatments, or adjusting the temperature profile during fabrication[65].

Polyvinylidene fluoride (PVDF) is one of the most widely studied organic piezoelectric polymers for flexible pressure sensors. It is a semi-crystalline polymer with five polymorphs, namely α, β, γ, δ and ε phases. Among these phases, the β-phase provides the strongest piezoelectric response because of its polar chain conformation. Most PVDF-based studies accordingly aim to increase the β-phase content through mechanical stretching, electrical poling, thermal treatment or electrospinning. Electrospinning is commonly used because it combines fibre formation, mechanical stretching and electric-field polarisation, making PVDF suitable for flexible fibres, membranes and textile-based sensors. Other processing routes, including porous film formation and Langmuir-Blodgett deposition, have also been used to improve phase transition and electrical output. These studies show that PVDF is useful as a flexible piezoelectric polymer, but its performance depends strongly on processing conditions and phase control [66] [67] [68] [69] [70] [71].

Parylene C is another organic polymer relevant to flexible piezoelectric devices. It has long been used as an encapsulation material because it can be deposited by chemical vapour deposition as a conformal, uniform and pinhole-free thin film. Its electrical insulation, chemical stability, flexibility and reported biocompatibility make it compatible with micro-electromechanical and biomedical devices. Piezoelectric behaviour in Parylene C has also been reported, which is commonly associated with its asymmetric molecular structure and polarisation treatment. Compared with PVDF, Parylene C is less widely used as an active pressure-sensing layer, but its conformal deposition and encapsulation relevance make it useful when flexible piezoelectric films need protection or direct integration with soft device structures [32] [72] [73].

Organic piezoelectric polymers provide flexibility and processability that are difficult to obtain from many ceramic materials. However, compared with many piezoelectric ceramics, these polymers generally exhibit lower effective piezoelectric coefficients and generate less charge or voltage under comparable mechanical loading. This limitation is associated with their lower intrinsic polarisation and weaker electromechanical coupling. Processing-induced dipole alignment, phase control and the incorporation of high-permittivity or piezoelectric fillers are accordingly employed to enhance their sensing performance.

2.2.3 Composite Materials

Composite piezoelectric materials usually combine flexible polymers with ceramic particles, nanoparticles, nanowires or nanosheets. The ceramic component can act as a nucleation site for crystalline ordering and can also concentrate local stress during deformation, while the polymer component maintains flexibility and processability. ZnO and $BaTiO_3$ are widely used examples, and their nanostructures can be incorporated into polymer films, fibres or porous networks. The main challenges are particle aggregation, non-uniform stress transfer and reduced mechanical compliance at high loading. These issues mean that improved electrical output needs to be evaluated together with film quality, flexibility and cycling durability [74], [75], [76].

2.2.4 Bio-Derived Piezoelectric Materials and Chitosan-Based Materials

Natural piezoelectric biomaterials include amino acids, peptides, proteins, polysaccharides and viruses. These materials are studied for wearable and biomedical devices because they can offer non-toxicity, biocompatibility, degradability and sustainable sourcing. Examples include wood, bone, eggshell membrane, spider silk, chitin, cellulose, amino acids and peptides. Their electrical output is generally lower than that of many ceramic piezoelectric materials, but their ability to form soft and biologically compatible structures makes them relevant to temporary, implantable and skin-contact sensors. Chitosan is a particularly relevant polysaccharide in this group because it can be processed into flexible films and its molecular structure contains polar groups associated with electromechanical response [77].

- **Background of Chitosan**

Chitosan is a low-cost natural biopolymer derived from chitin, which is widely reported as the second most abundant natural polysaccharide after cellulose [78]. It can be obtained from crustacean-shell waste, so it’s a potentially renewable feedstock. Chitosan is widely used for biomedical applications, such as cellular scaffold or drug delivery platforms, due to its high biocompatibility, biodegradability and antibacterial properties. It can be processed in a very thin and highly compliant flexible film. The biocompatibility of chitosan is worthy of attention because it makes its application in the medical field promising. The viability of murine 3T3 embryonic fibroblasts on the chitosan film remained above 70% at both 24 and 72 h; under the conditions of that study, the tested films accordingly met the ISO 10993-5:2009 non-cytotoxicity criterion [79]. Hosseini et al. reported that the magnesium

electrodes degraded within minutes, whereas the glycine-chitosan film dissolved after a few days in phosphate-buffered saline (PBS, pH 7.4). They proposed poly(l-lactide-co-glycolide) (PLGA) encapsulation to extend the sensor operating period [19].

- **Structure of Chitosan**

Chitosan is a natural polysaccharide composed of β-1,4-D-glucosamine, exhibits piezoelectric behaviour due to its noncentrosymmetric crystal structure, and can be produced from chitin through the deacetylation process when the degree of deacetylation reaches 50% [80]. Chitin exists in three crystalline allomorphs as shown in **Figure 2.3**:

(1) α-chitin features antiparallel arrangement of molecular chains with strong intermolecular hydrogen bonds, the highest abundance and optimal stability;

(2) β-chitin has molecular chains bundled in parallel configurations, which leads to weak intermolecular forces and inferior stability;

(3) γ-chitin presents a mixed parallel and antiparallel arrangement of chains combining the characteristics of α- and β-forms [81], [82].

Exploring cost-effective and high-yield approaches to elevate the degree of deacetylation and obtain high-performance chitosan from biological waste including crustacean biomass, fungi and insects has become one of the popular research focuses among scholars in recent

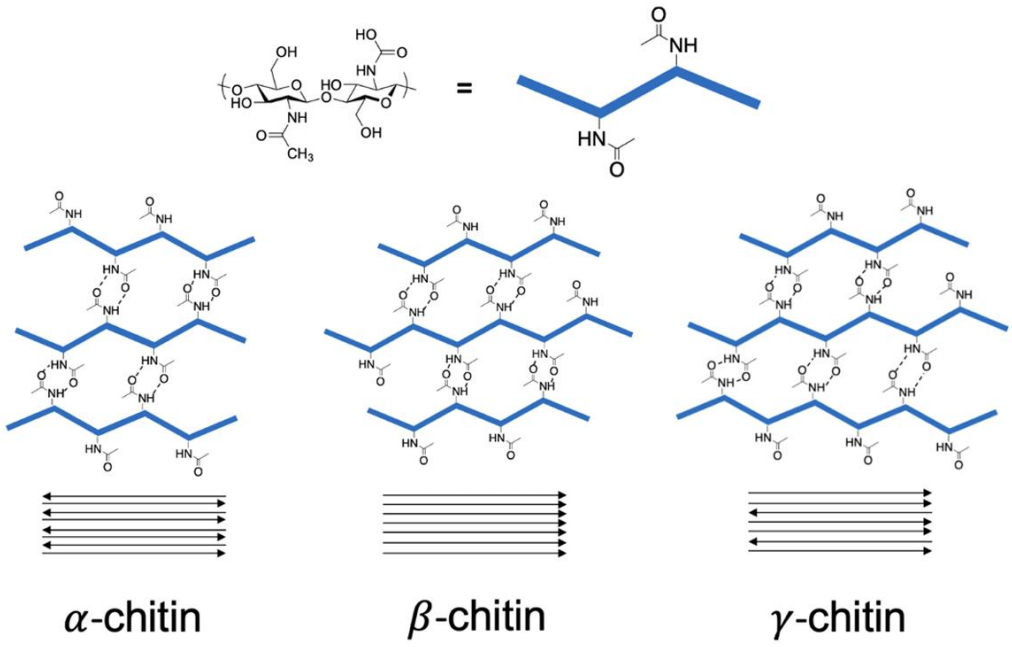


Figure 2.3 Schematic outlining the differences in the three polymorphs of chitin. The upper portion depicts how the chains are stacked via hydrogen-bonding interactions, while the lower portion illustrates how the direction of the chains changes as they are stacked [91].

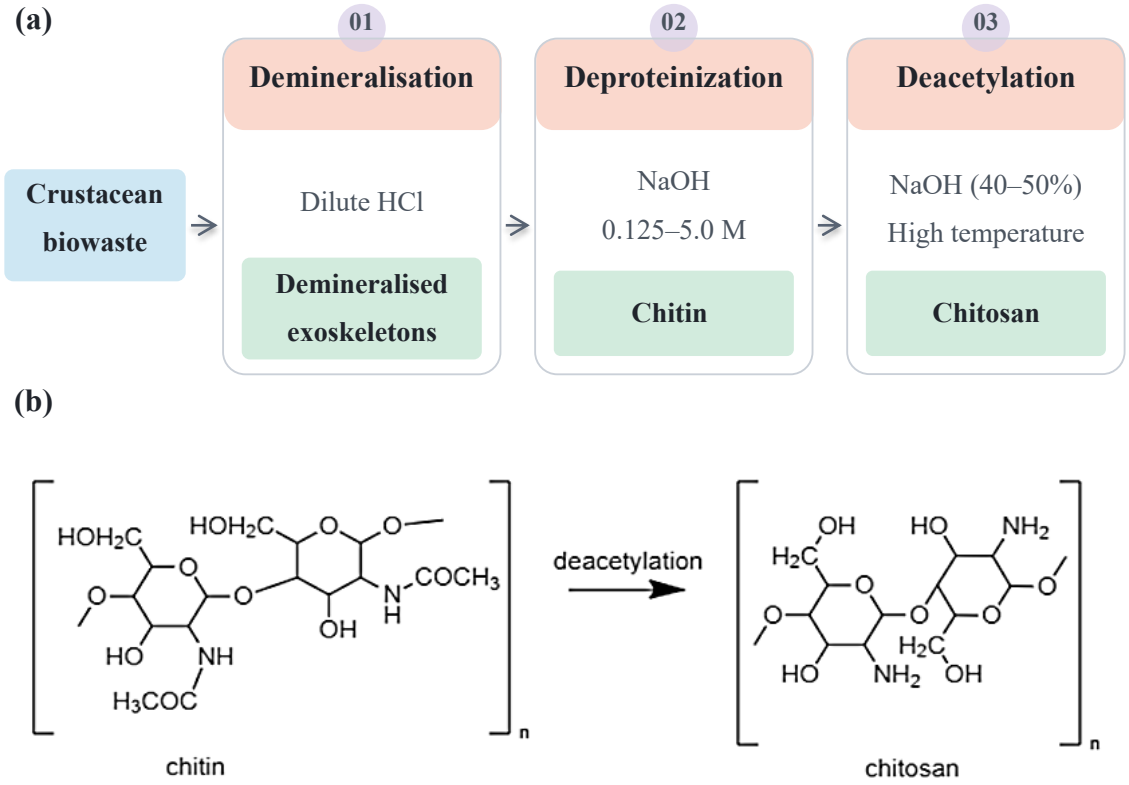


Figure 2.4 Preparation of chitosan from crustacean biowaste. (a) Conventional chemical extraction through sequential demineralisation, deproteinization and deacetylation. (b) Chemical structures showing deacetylation of chitin to chitosan, in which acetylamino groups are converted to amino groups.

years. Extracting chitosan from crustacean biowaste is one of the primary approaches. Conventional industrial production relies on the chemical extraction method. The process begins with demineralisation, where dilute hydrochloric acid is used to remove calcium carbonate from exoskeletons. Subsequently, deproteinization is carried out via alkaline hydrolysis with 0.125-5.0 M sodium hydroxide (NaOH). The final step is deacetylation through high-temperature treatment with highly concentrated 40-50% NaOH. This technique boasts mature processes, high yields and controllable degree of deacetylation, making it suitable for large-scale commercial manufacturing. Nevertheless, it suffers from massive consumption of acids and alkalis, high energy expenditure, and environmental pollution caused by waste effluents. The conventional chemical extraction route and the associated structural changes during deacetylation are illustrated in **Figure 2.4(a) an (b)**. Another eco-friendly alternative is the biological extraction method, which is predominantly applied at the laboratory scale. Deproteinization can be achieved with proteolytic enzymes, or simultaneous demineralisation and deproteinization can be realised through microbial fermentation employing lactic acid bacteria and proteolytic microorganisms. Chitosan produced by this method possesses a higher molecular weight and fully preserved bioactivity.

However, the high cost of commercial purified enzymes together with the long fermentation period of microorganisms restricts its large-scale industrial production. The last technique is an improved modification of the chemical route. Microwave irradiation provides auxiliary heating via electromagnetic fields, drastically shortening processing time: the deacetylation duration that originally takes two days is reduced to 60-180 minutes. Meanwhile, the alkali concentration can be lowered to 30% NaOH, cutting down chemical expenses and mitigating environmental contamination [83], [84].

The extraction procedure of chitosan from fungal biomass differs from that of crustacean feedstock: fungal raw materials do not undergo demineralization, and only deproteinization followed by deacetylation is required. Nevertheless, fungal cell walls contain abundant β-glucan, which hinders the extraction process and leads to low chitosan yield. To address this limitation, Alia Tasnim Hazmi et al. reviewed and compared four chemical extraction methods for fungal chitosan. The most widely adopted method is organic acid treatment combined with ambient-temperature alkaline treatment. This protocol boasts simple operation and low equipment demand, yet it produces chitosan with low yield and Degree of deacetylation (DDA). When organic acids are replaced with dilute mineral sulfuric acid, a chitosan yield of 28.7% can be achieved, whereas strong mineral acid brings severe environmental pollution and high toxicity. Another strategy retains organic acids while replacing ambient alkaline treatment with high-temperature heating assistance, this method yields chitosan with high DDA but entails high energy costs due to continuous high-temperature operation. The optimal technique is microwave-assisted organic acid-alkaline treatment extraction, which produces chitosan with a DDA of 94.6% and excellent crystallinity. Nevertheless, this method has a drawback of high overall costs arising from microwave equipment and chemical reagents [85].

Hisham et al. summarized that the main potential sources of chitosan currently consist of crustacean shells, the mainstream commercial raw material, fish scales, which account for 1% of the total weight of fish, are massively discarded into river systems and act as major aquatic pollutants, fungi and mushrooms, the second-largest group of organisms on Earth, whose cell walls contain chitin accounting for 1% to 15% of their dry weight and rank as the second most common source of chitin next to crustaceans, and insects, a novel alternative raw material without seasonal and geographical limitations [83]. Amran et al. extracted microbial chitosan from Aspergillus oryzae via extraction and deacetylation and further optimized film-forming parameters including acid solvent type, acid concentration and

mixing time through the one-factor-at-a-time (OFAT) method. Among tested organic acids, formic acid stood out: formic acid can fully protonate the amino groups of chitosan to improve solubility, reduce molecular agglomeration, form dense and uniform thin films, and simultaneously enhance mechanical strength and dipole ordering. The optimal fabrication condition, 0.25 M formic acid with 3 h mixing time, enabled pure commercial chitosan thin film to achieve optimal comprehensive performance, with a tensile strength of 129.29 MPa, electromechanical coupling factor of 0.0045, and piezoelectric coefficient d_{31} of 10 pC/N [86].

- **Performance Optimization Strategies for Chitosan-Based Piezoelectric Pressure Sensors**

Pristine chitosan thin films generally exhibit a piezoelectric coefficient of only 5-9 pC/N. When used as pressure sensors, their weak electrical output limits their practical applications in wearable sensing and implantable medical devices. Accordingly, enhancing the piezoelectric response, mechanical flexibility, and device output performance of chitosan-based materials has become an important research direction. Current performance optimization strategies mainly include fabrication-process regulation, incorporation of external functional fillers, and bio-based nanofiller reinforcement.

a) Fabrication Process Optimization

Post-fabrication processing without any foreign filler represents a low-cost ideal strategy to boost the piezoelectric performance of chitosan, while fully preserving its intrinsic biocompatibility. For instance, by tuning the crystalline ordering of chitosan via lactic acid dissolution and NaOH neutralization with different soaking times, Marzo et al. prepared 15 μm transparent chitosan thin films whose effective piezoelectric coefficient was boosted from 6 pC/N to 15.56 pC/N. Pressure sensors made from such films possess a linear working range of 0-0.5 kPa and a sensitivity of 80.3 mV/kPa, enabling the detection of minor pressure changes [79]. On this basis, the research team led by Papa optimized the fabrication protocol by combinatorially regulating three variables: the type of dissolution acid, NaOH neutralization duration, and vacuum annealing temperature. Characterizations reveal that the combination of lactic acid dissolution, 60 min NaOH treatment, and 1 h vacuum annealing at 140 °C facilitates the formation of the characteristic crystalline phase corresponding to the $2\theta = 10°$ diffraction peak, raising the piezoelectric coefficient d_{33} of chitosan to 27 pm/V, a value comparable to that of the commercial piezoelectric polymer PVDF [87].

b) Inorganic Piezoelectric Filler Reinforcement

Another prevalent method for boosting chitosan piezoelectricity is introducing nanofillers or inorganic piezoelectric fillers. Prokhorov analysed the performance of CS-ZnO nanocomposites containing 0-20 wt.% ZnO NPs and reported the highest piezoelectric coefficient d_{33} within that range at 15 wt.% ZnO[88]. A chitosan-$BaTiO_3$ piezopolymer was also synthesized for tissue engineering, exhibiting a d_{33} value of 11.29 pC/N[89].

c) Bio-Based Nanofiller Reinforcement

Apart from inorganic fillers, bio-based nanofillers have also been incorporated into chitosan matrices to enhance piezoelectric properties while retaining biodegradability and biocompatibility. Nicoletti et al. incorporated chitin nanocrystals (ChNCs), another sustainable bioderived filler, into the chitosan matrix. This strategy significantly boosted the crystallinity of thin films and raised the piezoelectric coefficient d_{33} from 8.9 pm/V to 18.7 pm/V. In addition, glycerol was introduced as a plasticizer to improve film flexibility, reducing Young's modulus from 875 MPa to 15 MPa and increasing the elongation at break from 8% up to 60%. Such nanocomposite films hold promising prospects in wearable physiological sensors and soft robotics [90]. Although the combination of rod-like cellulose nanocrystals (CNCs) and chitosan can enhance the piezoelectric coefficient, the value is still much lower than that of PVDF. Antonaci's team adopted sub-spherical cellulose nanocrystals as fillers to incorporate into the chitosan matrix, which overcomes the disadvantages of poor dispersion and weak piezoelectric performance of traditional rod-like CNCs and greatly improves the piezoelectric properties of the material, achieving a piezoelectric constant of 30 pC/N. The addition of CNCs reduces the Young's modulus of the material and makes it more mechanically compliant, rendering it suitable for flexible sensors. In addition, this composite film contains no inorganic fillers such as BTO and ZnO, it is fully biodegradable and free of heavy metal residues, holding broad application prospects in the fields of disposable wearable and implantable medical devices [91].

- **Chitosan-Based Piezoelectric Hydrogels for Biomedical Applications**

Hydrogel-based piezoelectric materials provide another approach to the use of chitosan in biomedical applications. Fan et al. reviewed piezoelectric hydrogels based on chitosan, gelatin and related biological macromolecules, highlighting their flexibility, biocompatibility and potential applications in wearable sensing and implantable medical devices, particularly those involving bone and skin tissues [92]. Xiong et al. successfully

combined chitosan piezoelectric gel with flexible circuits to realize wireless real-time sensing monitoring after Achilles tendon rupture surgery, addressing three major clinical demands including tendon repair, infection prevention and control, and rehabilitation monitoring [93]. These studies illustrate the potential of chitosan-based piezoelectric materials for biomedical sensing and tissue repair, complementing the film-based pressure sensors investigated in this thesis.

2.3 Performance Characterization of Piezoelectric Pressure Sensors

The performance of a piezoelectric pressure sensor is characterised by its output voltage, pressure sensitivity, frequency sensitivity, linearity, working range, response and recovery times, cyclic stability, repeatability and hysteresis. These parameters describe the sensor's response to applied pressure and the consistency of its output under repeated loading. Flexibility, biocompatibility and degradability are additional characteristics relevant to material selection and sensor design.

2.3.1 Sensitivity and Linearity

Sensitivity and linearity are two core and mutually correlated indicators for evaluating sensor performance. The pressure sensitivity S_P and frequency sensitivity S_f were determined from the slope of the output voltage against applied pressure and against frequency, respectively, as defined in **Equation 2.1** and **Equation 2.2**:

$$S_P = \frac{\Delta V}{\Delta P \text{ at a constant } frequency} \tag{2.1}$$

$$S_f = \frac{\Delta V}{\Delta f \text{ at a constant } pressure} \tag{2.2}$$

where ΔV is the change in output voltage, ΔP is the change in applied pressure, and Δf is the change in frequency. The sensitivity was obtained from the slope of the linear fitting given by **Equation 2.3**, using the least-squares method in OriginLab:

$$y = Sx + b \tag{2.3}$$

High sensitivity guarantees the precise detection of subtle pressure variations and improves pressure resolution, representing a key target for sensor performance optimization. Current

studies mainly enhance sensitivity through material modification, microstructure engineering, and fabrication process optimization [94].

Linearity describes the consistency between actual sensor response and ideal linear output. Due to the inherent viscoelasticity and nonlinear deformation of flexible materials, sensors cannot achieve absolute linear response within the full working range [95]. The coefficient of determination (R^2) is universally adopted to evaluate linearity, where a value closer to 1 indicates a smaller fitting deviation and higher linearity. The coefficient of determination (R^2) was calculated according to **Equation 2.4** to quantify the deviation between the fitted line and the measured values:

$$R^2 = 1 - \frac{\sum y_i (y_i - \hat{y}_i)^2}{\sum y_i (y_i - \bar{y})^2} \tag{2.4}$$

where y_i are the measured values, $\hat{y}_i$ the fitted values, and $\bar{y}$ the mean value of y_i.

Sensors with excellent linearity effectively simplify data processing procedures, reduce repeated recalibration operations, and improve overall measurement accuracy [95]. Structural gradient design is an effective strategy to suppress nonlinear mechanical deformation and improve linearity. Wu et al. proposed an ionic flexible sensor with a normal-direction graded hemisphere (GH) microstructure, which consists of 250 μm-radius large hemispheres layered with 25 μm-radius small hemispheres on the surface. The layered microstructures achieve sequential contact under compression, compensating for the nonlinearity and structural stiffening of single-scale structures. This design realizes an ultra-high linearity of R^2=0.99994 over a wide range of 0-600 kPa [96]. Similarly, Xu et al. constructed micro-hierarchical dome structures based on MWCNT/PDMS composites. The graded contact mode enables linear growth of contact area with increasing pressure, optimizing the sensor linearity to R^2 around 0.99 [97].

2.3.2 Working Range

The working range is defined as the pressure interval within which a sensor maintains stable and precise signal acquisition, bounded by its lower and upper detection limits. The minimum detectable pressure is commonly determined via stepwise loading experiments; the threshold is defined as the external pressure at which the sensor output signal surpasses three times the noise standard deviation. This parameter quantifies the sensor's capability to resolve weak pressure stimuli, a core performance indicator for faint-signal monitoring

applications including heartbeat recording, respiratory signal capture, and electronic skin systems. Optimizing this figure of merit can be achieved through sensitivity enhancement and noise suppression strategies.

Pressures for wearable physiological sensing are conventionally divided into three regimes: low pressure (< 10 kPa), medium pressure (10-100 kPa), and high pressure (> 100 kPa) [51]. Distinct application demands dictate disparate pressure detection windows. Electronic skin devices are designed to resolve ultra-subtle mechanical stimuli spanning 1 Pa to 1 kPa. Epidermal wearable sensors generally operate within a 1-10 kPa detection band [10]. By contrast, sensors dedicated to blood pressure and arterial pulse monitoring necessitate a medium-pressure measuring range of 10-100 kPa [52].

2.3.3 Stability and Durability

The stability and durability of a sensor are key factors in determining whether it can transition from the laboratory to commercial and practical applications, as these characteristics determine whether the sensor can withstand complex and variable real-world scenarios and meet required service life expectations. Typically, stability and durability refer to the sensor's ability to maintain its mechanical properties and key output signal metrics without degradation during continuous operation over extended periods (ranging from hours to months). It is also necessary to test the sensor's durability under specific environmental conditions, such as fluctuating temperatures, high humidity, and exposure to sweat, to ensure that sensor performance does not degrade or fail. For wearable flexible pressure sensors, which experience repeated and sustained bending, stretching, and compression, preventing irreversible damage, including wear, fracture, plastic deformation and ageing, presents a significant challenge.

To improve reliability and stability and further extend the service life of sensors, researchers have made significant improvements in recent years in terms of materials, structure, and encapsulation methods. More reliable materials have been adopted, such as fatigue-resistant materials capable of withstanding large deformations and high tensile stress, as well as inert materials resistant to oxidation and humidity. Recent studies have explored fatigue-resistant and flexible materials to improve the mechanical durability of wearable sensors[29]. Structures that allow for greater flexibility and large deformations, such as serpentine structures, are designed to reduce local stress concentrations. Sharma uniformly embedded MXene nanosheets into PVDF-TrFE fibers to create a 3D interconnected porous nanofiber

network, which significantly enhances the sensor's durability due to its excellent mechanical resilience and high toughness. High reliability is maintained over 10,000 cycles even under repeated loading and unloading cycles at high pressure (>167 kPa) [98].

2.3.4 Response/Recovery Times and Hysteresis

Response time denotes the time during which a sensor converts a pressure signal into an electrical signal. Conversely, recovery time measures the time required for the electrical signal to return to its steady-state value after the pressure signal is removed. Typically, response time is defined as the time taken for the electrical signal to vary from 10% to 90% of its steady-state value. It is generally evaluated using the transient signal response curve obtained by applying or removing a specific magnitude of transient pressure. This metric characterizes the electrical signal's ability to track and accurately capture changes in the pressure signal. For this reason, it is critical for applications requiring real-time measurement of rapid pressure fluctuations, such as pulse, motion, and finger manipulation monitoring. If the response and recovery times exceed acceptable limits, signal distortion and lag will occur, causing the measured value to deviate from the actual pressure.

Response time depends primarily on the viscoelasticity of the materials. When pressure is applied, the materials undergo elastic deformation and viscous flow, which increases the time required for the electrical signal to respond. For flexible polymers, high viscoelasticity results in longer response and recovery times. Researchers often employ measures such as reducing the thickness of the active layer, lowering the viscoelasticity of the materials, or introducing porous microstructures to improve the dynamic characteristics of the sensors. Signore et al. developed a flexible piezoelectric pressure sensor using an AlN thin film, which exhibited a response time of approximately 35 ms, as shown in **Figure 2.5(a)**. The response time was evaluated from the voltage waveform after low-pass filtering and was defined as the rise time between 10% and 90% of the output response[99].

Hysteresis refers to the difference in the sensor's electrical output signal between the rising and falling phases of pressure for a given pressure level. This parameter characterizes the sensor's accuracy and the amount of energy dissipated during deformation. Hysteresis in flexible materials primarily stems from the materia's viscoelasticity and friction at material interfaces. The magnitude of the hysteresis can be measured by dividing the maximum output signal difference between the forward and reverse directions by the full-scale output voltage span across the measurement range [56]. The hysteresis of this AlN sensor was

evaluated by measuring the output voltage as the applied pressure was increased and subsequently decreased. As illustrated in **Figure 2.5(b)**, the sensor exhibited similar output responses in both directions, indicating low hysteresis under the reported test conditions[99].

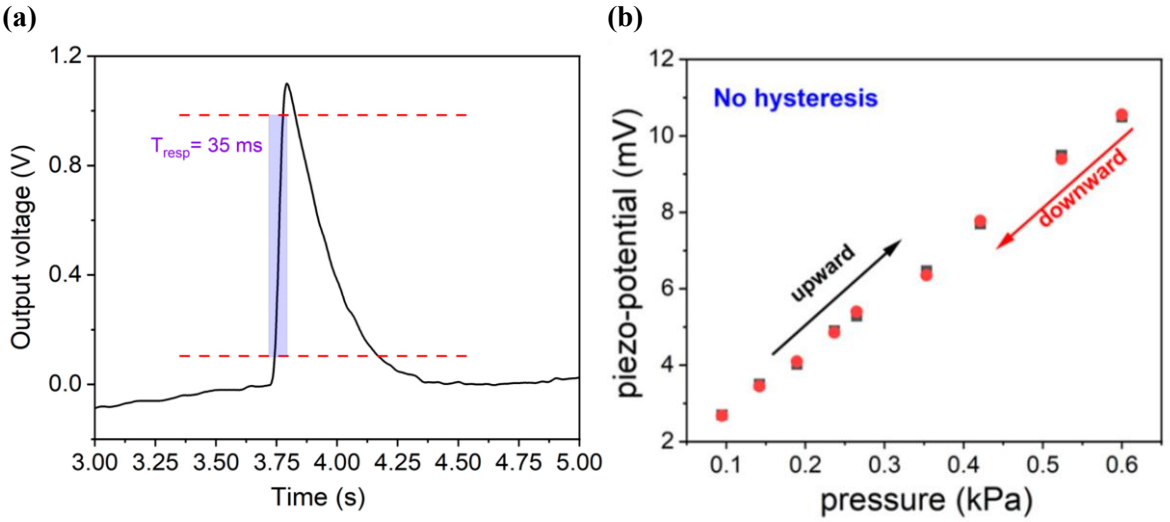


Figure 2.5 Transient response and pressure hysteresis of an AlN piezoelectric sensor. (a) A filtered voltage waveform with a reported 10% to 90% rise time of approximately 35 ms. (b) Voltage readings during increasing and decreasing pressure, enlarged from the calibration inset. The measured curves show low hysteresis under the reported conditions [98].

2.3.5 Flexibility, Biocompatibility, and Degradability

For pressure sensors intended for medical, wearable, and especially implantable use, flexibility, biocompatibility, and degradability are additional requirements as important as electrical performance. Flexibility ensures conformal contact with the skin and mechanical compliance during movement, biocompatibility requires that materials in contact with skin or tissue provoke no cytotoxicity, irritation, or adverse immune response, and degradability allows transient or implantable devices to be safely resorbed at the end of their service life, avoiding secondary removal surgery [64]. Hosseini et al. developed a flexible piezoelectric pressure sensor based on a β-glycine/chitosan film. The fabricated sensor could be bent, demonstrating its flexibility, as illustrated in **Figure 2.6(a)** [19]**.** De Marzo et al. evaluated the cytotoxicity of chitosan and the constituent materials of chitosan piezoelectric transducers using murine 3T3 embryonic fibroblasts. The results presented in **Figure 2.6(b)** show that cell viability remained above 70% after both 24 and 72 h, indicating that the tested materials were noncytotoxic under the reported experimental conditions [79]. Wrońska et al.

investigated the biodegradability of chitosan composite films in a soil environment. **Figure 2.6(c)** presents the appearance of a CS-ZnO 20:1 film before burial and after 4, 6 and 8 weeks. The film progressively degraded during soil burial, with complete degradation reported after 8 weeks under the investigated conditions[100].

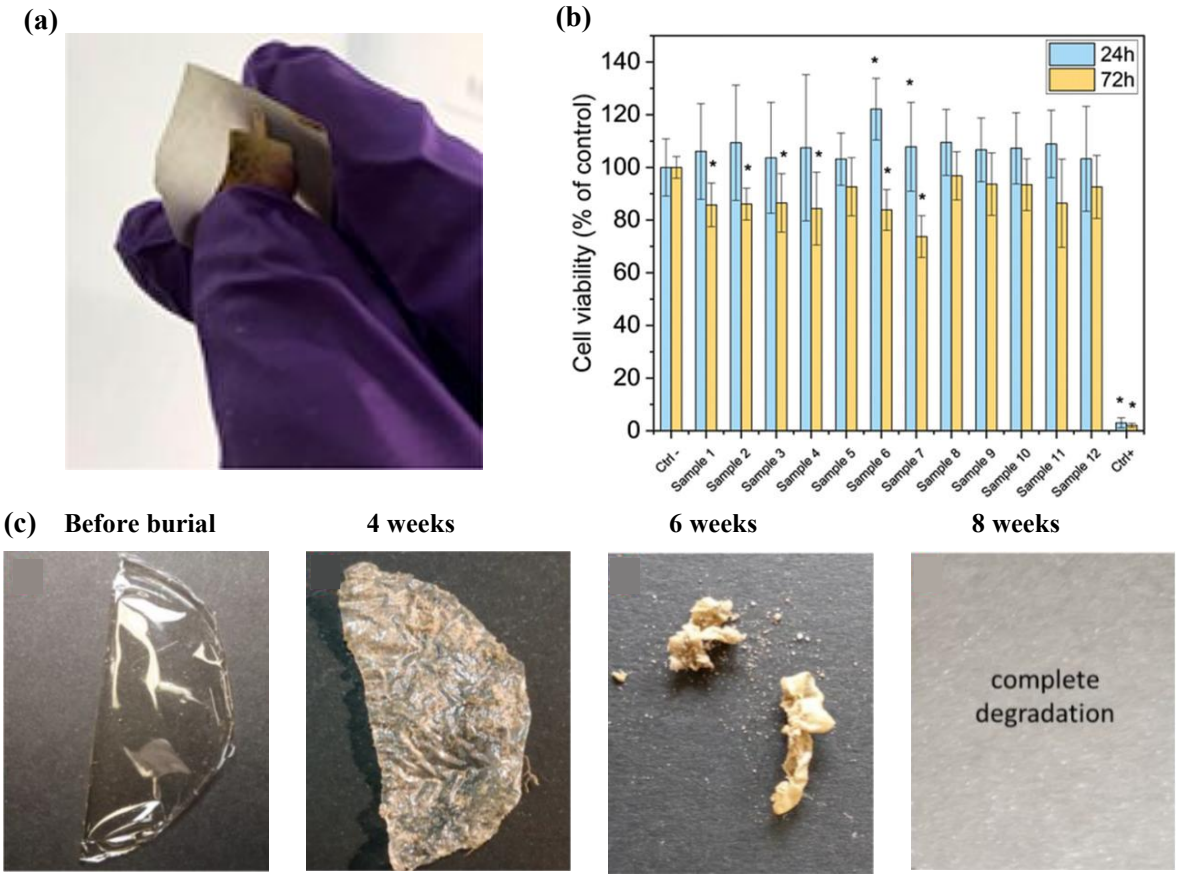


Figure 2.6 Physical and biological assessment of flexible materials. (a) A bent β-glycine/chitosan sensor [23]. (b)Viability of murine 3T3 embryonic fibroblasts after 24 and 72 h of exposure to chitosan and constituent materials of chitosan piezoelectric transducers [88]. (c) CS-ZnO 20:1 films before burial and after 4, 6 and 8 weeks in soil at room temperature. The 20:1 designation is the molar ratio of chitosan amino groups to zinc acetate precursor [100].

2.4 Applications of the Piezoelectric Pressure Sensors

Flexible piezoelectric pressure sensors feature miniaturization, high sensitivity, fast response, self-powering capabilities, and exceptional extensibility, flexibility, and conformability, making them suitable for a wide range of applications. They can convert minute mechanical vibrations or pressure into electrical signals to detect body movements, for example by tracking joint motion and gait, detecting laryngeal vibrations for voice recognition, and

monitoring eye movements associated with driver fatigue. They can also be arranged in sensor arrays to detect pressure distribution maps of the body, palms, or soles of the feet, enabling touch sensing or gait analysis. Non-invasive methods can capture physiological signals such as heart rate, pulse, respiration, and blood pressure, which are commonly used in medical monitoring and diagnosis, while implantable devices provide further monitoring of organs such as the heart, lungs, stomach, and bladder. Furthermore, the self-powered capability of piezoelectric pressure sensors allows for long-term, real-time acquisition of data on body movement and physiological information. In recent years, advancements in wireless transmission and artificial intelligence technologies have further driven the development of pressure sensors in fields such as healthcare, human-computer interaction, and soft robotics.

2.4.1 Health Surveillance and Biomedical Applications

Pressure sensors deployed at diverse body locations can capture data on body pressure distribution, physiological signals, and human motion. Such data can support health monitoring and assist disease diagnosis and treatment. With NFC, Bluetooth or Wi-Fi, the data can be transmitted to mobile devices or databases for analysis using statistical or machine-learning methods, potentially supporting personalised health management and remote monitoring.

- **Cardiovascular Monitoring**

For cardiovascular disorders such as arrhythmia, atrial septal defect, atherosclerosis, arterial hypertension (HTN), and coronary heart disease, extensive research has demonstrated that long-term real-time monitoring of blood pressure, pulse and heart rate serves as an effective tool for early screening, diagnosis and prevention. Conventional measurement approaches including auscultation, oscillometry and tonometry usually rely on bulky, large-sized instruments, making continuous non-invasive monitoring unachievable [101], [102]. Based on data from the Global Burden of Disease (GBD) 2019 study, the Institute for Health Metrics and Evaluation (IHME) at the University of Washington projects that the global crude prevalence of cardiovascular disease will nearly double from 598 million in 2025 to 1.14 billion in 2050, and crude mortality is expected to rise by 73.4% [103]. Min et al. fabricated a flexible piezoelectric pressure sensor for blood pressure monitoring by employing a 2 μm ultrathin flexible PZT film as the active layer, encapsulated with PDMS and medical-grade adhesive. Attached to the radial artery of the wrist, the sensor film can

effectively detect the micro-pressure ranging from 0 to 10 kPa generated by arterial pulsation and delivers a fast response time of 23 ms. In clinical validation tests, the sensor exhibited a measurement bias close to zero, meeting the accuracy requirements for medical wearable blood-pressure devices as show in **Figure 2.7** [104].

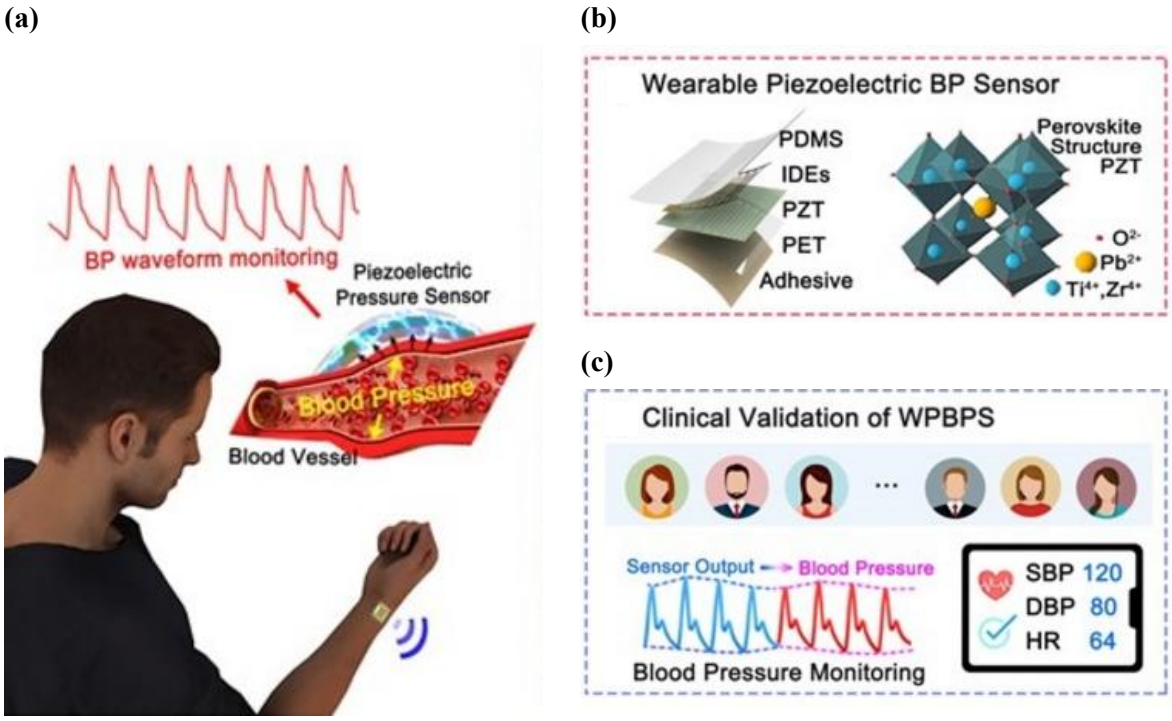


Figure 2.7. Wearable piezoelectric blood pressure monitoring: (a) wrist attachment, (b) sensor structure and (c) conversion of sensor output to estimated blood pressure [104].

- **Respiratory Monitoring**

Piezoelectric pressure sensors (PPS) are adopted for respiratory monitoring. They are placed at the nostrils or mouth to detect airflow fluctuations or attached to the thorax and abdomen to record expansion and contraction movements. Parameters including respiratory frequency and breathing amplitude can be extracted from the measured signals, which enables the discrimination of abnormal respiratory conditions such as Obstructive Sleep Apnea Syndrome (OSAS) and provides objective evidence for the early diagnosis and long-term management of pulmonary disorders.

The pressure sensor adopts a sandwich-laminated structure, with the interlayer consisting of a porous PVDF ferroelectret film fabricated via dimethylhexanediol (DMHD) sacrificial templating, and the top and bottom layers consisting of dense, pore-free, pristine PVDF piezoelectric films. Benefiting from the synergistic coupling of piezoelectric and ferroelectret effects, this design achieves an ultrahigh sensitivity of 595.85 mV/kPa within

the low-pressure regime of 0-25 kPa, making it well-suited for detecting the subtle airflow pressure generated by nasal and oral respiration. Integrated into the inner airflow channel of a facial mask and equipped with miniature data acquisition modules and Bluetooth wireless transmission, the sensor can transmit real-time voltage waveforms to user terminals. Combined with convolutional neural network (CNN) and bidirectional long short-term memory (BiLSTM) temporal network algorithms, the system enables real-time monitoring and classification of four respiratory patterns(normal breathing, weak respiration, coughing and apnoea),achieving 100% classification accuracy [105].

- **In Vivo Implantable Monitoring**

Wearable or attachable sensors can only acquire superficial physiological signals on the body surface, whereas implantable sensors enable direct and accurate detection of physiological information such as cardiovascular activity, cardiac pulsation, intestinal peristalsis, and intracranial pressure. Piezoelectric pressure sensors feature self-powered functionality, eliminating reliance on batteries and thus exhibiting prominent advantages in the field of implantable medical devices.

Wang's team adopted β-phase PVDF piezoelectric thin film as the intermediate active layer of the sensor, with 6 μm-thick silver thin films coated as the top and bottom electrodes. Subsequently, 70 μm-thick polyimide (PI) films were utilized as encapsulation layers to effectively shield the entire sensor. To achieve reliable conformal adhesion between the sensor and intravascular tissues in vivo, an additional 200 μm-thick adhesive hydrogel (AH) layer was integrated. The AH was fabricated from mussel adhesive proteins (MAPs), porcine skin-derived gelatin, acrylic acid, N-hydroxysuccinimide (NHS) ester, and α-ketoglutaric acid, enabling direct attachment onto vascular tissues. In in vitro tests, the sensor delivered a high open-circuit voltage output of 8.3 V and maintained stable performance over 6000 bending cycles. Further in vivo experiments conducted by attaching the sensor to the outer wall of porcine arteries demonstrated its capacity to precisely distinguish subtle arterial blood pressure fluctuations as small as 2 mmHg as shown in **Figure 2.8** [106].

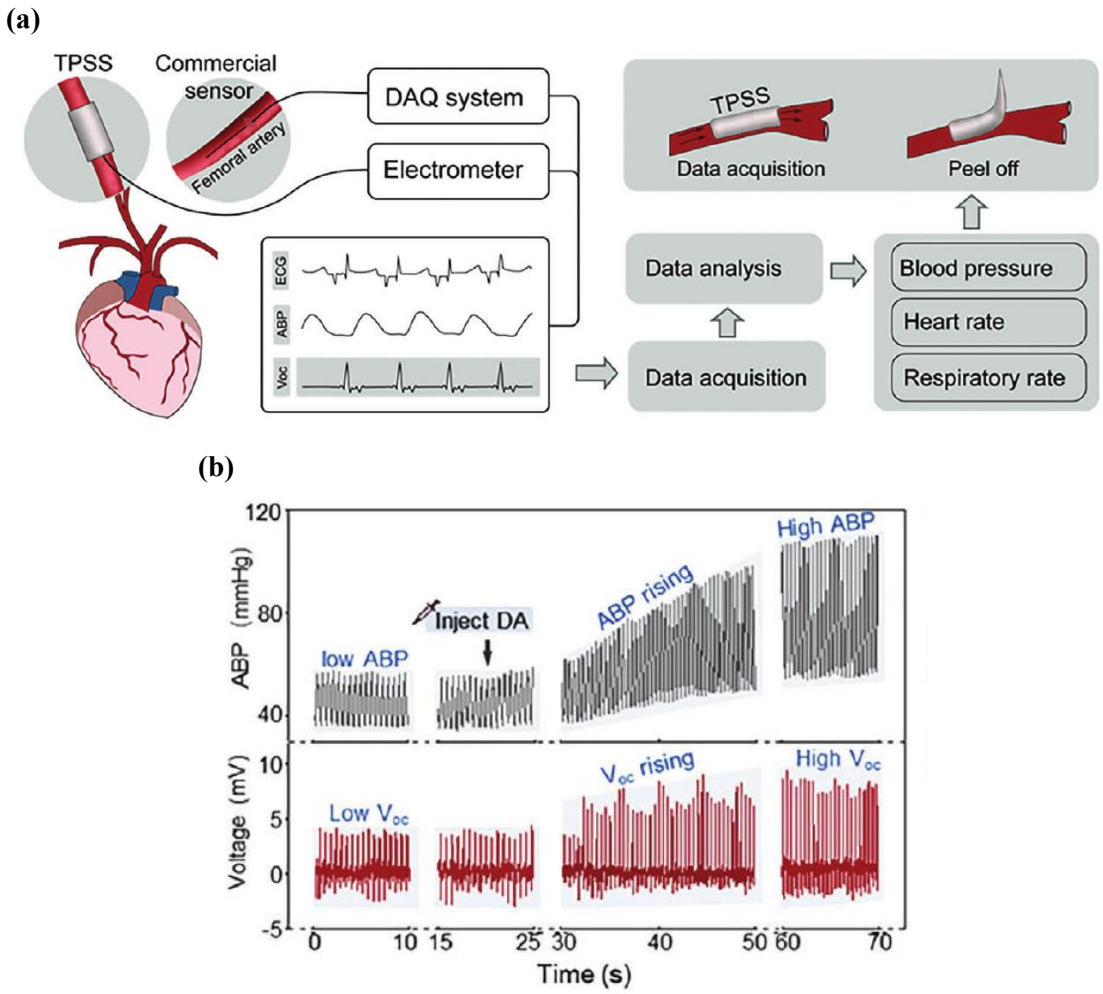


Figure 2.8. In vivo arterial monitoring: (a) the tissue adhesive sensor and reference system and (b) simultaneously recorded arterial pressure and piezoelectric output [106].

2.4.2 Joint motion and pressure distribution monitoring

Piezoelectric pressure sensors deployed on body joints, skin surface, throat and other positions can capture key motion signals and pressure distribution data, which can be applied to gait analysis and movement monitoring, as well as pressure ulcer prevention. These sensors enable real-time quantitative monitoring of postoperative rehabilitation progress, identification of osteoarthritis, detection of abnormal mechanical loads, and screening for tissue injury risks [107]. Guo's group fabricated high-β-phase PVDF nanofibre piezoelectric films via near-field electrospinning driven by a triboelectric self-powered device (T-NFES). A double-layer series structure was adopted, with MWCNT films on both sides serving as electrodes and spin-coated PDMS films providing encapsulation and protection. The device achieves a high sensitivity of 0.2768 V kPa^{-1} within the pressure range of 1-75 kPa. Combined with the long short-term memory (LSTM) deep learning network model, the pure

film-based sensor realises automatic recognition of six types of wrist joint rehabilitation motions with a high test accuracy of 92.6%, exhibiting promising applicability in human motion monitoring and intelligent rehabilitation training systems [108]. An anisotropic composite piezoelectric film is fabricated by incorporating 200 nm BTO nanoparticles into a polydimethylsiloxane (PDMS) matrix. Copper wires and silver paste are employed to draw out stretchable electrodes, followed by thin Ecoflex encapsulation to assemble anisotropic piezoelectric sensors (APS). Two APS units are orthogonally stacked in a cross configuration with PDMS serving as the adhesive interlayer, the two layers feature opposite poling directions and output independent piezoelectric signals. This stacked anisotropic piezoelectric sensor (s-APS) architecture can effectively distinguish eight distinct types of joint motions and quantitatively detect both the bending direction and bending magnitude of human joints. It holds promising application prospects in medical posture correction, sports fatigue monitoring, and human motion capture for rehabilitation training as illustrated in **Figure 2.9** [109].

2.4.3 Human-Machine Interaction and Soft Robotics

Flexible Piezoelectric Pressure Sensors serve as a bridge connecting humans and machines,

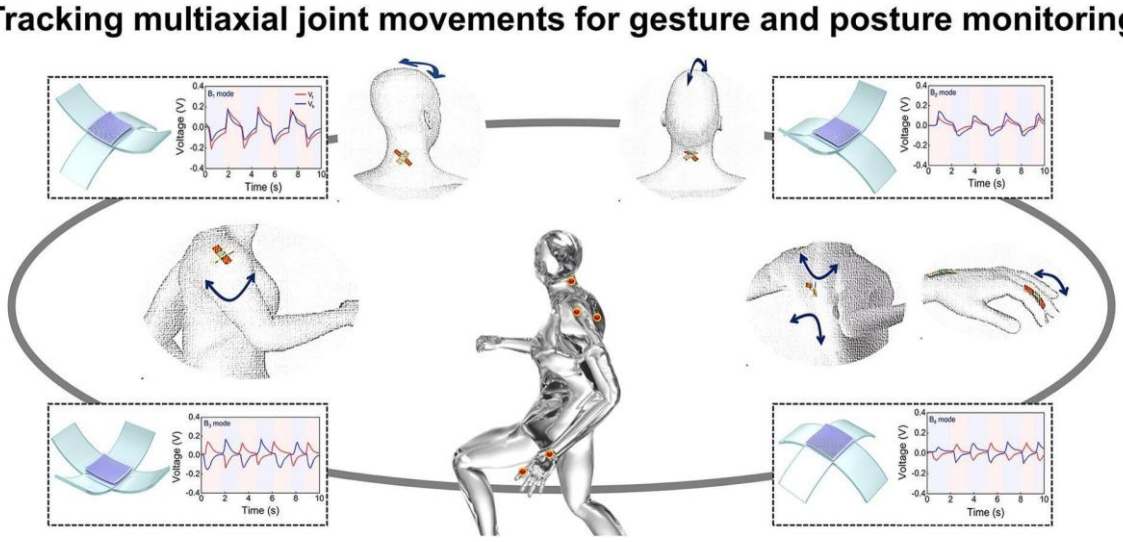


Figure 2.9. Sensor locations and representative two channel outputs for multiaxial joint motion monitoring [109].

converting subtle human movements or pressure distribution into machine-readable control signals. Combined with algorithms to boost recognition accuracy, they realize human-machine interactive robot control. Conventional control relies on manual operation via buttons or joysticks, by contrast, human-machine interfaces (HMI) adopt pressure sensors to

implement gesture recognition, enabling machines to perceive human intentions. Conversely, minor vibrations or pressure variations generated by machines can be transmitted back to humans as tactile feedback via the sensors to support real-time bidirectional interaction. This principle can also be applied to the development of Soft Robotics. Flexible Piezoelectric Pressure Sensors are designed to mimic human cutaneous sensory systems to perceive and respond to mechanical stimuli. When deployed at key positions such as grippers, robotic fingers, manipulator arms or exoskeletons, they are continuously and real-timely detect contact force and pressure distribution. This facilitates dexterous grasping of fragile, soft or irregularly shaped objects. Moreover, subtle force signatures captured by the sensors can be leveraged to discriminate the texture and geometry of target objects. Bouyam et al. developed a PVDF piezoelectric sensor-based system targeting individuals with tetraplegia who retain only functional facial and lingual muscles. The system enables powered wheelchair control via winking and tongue movements as presented in **Figure 2.10**. Six-channel thin-film piezoelectric sensors are deployed: two sensors placed beneath the eyes to capture winking gestures, and four sensors mounted around the lip contour to record tongue motions. Combined with machine learning classification algorithms, the system achieves an average classification accuracy of 98.3% for precise forward and steering control of the wheelchair [110]. An electronic skin developed by Qiu's team integrating piezoelectric pressure sensors and liquid metal strain sensors can detect dynamic touch stimuli and static

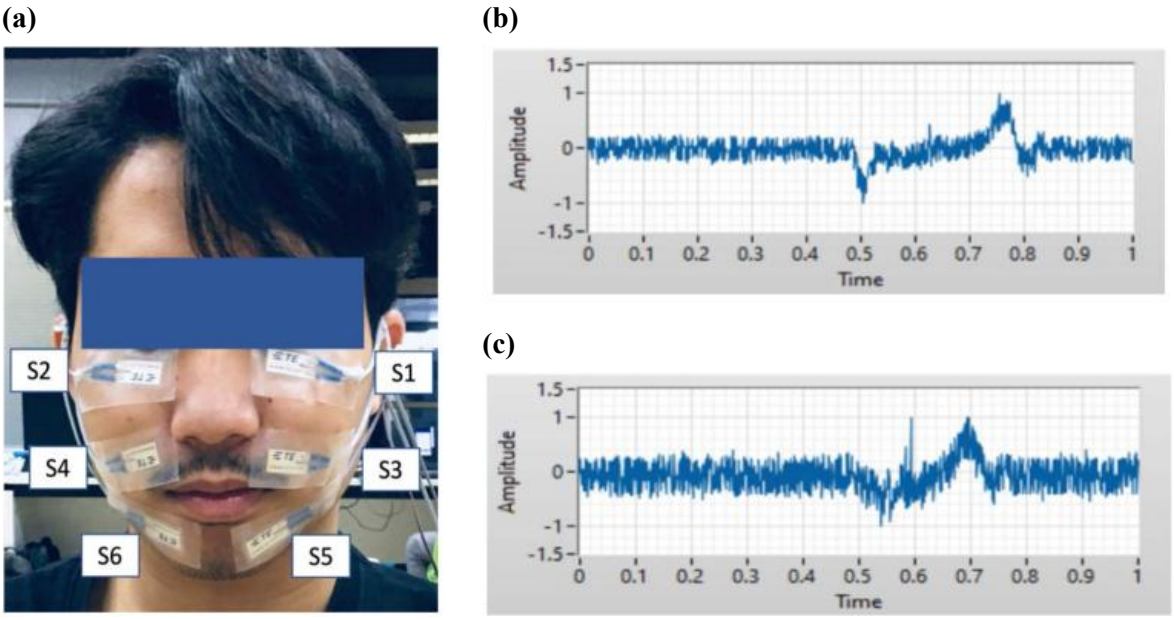


Figure 2.10. Human machine interaction: (a) facial sensor placement, (b) the signal from left eye winking and (c) the signal from tongue movement [110].

deformation respectively to identify the softness of objects. Furthermore, a hybrid GRU-CNN neural network is adopted to train the recognition model, boosting its classification accuracy to 98.95%. This system holds promising application prospects in scenarios including minimally invasive surgical robots, prosthetic rehabilitation, and soft robotics as shown in **Figure 2.11**[111].

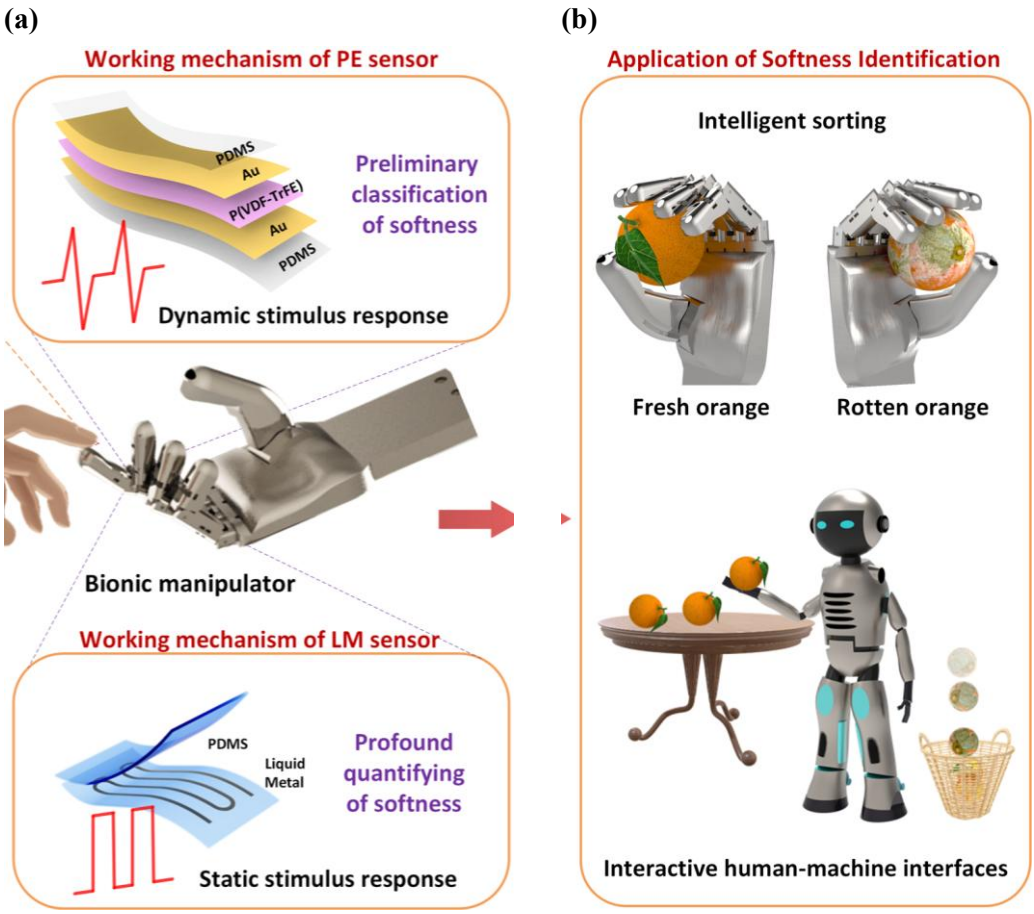


Figure 2.11. Electronic skin for robotic softness identification: (a) piezoelectric and liquid metal sensing mechanisms and (b) robotic manipulation and sorting [111].

2.5 Summary and Research Gaps

The reviewed literature shows substantial progress in flexible pressure sensors, self-powered transduction mechanisms and piezoelectric materials. Piezoresistive and capacitive sensors are effective for many static and dynamic pressure measurements, but they generally require external power or readout circuitry. Triboelectric sensors provide self-powered operation but are affected by contact wear, humidity sensitivity and high impedance. Piezoelectric pressure sensors are consequently suitable for self-powered dynamic pressure detection, provided that

the active material can generate a reliable output while remaining flexible and compatible with wearable use.

The literature points to four research gaps. First, pure chitosan films require more systematic evaluation as self-powered piezoelectric pressure sensors under controlled pressure and frequency conditions. Secondly, chitosan-based composite films need further study to determine whether output improvement can be achieved without compromising film quality and flexibility. Thirdly, bio-derived piezoelectric films still need more complete evaluation under wearable conditions, including repeated loading, mechanical deformation and practical attachment formats. Finally, standardised comparisons of sensitivity, response time, repeatability and device-to-device variation remain limited across flexible pressure-sensor studies. These gaps provide the literature basis for the experimental work described in the following chapters.

Overall, this chapter shows that piezoelectric pressure sensors are well suited to dynamic pressure detection, but their performance depends strongly on material selection and film structure. Chitosan is relevant because it combines bio-derived origin, solution processability, flexibility and degradability. Its lower electrical output compared with many ceramic materials explains why both pure chitosan films and chitosan-based composite films continue to be investigated in the literature.

Chapter 3 Methodology

3.1 Materials

All materials and equipment used in the experimental work in this thesis are listed in Table 3.1 and Table 3.2. All reagents and materials were used in their original condition as received.

Table 3.1 Reagents and materials used in the experiment.

Material	Form and key specification	Supplier
Chitosan	low molecular weight, 9012-76-4, MFCD00161512	Merck Life Science, UK
Acetic acid	glacial, ReagentPlus®, ≥99%, 64-19-7, MFCD00036152	Merck Life Science, UK
$BaTiO_3$	nanopowder (cubic), 50 nm (SEM), 99.9% trace metals basis, MFCD00003447	Merck Life Science, UK
ZnO	nanoparticles, <100 nm particle size (TEM), ≤40 nm avg. part. size (APS), 20 wt.% in H_2O, 1314-13-2, MFCD00011300	Merck Life Science, UK
Parylene C dimer	Parylene C	Specialty Coating Systems Inc., USA
Copper tape	Conductive, 100 μm thick	RS Components, UK
Polyimide (Kapton) tape	Outer encapsulation,25 μm thick	RS Components, UK
Conductive carbon adhesive tape	Double-sided, AGG3939C, 50 mm × 20 m	Agar Scientific, UK
Silver	Conductive adhesive	RS Components, UK

Table 3.2 Main instruments and equipment used in the experiment.

Equipment	Model	Manufacturer
Field-emission scanning electron microscope (FE-SEM)	Nova Nano SEM	FEI Company, Hillsboro, Oregon, USA
X-ray diffractometer (XRD)	Mini Flex 600	Rigaku Corporation, Tokyo, Japan
Fourier-transform infrared spectrometer (FTIR)	Jasco FTIR-4100	JASCO Corporation, Tokyo, Japan
Atomic force microscope (AFM)	Dimension 3100, with Nano Scope software	Bruker Corporation, Billerica, Massachusetts, USA
Raman spectrometer	LabRAM HR	Horiba Jobin Yvon, Palaiseau, France
Optical 3D measurement system	Infinite Focus G4	Alicona Imaging GmbH, Graz, Austria
d_{33} meter	ZJ-6B Quasi-Static d_{33}/d_{31} Meter	JKZC, Beijing, China
Impedance analyser	4294A	Agilent Technologies, Santa Rosa, California, USA
Tensile machine	Instron 3367	Instron, Norwood, Massachusetts, USA
Loading vibration system	TV 50018	TIRA GmbH, Schalkau, Germany
Ultrasonic bath	Camsonix C575T	Camlab Ltd, Cambridge, UK

Digital storage oscilloscope	DSOX3014T	Keysight Technologies, Santa Rosa, California, USA
Parylene C coating system (CVD)	SCS Labcoter 2 (PDS 2010)	Specialty Coating Systems Inc., Indianapolis, Indiana, USA
Bluetooth chip	nRF52840 SoC	Nordic Semiconductor ASA, Trondheim, Norway

3.2 Method

3.2.1 Preparation of Piezoelectric Films

To prepare the chitosan solution, a low-molecular-weight chitosan powder (Merck Life Science, UK, CAS 9012-76-4) with a degree of deacetylation of 75-85% was used as the starting material. First, 2 g of chitosan powder was mixed with 1 mL of acetic acid and 100 mL of deionised water to obtain a 2% (w/v) chitosan solution, and a magnetic stir bar was then added. The solution was placed on a magnetic stirrer and heated to 60-70 °C, and was then sonicated at 37 kHz for 30 min. After thorough mixing, the solution was degassed under vacuum for 1-2 h, until the visible bubbles in the solution had largely disappeared. The prepared chitosan solution was subsequently used for the pure chitosan films and as the polymer matrix for the CS-ZnO and CS-BTO composite films.

For the chitosan-based composite films, the inorganic filler content was calculated as the weight percentage (wt.%) of the filler relative to the combined mass of the filler and chitosan using Equation 3.1:

$$\text{wt.\%} = \frac{m_{\text{filler}}}{m_{\text{filler}} + m_{\text{CS}}} \times 100\% \tag{3.1}$$

where m_{filler} is the mass of the inorganic filler and m_{CS} is the mass of chitosan. For ZnO supplied as a 20 wt.% aqueous dispersion, the ZnO mass was calculated from the amount of dispersion used and its stated ZnO content. For BTO powder, the weighed powder mass was used directly. Water and acetic acid were not included in the calculation.

The thickness of the chitosan films was controlled by varying the volume of solution cast into the inner circular area at the base of polystyrene Petri dishes of the same size. For films prepared under the same thickness condition, the casting volume, spin-coating and drying conditions were kept consistent. After drying, the thickness of the prepared films was measured using a thickness gauge (Logitech CG10).

3.2.2 Fabrication of Pressure Sensor

The active film was positioned between the upper and lower copper electrodes to form a sandwich structure. Double-sided conductive carbon adhesive tape (AGG3939C, Agar Scientific, UK) was applied between each surface of the film and the corresponding copper electrode to provide electrical contact and maintain stable interfacial contact during mechanical loading. Šutka et al. reported that electrical signals generated by friction and contact separation can be mistaken for piezoelectric output [112]. Accordingly, the bonded interfaces were intended to restrict relative sliding and repeated contact and separation, which could reduce potential triboelectric contributions to the measured electrical output. The assembled device was subsequently encapsulated with polyimide tape to provide electrical insulation and mechanical protection.

3.3 Material Characterisation of Piezoelectric Films

A comprehensive understanding of piezoelectric material characteristics is critical for evaluating the performance and elucidating the working mechanism of the fabricated pressure sensors. These characteristics include surface properties, microstructural and crystalline phase features, mechanical properties, and electrical output characteristics.

3.3.1 Surface Characterisation of Piezoelectric Films

- **Scanning Electron Microscopy (SEM)**

The surface morphology of the films was characterised by field-emission scanning electron microscopy (FE-SEM, FEI Nova NanoSEM). Due to the low conductivity of the polymer and composite films studied, the samples were fixed to the specimen stub with conductive tape before testing, and a thin layer of platinum (Pt) was deposited on the surface by sputter coating to avoid charge accumulation during imaging. Images were then acquired in secondary-electron mode and then used to examine the surface morphology and film quality

of each film (such as surface flatness, cracks and pores), with particular attention to the dispersion of ZnO and $BaTiO_3$ nanoparticles within the chitosan matrix and the appearance of agglomeration at higher loading.

- **Atomic force microscopy (AFM)**

The surface topography of the PAC films was characterized by atomic force microscopy (AFM, Bruker Dimension 3100) operated with NanoScope software, on a scan area of 5 μm × 5 μm. AFM provided nanoscale topographic and phase images from which the surface roughness was obtained, complementing the larger-area roughness measured by optical profilometry.

- **Optical 3D profilometry**

The surface roughness and morphology of the PAC films were measured using an optical 3D measurement system based on focus variation (Alicona InfiniteFocus G4). AFM resolves nanoscale features within a small area, whereas the focus-variation system characterises the surface profile at the micrometre scale, providing information on both the roughness and overall morphology of the film.

3.3.2 Microstructural and Crystalline Phase Structure of Piezoelectric Films

- **X-ray diffraction (XRD)**

The crystalline structure and phase composition of the films were determined by X-ray diffraction (XRD, Rigaku MiniFlex 600) with Cu-Kα radiation (λ = 0.15406 nm) and data collected in the 2θ range of 10° to 70° at a step size of 0.01° and a scan speed of 5°/min. XRD was used to confirm the semicrystalline nature of chitosan and Parylene C. For the CS-ZnO and CS-BTO composites, it was used to verify that the ZnO or BTO reflections were present alongside those of the chitosan matrix without secondary phases. The degree of crystallinity was determined from the diffraction pattern using **Equation 3.2**[113]:

$$X_c = \frac{A_c}{A_c + A_A} \times 100\ (\%) \tag{3.2}$$

where A_C is the integrated area of the crystalline peaks and A_A is the area under the curve of the amorphous peak. These areas were determined by curve fitting using OriginPro (OriginLab Corporation). The mean crystallite size was estimated from the broadening of the principal reflection using the **Scherrer Equation 3.3**[114]:

$$D = \frac{K\lambda}{\beta \cos\theta} \tag{3.3}$$

where D is the crystallite size (nm), K is shape factor also known as the Scherrer constant (0.9), λ is the wavelength of incident radiation (0.15406 nm), β is the full width at half maximum (FWHM) of the reflection in radians, and θ is the Bragg angle of peak position in radians.

- **Fourier-transform infrared spectroscopy (FTIR)**

The chemical structure of the films was investigated by Fourier-transform infrared spectroscopy (FTIR, Jasco FTIR-4100). The spectra were recorded across 4000-600 cm^{-1} at a resolution of 2 cm^{-1}, averaged over 64 scans. The results were used to identify the functional groups of the films and from shifts or changes in the relative intensity of characteristic bands to assess whether hydrogen bonding or other interfacial interactions were present within the composite materials.

- **Raman spectroscopy**

Raman spectroscopy was performed to examine the molecular structure of the PAC films using a LabRAM HR system (Horiba Jobin Yvon) equipped with a Ventus 532 nm laser (100 mW). The Raman spectra were used to identify the characteristic bands of PAC and to follow the changes in these bands with film thickness. This technique was applied only to the PAC films.

3.3.3 Mechanical Characterisation of Piezoelectric Films

The mechanical response of the films was characterised by tensile testing using a universal testing machine (3367)**.** Film specimens were clamped and extended at a constant rate, and the resulting stress-strain curve was recorded. The Young's modulus was calculated from the linear (elastic) region of the force-displacement curves using **Equation 3.4**[115]**:**

$$\mathrm{E} = \frac{\mathrm{dF}}{\mathrm{d\Delta L}} \frac{\mathrm{L_0}}{\mathrm{A}} \tag{3.4}$$

where E is the Young's modulus, $\frac{dF}{d\Delta L}$ is the slope of the force-displacement curve in the elastic region, L_0 is the original length of the specimen, and A is the cross-sectional area. Tensile testing was used to assess the stiffness and deformability of the films relevant to wearable application.

3.3.4 Electrical Characterisation of Piezoelectric Films

- **Dielectric and impedance measurement**

The relative permittivity (ε_r) is another important material parameter that quantifies the capacity to store charge under an applied electric field. The dielectric and impedance behaviour of the films was characterised using an impedance analyser (Agilent 4294A), which records the impedance as a function of frequency under a small alternating voltage applied across the electrode film. The capacitance was obtained from the impedance analysis. The tested film, serving as the piezoelectric layer in a sandwich structure between the two electrodes, was treated as a parallel-plate capacitor, and the ε_r was obtained from the measured capacitance using **Equation 3.5**[19]**:**

$$\varepsilon_r = \frac{\varepsilon_c}{\varepsilon_0} = \frac{Cd}{\varepsilon_0 A} \tag{3.5}$$

where C is the capacitance, d is the film thickness, ε_0 is the permittivity of free space (8.85 $\times$ 10^{-12} F/m), and A is the electrode area. These measurements were used to assess the charge storage and transport behaviour of the films.

- **Piezoelectric coefficient (d_{33})**

The piezoelectric coefficient d_{33} is a key indicator of the piezoelectric performance of a material, representing the electric charge generated per unit applied force and thus its efficiency in converting mechanical energy into electrical energy. It was measured by the quasi-static (Berlincourt) method using a d_{33} meter (ZJ-6B Quasi-Static d_{33}/d_{31} Meter, Beijing JKZC). A force of approximately 0.25 N was applied at 110 Hz, a frequency well below the reported fundamental resonance of the tested sample. Mechanical probes supported the sample, provided the electrical contact, and measured the charge response using **Equation 3.6** [116]:

$$d_{33} = \frac{Q}{F} \tag{3.6}$$

where Q is the generated charge and F is the applied force. The value reported for each film was averaged over several measurement points.

- **Output voltage measurement**

The output performance of the pressure sensors was characterised under periodic compressive loading using a tuneable-frequency vibration system (TV 50018, TIRA GmbH). The applied pressure and excitation frequency were set using VibrationVIEW software (Version 2017.1.2.0), which controlled the vibration system during testing. An additional force sensor positioned beneath the sample was used to provide an independent real-time check of the applied load. The corresponding output voltage was recorded using a digital storage oscilloscope (Keysight DSOX3014T) connected across the device electrodes. The test setup is shown in **Figure 3.1**. To evaluate the output voltage and sensitivity, the applied pressure and frequency were varied independently: a pressure-increment test was carried out at a fixed frequency, and a frequency-increment test at a fixed pressure, within the ranges given in the corresponding results chapter. For each sensor type, at least eight samples were tested, and the output responses were averaged across the samples. Each set of measurements comprised at least 20 repeated measurements, with the corresponding mean values used for subsequent performance analysis and sensitivity calculations.

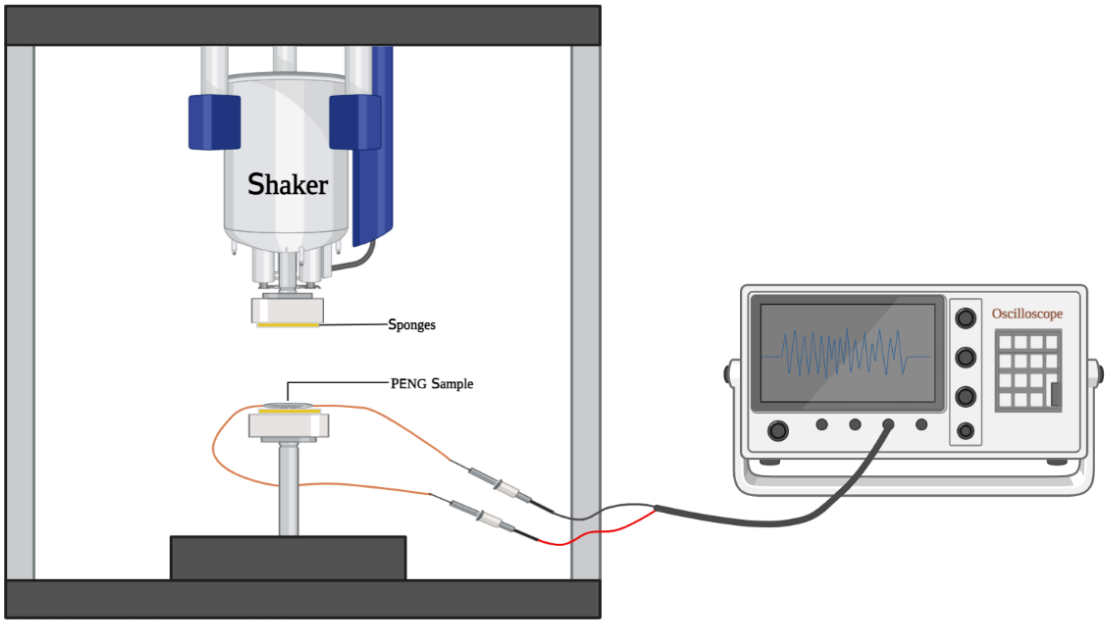


Figure 3.1 Schematic of the vibration test setup (TV 50018, TIRA GmbH), a tuneable pressure and frequency loading system used for pressure sensor characterisation.

Chapter 4: Pure Chitosan-Based Flexible Self-Powered Piezoelectric Pressure Sensor for Pacinian Corpuscle Mimicry

4.1 Introduction

Human skin contains many mechanoreceptors that detect mechanical stimuli such as pressure, vibration, texture, and deformation, and transmit the resulting neural signals through the peripheral nerves and the spinal cord to the somatosensory cortex, where they are perceived. The mechanoreceptors responsible for pressure detection are commonly divided into two types: slowly adapting (type-I) receptors, which respond to static and sustained stimulation, and rapidly adapting (type-II) receptors, which respond to dynamic stimulation, producing signals at the onset and the offset of a stimulus rather than during steady loading[117]. A pressure sensor that emulates these mechanoreceptors and converts the mechanical stimuli of the human body into electrical signals is a key component for artificial tactile sensor[118]. Among the various pressure sensors, resistive and capacitive types offer high sensitivity, but they generally require an external bias voltage or a battery, which limits their long-term use in wearable applications [119]. A piezoelectric pressure sensor, by contrast, converts mechanical deformation directly into an electrical signal through the direct piezoelectric effect, without an external power supply, which makes it particularly suited to the detection of dynamic pressure signals such as pulse and vibration.

The Pacinian corpuscle is a representative rapidly adapting mechanoreceptor, it lies in the deepest subcutaneous layer of the skin, is the most sensitive to high-frequency vibration, and is mainly responsible for detecting dynamic stimuli such as high-frequency vibration and deep pressure as illustrated in **Figure 4.1**[120]. It responds quickly to mechanical stimulation, generating signals only at the onset and offset of the stimulus rather than under sustained static pressure, as shown in **Figure 4.1(a)**. The piezoelectric pressure sensor operates in a comparable way, producing an electrical signal mainly under dynamic deformation. In the self-powered piezoelectric pressure sensor studied here, the piezoelectric layer is sandwiched between top and bottom electrodes and insulation layers, so that dynamic compression generates a voltage output that mirrors the response of the Pacinian corpuscle, and the structure can hence be regarded as an artificial mechanoreceptor that emulates its

dynamic pressure- and vibration-sensing role[121], as shown in **Figure 4.1(b)**. It should be noted that the analogy adopted here is functional, concerning the dynamic sensing behaviour of the receptor rather than its detailed biological structure.

Inorganic piezoelectric ceramics such as lead zirconate titanate generally provide a strong electrical output, but their rigidity, brittleness, and processing requirements restrict their direct use in flexible wearable sensors [10]. Natural polymers, by contrast, offer better compliance and solution processability. Among these, chitosan is a natural polysaccharide obtained by the deacetylation of chitin, which is the second most abundant polysaccharide in nature after cellulose and is widely found in the shells of crustaceans such as shrimp and crabs, producing chitosan from this kind of biological waste turns a waste resource into a useful material and makes it abundant, low-cost, and renewable [19]. Beyond this advantage in sourcing, chitosan is also solution-processable, flexible, and reported to be biocompatible and biodegradable. In addition, the polar functional groups of the chitosan molecule, together with its semi-crystalline polymeric structure, provide a material basis for generating measurable electrical signals under mechanical stimulation[84]. Accordingly, this chapter investigates pure chitosan, focusing on its self-powered response under dynamic pressure and its feasibility as an artificial mechanoreceptor.

A flexible self-powered pressure sensor is fabricated using a chitosan film as the piezoelectric layer, with a simple sandwich structure in which the chitosan film is embedded between top and bottom copper electrodes and encapsulated with polyimide for insulation. Film thickness is an important factor affecting the sensing performance, since for a piezoelectric sensor, the thickness is not only a geometrical parameter but may also influence the strain transfer, the deformation, the charge generation, and the voltage output, two chitosan films of different thickness were accordingly prepared and compared, so that the influence of the chitosan-layer thickness on the sensing response could be examined.

With these sensors prepared, the chapter proceeds as follows. The surface morphology, crystalline structure, and chemical structure of the chitosan films are first characterised, in order to establish the material basis for the subsequent discussion of the sensing results. The dynamic pressure-sensing capability of the sensors, and their feasibility for functionally emulating the dynamic sensing behaviour of the Pacinian corpuscle are then evaluated by analysing the output response of the two films under different pressures and frequencies.

Finally, the solubility of the chitosan films is examined as an indication of their potential as a degradable flexible-electronic material.

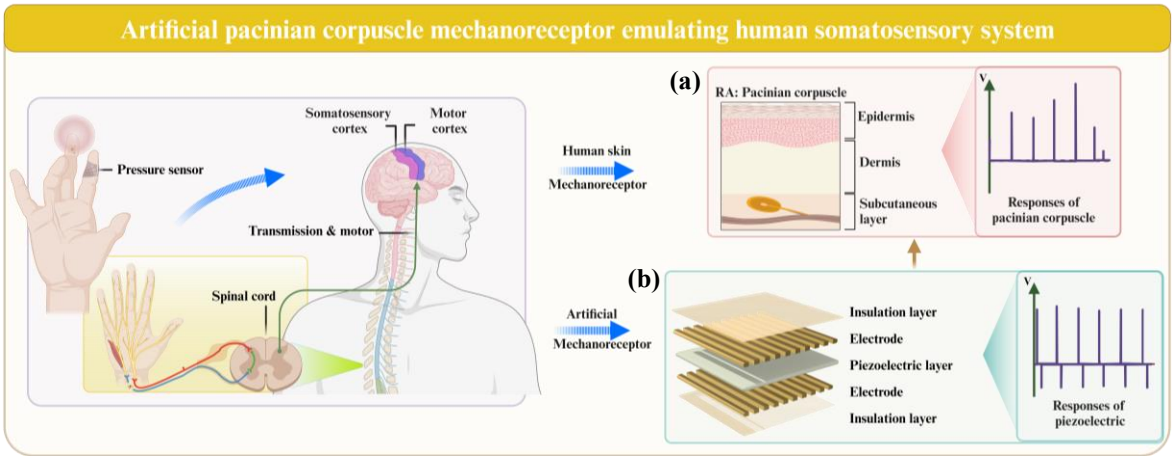


Figure 4.1 Artificial Pacinian corpuscle mechanoreceptor emulating the human somatosensory system. The left panel shows the transmission of a pressure signal from a sensor on the fingertip through the peripheral nerves and spinal cord to the somatosensory and motor cortices. (a) The Pacinian corpuscle, a rapidly adapting (RA) mechanoreceptor located in the subcutaneous layer beneath the epidermis and dermis, responds to dynamic stimuli and produces a signal only when the stimulus changes. (b) The artificial mechanoreceptor, a sandwich-structured piezoelectric sensor comprising a piezoelectric layer between electrodes and insulation layers, generates a voltage output under dynamic compression that emulates the dynamic response of the Pacinian corpuscle.

4.2 Method

4.2.1 Preparation of Chitosan Films

To prepare the chitosan films, a low-molecular-weight chitosan powder (Merck Life Science, UK, CAS 9012-76-4) with a degree of deacetylation of 75-85% was used as the starting material. The preparation of the flexible chitosan films is illustrated schematically in **Figure 4.2**. First, 2 g of chitosan powder was mixed with 1 mL of acetic acid and 100 mL of deionised water to obtain a 2% (w/v) chitosan solution, and a magnetic stir bar was then added. The solution was placed on a magnetic stirrer and heated to 60-70 °C, and was then sonicated at 37 kHz for 30 min. After thorough mixing, the solution was degassed under vacuum for 1-2 h, until the visible bubbles in the solution had largely disappeared. The chitosan solution was subsequently drop-cast onto a polystyrene Petri dish and spin-coated for 30 s at 1000 rpm to ensure a uniform spreading throughout the dish, after which it was dried in a heater at 38.7 °C. Once fully dried, the chitosan film was mechanically flexible and optically transparent, and could be readily peeled from the dish, exhibiting good

flexibility and mechanical robustness under repeated bending and twisting. The prepared chitosan films were measured for thickness with a thickness gauge (Logitech CG10), and two films of different measured thickness were selected for the subsequent tests. The thinner film, of approximately 50 µm, is referred to as chitosan film S1 (Chi-S1), and the thicker film, of approximately 85 µm, as chitosan film S2 (Chi-S2).

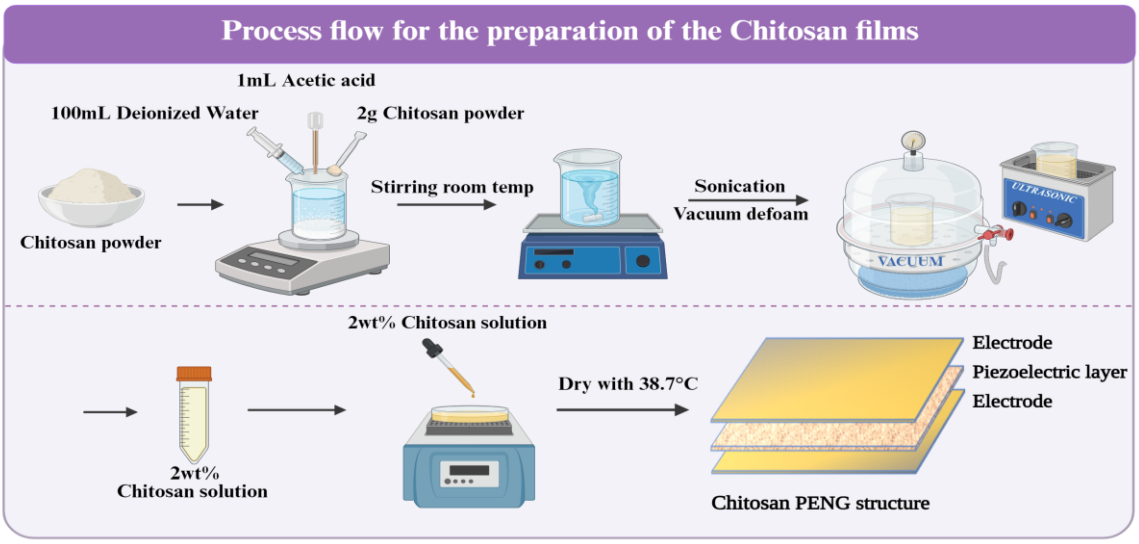


Figure 4.2 Preparation of chitosan films and sensors.

4.2.2 Fabrication of Chitosan Sensor

The chitosan films were assembled into pressure sensors with a sandwich structure, as illustrated in **Figure 4.2**, in which the chitosan film served as the piezoelectric layer between two copper electrodes. Copper tape was used as the top and bottom electrodes, providing both the electrical contact for collecting the charge generated by the chitosan layer and the mechanical support for the device, with a conductive connection made to external wires for measurement. The adhesive backing of the copper tape was attached to the flexible substrate and served only for mechanical fixation. The copper surface in contact with the chitosan film was free of adhesive, with no adhesive layer present at the electrode-film interface used for voltage and current measurements. Aluminium foil was used as the top and bottom electrodes in preliminary pure-chitosan devices. Copper electrodes were subsequently adopted because they provided suitable electrical contact and mechanical stability within the flexible sandwich structure. The assembled device was then encapsulated with polyimide tape on the outer surfaces, which provided electrical insulation and mechanical protection against the external environment while preserving the overall flexibility of the sensor.

4.3 Results and Discussion

4.3.1 Material Characterisation

- **Morphology of chitosan using SEM**

The surface morphology of the chitosan films was examined by scanning electron microscopy, as shown in **Figure 4.3**. Chi-S1 and Chi-S2 were imaged at comparable magnifications and at a 2 μm scale. The films presented a relatively flat, dense and continuous surface, with a fine texture, and no obvious large pores, cracks or particulate features were observed. Such a continuous morphology indicates that the solution-casting method produced a well-formed chitosan film. A small number of isolated bright specks and faint marks were visible on the surface, as these are not connected to the surrounding film texture and do not recur in a regular pattern, they are likely to be associated with sample preparation or surface contamination rather than with the film-forming structure of the chitosan itself. Importantly, the thinner Chi-S1 and the thicker Chi-S2 showed essentially the same surface morphology, which indicates that, at the scale of the present SEM observation, the difference in thickness did not introduce any obvious large-scale surface defects.

From the perspective of the sensor structure, the surface continuity of the chitosan film is important for obtaining a repeatable output. Since the sensor in this chapter uses a sandwich structure in which the chitosan film is held between upper and lower copper electrodes, the contact between the piezoelectric layer and the electrodes directly affects the collection of charge under applied pressure and the stability of the output signal. If the film surface

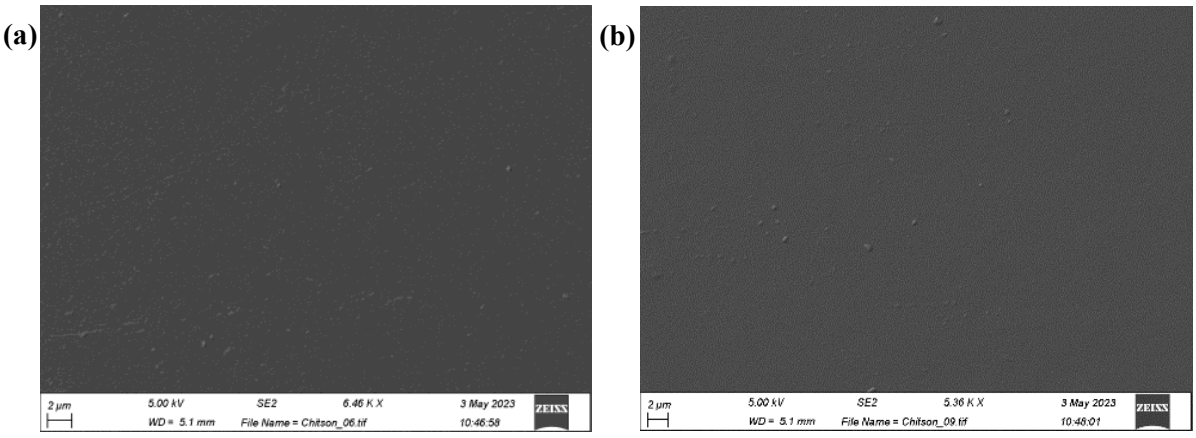


Figure 4.3 SEM images of the chitosan films at 2 μm scale: (a) the thinner Chi-S1 and (b) the thicker Chi-S2.

contained obvious cracks, pores, or large aggregated particles, this could lead to uneven local contact, stress concentration, or unstable charge-collection paths, and so reduce the repeatability of the output voltage. By contrast, both Chi-S1 and Chi-S2 present a continuous and dense surface morphology, indicating that both films are suitable as the piezoelectric layer in a sandwich-structured sensor.

- **Structural characterisation of chitosan using XRD**

The crystalline structure of the films was examined by X-ray diffraction, and the diffraction patterns are presented in **Figure 4.4**. Both Chi-S1 and Chi-S2 displayed two broad diffraction peaks, centred at 2θ values of approximately 10° and 20°, which correspond to the (020) and (200) planes of chitosan[84]. The peak near 10° is generally attributed to the hydrated crystalline regions of chitosan, where the polysaccharide chains pack together with water molecules held in the lattice, while the peak near 20° reflects the more regular crystalline packing of the chitosan backbone[88]. Both peaks are broad and relatively weak, and no other sharp reflections appear, which indicates that the films show semi-crystalline characteristics, with ordered crystalline regions coexisting with amorphous regions. This is consistent with the behaviour generally reported for solution-cast chitosan films[122]. The diffraction patterns of Chi-S1 and Chi-S2 were highly similar, indicating that, within the resolution of this measurement, the difference in thickness did not produce a discernible change in the crystalline structure.

Compared with a fully amorphous polymer, a semi-crystalline polymer contains regions of partially ordered molecular chains, which may help the polar groups to undergo changes in orientation or in local charge distribution under an external mechanical stimulus, while the amorphous regions provide flexibility and deformability, allowing the film to deform reversibly under periodic compression. The coexistence of ordered crystalline regions and amorphous regions in the chitosan film, consequently, helps to meet the two basic requirements of flexible deformation and electrical-signal generation at the same time.

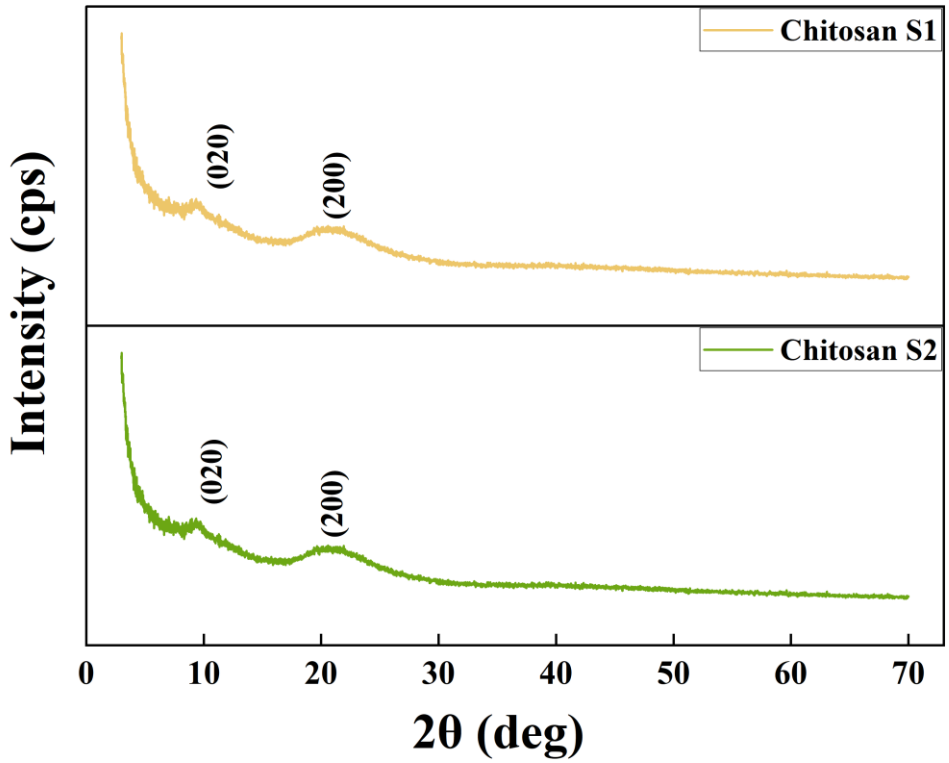


Figure 4.4 XRD patterns of the chitosan films Chi-S1 and Chi-S2.

- **Chemical characterisation of chitosan using FTIR**

The chemical structure was examined by Fourier-transform infrared spectroscopy, and the spectra are presented in **Figure 4.5**. For visual clarity and direct comparison of the characteristic absorption bands, the spectra of Chi-S1 and Chi-S2 were vertically offset. Accordingly, the y-axis is presented as transmittance in arbitrary units (a.u.) rather than as absolute percentage transmittance; this graphical offset does not affect the peak positions or their assignments. Both spectra show the characteristic absorption bands of chitosan. The band at approximately 2908 cm^{-1} corresponds to the C-H stretching vibration of the polysaccharide backbone, while the band at approximately 1556 cm^{-1} is attributed to the N-H bending of the amine groups and the amide II vibration. The bands at approximately 1410 and 1225 cm^{-1} are associated with the C-N stretching and the C-O-C vibrations of the glycosidic linkage, and the strongest band, at approximately 1032 cm^{-1}, corresponds to the C-O stretching of the polysaccharide backbone. The further bands at approximately 868 and 577 cm^{-1} are associated with the ring vibrations of the saccharide units. These bands confirm that the cast films retain the molecular structure of chitosan [123]. The spectra of Chi-S1 and Chi-S2 are consistent with each other, confirming that the chemical structure of chitosan is retained in both films, so that the difference in the output response of the two sensors is more appropriately discussed in terms of the film thickness than attributed to a detectable

change in chemical structure. From the perspective of the piezoelectric response, the presence of these polar functional groups provides a molecular-level basis for the generation of an electrical signal by the chitosan film under mechanical stimulation. The hydroxyl and amine groups are strongly polar, and when the film is periodically compressed, the chain spacing, the inter-chain hydrogen bonding, and the relative orientation of the polar groups may change with the deformation, leading to a change in the local charge distribution within the film and a measurable voltage output at the electrodes. This process indicates that the polar chemical structure of chitosan itself is an important basis for its electrical response in the absence of an added piezoelectric phase.

The SEM, XRD and FTIR results show that the two chitosan films have similar surface morphology, crystalline structure and chemical structure. Within the resolution of these characterisation methods, Chi-S1 and Chi-S2 did not show an obvious difference in morphology, crystalline structure or chemical structure, so that such a difference is more appropriately discussed in terms of the piezoelectric-layer thickness and the associated change in mechanical response.

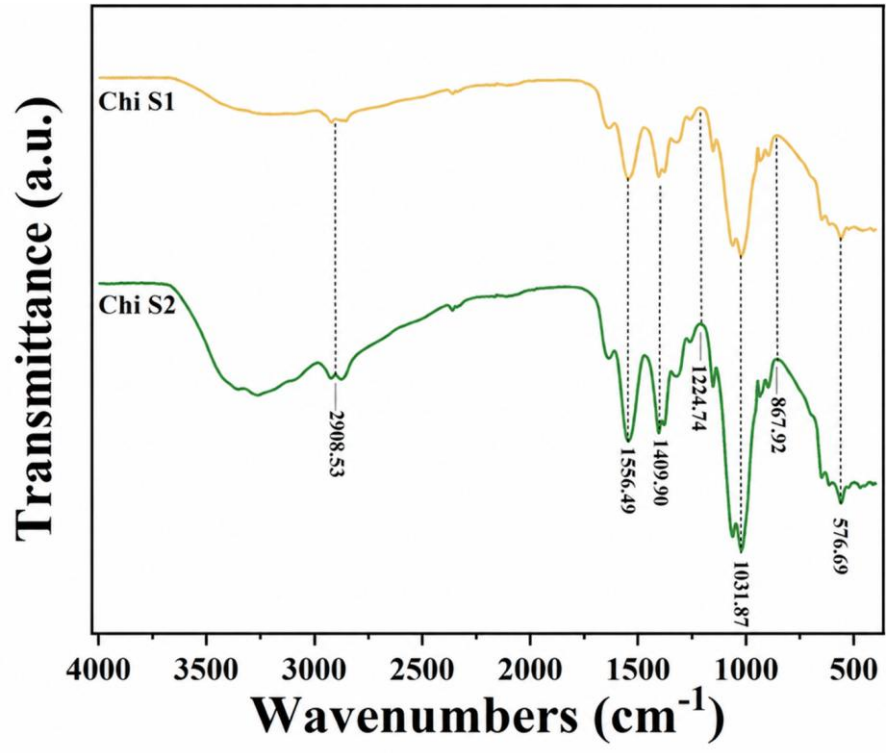


Figure 4.5 FTIR spectra of the chitosan films Chi-S1 and Chi-S2.

4.3.2 Pressure Sensor Characterisation

The output characteristics of the chitosan sensors were measured using a tuneable-frequency vibration system (TV 50018, TIRA GmbH), which applies periodic compressive loads, and

the generated voltage was recorded with a digital storage oscilloscope. When a compressive load is applied to the chitosan film, the film deforms and generates a charge on the electrodes through the direct piezoelectric effect, when the load is removed, a charge of the opposite sign is produced, so that periodic compression gives the alternating output characteristic of a piezoelectric sensor. A pressure-increment test was first carried out at a fixed frequency of 8 Hz, with the applied pressure increased in steps of 10 kPa from 20 kPa to 80 kPa, a frequency-increment test was then carried out at a fixed pressure of 80 kPa, with the frequency increased in steps of 1 Hz from 2 Hz to 8 Hz. The output voltages of Chi-S1 and Chi-S2 at each pressure and frequency step are presented in **Figure 4.6**. As can be seen directly from these plots, the area enclosed by the data points increases progressively as the applied pressure or the loading frequency increases, indicating that the output voltage of both films rises steadily. The plots further show that, at 80 kPa, the maximum output voltage reached approximately 2.61 V for Chi-S1 in **Figure 4.6(a)** and 2.93 V for Chi-S2 in **Figure 4.6(b)**. Similarly, at 8 Hz, the output voltage reached 2.81 V for Chi-S1 in **Figure 4.6(c)** and

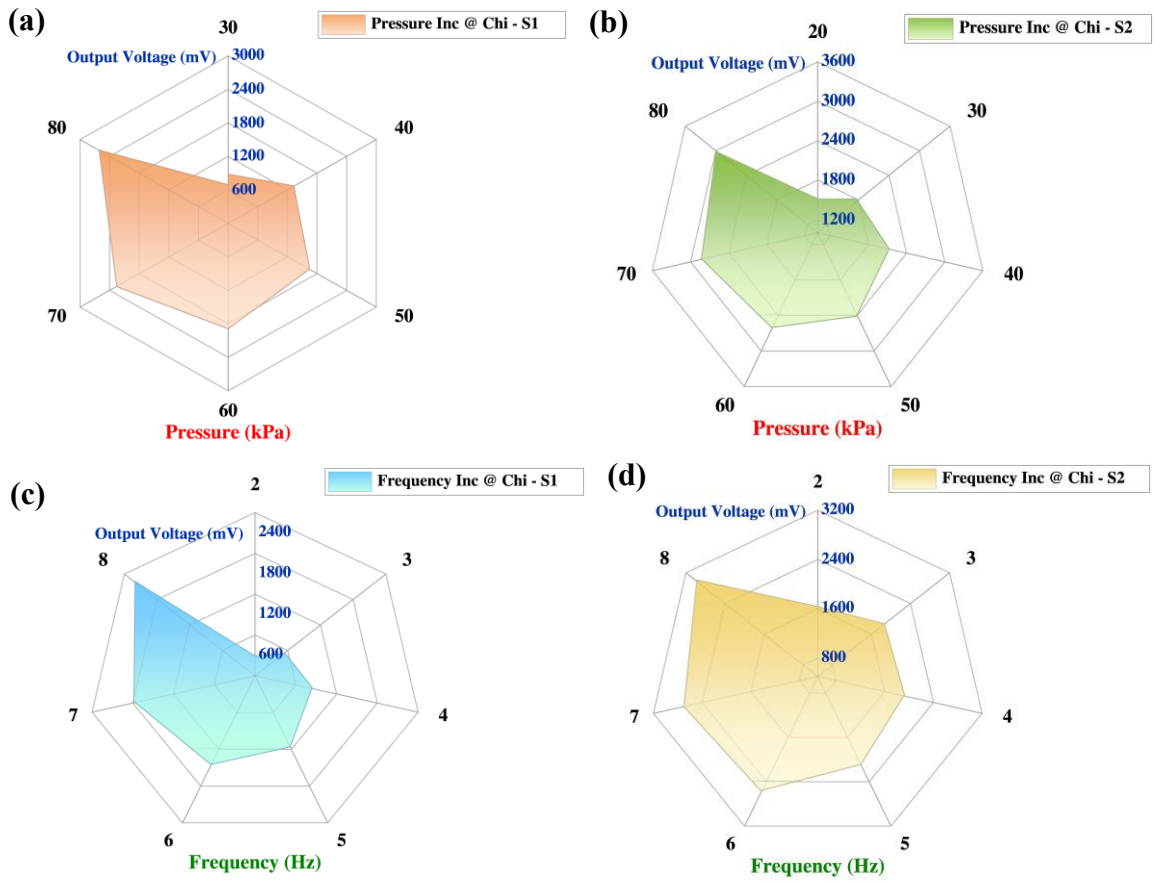


Figure 4.6 Plots of the output voltage of the chitosan sensors: (a) Chi-S1 and (b) Chi-S2 under different pressures from 20 to 80 kPa at a fixed frequency of 8 Hz, (c) Chi-S1 and (d) Chi-S2 under different frequencies from 2 to 8 Hz at a fixed pressure of 80 kPa.

2.97 V for Chi-S2 in **Figure 4.6(d).** The rise of the output voltage with pressure is expected: a higher load directly produces a larger deformation of the chitosan film, which increases the pressure-induced voltage output. The rise of the output with loading frequency can be explained by the higher rate of deformation of the film: at a higher frequency, the number of compressions-release cycles per unit time increases and the film deforms more rapidly, so that the output voltage increases with frequency. Notably, this clear dependence of the output on the loading frequency is particularly relevant to the artificial Pacinian corpuscle function targeted in this chapter, since it reflects a sensitivity to the rate of the mechanical stimulus that parallels the behaviour of the Pacinian corpuscle as a rapidly adapting receptor responding mainly to dynamic and vibratory stimuli.

The pressure sensitivity S_P was taken as the slope of the output voltage against the applied pressure at a constant frequency, as defined by **Equation 2.1**, and the frequency sensitivity

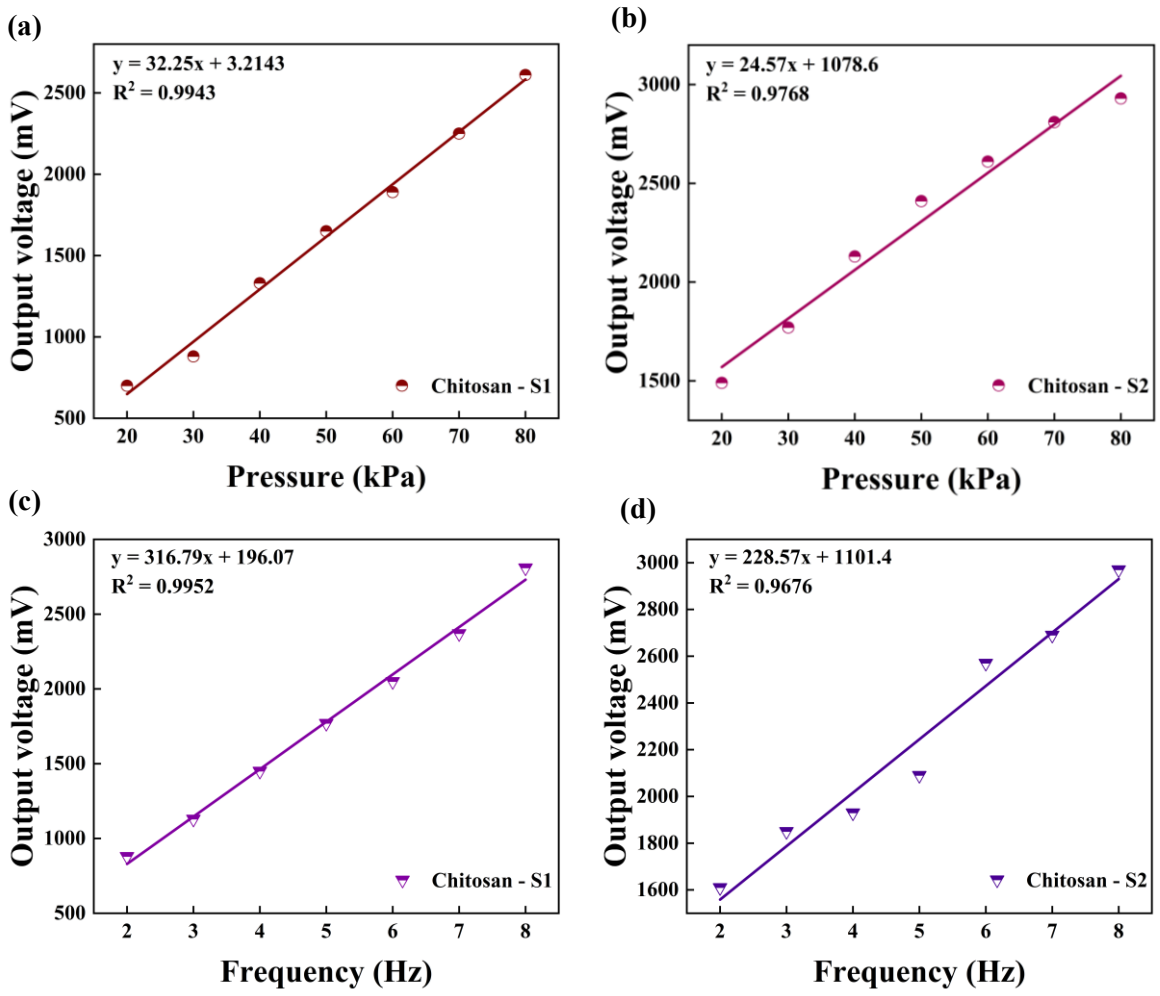


Figure 4.7 Linear fits of the output voltage of the chitosan sensors: (a) Chi-S1 and (b) Chi-S2 against applied pressure, giving pressure sensitivities of 32.25 mV/kPa and 24.57 mV/kPa, and (c) Chi-S1 and (d) Chi-S2 against loading frequency, giving frequency sensitivities of 316.79 mV/Hz and 228.57 mV/Hz.

S_f as the slope of the output voltage against the loading frequency at a constant pressure, as defined by **Equation 2.2**. The pressure sensitivities $\boldsymbol{S_P}$ are 32.25 mV/kPa for Chi-S1 and 24.57 mV/kPa for Chi-S2 as illustrated in **Figure 4.7(a)** and **(b)**, and the frequency sensitivities $\boldsymbol{S_f}$ are 316.79 mV/Hz for Chi-S1 and 228.57 mV/Hz for Chi-S2 shown in **Figure 4.7(c)** and **Figure 4.7 (d)**, respectively. The coefficient of determinisation R^2 of each fit is close to unity, indicating a good linear relationship between the output voltage and the applied pressure or frequency within the measured range, so that the applied stimulus can be recovered from the output voltage through this linear relationship.

The comparison shows that film thickness affects the sensitivity and the maximum output voltage in different ways. The slightly higher maximum output voltage of Chi-S2 is consistent with the expected thickness dependence of piezoelectric voltage output. For films with comparable material properties, electrode area and applied force, increasing the film thickness reduces the capacitance and increases the measured voltage for a given generated charge [124]. Similar thickness-dependent voltage behaviour has been reported for piezoelectric polymer films under periodic compression [125]. The higher sensitivity of Chi-S1 is not predicted by this ideal relation, indicating that film thickness alone does not determine the measured response. The sensitivity and the maximum output voltage should thus not be treated as equivalent, since the former reflects the slope of the stimulus-response relationship, while the latter reflects the peak output amplitude within the tested range. For a self-powered dynamic pressure sensor intended to resolve small changes in pressure or frequency, the sensitivity is the more relevant performance metric, and so that Chi-S1 is more favourable where pressure and frequency resolution are the main criteria, while the higher maximum output voltage of Chi-S2 indicates that the thicker film retains a stronger voltage-output capability, the comparison between the two thicknesses illustrates how the film thickness can be used to balance sensitivity against output magnitude.

To further examine the output stability of the sensor under dynamic loading, the output voltage versus time recorded in the pressure-increment test described above is shown in **Figure 4.8(a)**. At each pressure step, the sensor produced a regular alternating voltage waveform with a consistent period, the peak height was essentially the same from one loading cycle to the next, and the waveform peaks rose steadily as the pressure step increased, with clear and smooth transitions between steps, reflecting a good repeatability and a monotonic response of the output voltage to the applied pressure.

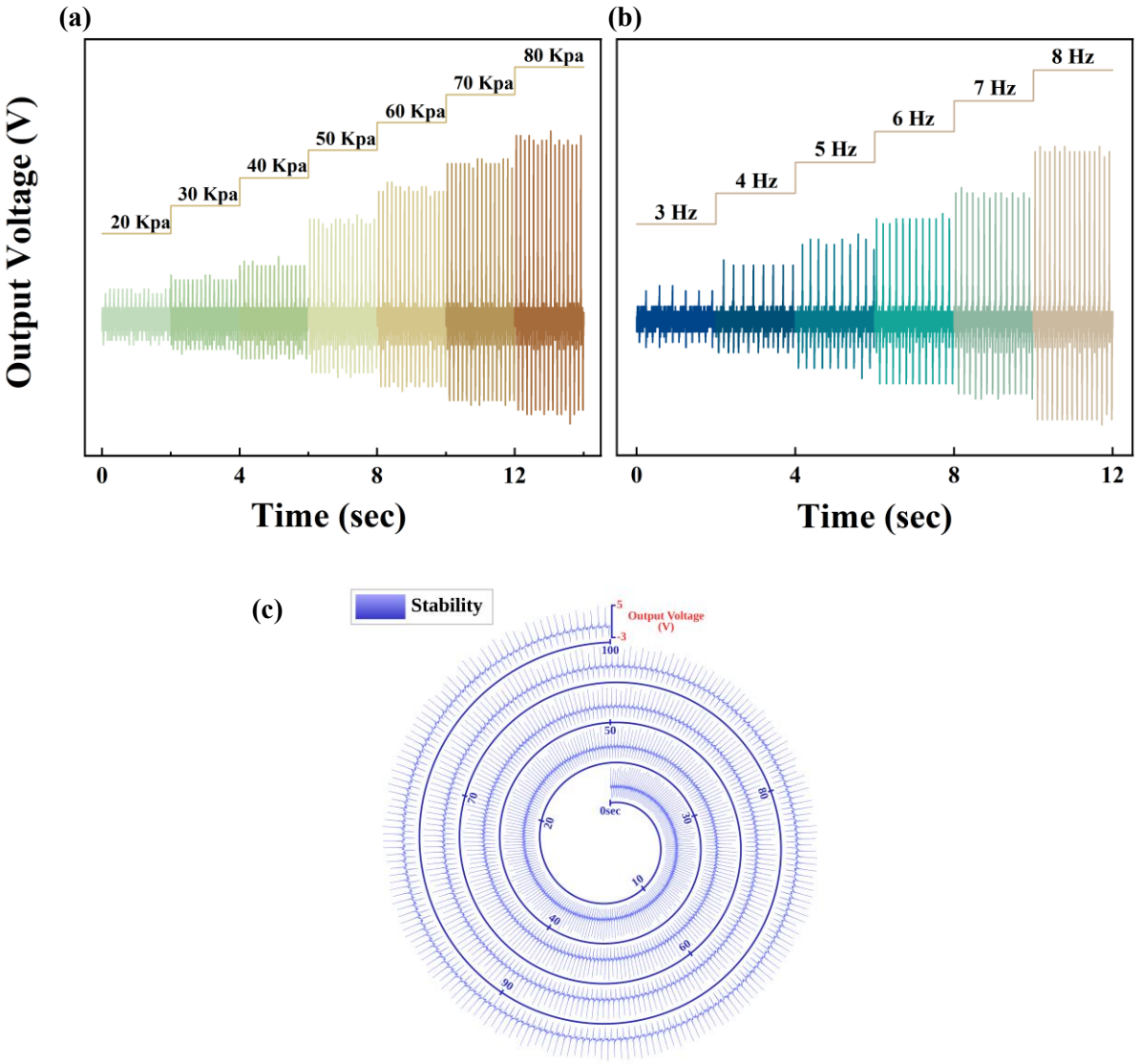


Figure 4.8 Output voltage versus time of the chitosan sensors: (a) under stepwise increasing pressure from 20 kPa to 80 kPa at a fixed frequency of 8 Hz, (b) under stepwise increasing frequency from 2 Hz to 8 Hz at a fixed pressure of 80 kPa, and (c) cyclic stability over 1000 periodic compression cycles.

The corresponding output voltage versus time from the frequency-increment test is shown in **Figure 4.8(b)**. As the frequency increased, the number of output pulses per unit time increased and the time interval between adjacent peaks shortened accordingly, while each pulse retained a clear and regular waveform profile, at the same time, the peak output rose with frequency and the amplitude remained stable across consecutive cycles at a given frequency, indicating that the sensor provided a repeatable dynamic response without obvious distortion across a wide range of loading frequencies.

Subsequently, to gain a deeper understanding of the reliability of the chitosan pressure sensor, over 10^3 cycle tests were conducted at a frequency of 8 Hz and a pressure of 80 kPa. The experimental results are plotted in **Figure 4.8(c).** The sensor exhibits good cycle stability,

with virtually no fluctuation in the output voltage. These data demonstrate that the chitosan sensor possesses outstanding stability and durability for applications requiring long-term, continuous, high-precision detection.

These results indicate that the chitosan sensor converted dynamic mechanical inputs into electrical output signals under increasing pressure, increasing frequency and repeated compression, without requiring an external power supply. Its response to dynamic compression and the dependence of the output signal on loading frequency functionally emulated the sensitivity of Pacinian corpuscles to time-varying mechanical stimuli, supporting the use of the chitosan sensor as an artificial analogue of this rapidly adapting mechanoreceptor.

4.3.3 Aqueous Dissolution

The solubility of the chitosan films was assessed by immersing the films in slightly acidic deionised water (pH 6.5) and recording changes in their appearance over time. As shown in Figure 4.9, the film gradually dissolved in the solution, with visible changes within the first 5 min. Only small remnants were visible after 25 min, and almost no film remained visible after 45 min. This dissolution may be associated with the molecular structure of chitosan and its hydrophilicity: the amine and hydroxyl groups along the polysaccharide backbone are hydrophilic and readily form hydrogen bonds with water, so that the film swells and the chains become progressively solvated, while the protonation of the amine groups under slightly acidic conditions may further promote the dissolution of the chitosan chains into the surrounding aqueous medium [19]. These results show that the chitosan film undergoes a clear and rapid dissolution in a slightly acidic aqueous environment, providing a basis for its use as a degradable flexible-electronic material. The biodegradation of chitosan under biologically active conditions has previously been reported [100]. The dissolution observed in this study also suggests that aqueous treatment could facilitate the separation of the chitosan film from other sensor components during material recovery. In a related study, Ahmad et al. demonstrated the recovery and reuse of silver nanowires from electronic devices using chitosan substrate[126].

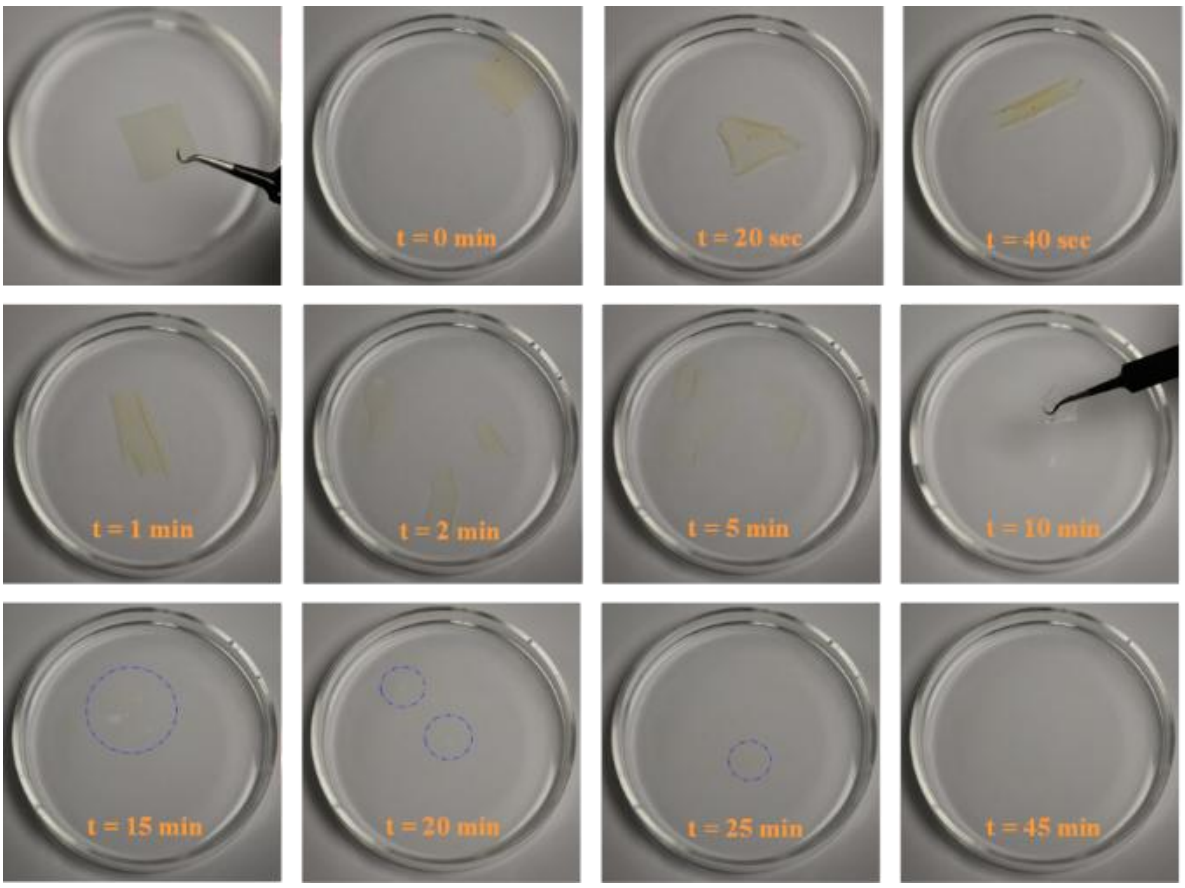


Figure 4.9 Dissolution of the chitosan film in deionised water (pH 6.5): (a) time-dependent dissolution of the chitosan film during immersion.

4.4 Summary

In summary, this chapter developed a flexible, self-powered pressure sensor based on pure chitosan, fabricated by a simple, low-cost, solution-based route. The two sensors exhibited a pressure sensitivity of 32.25 mV/kPa (Chi-S1) and 24.57 mV/kPa (Chi-S2), and a frequency sensitivity of 316.79 mV/Hz and 228.57 mV/Hz, respectively, across the pressure and frequency ranges tested. These characteristics indicate potential for use in applications such as electronic skin, prosthetics, and soft robotics. Furthermore, the chitosan films were transparent, biocompatible, and readily soluble under mildly acidic aqueous conditions, suggesting their suitability as a substrate material for flexible and biomedical devices.

Chapter 5: Chitosan-ZnO Flexible Self-Powered Piezoelectric Pressure Sensor for Artificial Mechanoreceptor Applications

5.1 Introduction

Chapter 4 systematically evaluated the material characteristics and piezoelectric performance of pure chitosan films used as the piezoelectric layer in flexible, self-powered piezoelectric pressure sensors. Next, the potential of these films for dynamic pressure sensing and the emulation of an artificial mechanoreceptor was explored. Accordingly, this chapter moves beyond demonstrating chitosan's piezoelectric sensing capability to investigate whether compositing can increase its piezoelectric output while retaining flexibility. The common strategy is to composite the chitosan with an inorganic nanomaterial that has a strong piezoelectric response [9]. Zinc oxide (ZnO) is an abundant, low-cost and lead-free piezoelectric nanomaterial whose piezoelectric response arises from its polar wurtzite structure, which has led to its wide use in flexible and wearable piezoelectric devices[8], [127]. ZnO nanoparticles (ZnO NPs) can be dispersed in a chitosan solution and cast into a composite film without the need for a cleanroom. Chitosan is a hydrophilic polymer with -NH_2 and -OH side groups that can interact with the ZnO nanoparticles through hydrogen bonding to form the composite film. As both chitosan and ZnO are piezoelectric, the two materials are expected to contribute jointly to the charge generated under deformation, which increases the output voltage and the sensitivity of the composite sensor. Adding ZnO also improves the mechanical and antibacterial performance of the CS-ZnO films [128]. Previous studies report, however, that the Young's modulus and the piezoelectric coefficient d_{33} of chitosan films first rise and then decline as the ZnO NP content increases, reaching a peak at around 15 wt.% [129], [88]. At higher loadings, the agglomeration of the nanoparticles and the embrittlement of the film reduce its ductility and increase the risk of cracking or fracture, which is detrimental to wearable applications [128], [122]. Three nominal ZnO concentrations of 5, 10 and 15 wt.% are accordingly used to prepare chitosan-ZnO (CS-ZnO) composite films, with the pure chitosan film from Chapter 4 as a reference. A maximum loading of 15 wt.% is set to balance the increase in piezoelectric output against the flexibility required for wearable applications.

Multiple receptor types are distributed across the skin and collectively perceive stimuli such as pressure, vibration, texture, tension, temperature and pain. Similarly, an artificial tactile system requires an array of sensing units to acquire the magnitude and the spatial distribution of an applied pressure at the same time. Next, the sensor array is combined with a wireless readout module, its output signals can be transmitted to a mobile device for real-time monitoring, recording and further analysis. This chapter examines the dynamic pressure response of the individual CS-ZnO sensor and applies a representative composite to spatial pressure mapping, wireless readout and gesture detection, to assess its potential as the sensing unit of an artificial mechanoreceptor. **Figure 5.1(a)** illustrates a human tactile sensing system made up of a series of receptors, including mechanoreceptors, thermoreceptors, chemoreceptors and nociceptors, that detect sensory stimuli and physical movements such as pressure, vibration, texture, stretch or tension, temperature and pain. **Figure 5.1(b)** shows that an artificial tactile sensing system with similar capabilities can be built on the model of the human tactile sensing system. Such a system, able to combine wireless transmission with wearable operation, has considerable potential in areas that include electronic skin, prosthetics, human-machine interfaces and health monitoring. **Figure 5.1(d)** shows an application in which several self-powered wearable pressure sensors are placed on a runner's body and integrated with a wireless communication module. This module collects the real-time body-movement signals shown in **Figure 5.1(c)** and transmits them through a Bluetooth module to a mobile phone or another terminal for recording and storage.

This chapter begins with the preparation of CS-ZnO composite films with different ZnO contents and examines their morphology, crystalline structure and chemical interactions by SEM, XRD, FTIR. The dielectric properties and the piezoelectric coefficient d_{33} of the composite films are then measured, and the output voltage, pressure sensitivity, frequency sensitivity, response and recovery times and cyclic stability of the 5, 10 and 15 wt.% CS-ZnO sensors are compared at different pressures and loading frequencies. The dissolution of the CS-ZnO films in slightly acidic deionised water is then examined. Finally, a dynamic pressure sensor array is fabricated from the 15 wt.% composite and integrated with a microcontroller and a wireless communication module for remote, real-time data transmission. The potential applications of this array are also considered, ranging from human health monitoring and the collection of personalised medical data to the remote

detection of deformation and pressure distribution in smart manufacturing, which could support intelligent control systems.

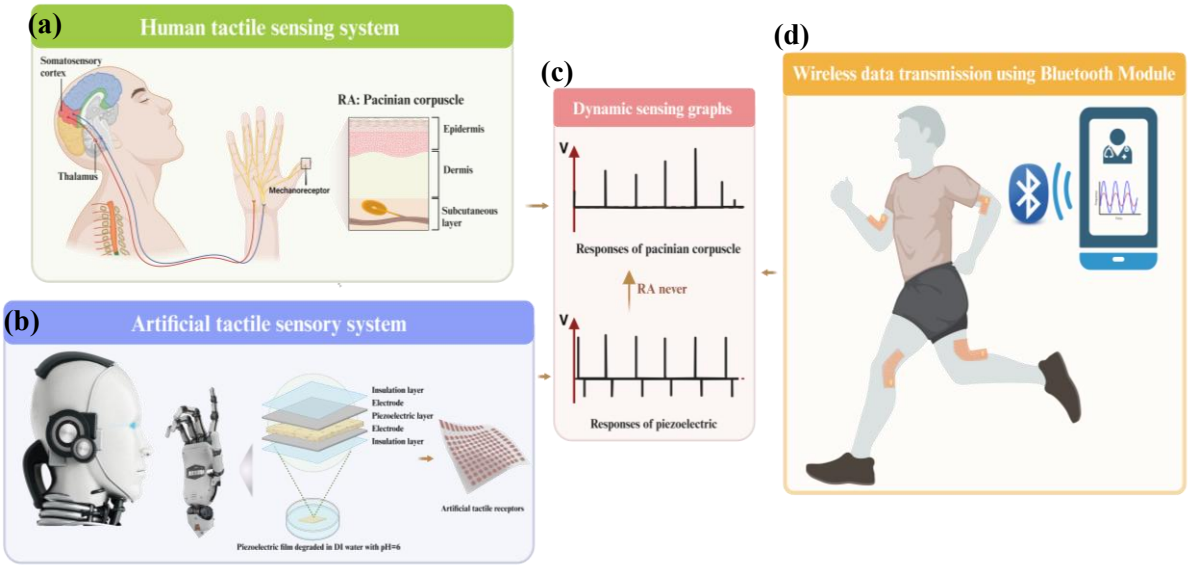


Figure 5.1 The human tactile sensing system, which functions as an array of receptors (a), and an equivalent artificial tactile sensory system (b), with the typical dynamic sensing signals (c) of a rapidly adapting (type-II) mechanoreceptor and an example wearable scenario on a runner (d).

5.2 Methodology

5.2.1 Preparation of CS-ZnO Films

The CS-ZnO composite films were prepared by adding ZnO NPs to the chitosan solution used to prepare the pure films as illustrated in **Figure 5.2.** ZnO NPs were dispersed in 10 mL of deionised water with 0.1 mL of acetic acid added to aid dispersion, and the suspension was combined with the prepared 2%(w/v) chitosan solution in the ratios required to give nominal ZnO concentrations of 5, 10 and 15 wt.%. Each mixture was sonicated and degassed under vacuum as before to obtain a uniform and stable colloidal solution. Finally, the CS-ZnO solution was cast onto a copper substrate for easy to peel off the CS-ZnO film in a polystyrene Petri dish and spin-coated at 100 rpm for 30 s to spread it evenly, after which it was dried in a controlled-environment chamber at 38.7 °C for approximately 4 h to form the CS-ZnO composite film.

5.2.2 Fabrication of CS-ZnO Sensors

The CS-ZnO films were assembled into pressure sensors with the same sandwich structure used for the pure chitosan sensor, as illustrated in **Figure 5.2**, in which the composite film served as the piezoelectric layer between two copper electrodes. Initially, the films of each ZnO concentration were cut into 2 × 2.5 cm pieces, and copper electrodes slightly smaller than the film were prepared so as to avoid short-circuiting at the edges. The electrodes were then fixed to the top and bottom faces of the film to collect the charge generated under applied pressure, and the assembled sensor was encapsulated with Kapton tape to protect it from the external environment and to preserve its flexibility and stability.

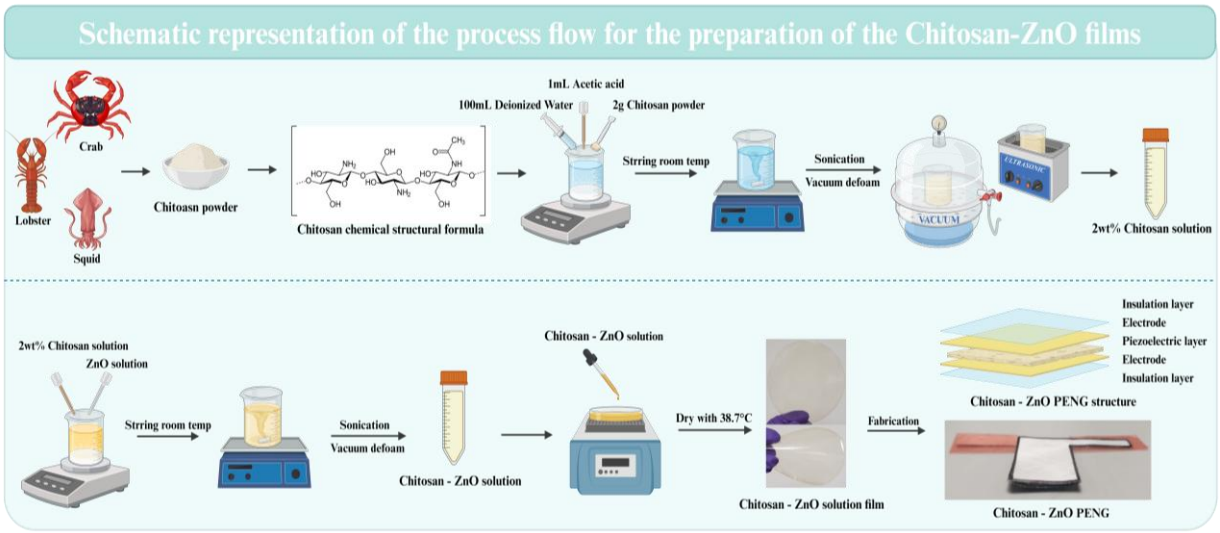


Figure 5.2 Schematic representation of the process flow for the preparation of flexible CS-ZnO films.

5.3 Results and Discussion

5.3.1 Material Characterisation

To understand the structural, chemical and morphological characteristics of the films, SEM, XRD and FTIR were performed on the ZnO NPs, the pure chitosan film and the CS-ZnO composite films, as presented in **Figures 5.3-5.5.**

- **Morphology of CS-ZnO films using SEM**

The surface morphology of the ZnO NPs, the pure chitosan film and the CS-ZnO composite films was examined by SEM, as shown in **Figure 5.3.** The ZnO NPs appeared as fine particles of an approximately regular spherical shape, with sizes in the range of approximately 70-100 nm. This is somewhat larger than the nominal particle size of the supplied powder, which points to a degree of particle aggregation during drying. The pure

chitosan film showed a relatively flat, dense, smooth and continuous surface, consistent with the morphology described in the previous chapter and with the compact packing of the

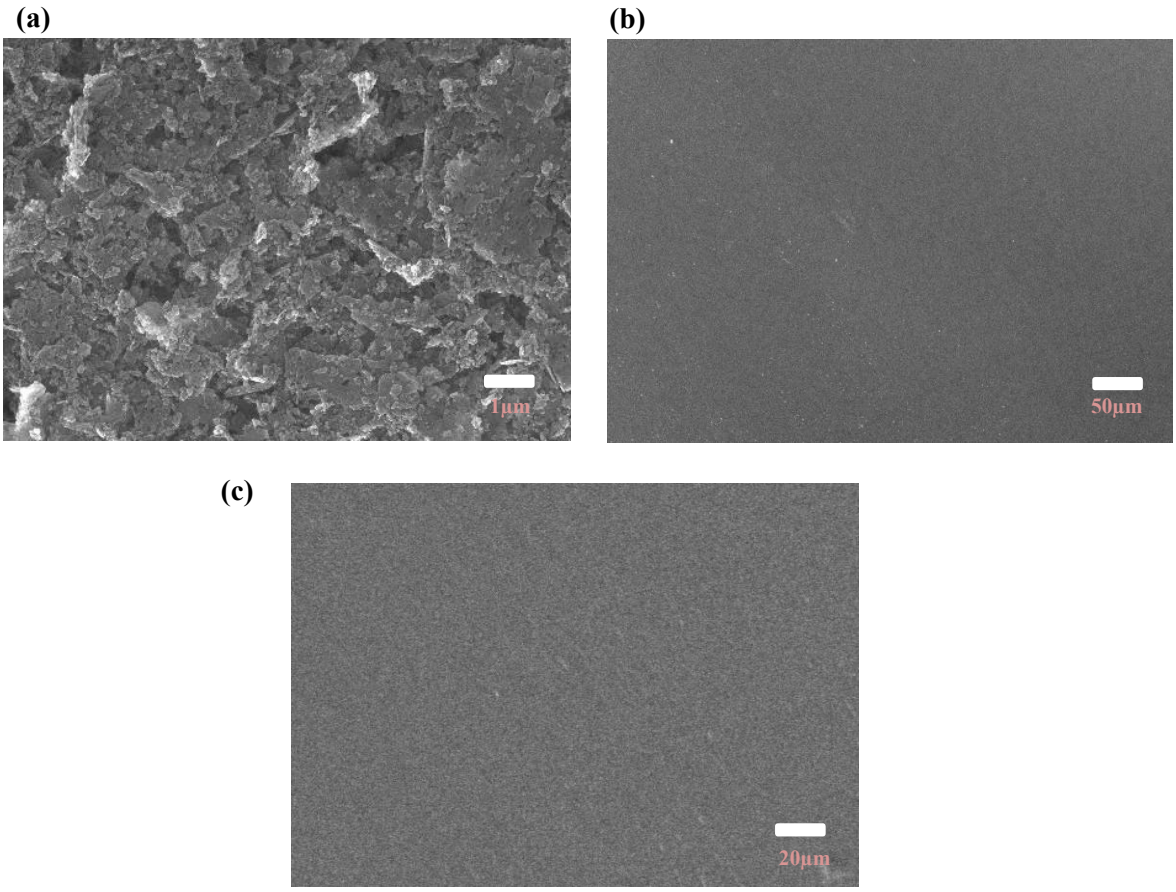


Figure 5.3 SEM images for (a) pure ZnO film, (b) pure chitosan film, and (c) CS-ZnO film.

polysaccharide chains. After the addition of ZnO, the smooth chitosan surface was modified to a coarser surface with a uniform granular morphology, with the ZnO particles distributed across the film. At the lower concentrations the particles were distributed relatively uniformly within the chitosan, which indicates that the ZnO was successfully incorporated and homogeneously dispersed within the chitosan. As the ZnO concentration increased from 5 to 15 wt.%, the particle coverage increased, and at the highest concentration of 15 wt.% the particles were more densely packed and some local clustering was visible. This suggests that a higher ZnO concentration increases the tendency of the particles to aggregate within the film.

- **Structural characterisation of CS-ZnO films using XRD**

The crystalline structure of the pure ZnO, chitosan and the CS-ZnO composite film was examined by X-ray diffraction, and the patterns are presented in **Figure 5.4.** The ZnO NPs

showed sharp diffraction peaks at 2θ values of approximately 31.76°, 34.47°, 36.26°, 47.57°, 56.65°, 62.95° and 67.94°. These peaks are indexed to the (100), (002), (101), (102), (110), (103) and (112) planes of the hexagonal wurtzite structure of ZnO (JCPDS card no. 36-1451). The sharpness and high intensity of the reflections indicate that the ZnO NPs are well crystallised, and the indexed planes confirm that they adopt the polar wurtzite phase responsible for the piezoelectric response of ZnO. The pure chitosan film showed two broad reflections at approximately 9.33° and 20.45°, corresponding to the (020) and (200) planes of chitosan [123]. The breadth of these reflections reveals that the chitosan film is only semi-crystalline and is dominated by an amorphous fraction, consistent with the hydrogen-bonded packing of the polysaccharide chains [123]. In the CS-ZnO composite, the sharp wurtzite ZnO reflections observed in the pure ZnO powder were clearly reduced in intensity, although weak diffraction features remained visible between 30° and 40°. In contrast to the powder reference, which consists predominantly of highly crystalline ZnO, the composite contains ZnO nanoparticles embedded within the semicrystalline chitosan matrix. The lower proportion of ZnO in the composite reduces its relative contribution to the diffraction pattern, while diffuse scattering from the chitosan matrix may further reduce the visibility of the characteristic ZnO reflections. A similar reduction in ZnO diffraction peak intensity has been reported in chitosan composites containing ZnO [130].The degree of crystallinity of the composite was determined from the diffraction pattern using **Equation 5.1**:

$$X_c = \frac{A_c}{A_c + A_A} \times 100\ (\%) \tag{5.1}$$

where A_c is the integrated area of the crystalline peaks and A_A is the area under the curve of the amorphous peak. The composite gave a degree of crystallinity of 67.03%, which is higher than that of the largely amorphous pure chitosan and reflects the addition of the crystalline ZnO, possibly together with some ordering of the chitosan chains around the particles [130]. The mean crystallite size was estimated from the broadening of the principal reflection using the Scherrer equation, **Equation 5.2**:

$$D = \frac{K\lambda}{\beta \cos\theta} \tag{5.2}$$

where D is the crystallite size, K is the Scherrer constant (0.9), λ is the wavelength of the incident radiation (0.15406 nm), β is the full width at half maximum of the reflection in radians, and θ is the Bragg angle. This gave a crystallite size of approximately 4.32 nm for

the composite, consistent with the nanoscale ZnO crystallites distributed in the film. The full width at half maximum is inversely related to the crystallite size, and the value used here was taken from the reflection at approximately 11.94°. The change in the crystallite size and in the overall crystallinity on adding the ZnO has been reported to alter the crystalline structure of chitosan, through the formation of new crystalline order or a change in grain growth, and is associated with an increase in the piezoelectric response of the film [129], [88]. The increased crystalline fraction and the nanoscale crystallite size are both relevant to the piezoelectric behaviour of the composite. The crystalline wurtzite ZnO contributes a stronger and more directional piezoelectric response than the semi-crystalline chitosan alone, and a higher crystalline fraction increases the proportion of the film that provides this response [129], [131]. The slight shifts in the ZnO peak positions in the composite, relative to the pure ZnO, are consistent with an interaction between the ZnO surface and the chitosan, which is examined further by FTIR in the following section. The accompanying changes in the full width at half maximum, relative to the pure ZnO, are consistent with a change in the ZnO crystallite size on forming the composite, indicating a structural relationship between the ZnO particles and the chitosan.

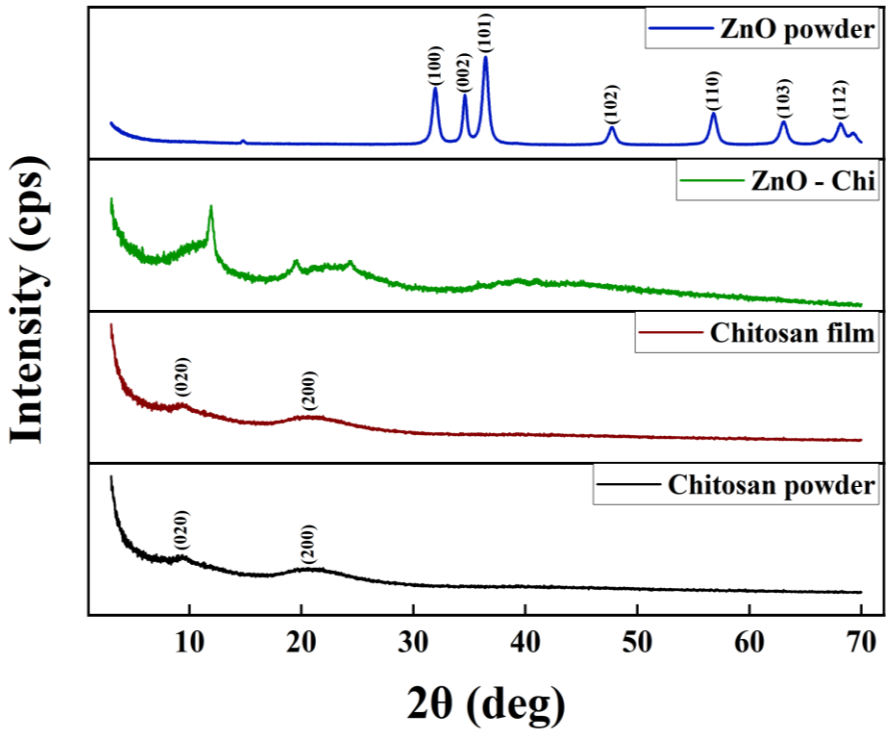


Figure 5.4 XRD patterns of the ZnO NPs, the pure chitosan film and the CS-ZnO composite film, showing the wurtzite ZnO reflections (indexed to JCPDS 36-1451) and the (020) and (200) reflections of chitosan, with both sets of reflections retained in the composite.

- **Chemical characterisation of CS-ZnO films using FTIR**

The chemical structure of the films was examined by Fourier-transform infrared spectroscopy, and the spectra are presented in **Figure 5.5.** Spectra were recorded for the pure chitosan film in both thin and thick forms, for the composite at 5 and 15 wt.% ZnO, and for the pure ZnO. The pure chitosan film showed bands at approximately 3460, 2887, 1718, 1575, 1450, 1356 and 1070 cm^{-1}, which confirm the chitosan structure [84]. The band near 3460 cm^{-1} corresponds to O-H stretching and the band near 2887 cm^{-1} to C-H stretching, the bands near 1718, 1575 and 1070 cm^{-1} are associated with the C=O and N-H groups, and the bands near 1450 and 1356 cm^{-1} are associated with the primary and secondary hydroxyl structures of the CH-OH and CH_2-OH groups [132]. The pure ZnO showed only low-intensity bands below 1000 cm^{-1}, with the band near 500 cm^{-1} corresponding to Zn-O stretching.

In the composite spectrum, these chitosan bands were retained but shifted, and the Zn-O band of the ZnO appeared. The band at approximately 2908 cm^{-1} corresponds to the C-H stretching of the polysaccharide backbone, the band at approximately 1556 cm^{-1} to the N-H bending of the amine groups and the amide vibration, and the bands at approximately 1410 and 1225 cm^{-1} to the C-N stretching and the C-O-C vibrations of the glycosidic linkage. The strong band at approximately 1032 cm^{-1} corresponds to the C-O stretching of the backbone, and the bands at approximately 868 and 577 cm^{-1} to the ring vibrations of the saccharide units and to the Zn-O vibration of the added ZnO. The shifts of these composite bands relative to the pure chitosan are attributed to interactions between the amine and hydroxyl groups of the chitosan and the surface of the ZnO particles [123], [132]. These interactions include hydrogen bonding between the -OH and $-NH_2$ groups of the chitosan and oxygen- or hydroxyl-related sites on the ZnO surface, as well as possible coordination between the Zn^{2+} ions and the O or N donor atoms. They change the vibrational frequencies, which shows that the ZnO is incorporated into the chitosan and alters its local molecular environment [133], [123]. The retention of the chitosan bands and the emergence of the Zn-O band confirm the presence of both components and the formation of the CS-ZnO composite. The thicker chitosan film exhibited slightly higher band intensities than the thinner film. This difference is attributed to its higher proportion of the Type-I conformation, which increases the likelihood of interaction with the infrared beam. The retention of the chitosan bands and the emergence of the Zn-O band confirm the presence of both components and the formation of the CS-ZnO composite. The thicker chitosan film exhibited slightly higher band

intensities than the thinner film. This difference is attributed to its higher proportion of the Type-I conformation, which increases the likelihood of interaction with the infrared beam. Among the composites, the band intensities at 5 wt.% were slightly higher than at 15 wt.%, which is attributed to stronger chemical interactions around some functional groups at the lower content and to a degree of ZnO aggregation at the higher content that reduces the available particle surface area. The way in which the ZnO is incorporated into the chitosan, established by the characterisation above, is reflected in the dielectric and piezoelectric behaviour examined in the following section.

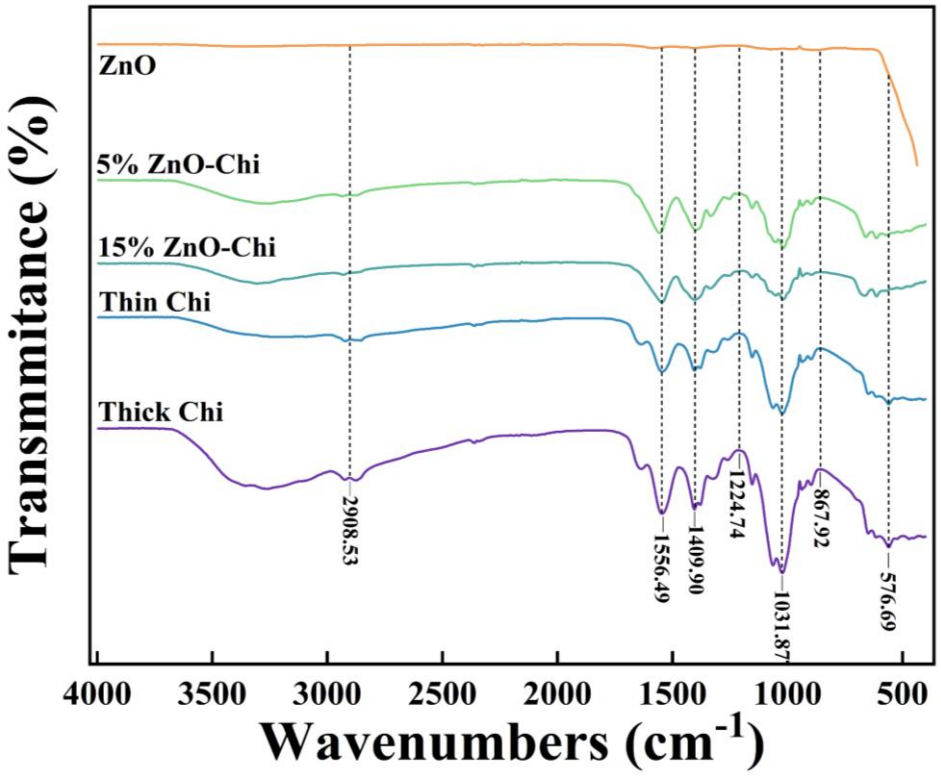


Figure 5.5. FTIR spectra of the pure chitosan film and the CS-ZnO composite film, showing the characteristic chitosan bands together with the Zn-O vibration of the added ZnO.

5.3.2 Dielectric and Piezoelectric Properties

The dielectric behaviour of the films was characterised by measuring their capacitance and impedance with an impedance analyser, as shown in **Figure 5.6**. The peak impedance of pure chitosan was 6152 Ω at 74.3 MHz, compared with 4202.7 Ω at 79.2 MHz, 4512.1 Ω at 76.1 MHz and 3938.5 Ω at 77.1 MHz for the 5, 10 and 15 wt.% CS-ZnO films, respectively. The corresponding minimum impedance values were 8.7 Ω at 41.3 MHz, 5.4 Ω at 52.7 MHz, 7.8 Ω at 46.9 MHz and 8.1 Ω at 47.7 MHz. All three composite films showed lower peak impedance values than pure chitosan, although the peak impedance did not decrease consistently with increasing ZnO concentration. The capacitance of both the pure chitosan

and the CS-ZnO films decreased with increasing frequency. Over the measured range, the capacitance of the pure chitosan film decreased from approximately 0.4 nF at about 8.7 MHz to approximately 0.34 pF at about 74 MHz, and the capacitance of the CS-ZnO composite decreased from approximately 0.47 nF at about 8 MHz to approximately 0.49 pF at about 77 MHz. At each frequency and ZnO concentration the composite gave a higher capacitance than the pure chitosan film. The higher capacitance indicates that the added ZnO increases the ability of the film to store charge. Treating the film between the two electrodes as a parallel-plate capacitor, the relative permittivity was obtained from the measured capacitance using **Equation 5.3**:

$$\varepsilon_r = \frac{\varepsilon_c}{\varepsilon_0} = \frac{Cd}{\varepsilon_0 A} \tag{5.3}$$

where C is the capacitance, d is the film thickness, ε_0 is the permittivity of free space, and A is the electrode area. The pure chitosan film gave a relative permittivity of approximately 6.2, and the higher capacitance of the composite corresponds to a higher permittivity. This is consistent with the higher permittivity of ZnO compared with chitosan and with reports on other ZnO-polymer piezoelectric composites [134]. The relative permittivity of

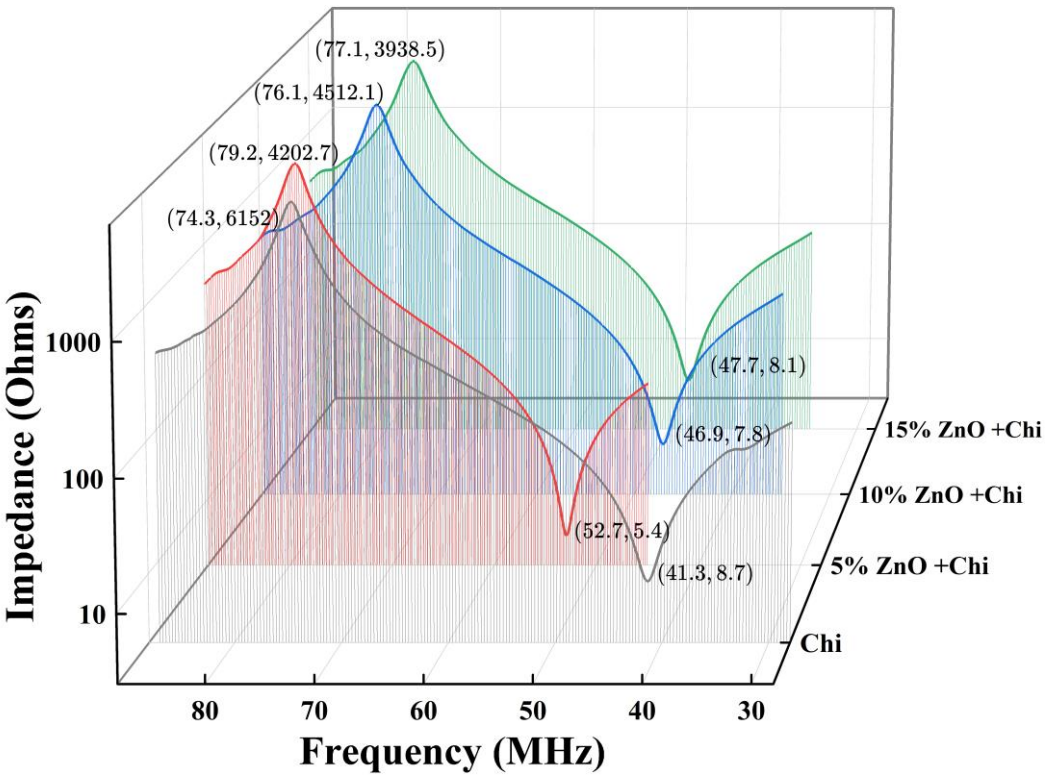


Figure 5.6 Impedance of the pure chitosan and CS-ZnO films as a function of frequency, from which the capacitance and permittivity were obtained.

approximately 6.2 was obtained using an electrode area of 5 cm^2 and a film thickness of 50 µm. The higher capacitance and relative permittivity indicate an increased charge-storage capability and dielectric response of the composite.[130]. The measured voltage output of a piezoelectric pressure sensor is, however, also governed by the piezoelectric coefficient, the film thickness, the effective electrode area, the degree of mechanical deformation, the interfacial contact and the input impedance of the measurement circuit. The higher dielectric response is therefore considered in combination with the d_{33} results and the subsequent voltage-output measurements.

The piezoelectric response of the films was quantified by the piezoelectric charge coefficient d_{33}, measured by the quasi-static method and obtained from the charge generated per unit applied force using **Equation 5.4**:

$$d_{33} = \frac{Q}{F} \tag{5.4}$$

where Q is the charge generated and F is the applied force. The d_{33} increased with the ZnO concentration, from approximately 7 pC/N for the pure chitosan film to 9, 12 and 16 pC/N for the composites with 5, 10 and 15 wt.% ZnO, respectively as shown in **Figure 5.7**. The addition of the ZnO NPs therefore produced nearly a 2.3-fold increase in d_{33} at 15 wt.%. This increase reflects the contribution of the polar wurtzite ZnO, which has a higher

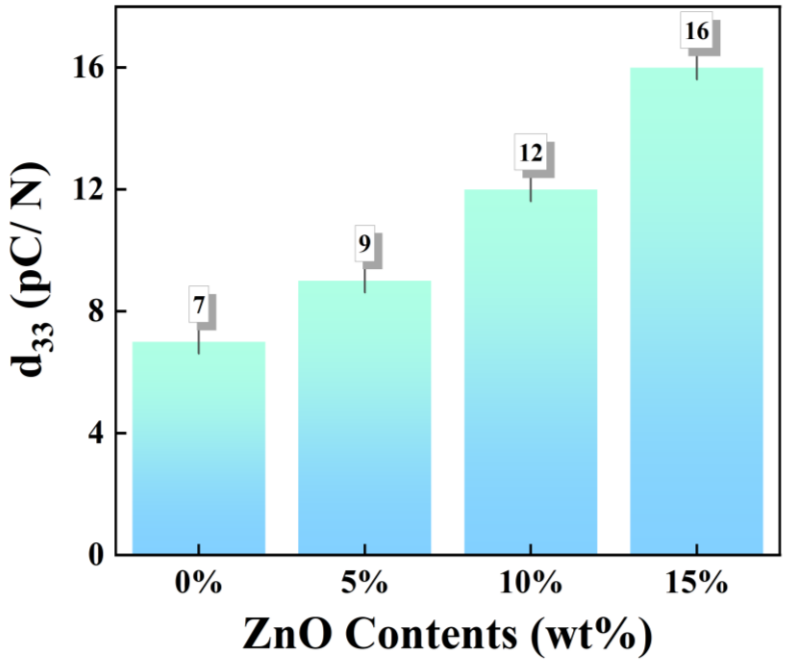


Figure 5.7 piezoelectric coefficients of pure chitosan film, and composite films with 5 wt.%, 10 wt.%, and 15 wt.% of ZnO.

piezoelectric coefficient than the chitosan, so that a higher ZnO concentration provides more piezoelectric material and more sites for charge generation under deformation. The trend agrees with the reported increase of the piezoelectric coefficient of chitosan films with ZnO concentration up to around 15 wt.% [129], [131]. The increase in d_{33} with ZnO concentration is consistent with the higher sensor output of the composites examined in the next section.

5.3.3 Pressure Sensor Characterisation

The output characteristics of the CS-ZnO sensors were measured using the tuneable-frequency vibration system, with the generated voltage recorded on a digital storage oscilloscope, under the same conditions used for the pure chitosan sensor in the previous chapter. A pressure-increment test was carried out at a fixed frequency of 8 Hz, with the applied pressure increased in steps of 10 kPa from 20 to 80 kPa, and a frequency-increment test was then carried out at a fixed pressure of 80 kPa, with the frequency increased in steps of 1 Hz from 2 to 8 Hz. The output voltages of the pure chitosan film and the 5, 10 and 15 wt.% composites at each pressure and frequency step are presented in **Figure 5.8(a) and (b),** and the output response of the composites with increasing pressure and frequency is summarised in **Figure 5.9(a)-(f)**. The output voltage of all the sensors increased with both the applied pressure and the loading frequency. At each condition the output also increased with the ZnO concentration, so that the 15 wt.% composite gave the highest output of the four composites. At 8 Hz, its output rose from a minimum of approximately 2.4 V at 20 kPa to a maximum of approximately 6.7 V at 80 kPa, compared with a maximum of approximately 2.6 V for the pure film. The increase of the output with the ZnO concentration follows the higher piezoelectric coefficient of the composites. The increase of the output with the applied pressure follows from the piezoelectric effect, in which a larger deformation of the film displaces more charge at the electrodes. The increase with frequency reflects the faster rate of deformation at higher frequencies, which generates the charge more rapidly and leaves less time for it to dissipate before it is measured. The output increased more steeply with the applied pressure than with the loading frequency, since the applied pressure directly controls the degree of deformation, and hence the charge generated in the piezoelectric layer, whereas a change in frequency produces a smaller change in the deformation generated in each cycle. The added ZnO improves the response to frequency through its higher piezoelectric coefficient and the associated increase in charge generation [21].

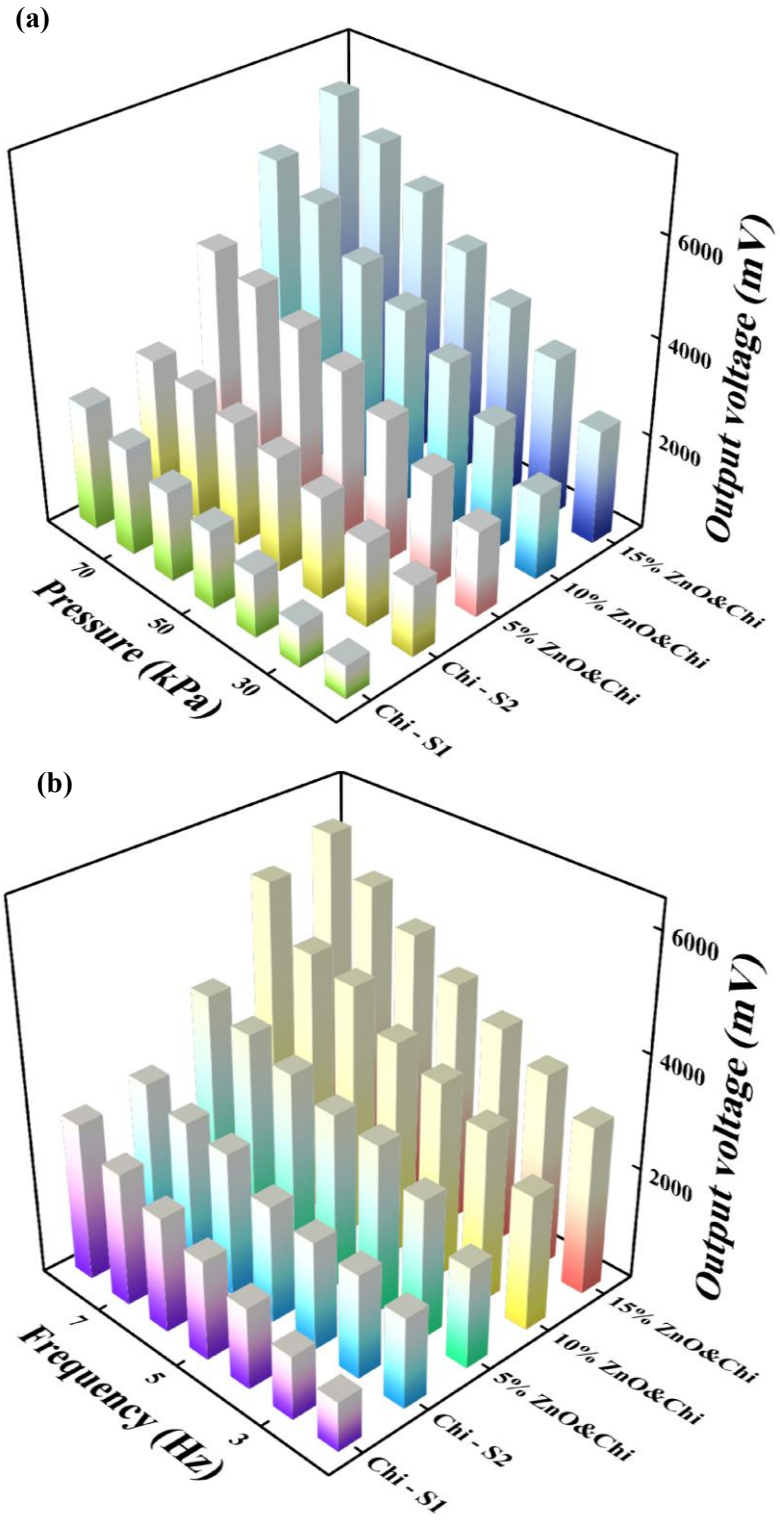


Figure 5.8. Pressure-sensing performance of the CS-ZnO sensors: output voltage of the pure chitosan film and the 5, 10 and 15 wt.% composites as a function of (a) applied pressure at 8 Hz and (b) loading frequency at 80 kPa.

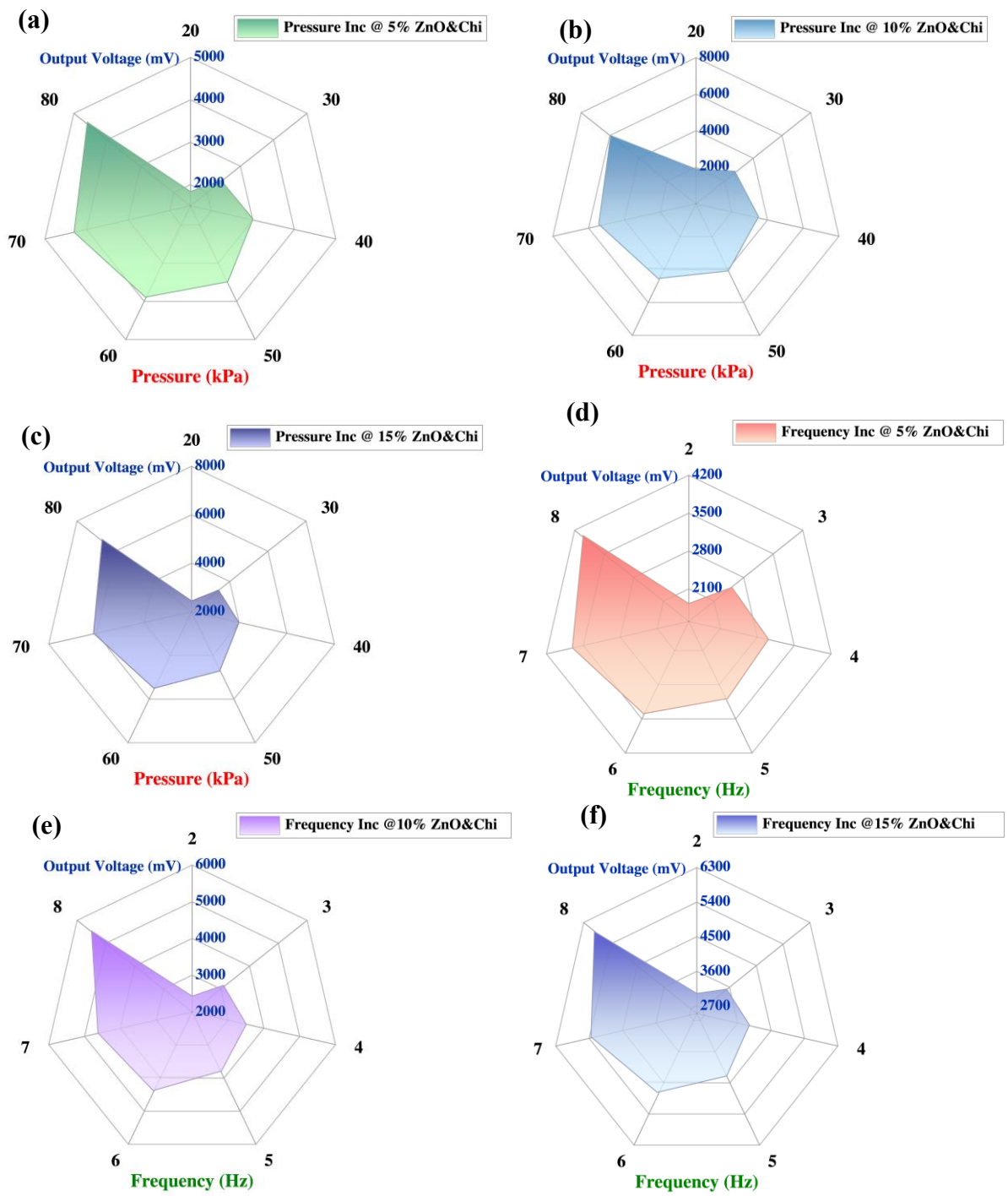


Figure 5.9. Output-voltage response of the composites with (a)-(c) increasing applied pressure and (d)-(f) increasing loading frequency for the 5, 10 and 15 wt.% concentrations, respectively.

The pressure sensitivity S_P and the frequency sensitivity S_f were obtained as the slopes of the output voltage against the applied pressure and against the loading frequency, as defined in **Equation 5.5** and **Equation 5.6**:

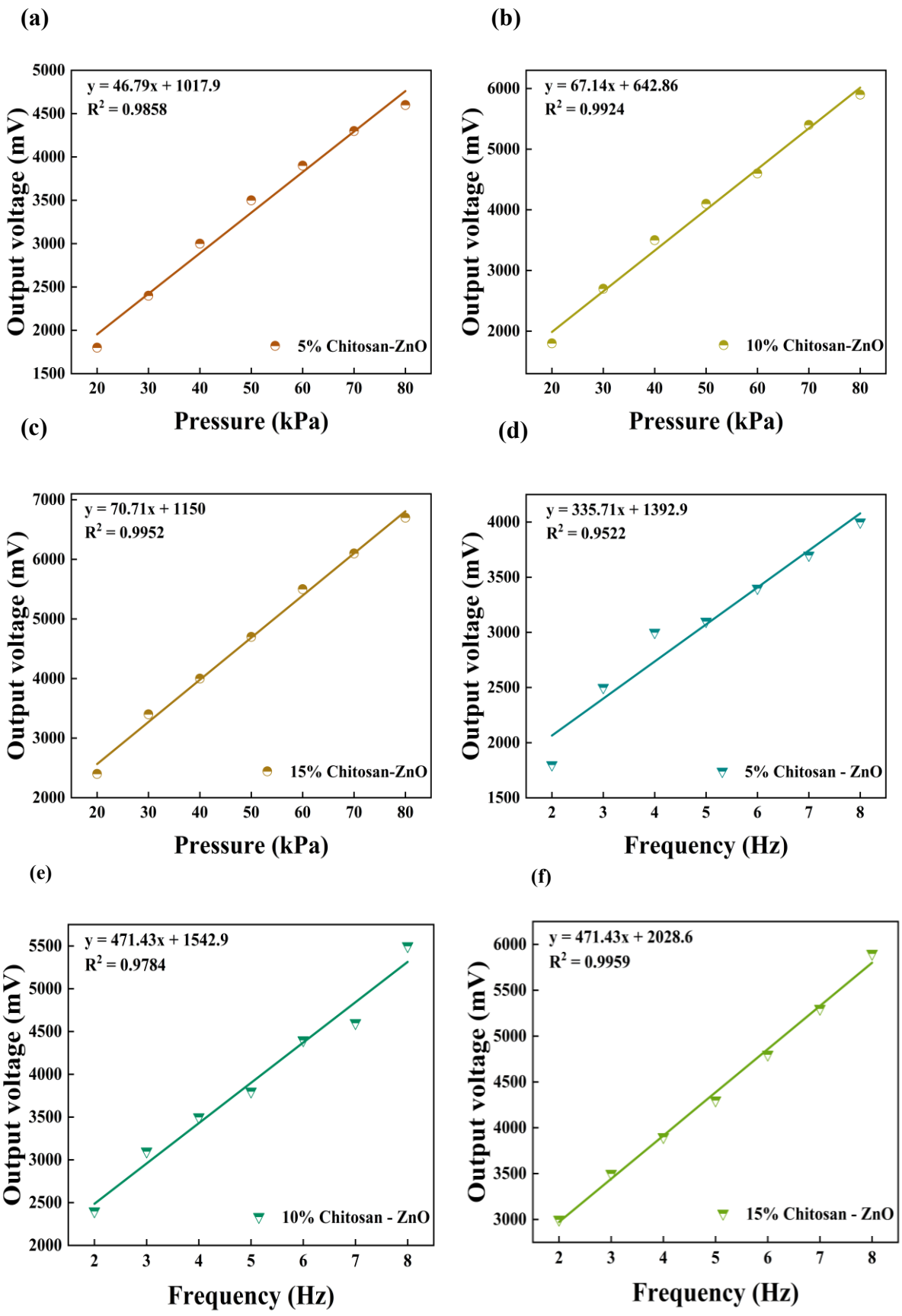
$$S_P = \frac{\Delta V}{\Delta P \text{ at a constant } frequency} \tag{5.5}$$

$$S_f = \frac{\Delta V}{\Delta f \text{ at a constant pressure}} \tag{5.6}$$

where ΔV is the change in output voltage, ΔP the change in applied pressure at a constant frequency, and Δf the change in loading frequency at a constant pressure. The sensitivities were obtained as the slope of a straight line fitted to the measured data by the least-squares method, and the quality of each fit was quantified by the coefficient of determination R^2 given by **Equation 5.7**:

$$R^2 = 1 - \frac{\sum_i (y_i - \hat{y}_i)^2}{\sum_i (y_i - \bar{y})^2} \tag{5.7}$$

where y_i are the measured values, $\hat{y}_i$ the fitted values, and $\bar{y}$ the mean value of y_i. The fitted output-pressure and output-frequency relationships are presented in **Figure 5.10**, in which the pure chitosan reference is the 50 μm film (denoted Chi-S1) and the 85 μm film (Chi-S2) characterised in the previous chapter 4 is included for comparison. The pressure sensitivity increased from 32.25 mV/kPa for the pure chitosan film to 46.79, 67.14 and 70.71 mV/kPa for the composites with 5, 10 and 15 wt.% ZnO. The frequency sensitivity increased from 316.79 mV/Hz for the pure film to 335.71 mV/Hz at 5 wt.% and reached 471.43 mV/Hz at both 10 and 15 wt.%. The coefficient of determination R^2 was close to unity in each case. The pressure sensitivity therefore increased steadily with the ZnO concentration, whereas the frequency sensitivity rose up to 10 wt.% and then levelled off, with the 10 and 15 wt.% composites giving the same value. Of the four composites, the 15 wt.% composite gave the highest-pressure sensitivity and shared the highest frequency sensitivity with the 10 wt.% composite, about 2.2 times the pressure sensitivity and 1.5 times the frequency sensitivity of the pure chitosan film. This levelling-off is consistent with the increased stiffness of the film and the clustering of ZnO particles at the higher concentration seen in the SEM images. These factors limit the further increase of the dynamic response, even though the quasi-static coefficient d_{33} continues to rise. The highest concentration is therefore close to the practical limit of the improvement available from the added ZnO. The pressure sensitivity of


(a)
y = 46.79x + 1017.9
R² = 0.9858
5% Chitosan-ZnO
Output voltage (mV)
Pressure (kPa)
(b)
y = 67.14x + 642.86
R² = 0.9924
10% Chitosan-ZnO
Output voltage (mV)
Pressure (kPa)
(c)
y = 70.71x + 1150
R² = 0.9952
15% Chitosan-ZnO
Output voltage (mV)
Pressure (kPa)
(d)
y = 335.71x + 1392.9
R² = 0.9522
5% Chitosan - ZnO
Output voltage (mV)
Frequency (Hz)
(e)
y = 471.43x + 1542.9
R² = 0.9784
10% Chitosan - ZnO
Output voltage (mV)
Frequency (Hz)
(f)
y = 471.43x + 2028.6
R² = 0.9959
15% Chitosan - ZnO
Output voltage (mV)
Frequency (Hz)

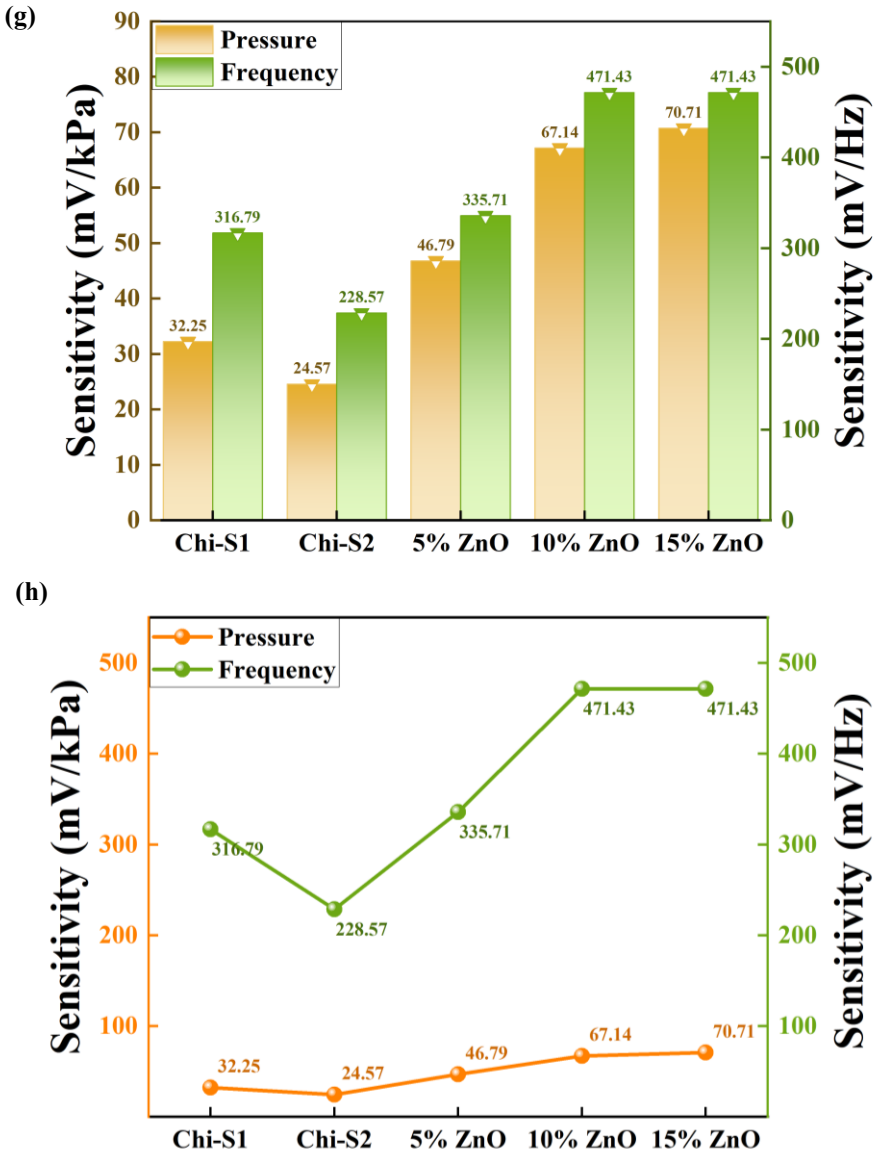


Figure 5.10 Linear fits of the output voltage used to obtain the sensitivities: output voltage against applied pressure for the composites with (a) 5, (b) 10 and (c) 15 wt.% ZnO, and output voltage against loading frequency for the composites with (d) 5, (e) 10 and (f) 15 wt.% ZnO, with the fitted line and the coefficient of determination shown in each panel. (g) Piezoelectric sensitivity value compares and for various sensors including bare chitosan with different thicknesses of 50 µm (Chi-S1) and 85 µm (Chi-S2), and CS-ZnO sensor doped with various concentrations of ZnO such as 5, 10, 15 wt.% under applied pressure and frequency and (h) the sensitivities' linear relationship.

70.71 mV/kPa obtained for the 15 wt.% composite is comparable to or higher than the values reported for several flexible piezoelectric pressure sensors, including those based on nanowire/graphene heterostructures [135], boron nitride nanosheets [136], PVDF-TrFE films [137], PVDF-MoS_2 composites [138] and PZT thin films [10], and is higher than that reported for the biodegradable glycine-chitosan pressure sensor demonstrated previously [19]. This comparison should be treated cautiously, as the pressure range, the loading frequency, the device geometry and the measurement conditions differ between studies. For pressure sensors employed in wearable applications, it is important to maintain a consistent output under repeated mechanical stimulation. Thus, the cyclic stability of the 15 wt.% composite was assessed at 8 Hz and 80 kPa over 1000 compression cycles, as shown in **Figure 5.11**. The output remained repeatable, with no obvious signal failure or abrupt change, which points to a reasonable cyclic stability under repeated loading.

The dynamic response of the sensor to a randomly applied pressure is shown in **Figure 5.12.** The response and recovery times of the 15 wt.% composite were both found to be approximately 12 ms, which is suitable for the real-time tracking of dynamic pressure in wearable monitoring [16]. Across sensitivity, output and cyclic stability, the 15 wt.%

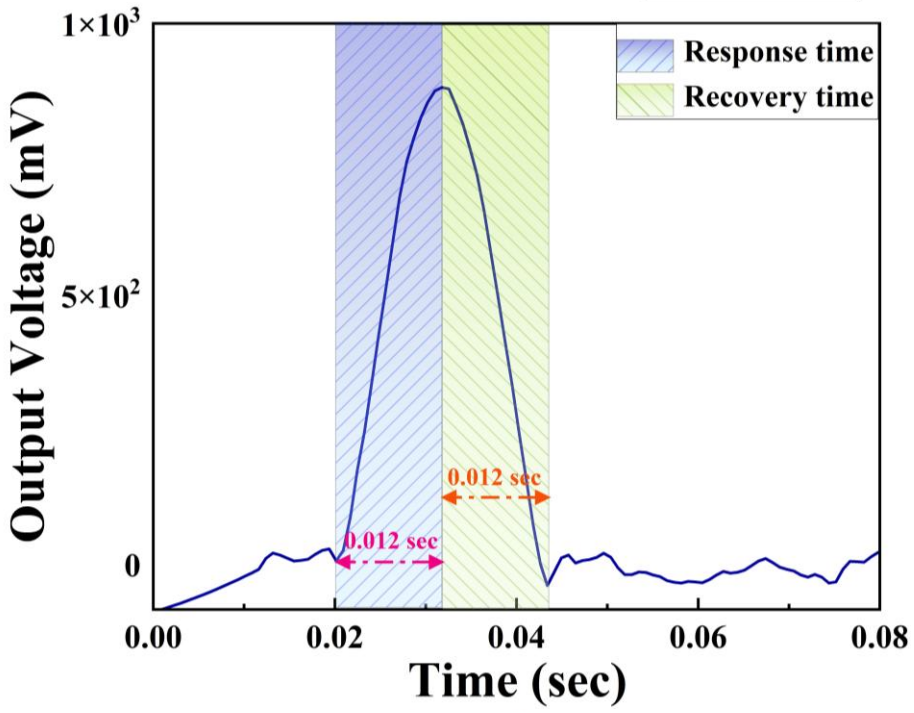


Figure 5.12. Dynamic response of the 15 wt.% CS-ZnO sensors to a randomly applied pressure, showing response and recovery times of approximately 12 ms each.

composite gave the most balanced overall sensing performance among the tested compositions and was selected for the array and application demonstrations in Section 5.4.

5.3.4 Aqueous Dissolution

To investigate whether the aqueous dissolution behaviour of the 15 wt.% CS-ZnO composite film was similar to that of pure chitosan, dissolution tests were therefore conducted. The composite film dissolved rapidly in slightly acidic deionised water at pH 6.5-6.6, and the process was recorded throughout the test, as shown in **Figure 5.13**. Approximately 50% of the composite film remained visible after 30 min, and almost no visible film remained after 2 h. This test shows that the addition of ZnO NPs does not prevent the dissolution process of chitosan.

These observations are consistent with redissolution of chitosan. Similarly, the pure chitosan film, the composite was cast from an acetic acid solution without subsequent neutralisation. Chitosan can therefore retain protonated amino groups associated with acetate counterions, favouring hydration and redissolution in water. Dissolution does not require cleavage of the polymer chains, whereas biodegradation involves their breakdown through enzymatic or microbial activity. No enzymes or microorganisms were added to the immersion medium, and neither the molecular weight of chitosan nor any degradation products were measured.

Biodegradation of CS-ZnO films has been investigated under soil burial conditions. Wrońska et al. reported complete weight loss after eight weeks for films containing ZnO formed in situ using NH_2 molar ratios of 20:1 and 10:1 [100]. Any ZnO NPs released during

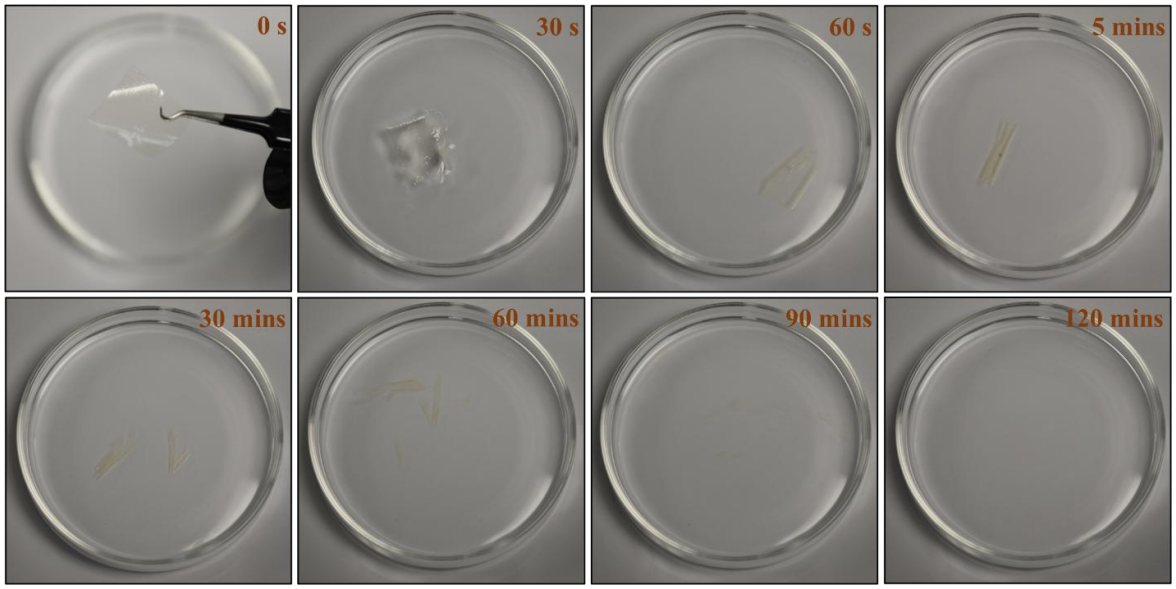


Figure 5.13. Photographs of the 15 wt.% CS-ZnO composite film in deionised water (pH 6.5-6.6) at regular time intervals, showing approximately complete dissolution within 2 h.

dissolution of chitosan can themselves undergo dissolution in water, releasing Zn^{2+} ions. Mudunkotuwa et al. observed ZnO dissolution at pH 7.5, with greater dissolution for smaller particles and in the presence of citric acid [139]. This inorganic dissolution process is distinct from biodegradation of the chitosan chains.

5.4 Applications

5.4.1 Wireless Data Transmission

To enable remote monitoring of the array output, the sensor array was integrated with a wireless transmission system based on a Nordic nRF52840 system-on-chip, as shown in **Figure 5.14.** The nRF52840 combines a 12-bit analogue-to-digital converter with a Bluetooth Low Energy module supporting a data rate of up to 2 Mbps, providing both signal acquisition and wireless communication. The array was used to demonstrate spatial pressure mapping, whereas the wireless experiment used a five-channel sensing arrangement as a readout demonstration. The purpose of this experiment was to verify that the CS-ZnO sensor output could be interfaced with a low-power Bluetooth module for remote display and recording, rather than to acquire data wirelessly from all array elements. A five-channel arrangement of the sensor array was connected to an Adafruit Feather nRF52840 development board. The data were transmitted to a mobile-phone application over the Bluetooth Low Energy link through the serial peripheral interface, with the firmware developed in the Arduino environment. The transmitted output was grouped into three pressure levels for display, corresponding to a low level below 1.8 V, a medium level between 1.8 and 2.5 V, and a high level above 2.5 V. The system transmitted the pressure level recorded by the array to the mobile phone in real time, demonstrating the wireless readout required for a self-powered artificial mechanoreceptor system and indicating its use for remote pressure monitoring. Here, self-powered refers to the piezoelectric sensing element, which generates an electrical signal under pressure without an external bias voltage, while the wireless readout circuit and the Bluetooth module still require an independent power supply.

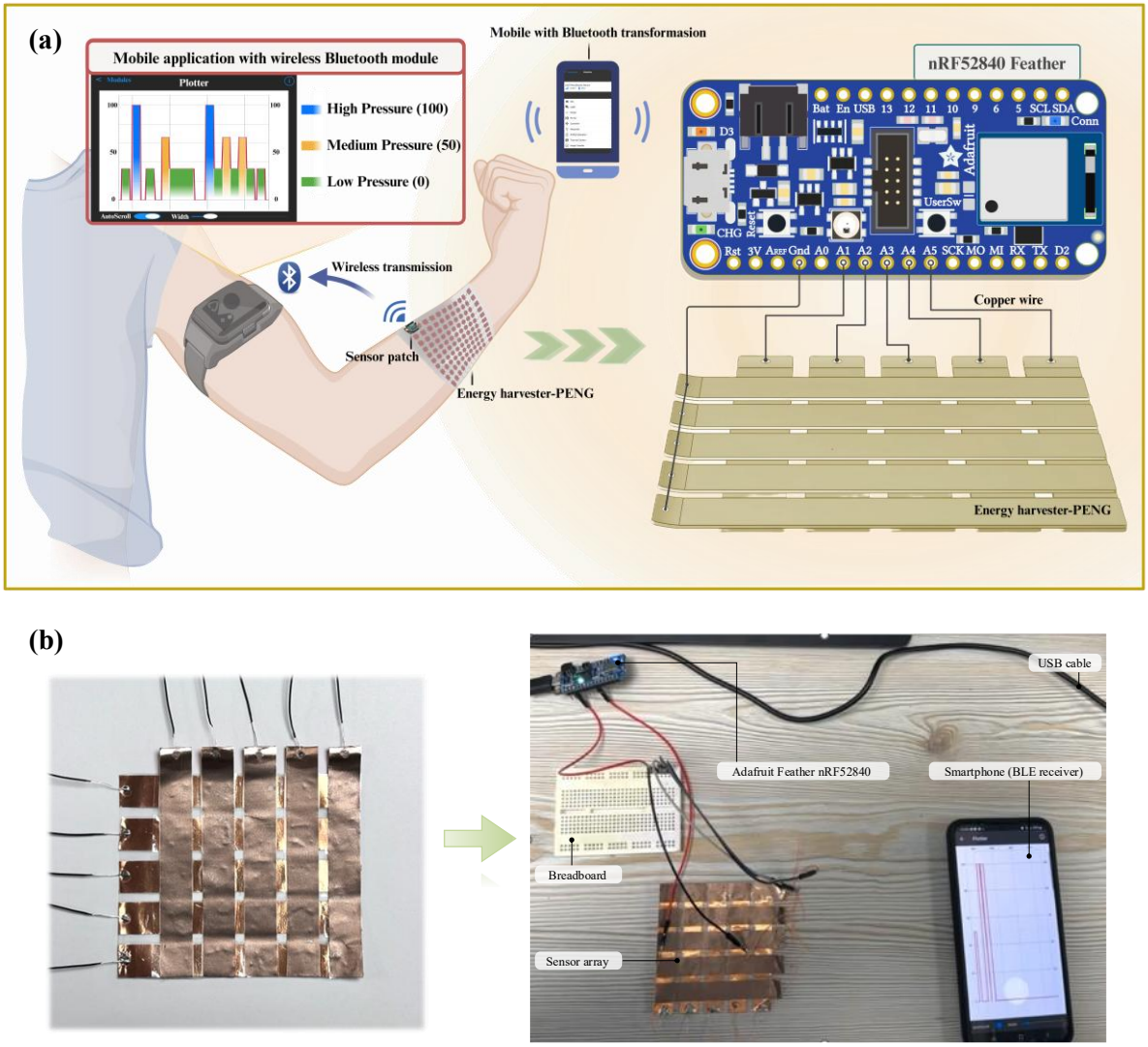


Figure 5.14. Wireless transmission of the CS–ZnO sensor array output through the nRF52840 BLE module: (a) system schematic; (b) photographs of a fabricated 5 × 5 sensor array and the corresponding wireless monitoring setup.

5.4.2 Sensor Array and Spatial Pressure Mapping

To demonstrate spatially resolved pressure sensing, a dynamic pressure sensor array was fabricated from the 15 wt.% CS-ZnO composites, consisting of individual sensing elements, as shown in Figure 5.15. Each element operates as an independent self-powered pressure sensor, so that the array reports the local pressure. When objects were placed on the array, the output voltage of each element varied with the local pressure. The acquired electrical signals were subsequently processed using the modified software system described in Section 5.4.1, which assigned response levels according to the output characteristics of different sensing positions. The distribution of the classified responses across the array was

plotted as a map, in which higher response levels indicate stronger local electrical responses. The higher response regions are shown in darker shades and the lower-response regions in lighter shades. Figure 5.15(a) shows the software-classified response map across the array, in which the higher-output cells reproduce the contact pattern of the object. The numerical values (1, 2, 3 and 6) represent software-assigned response levels rather than directly measured output voltages. Figure 5.15(c) presents the 3D response distribution corresponding to the letter 'C', obtained from the experimentally acquired sensor signals and subsequent software processing conducted within the research group. The height and colour of the 3D surface represent the relative electrical response at different sensing positions rather than the physical height of the contacting object. The higher-response regions reproduce the principal features of the 'C' demonstrating the feasibility of spatial contact detection using the CS-ZnO sensor array. Similar spatial mapping approaches using the voltage responses of piezoelectric sensor arrays have been reported by He et al. [140]. Figure 5.15(b) and (d) present conceptual 2D and 3D representations of the letters 'UofG', respectively, illustrating the potential application of the sensor array in more complex

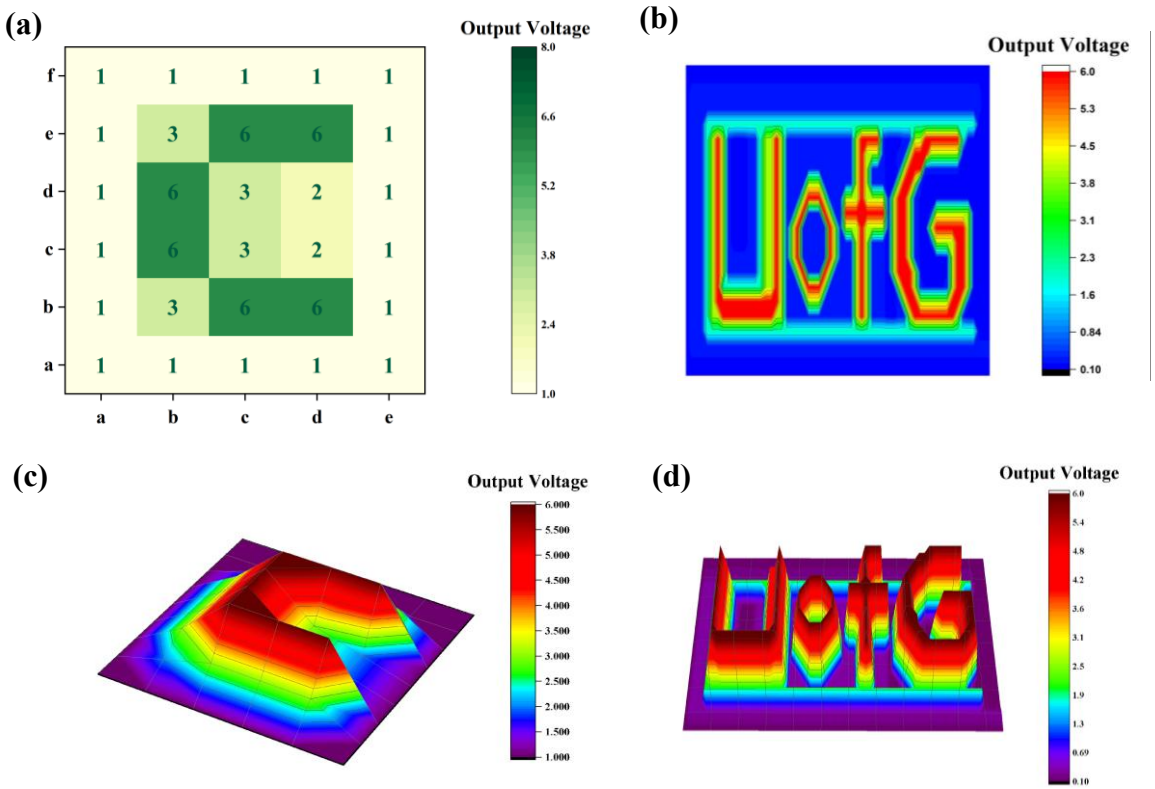


Figure 5.15 Outputs from the CS-ZnO sensor array: (a) the output-voltage map across the array, reproducing the contact pattern of a letter block, (b) a 2D pressure map of the letters 'UofG', and 3D pressure maps of (c) the letter 'C' and (d) the letters 'UofG', reproducing the contact shapes of the objects.

contact-pattern mapping. These results demonstrate the ability of the CS-ZnO sensor array to distinguish relative electrical responses at different sensing positions, supporting its potential for object-contact pattern mapping and spatial pressure-distribution sensing. Such spatially resolved, self-powered pressure mapping is increasingly used in flexible sensors for intelligent perception systems, in which the morphology and structure of the sensing material govern the response. It is also relevant to piezotronics and neuromorphic tactile devices [3], [141] [142].

5.4.3 Wearable Gesture Detection

To demonstrate wearable use, the 15 wt.% CS-ZnO sensor was integrated with the hand and used to detect hand and finger movements, as shown in **Figure 5.16.** Different gestures produced distinct output-voltage responses through the corresponding changes in pressure on the sensor. The applied pressure range of approximately 2-30 kPa, flexion of a finger gave outputs of approximately 49-260 mV, a scissor gesture gave approximately 210-840 mV, and a curved-hand gesture gave approximately 0.32-1.71 V, as shown in **Figure 5.16.** Since the piezoelectric response relates the applied pressure directly to the output voltage, each gesture produced a characteristic real-time signal, and the different gestures could be distinguished from the amplitude and shape of their output. The experimental results show that different hand gestures generate distinguishable voltage amplitudes and waveform patterns, providing an initial basis for gesture differentiation. However, both the magnitude and rate of movement may influence the recorded signals. Future work will investigate signal preprocessing, feature extraction and machine learning algorithms, such as support vector machines (SVM) and decision trees (DT), to enable more accurate and reliable gesture classification. This kind of self-powered gesture detection is relevant to wearable human-machine interfaces and to the monitoring of body movement [143]. This demonstrates the use of the CS-ZnO sensor for the wearable detection of hand movements, which, combined with the sensor array and the wireless transmission described above, supports its use as the sensing element of a self-powered artificial mechanoreceptor system based on a biodegradable CS-ZnO film.

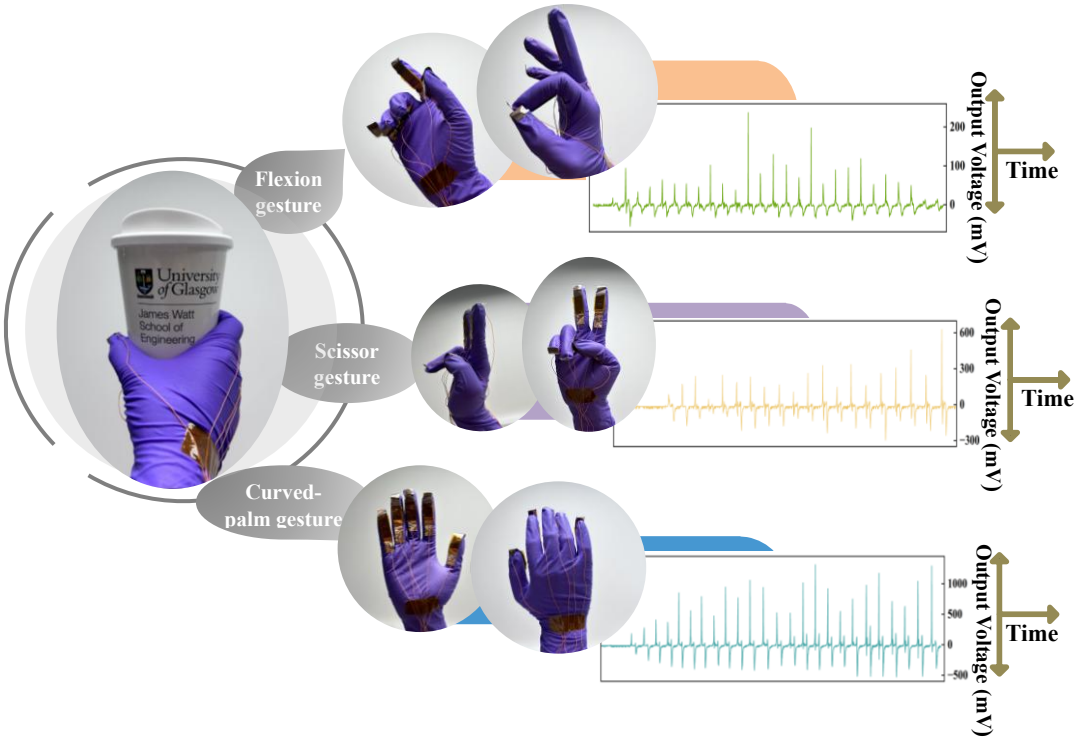


Figure 5.16. Detection of hand gestures using the wearable 15 wt.% CS-ZnO sensor, showing the output voltage responses for (a) flexion of a finger, (b) a scissor gesture, and (c) a curved-hand gesture.

5.5 Summary

This chapter examined a CS-ZnO composite as a self-powered piezoelectric material for dynamic pressure sensing, with the aim of increasing the output of the chitosan sensor while retaining its solubility. CS-ZnO films were prepared by adding ZnO nanoparticles to the chitosan solution at nominal concentrations of 5, 10 and 15 wt.%, with the pure chitosan film as a reference, and were assembled into sandwich-structured sensors with copper electrodes and Kapton encapsulation. SEM, X-ray diffraction and Fourier-transform infrared spectroscopy showed that the wurtzite ZnO was incorporated and dispersed in the chitosan, that the degree of crystallinity increased, and that the chitosan structure was preserved with an interaction between its polar groups and the added ZnO. The added ZnO increased both the permittivity and the piezoelectric coefficient of the film, with d_{33} rising from approximately 7 pC/N for the pure film to 16 pC/N for the 15 wt.% composite. The output voltage and the sensitivity increased with the ZnO concentration, the pressure sensitivity rising from 32.25 to 70.71 mV/kPa and the frequency sensitivity from 316.79 to 471.43 mV/Hz, while the frequency sensitivity levelled off above 10 wt.% as the particles began to cluster. The 15 wt.% composite showed a response and recovery of about 12 ms, a repeatable

output over 1000 compression cycles, and almost complete dissolution in slightly acidic water within 2 h and was then used to demonstrate a sensor array for spatial pressure mapping, a wireless transmission system and the detection of hand gestures.

These results show that adding ZnO to chitosan increases the output and sensitivity of the self-powered sensor while preserving the solubility of the CS-ZnO film, and that the 15 wt.% composite is suitable as the sensing element of an artificial mechanoreceptor system. The levelling-off of the response at the highest concentration, associated with the clustering of the particles, marks a limit to the improvement available from the added ZnO.

Chapter 6: Chitosan-$BaTiO_3$ Composite Flexible Self-Powered Pressure Sensor for a Wireless Gait-Monitoring Insole

6.1 Introduction

Flexible, self-powered pressure sensors are increasingly applied to personalised health monitoring, for which the sensing layer should remain biocompatible and biodegradable to limit any adverse effect on the body and the environment. Chitosan-based piezoelectric films meet this requirement. The previous chapter examined CS-ZnO composite sensors as one route to raising the output response of pure chitosan. In comparison with the pure chitosan sensor, the CS-ZnO composites showed higher device voltage sensitivity and a higher measured piezoelectric coefficient. Among 10 wt.% and 15 wt.% ZnO sensors, the frequency sensitivity showed a plateau, clearly indicating that increase in the concentration of the inorganic ceramic phase does not necessarily produce a proportional increase in dynamic sensing response. At higher ZnO concentrations, nanoparticle agglomeration also became apparent and limited the suitability of the films for conformable wearable use. This chapter therefore examines a second composite route: combining chitosan with BTO as a high-permittivity perovskite ceramic filler to balance flexibility and output amplitude.

$BaTiO_3$ is recognised for its exceptional dielectric response [144]. Compared with the ZnO route, BTO was selected to introduce a more highly polarisable perovskite filler and a larger dielectric contrast with the chitosan matrix. This contrast was expected to influence interfacial polarisation, local electric-field distribution and mechanical stress transfer, thereby providing a route to a stronger device-level voltage response through the combined dielectric and mechanical behaviour of the composite rather than through the piezoelectric charge coefficient alone. BTO was therefore investigated as a complementary filler to ZnO, allowing two lead-free ceramic systems with different structural and dielectric characteristics to be evaluated within the same chitosan matrix. When combined with chitosan, the resulting composite material enhances the overall piezoelectric effect, elevating output voltage and current. Moreover, this combination broadens its biomedical application prospects. Specifically, the high dielectric constant of BTO coupled with the environmentally friendly characteristics of chitosan paves the way for the creation of high-

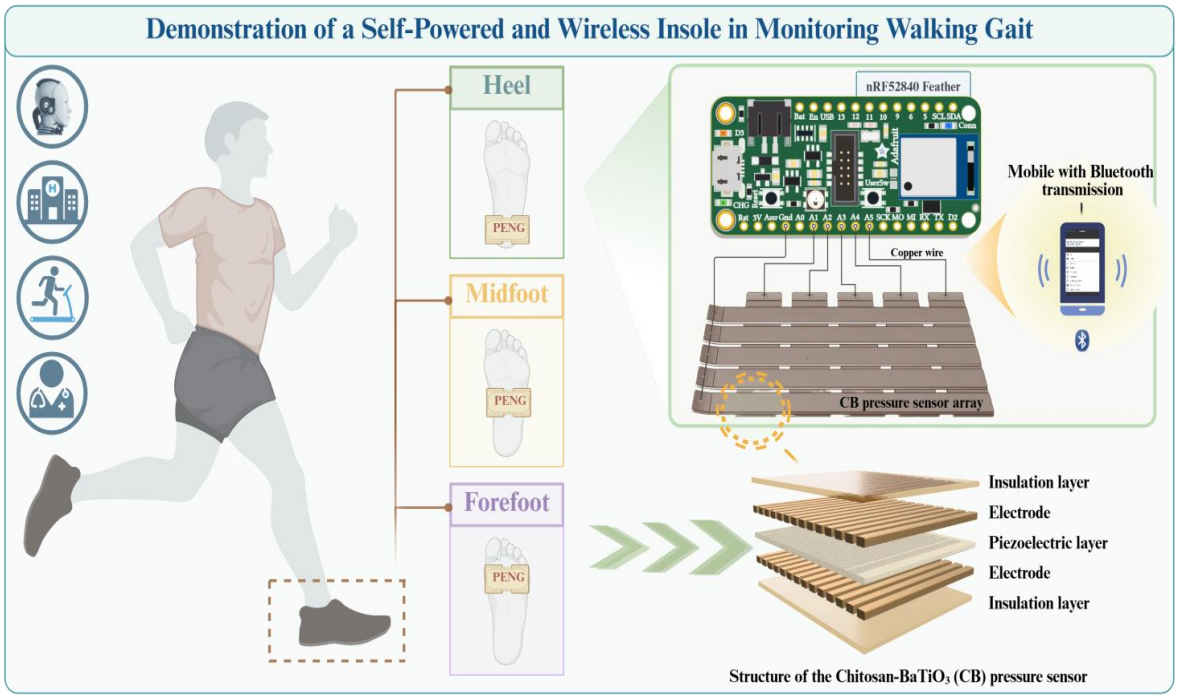


Figure 6.1 Schematic illustration of a wearable wireless insole incorporating zero-bias piezoelectric sensing elements for gait monitoring. The insole integrates sensors at the heel, midfoot and forefoot, while an independently powered Bluetooth module (nRF52840 Feather) transmits the data to a mobile device. The insets show the structure of a CS-BTO pressure sensor, with potential applications highlighted, including human-machine interaction, telemedicine, sports monitoring, and personalised healthcare.

performance, biocompatible, cost-effective and sustainable piezoelectric materials. CS-BTO materials have been examined from several angles, but their use as flexible self-powered pressure sensors remains limited. Murugan et al. examined chitosan containing BTO particles of around 120 nm for the detection of dynamic vibration at 80 Hz and 1 g acceleration, but did not examine flexible pressure-sensor operation, self-powered pressure output or wearable integration [145]. Pongampai et al. added BTO nanorods to chitosan films and reported a higher electrical output, but the study addressed the coupling of triboelectric and piezoelectric effects rather than the piezoelectric pressure-sensing response on its own [146]. Prokhorov et al. reported the piezoelectric properties and biological response of CS-BTO composites, but focused mainly on cell response rather than pressure-sensor performance [89]. These studies provide the background for this chapter and show the need for a pressure-sensor study that links the CS-BTO film structure, the piezoelectric response and wearable pressure monitoring.

This chapter first shows the preparation of a flexible, self-powered pressure sensor based on a CS-BTO composite film, with BTO nanoparticles (NPs) dispersed in chitosan at three

concentrations (5, 10 and 15 wt.%) as the piezoelectric layer. The same concentration range used for the CS-ZnO system was retained to support a direct comparison of filler type and to determine whether the dielectric and interfacial advantages of BTO could increase device output while maintaining an acceptable balance between nanoparticle dispersion, mechanical stiffness and wearable flexibility. The surface morphology, crystal structure and chemical interactions of the films are characterised by SEM, XRD, FTIR and the dispersion of BTO with concentration is quantified. The piezoelectric coefficient, output voltage, sensitivity, response and recovery times, cyclic and bending durability, and mechanical stiffness are then assessed.

Finally, using the CS-BTO film, a biocompatible self-powered dynamic pressure sensor is developed for an insole application. The CS-BTO sensor is configured as an array and integrated with a wireless Bluetooth module (nRF52840 Feather) to demonstrate a self-powered insole for gait monitoring, shown in **Figure 6.1** [147], [148]. The array distinguishes participants of different body weight and transmits the recorded signals to a mobile device, following the wireless approach established for the CS-ZnO sensor in the previous chapter [21].

6.2 Materials and Methods

6.2.1 Preparation of CS-BTO Composite Films

The CS-BTO composite films were prepared by adding BTO nanoparticles to the prepared chitosan solution following the route illustrated in **Figure 6.2**. 0.1, 0.2 and 0.3 g of BTO nanoparticles were separately added to 100 mL aliquots of the 2% (w/v) chitosan solution to give nominal BTO concentrations of 5, 10 and 15 wt.%. Each suspension was sonicated and degassed under vacuum as before to obtain a uniform and stable suspension. Finally, the CS-BTO suspension was cast onto a polystyrene Petri dish lined with poly (vinyl chloride) (PVC) film and spin-coated at 1000 rpm for 30 s to spread it evenly, after which it was dried in an oven (Memmert UF55) at 39 °C for 10 h to form the composite film. The pure chitosan film used for comparison was the one prepared in Chapter 4. The thickness of the composite films was measured with a thickness gauge (Logitech CG10).

6.2.2 Fabrication of the CS-BTO Sensor

The CS-BTO films were fabricated into pressure sensors with the same sandwich structure used for the pure chitosan and CS-ZnO sensors, in which the composite film served as the piezoelectric layer between two copper electrodes, as illustrated in **Figure 6.2**. The pure chitosan film and the 5, 10 and 15 wt.% CS-BTO films were each cut into 2.5 cm × 2.5 cm pieces from randomly selected regions of the films, and copper electrodes slightly smaller than the film were prepared to avoid short-circuiting at the edges. The electrodes were fixed to the upper and lower faces of the film to collect the charge generated under applied pressure. The sensor was then encapsulated with polyimide (Kapton) tape to reduce the influence of humidity, perspiration and incidental water contact during operation, and to preserve the flexibility and stability of the device.

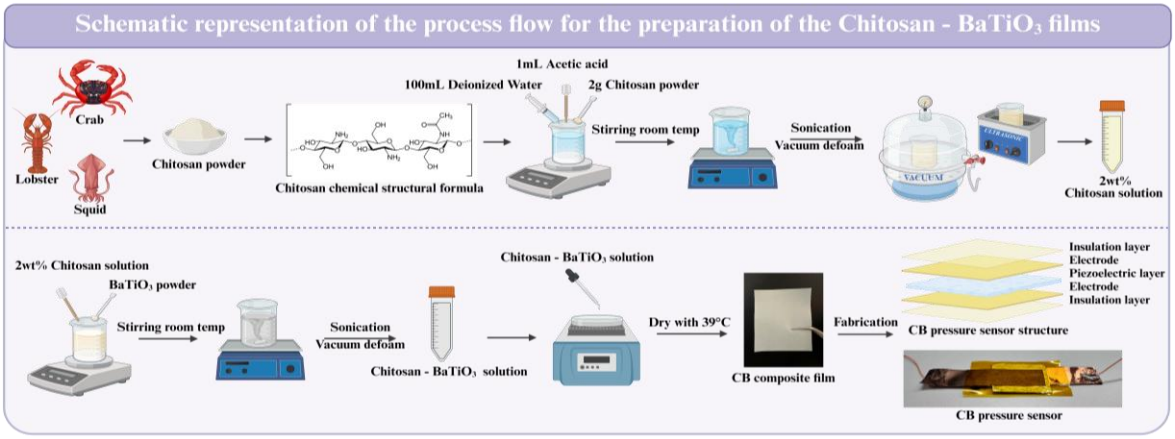


Figure 6.2 Schematic illustration of the fabrication process for CB composite films derived from marine bio-waste and subsequent assembly into a CB pressure sensor device.

6.2.3 Statistical Methods

The dispersion of BTO within the chitosan was quantified from the scanning electron micrographs using image analysis in ImageJ. Each micrograph was converted to an 8-bit greyscale image to obtain the intensity histogram for segmentation, and the contrast was adjusted to 0.6% saturated pixels so that the nanoparticles were clearly distinguishable from the surrounding chitosan, after which the particle regions were isolated by thresholding. The agglomeration fraction (AF) was then defined as the ratio of the total projected area of the agglomerates to the area of the analysed region of interest (ROI), expressed as a percentage in **Equation 6.1**:

$$AF = \frac{\sum Area_{agglomerates}}{Area_{ROI}} \times 100\% \quad (6.1)$$

where $Area_{agglomerates}$ is the total projected area of the BTO agglomerates and $Area_{ROI}$ is the total area of the analysed region. A higher AF therefore corresponds to a larger projected area fraction classified as agglomerates within the analysed ROI.

6.3 Results and Discussion

6.3.1 Material Characterisation

To explore the microstructural changes that occur during the process of fusing chitosan with different concentrations of BTO NPs, a range of analytical techniques were employed, including SEM, XRD and FTIR.

- **Morphology of CS-BTO films using SEM**

The surface morphology of the composite films was examined by field-emission SEM (FEI Nova Nano), and representative micrographs for the three concentrations are shown in **Figure 6.3(a)-(c)**. The bright features correspond to BTO nanoparticles dispersed within the chitosan. At 5 wt.%, the nanoparticles are distributed non-uniformly within the imaged region, with areas of higher apparent particle density adjacent to areas containing fewer visible particles, as shown in **Figure 6.3(a)**. At 10 wt.%, the particles remain distinguishable but form moderate clusters with areas containing fewer visible particles between them, as shown in **Figure 6.3(b),** whereas at 15 wt.% the particles are more closely spaced, with local agglomeration evident across much of the observed region, as shown in **Figure 6.3(c)**. This clustering at higher BTO concentrations is consistent with the behaviour of ceramic-polymer composites [149]. The observed local variations may be associated with incomplete nanoparticle dispersion or redistribution during film formation, but do not necessarily indicate non-uniform film thickness. Clustering may affect local stress transfer and, where associated with surface unevenness, electrode contact during sensor fabrication. Shin et al. reported high piezoelectric output from $BaTiO_3$ hysteresis P(VDF-HFP) composite films with optimised nanoparticle clustering [150]. This indicates that local clustering does not necessarily lead to reduced piezoelectric output, although its effect on the present CS-BTO sensors cannot be determined from the SEM images alone. Possible region-to-region variations in the measured sensor response have not been independently quantified.

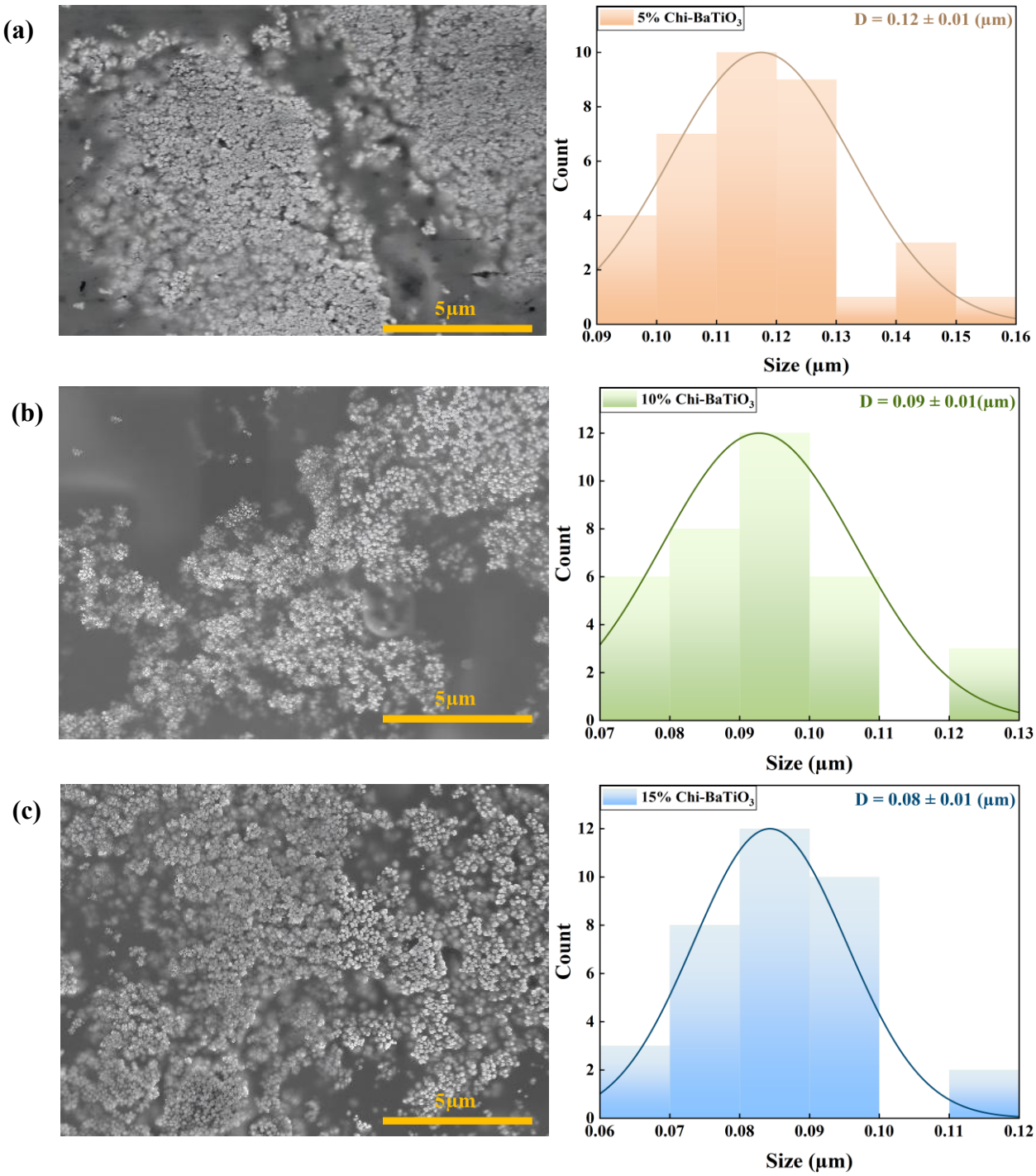


Figure 6.3 SEM images and corresponding particle-size distribution histograms of the CS-BTO composite film at $BaTiO_3$ concentrations of (a) 5 wt.%, (b) 10 wt.% and (c) 15 wt.%. Scale bars, 5 µm.

The particle size distribution obtained from the micrographs (N=50) gives average diameters of 0.12, 0.09 and 0.08 µm for the 5, 10 and 15 wt.% composites, respectively **Figure 6. 3(a)-(c)**, indicating a denser and more finely divided particle population at higher concentration. The agglomeration fraction (AF) of BTO at different concentrations was further calculated using **Equation 6.1.** The AF values for different concentrations (5, 10, 15 wt.%) were

obtained as the 45%, 54%, and 56%, respectively, indicating an increasing projected area fraction classified as agglomerates within the analysed SEM regions.

- **Structural characterisation of CS-BTO films using XRD**

The crystalline structure of the films was determined by XRD (Rigaku MiniFlex 600, step size 0.01°, scanning range 10-70° 2θ), and the patterns are shown in **Figure 6.4**. The BTO powder produced sharp and intense reflections at 2θ values of 22.3°, 31.7°, 39°, 45°, 51.1°, 56.4° and 66°, confirming a crystalline perovskite BTO structure [151], [152]. The BTO powder used in this study was specified as cubic by the supplier, as reported in **Table 3.1**, and the absence of resolved splitting between the (002) and (200) diffraction peaks near 45° was resolved in the XRD pattern, consistent with the cubic phase assignment. The sharpness and intensity of these reflections indicate that the BTO particles are well crystallised. BTO provides the piezoelectric ceramic contribution to the composite. The pure chitosan film, by contrast, produced two broad and low-intensity reflections near 9° and 20°, associated with the (020) and (200) planes of chitosan. The breadth of these features shows that the film is only semicrystalline and is dominated by an amorphous fraction, in keeping with the hydrogen-bonded packing of the polysaccharide chains.

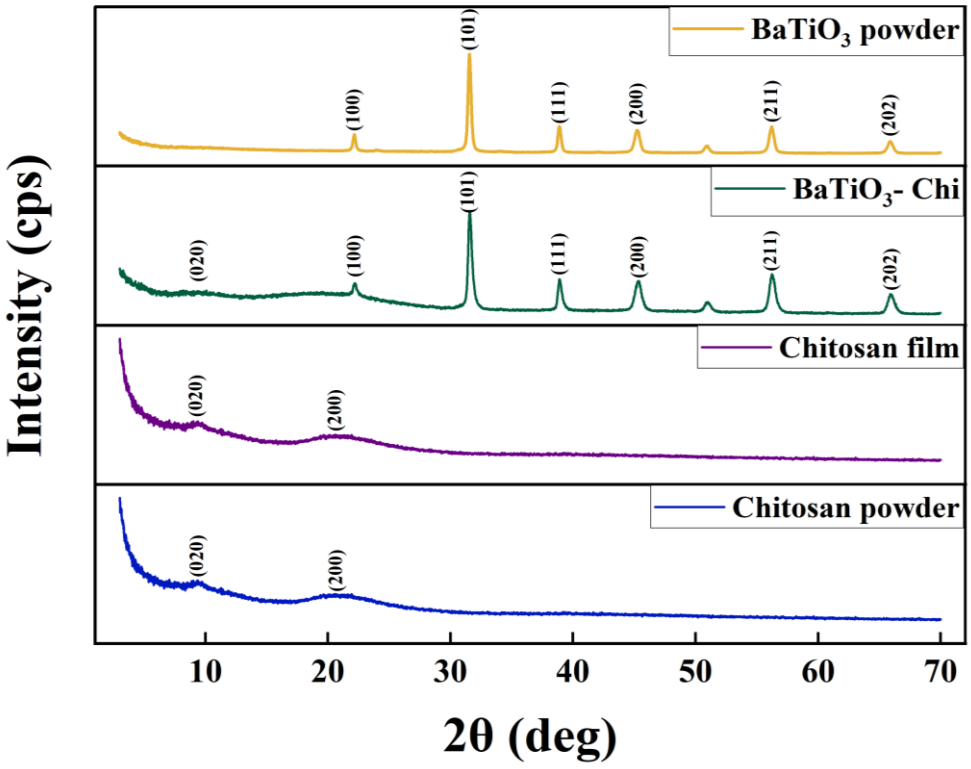


Figure 6.4 XRD patterns of BTO powder, the CS-BTO composite films, the pure chitosan film and chitosan powder.

In the composite films, the full set of sharp crystalline BTO reflections appears together with the weak chitosan features, with no additional peaks. The pattern is dominated by the crystalline ceramic and the much weaker chitosan (020) contribution is largely masked, so that the composite shows stronger crystalline features than the pure chitosan film. The absence of any reflections attributable to a secondary phase, such as barium carbonate, indicates that BTO is incorporated into the chitosan without chemical alteration of the ceramic and that the crystalline perovskite structure is preserved through mixing, casting and drying. The retention of the BTO reflections without new peaks, accompanied only by small reductions in their relative intensity within the composite, is consistent with a physical interaction between the particle surfaces and the chitosan while the BTO crystal structure is retained.

- **Chemical characterisation of CS-BTO films using FTIR**

The chemical structure of the films and the interaction between chitosan and BTO were examined by FTIR (Jasco FTIR-4100), with spectra for the BTO powder, the pure chitosan films (Chi-S1 and Chi-S2) and the composites shown in **Figure 6.5**. The pure chitosan film displays the characteristic absorption bands of the polysaccharide [84], [123]. A broad and intense band near 3430 cm^{-1} arises from overlapping O-H and N-H stretching, and two bands at 2921 and 2908 cm^{-1} correspond to asymmetric and symmetric C-H stretching of the sugar ring, indicating that the sugar-ring framework is retained. The amide I band at 1655 cm^{-1} corresponds to C=O stretching coupled to the C-N mode and the amide II band at 1556 cm^{-1} to N-H bending, while the bands near 1410 and 1225 cm^{-1} are associated with C-N stretching and with the C-O-C vibration of the glycosidic linkage. The strong band near 1032 cm^{-1} corresponds to C-O stretching of the backbone and the band near 868 cm^{-1} to the ring vibration of the saccharide units. In the composite spectra, an additional band near 577 cm^{-1} corresponds to the Ti-O stretching of the TiO_6 octahedra of BTO, which confirms the presence of the ceramic alongside the chitosan.

The chitosan bands are retained in the composite at essentially their original positions. This indicates that the chitosan structure is preserved and that BTO is incorporated through physical interaction and hydrogen bonding at the particle surfaces rather than through chemical modification of the chitosan, in agreement with the XRD results. With increasing BTO concentration, the intensity of the C-H and the other chitosan bands decreases, which is attributed to the physical dilution of the chitosan by the larger ceramic fraction and to the

correspondingly weaker contribution of the chitosan to the spectrum. The retention of the O-H, N-H and amide bands, together with the appearance of the Ti-O band of BTO, confirms that both components are present in the composite. The polar hydroxyl and amine groups of the chitosan identified here, together with the incorporated BTO, are the structural features that underlie the charge generated by the film under mechanical loading.

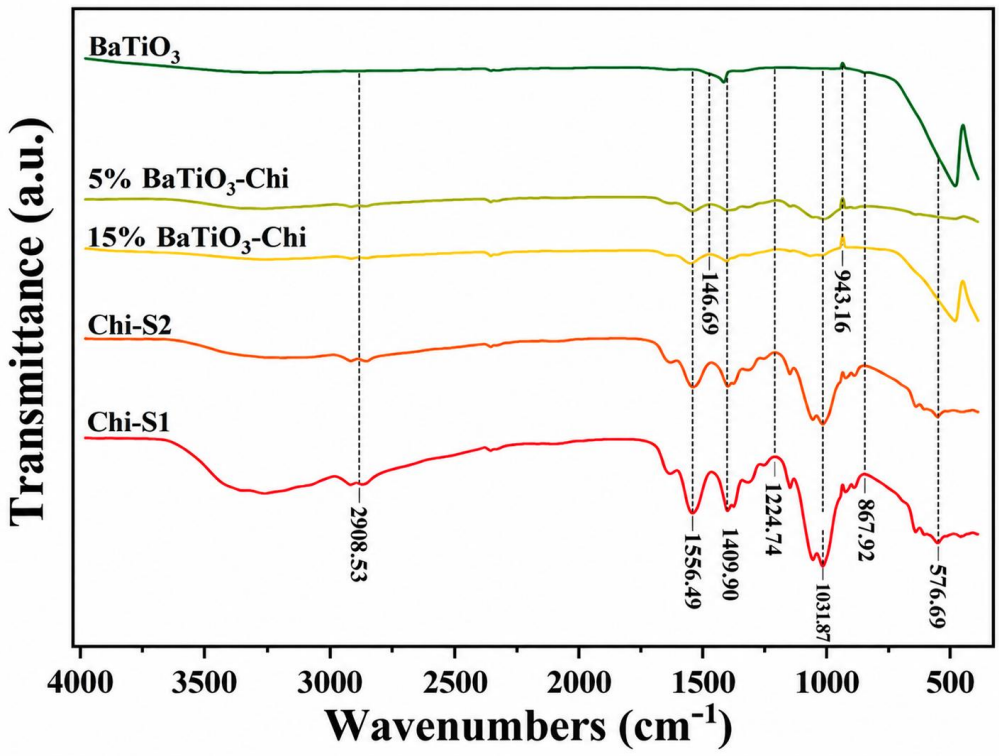


Figure 6.5 FTIR spectra of BTO powder, the CS-BTO composite films, and the pure chitosan films Chi-S1 and Chi-S2.

6.3.2 Piezoelectric Coefficient (d_{33})

The piezoelectric coefficient d_{33} was measured by the quasi-static (Berlincourt) method described in Chapter 3, applying a force of 0.25 N at 110 Hz and obtaining the charge generated per unit applied force using **Equation 6.2**:

$$d_{33} = \frac{Q}{F} \tag{6.2}$$

where Q is the charge generated and F is the applied force. As shown in **Figure 6.6**, d_{33} increases from 7 pC/N for the pure chitosan film to approximately 13 pC/N for the 15 wt.% CS-BTO composites, an increase of roughly twofold. This increase is consistent with the higher piezoelectric coefficients reported for BTO composites [140], [151]. For comparison, the 15 wt.% CS-ZnO film exhibited a d_{33} of approximately 16 pC/N, whereas the CS-BTO

film exhibited approximately 13 pC/N, about 19% lower. This difference may be associated with the distinct polarisation behaviour of the two fillers, as well as differences in nanoparticle dispersion and interfacial interactions within the chitosan matrix [88], [89]. However, the individual contributions of these factors were not independently quantified.

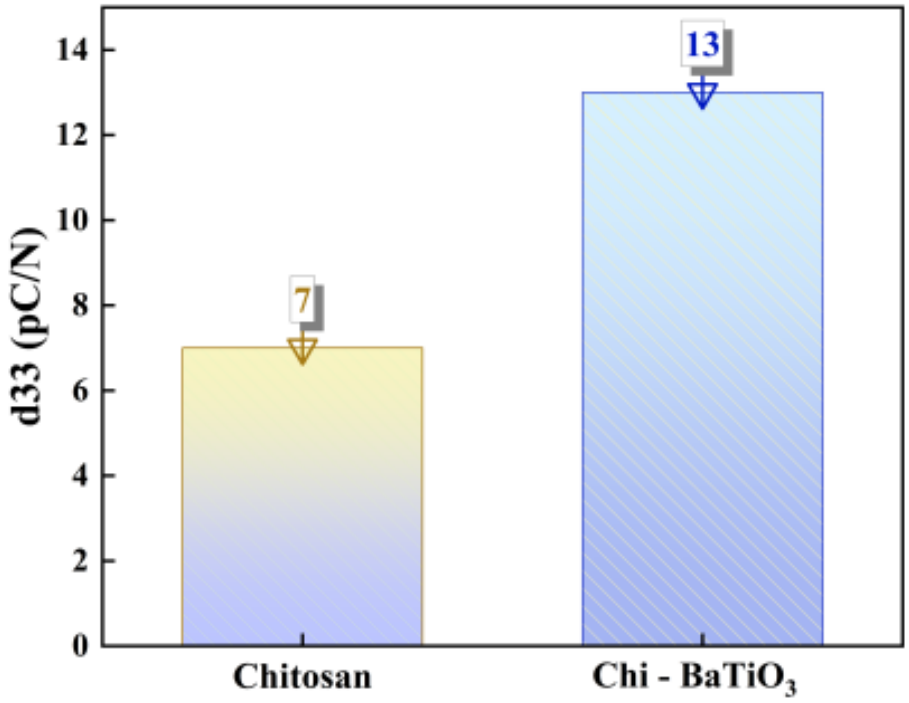


Figure 6.6 Piezoelectric coefficient d_{33} of the pure chitosan film and the 15 wt.% CS-BTO composites.

6.3.3 Pressure Sensor Characterisation

The sensor produces an electrical output through the direct piezoelectric effect of the composite film. When a compressive load is applied, the film deforms and a charge of one sign accumulates on the electrodes, and on release a charge of the opposite sign is generated, so that periodic compression yields the alternating voltage characteristic of a piezoelectric sensor. The output rises with applied pressure since a higher load produces a larger deformation and therefore a greater generated charge, and it rises with loading frequency since the film then undergoes more compression-release cycles per unit time and deforms at a higher rate. The output increases further with BTO concentration, consistent with the higher piezoelectric coefficient of the composite and with the high dielectric constant of the BTO particles, both of which act to raise the charge delivered to the electrodes for a given mechanical input.

The output voltage of the sensors was characterised under controlled compressive loading using a tuneable-frequency vibration system (TV 50018, TIRA GmbH), which applies periodic compressive loads, the generated voltage being recorded with a digital storage

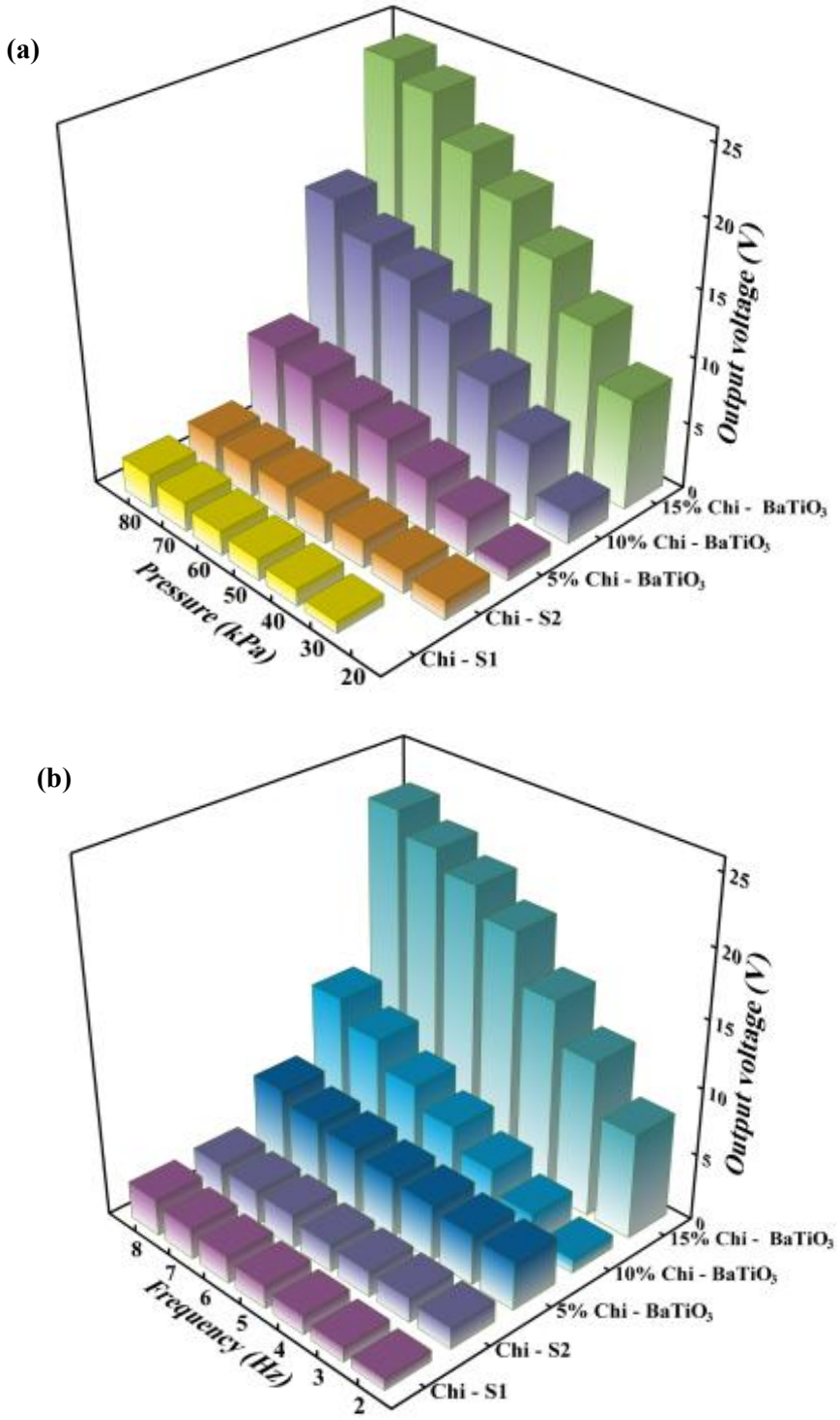


Figure 6.7 Output voltage of the CS-BTO sensors (a) under pressures from 20 to 80 kPa in 10 kPa increments at a fixed frequency of 8 Hz, and (b) under frequencies from 2 to 8 Hz in 1 Hz increments at a fixed pressure of 80 kPa.

oscilloscope (Keysight DSOX3014T). The output voltage results as the applied pressure were increased from 20 to 80 kPa in 10 kPa increments at a fixed frequency of 8 Hz and the output as the frequency was increased from 2 to 8 Hz in 1 Hz steps at a fixed pressure of 80 kPa. For all sensors the output voltage increases with both pressure and frequency and rises further with BTO concentration as shown in **Figure 6.7(a)** and **Figure 6.7(b)**. Over the pressure range, Chi-S1 produced an output of up to 2.61 V, while the 5, 10 and 15 wt.% composites rose from 1.01 to 7.6 V, from 2.4 to 16.7 V, and from 8.4 to 24.9 V, respectively. Over the frequency range, the 5 wt.% composite rose from 3.6 to 6.4 V, the 10 wt.% composite from 1.0 to 11.3 V, and the 15 wt.% composite from 7.9 to 23.3 V. Under a separate force-controlled excitation of 5 N at 5 Hz, both the output voltage and the output current increased with BTO concentration illustrated in **Figure 6.8 (a) and (b)**, corroborating under a fixed applied force the trends observed in the pressure- and frequency-controlled measurements. The sensitivity of each sensor was obtained from a linear fit of the output voltage as a function of applied pressure and of loading frequency, as defined in **Equation 6.3** and **Equation 6.4**:

$$S_P = \frac{\Delta V}{\Delta P \text{ at a constant } frequency} \tag{6.3}$$

$$S_f = \frac{\Delta V}{\Delta f \text{ at a constant pressure}} \tag{6.4}$$

where ΔV is the change in output voltage, ΔP is the change in applied pressure, and Δf is the change in frequency. The linearity of each fit was quantified by the coefficient of determination R^2 given by **Equation 6.5**:

$$R^2 = 1 - \frac{\sum_i (y_i - \hat{y}_i)^2}{\sum_i (y_i - \bar{y})^2} \tag{6.5}$$

where y_i are the measured values, $\hat{y}_i$ the fitted values, and $\bar{y}$ the mean value of y_i. All the resultes of these fits for the three composites, with the slope of each fit taken as the sensitivity are shown in the -**Figure 6.9 (a) - (f).** The pressure sensitivity rises from 32.25 mV/kPa for the pure chitosan film Chi-S1 to 105.21, 233.21 and 276.07 mV/kPa at 5, 10 and 15 wt.%, and the frequency sensitivity from 316.79 mV/Hz to 448.57, 1703.21 and 2564.29 mV/Hz across the same films. The 15 wt.% composite is 8.6 times as sensitive to pressure and 8.1 times as sensitive to frequency as the pure chitosan film, and its sensitivities are comparable to those reported for other flexible BTO based pressure sensors [149], [153]. Every fit gave a coefficient of determination of closing to 1between 20 and 80 kPa, which indicates a linear

response suitable for quantitative pressure measurement. This 8.6-fold higher than the twofold rise in d_{33}, so the coefficient does not account for the sensitivity of the composites. Adding more BTO also introduces more piezoelectrically active material, and the mean particle diameter falls from 0.12 to 0.08 μm and the film contains a larger number of finer particles that release charge under pressure and raise the effective piezoelectric response. As the BTO concentration increases the agglomeration fraction also rises, from 45% to 56%,

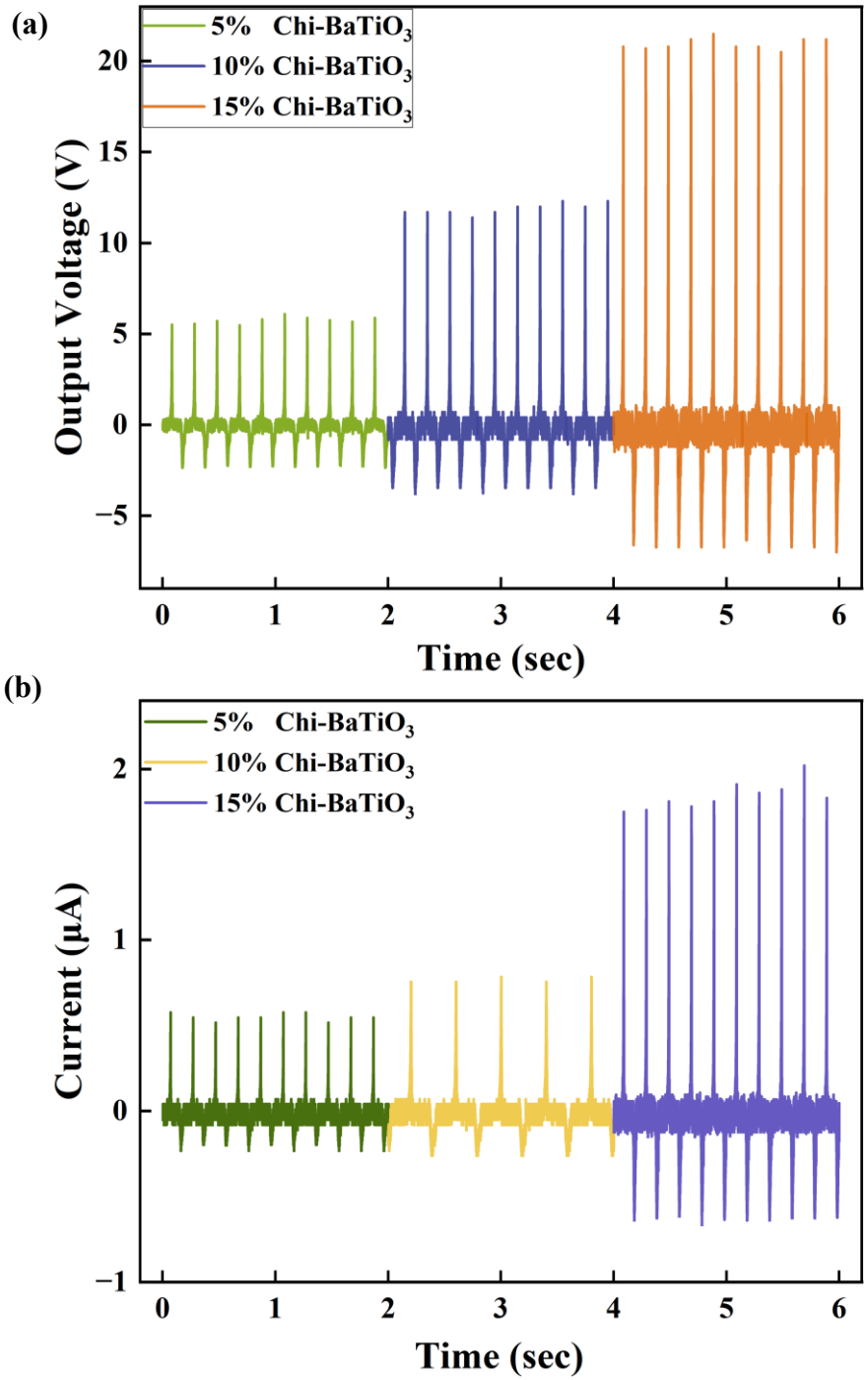


Figure 6.8. Electrical output of the CS-BTO sensors at different BTO concentrations under a fixed excitation of 5 N at 5 Hz: (a) output voltage and (b) output current.

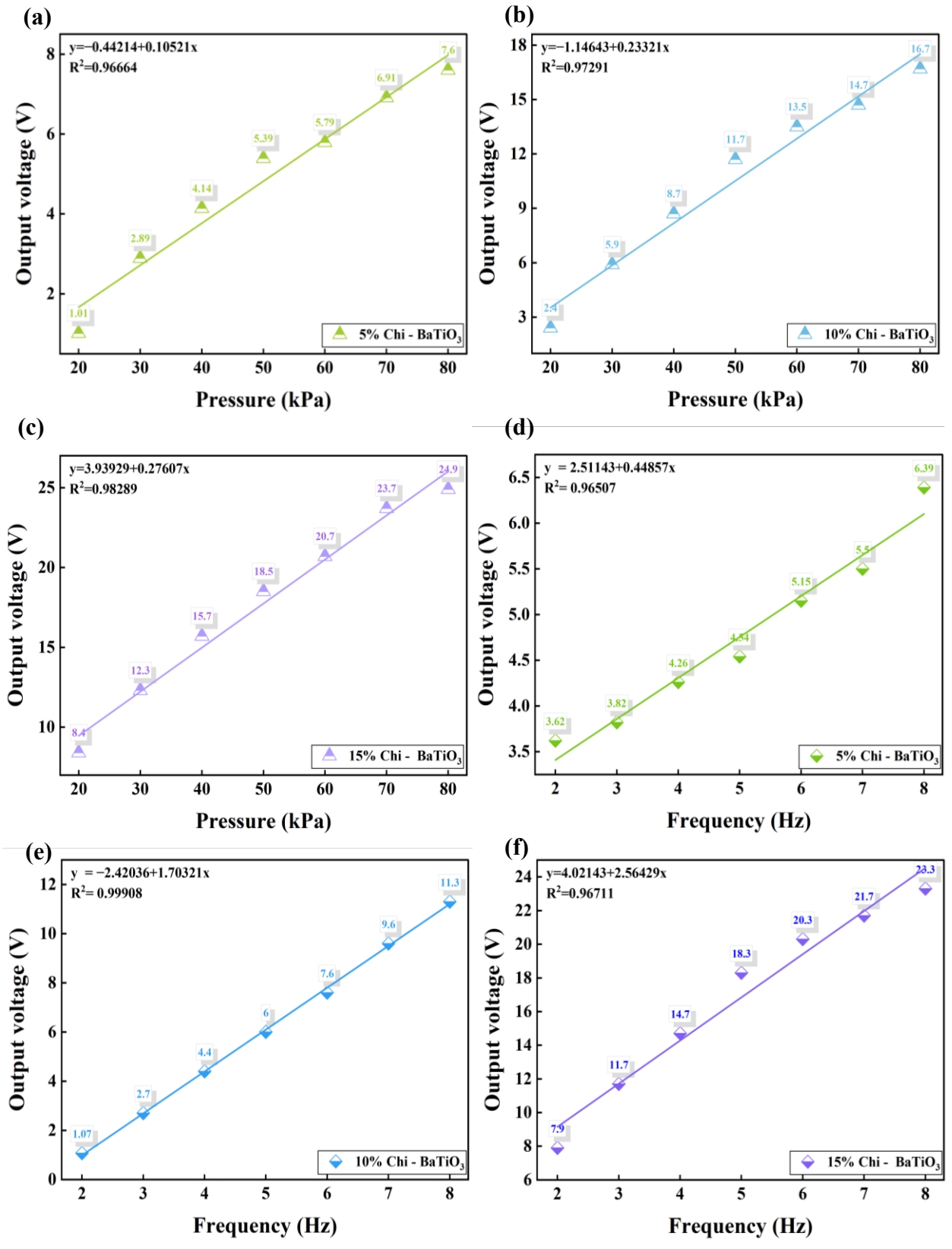


Figure 6.9 Linear fits of the piezoelectric response of the CS-BTO composites: (a)-(c) output voltage against applied pressure and (d)-(f) output voltage against frequency, for the 5, 10 and 15 wt.% composites.

while both pressure and frequency sensitivities continue to increase. Between 10 and 15 wt.% BTO, AF rises from 54% to 56%, whereas the pressure sensitivity increases from 233.21 to 276.07 mV/kPa and the frequency sensitivity from 1703.21 to 2564.29 mV/Hz. These results indicate that the observed local clustering did not prevent improved sensor response within the investigated concentration range. A similar trend has been validated by Ciomaga et al. in BTO nanocube and gelatin composite films, where the piezoelectric coefficient d_{33} increased from 7 pm/V in pure gelatin to 21 pm/V at 40 wt.% BTO loading [154]. Despite the lower d_{33}, the 15 wt.% CS-BTO sensor exhibited pressure and frequency sensitivities approximately 3.9 and 5.4 times those of the corresponding CS-ZnO sensor, respectively. Its maximum reported output voltage was also approximately 3.7 times higher under the respective device configurations. These results indicate that the measured voltage response is not determined by d_{33} alone. Film thickness and stiffness, active area, dielectric response, interfacial polarisation, stress distribution, electrode contact and readout impedance may also influence the measured output [8].

The transient response of the 15 wt.% CS-BTO sensors to a single pressure impulse is shown in **Figure 6.10(a).** Defining the response time as the time taken for the signal to rise from 10% to 90% of its steady-state amplitude and the recovery time as the corresponding 90% to 10% decay, the sensor exhibits a response time of 0.24 ms and a recovery time of 0.64 ms. The hysteresis of the sensor is defined as the difference in output voltage between the loading and unloading paths at the same applied pressure, reflects the measurement accuracy and the energy dissipated during deformation [155]. The pressure applied to the 15 wt.% CS–BTO sensor was increased stepwise from 20 to 80 kPa and then decreased back to 20 kPa at a fixed frequency of 8 Hz. Hysteresis was calculated using **Equation 6.6**:

$$H_{Full\ scale}\% = \frac{max|V_{loading} - V_{unloading}|}{V_{full\ scale}} \times 100\% \tag{6.6}$$

where $V_{loading}$ and $V_{unloading}$ are the output voltages on the loading and unloading paths and $V_{full\ scale}$ the full-scale output. As shown in **Figure 6.10(b)**, the loading and unloading curves follow closely matched paths, with a maximum output-voltage difference of 0.8 V at 50 kPa relative to a full-scale span of 16.5 V. The ratio of these two values gives a hysteresis of 4.85% at 8Hz. The observed hysteresis may arise from the viscoelastic deformation and delayed recovery of the chitosan matrix and from friction at interfaces within the sensor. Increasing the loading frequency reduces the time available for recovery between successive

cycles. Incomplete recovery may increase the difference between the loading and unloading outputs. The magnitude of this effect depends on the loading period relative to the relaxation times of the composite.

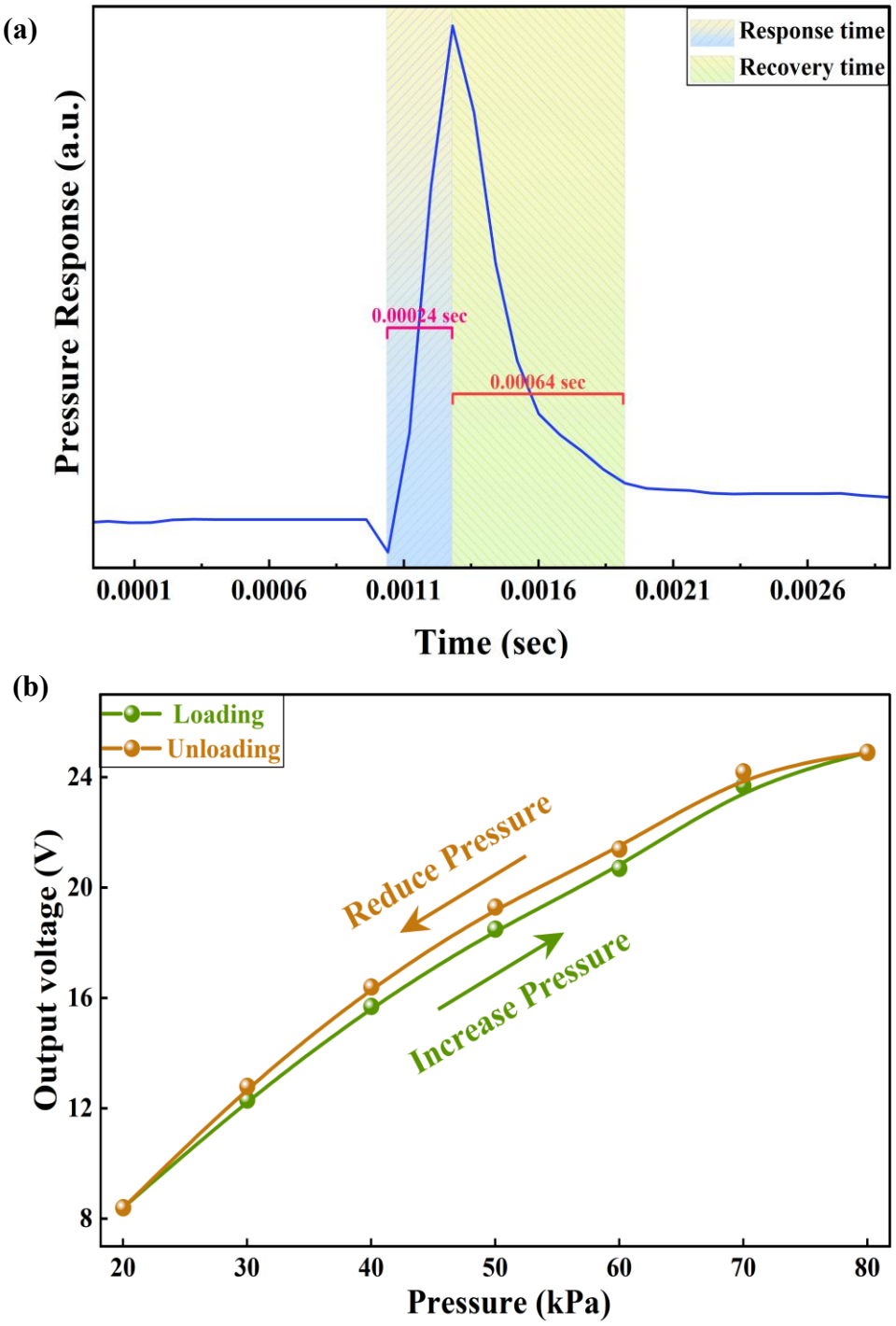


Figure 6.10. Dynamic response of the 15 wt.% CS-BTO sensors: (a) transient response to a single pressure impulse, showing a response time of 0.24 ms and a recovery time of 0.64 ms, (b) hysteresis under stepwise compressive loading and unloading between 20 and 80 kPa at a fixed frequency of 8 Hz.

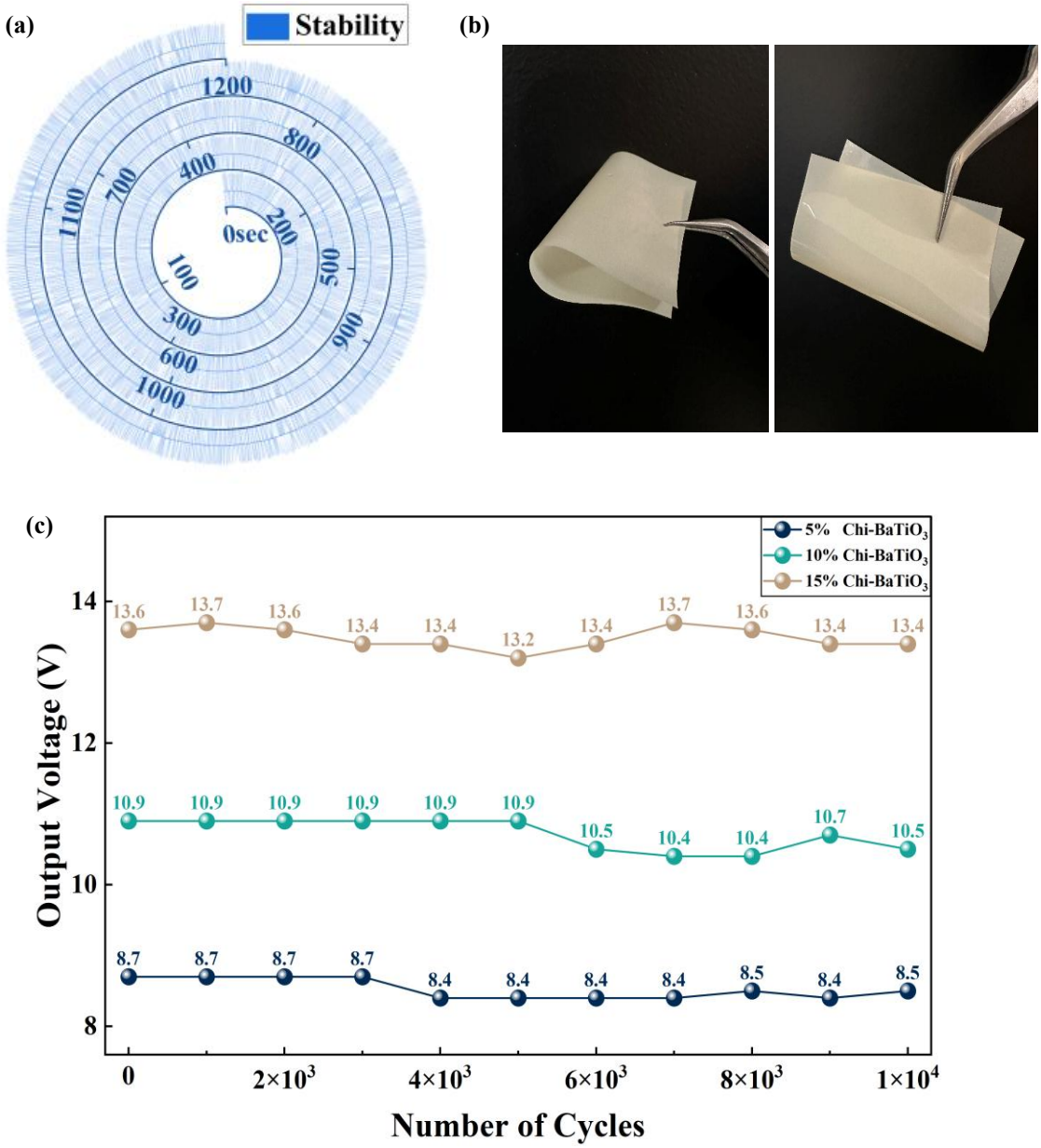


Figure 6.11 (a) Long-term stability under continuous cyclic loading, illustrated over 1200s with sustained, repeatable applied pressure. Bending reliability tests of the CB sensor: (b) CB film under bending deformation and (c) output-voltage stability after 10^4 bending cycles for different BTO concentration (5, 10 and 15 wt.%).

The durability of the sensor was assessed under both continuous cyclic compression and repeated bending. Under cyclic compression, the output remained consistent for 1200 s, confirming stable operation under sustained mechanical loading as **Figure 6.11(a)**. To assess suitability for conformable use, cyclic bending tests were performed using 3D printed fixtures that provide controlled bending angles between 0 and 180 degrees. The composite film under bending deformation is shown in **Figure 6.11(b)**, and the sensor maintained a stable output after 10^4 bending cycles for all three concentrations as **Figure 6.11(c)**, indicating that the composite tolerates repeated deformation without loss of function.

6.3.4 Mechanical Properties

The mechanical behaviour of the composite films was characterised by tensile testing using a universal testing machine (Instron 3367) with a gauge length of 40 mm, and the Young's modulus was obtained from the slope of the elastic region of the stress-strain response using **Equation 6.7**:

$$E = \frac{dF}{d\Delta L}\frac{L_0}{A} \tag{6.7}$$

where $\frac{dF}{d\Delta L}$ is the slope of the force-displacement curve, L_0 the initial gauge length, and A the cross-sectional area of the specimen. **Figure 6.12** shows the test configuration and the stress-strain curves of the composites. The curves show that the composite stiffens monotonically with BTO concentration, the 15 wt.% film being the stiffest of the three. The Young's modulus increases from 6.21 GPa at 5 wt.% to 9.14 GPa at 10 wt.% and 10.53 GPa at 15 wt.%. This stiffening may be attributed to the increasing volume fraction of rigid BTO NPs and to load transfer from the compliant chitosan to these particles [156]. The higher modulus at 15 wt.% identifies the cost that accompanies the higher piezoelectric output. The same BTO concentration that raises the sensitivity also reduces the compliance of the film. A higher BTO concentration therefore raises the piezoelectric output but lowers the mechanical conformability of the film.

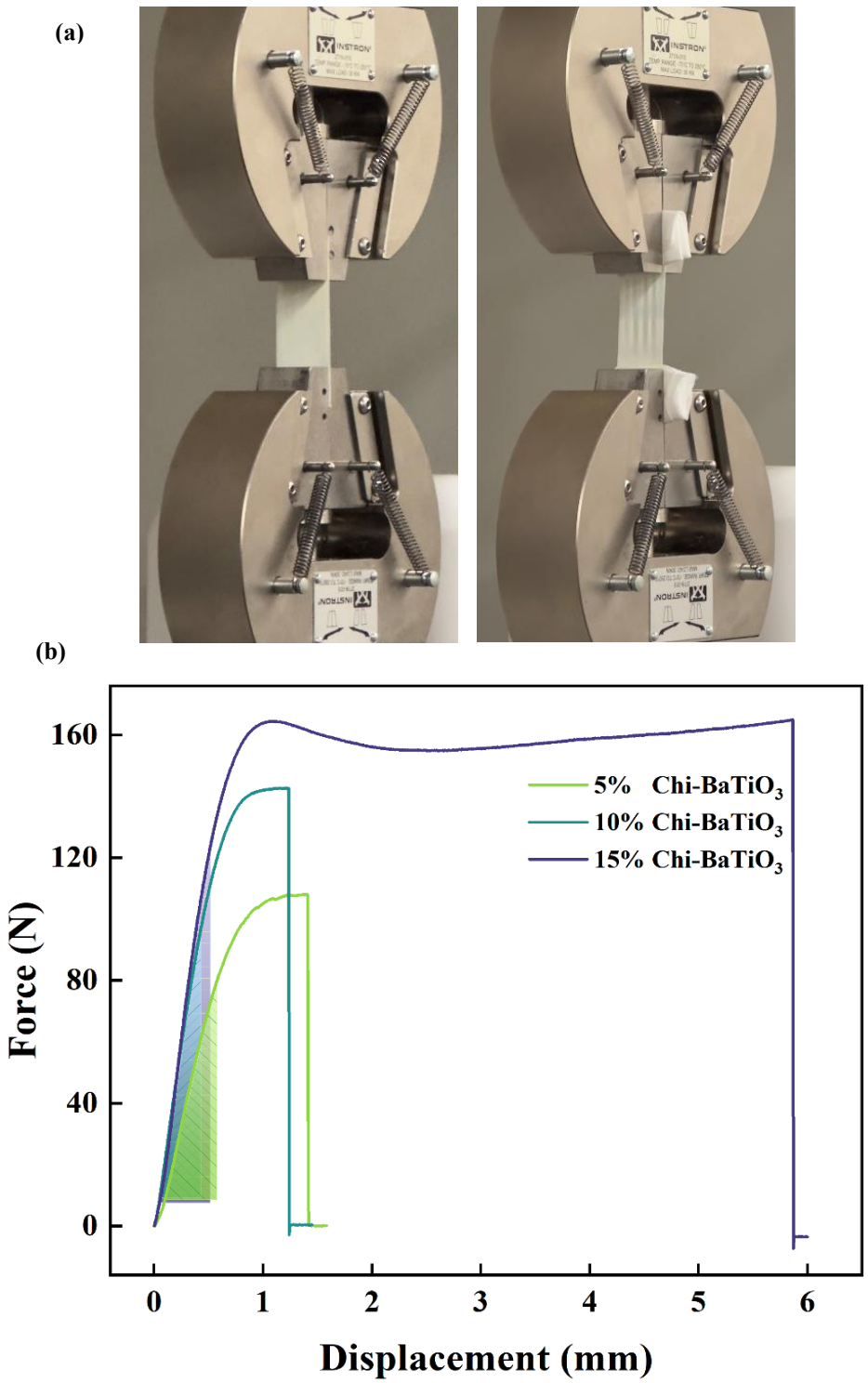
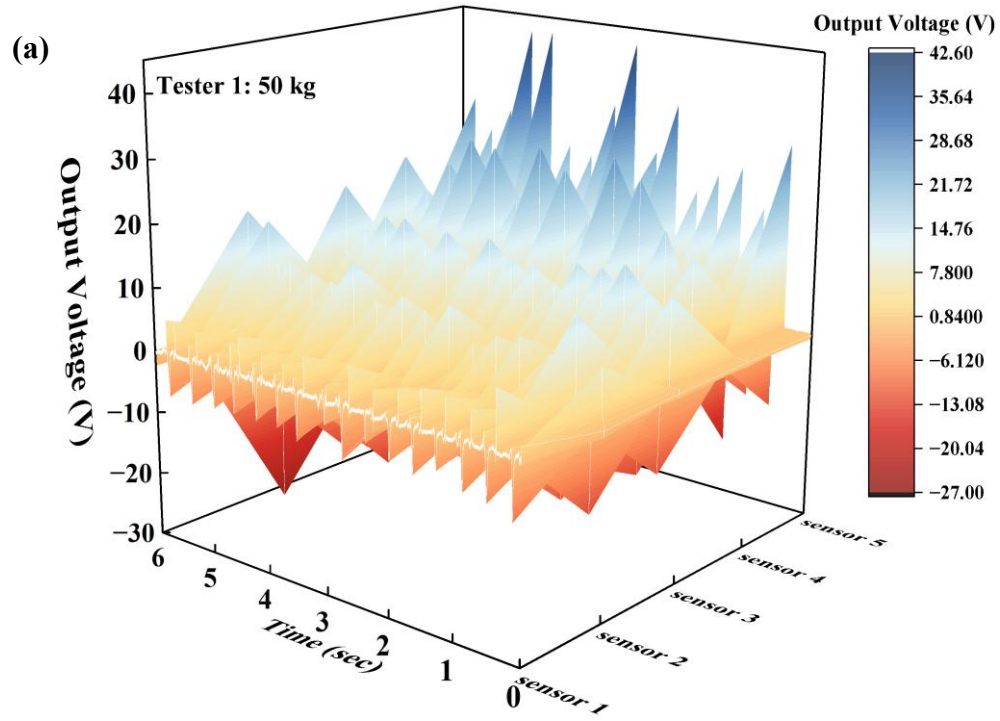


Figure 6.12. Stress-strain analysis of CS-BTO (a) Instron test set-up with the film specimen mounted in the grips, and (b) tensile force-displacement curves of CB films with different BTO loadings (5, 10 and 15 wt.%).

6.3.5 Application: Wireless Self-Powered Insole for Gait Monitoring

To demonstrate the use of the CS-BTO sensor in a wearable system, the device was incorporated into an insole, with sensor elements positioned to record the plantar pressure distribution during standing and walking. The output signals were recorded directly using an oscilloscope and the results from three participants of different body weight (50, 70 and 75 kg) is shown in **Figure 6.13 (a) - (c)**. The output voltage increases consistently with the body weight of the participant, indicating that the differences in applied load and can distinguish individuals by the pressure they applied. The insole was integrated with a wireless module based on the Nordic nRF52840 Feather, which transmits the recorded signals to a mobile device via Bluetooth, following the wireless approach established for the CS-ZnO sensor in the previous chapter [157]. Since the sensor generates its own electrical signal under applied pressure, the system operates without an external power source for the sensor element, and the wireless link enables the plantar pressure data to be monitored remotely. The combination of a self-powered, flexible sensor with a low-delay wireless link demonstrates a proof-of-concept insole for gait monitoring, with potential application in human-machine interaction, telemedicine and sports performance monitoring.



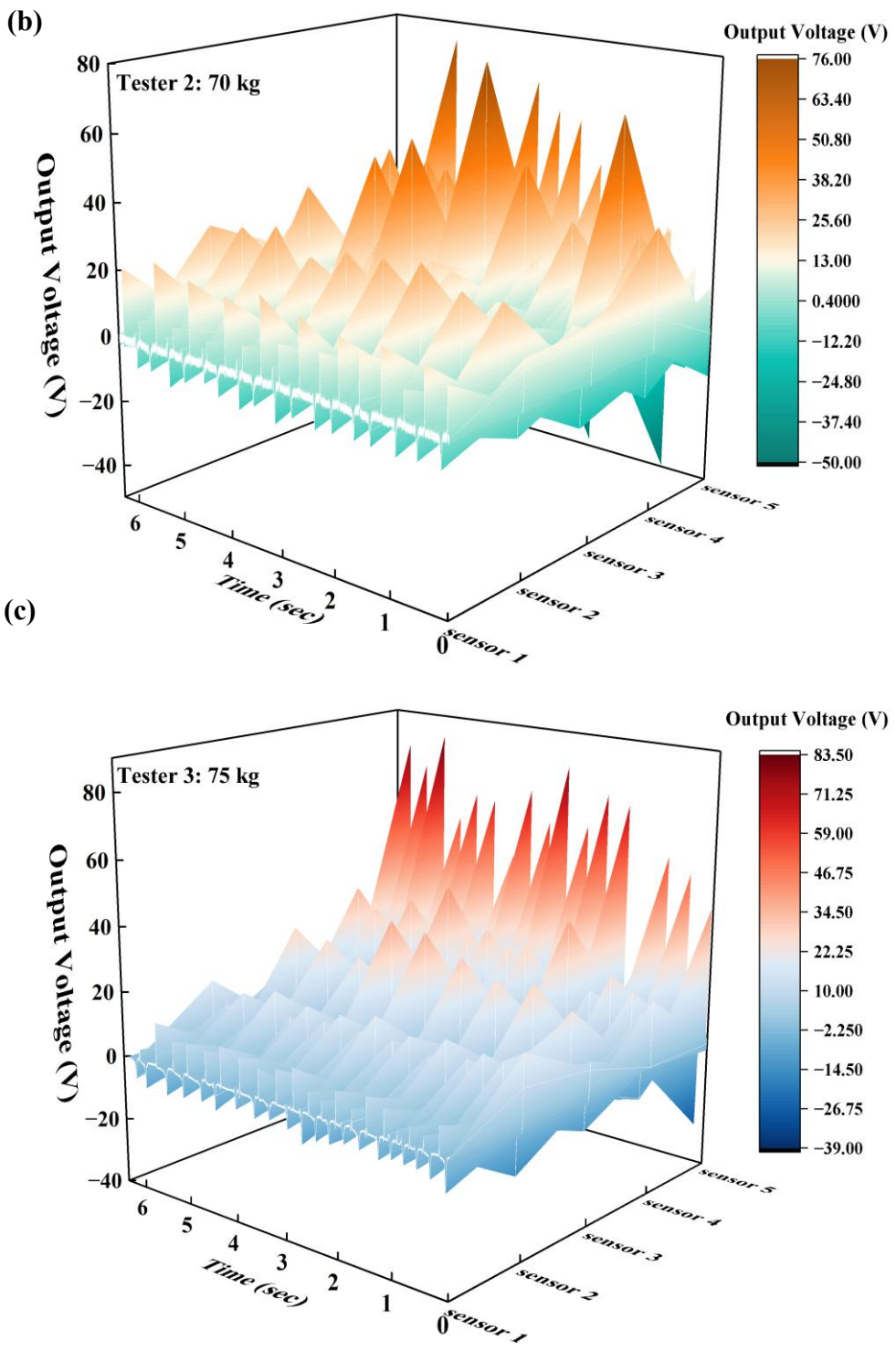


Figure 6.13 shows the output-voltage distribution of the CS-BTO sensor array recorded from participants with different body weights: (a) Tester 1 (50 kg), (b) Tester 2 (70 kg), and (c) Tester 3 (75 kg).

6.4 Summary

This chapter developed a flexible, self-powered pressure sensor based on a CS-BTO composite film, in which BTO NPs were dispersed in chitosan at 5, 10 and 15 wt.% to form the piezoelectric layer of a sandwich-structured device. SEM showed that the NPs were well dispersed at 5 wt.% but became increasingly agglomerated at higher concentration, a trend quantified by an AF that rose from 45% to 56%. XRD confirmed that the BTO phase was retained within the amorphous chitosan without a secondary phase, and infrared spectroscopy indicated that chitosan and BTO interacted through hydrogen bonding while the chitosan structure was preserved. The piezoelectric coefficient increased from 7 to 13 pC/N. Relative to the pure chitosan reference film, the 15 wt.% composite showed an 8.6-fold increase in pressure sensitivity (to 276.07 mV/kPa) and an 8.1-fold increase in frequency sensitivity (to 2564.29 mV/Hz). The sensor responded in 0.24 ms and recovered in 0.64 ms, and its output remained stable for 1200 s of cyclic loading and 10^4 bending cycles. The higher BTO concentration that raised the sensitivity also increased the Young's modulus of the film from 6.21 to 10.53 GPa, so that a higher output is accompanied by lower mechanical compliance. Configured with a wireless Bluetooth link, the sensor distinguished participants of different body weight and transmitted plantar pressure data to a mobile device, demonstrating a gait-monitoring insole. The CS-BTO composite therefore provides a lead-free, self-powered and flexible pressure sensor material whose output and sensitivity can be tuned through the BTO concentration, subject to the accompanying reduction in mechanical compliance.

Chapter 7: Parylene C Flexible Self-Powered Pressure Sensors for Wearable Systems

7.1 Introduction

The previous chapters have examined chitosan pressure sensors, as well as the performance enhancements achieved by incorporating zinc oxide (ZnO) and barium titanate (BTO) into chitosan films. Pure chitosan films have demonstrated the feasibility of using bio-derived films for flexible, self-powered dynamic pressure sensors. Subsequently, chitosan-zinc oxide (CS-ZnO) and chitosan-barium titanate (CS-BTO) composite films were further prepared, and the pressure and frequency responses were enhanced through the incorporation of inorganic piezoelectric nanoparticles. Taken together, these results demonstrate that chitosan films can serve as the basis for flexible pressure sensors, and that composite designs can enhance sensor output whilst maintaining the mechanical flexibility required for wearable devices.

Parylene C (PAC) is a biostable material widely used in biomedical devices and flexible electronic devices. Its chemical inertness, electrical insulation, mechanical flexibility and reported biocompatibility mean it is frequently employed as a coating, encapsulation layer and insulating layer [158]. Compared with extensively studied organic piezoelectric materials such as polyvinylidene fluoride (PVDF) and its copolymers, research into PAC as a pressure-responsive film in self-powered pressure sensors remains relatively limited [159]. However, PAC combines conformal deposition, flexibility and electrical insulation, making it suitable for the design of flexible pressure sensors, particularly in wearable applications requiring repeated deformation and long-term stable operation.

For piezoelectric pressure sensors, the output response is determined not only by the selected film material but is also influenced by the film thickness, capacitance, dielectric behaviour, d_{33}, and deformation behaviour under dynamic loading. For PAC, this relationship is of particular interest, as its thickness can be controlled via chemical vapour deposition (CVD). On this basis, PAC films with thicknesses of 10, 25 and 45 μm were fabricated and assembled into sandwich-structured flexible pressure sensors. By comparing these three sensors, the

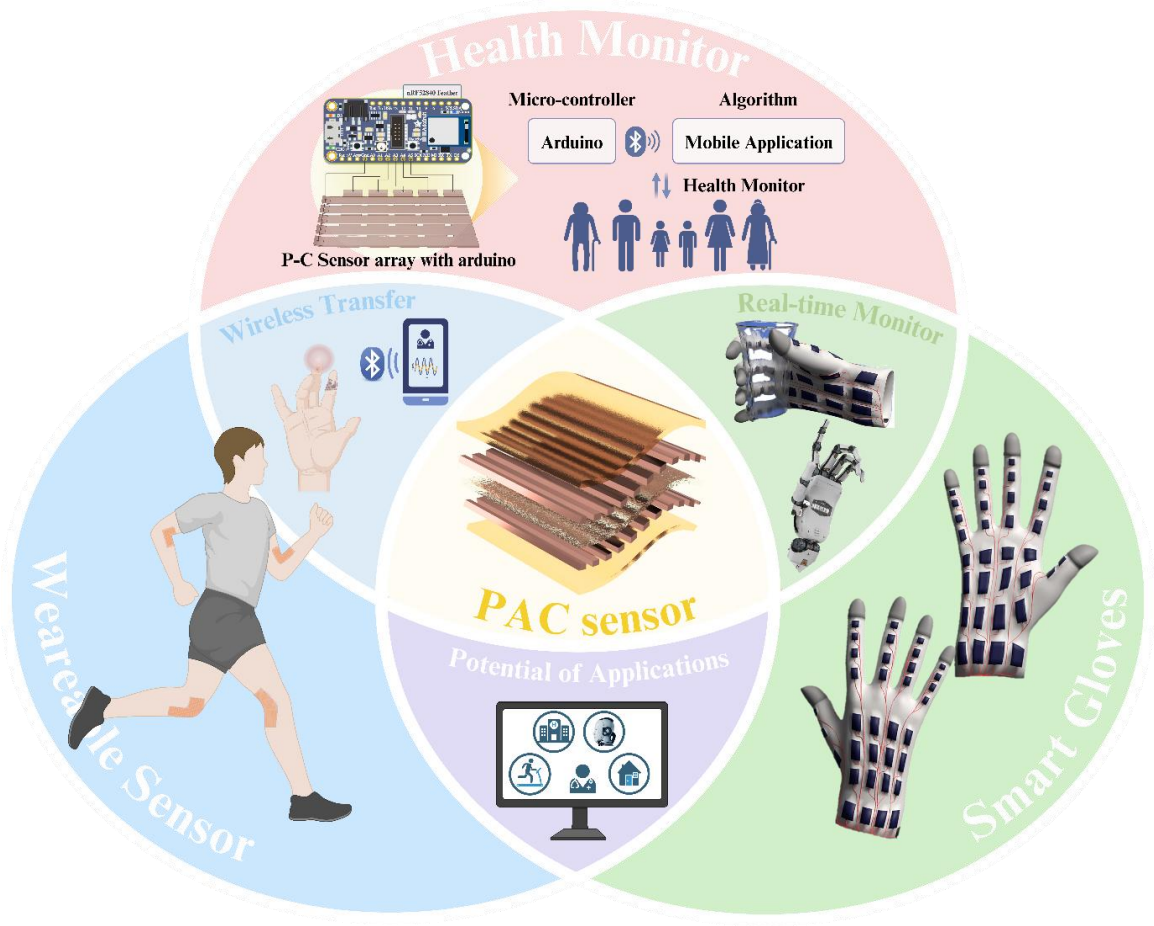


Figure 7.1 Overview of the wireless, real-time health-monitoring concept based on flexible PAC piezoelectric pressure sensors, showing the wearable sensor, smart glove, real-time monitoring and data transmission to a mobile application through an Arduino with Bluetooth connectivity.

influence of PAC thickness on dielectric behaviour, piezoelectric response and device output can be assessed under identical test conditions.

Firstly, the morphology, crystal structure and chemical characteristics of the PAC films were characterised. Subsequently, their dielectric and piezoelectric properties were analysed in further detail to investigate the influence of film thickness on capacitance, relative permittivity and d_{33}. The performance of the pressure sensors was then evaluated under controlled pressure and frequency loads, with pressure sensitivity, frequency sensitivity, response time and stability serving as the primary evaluation criteria. Based on these results, the relationship between PAC film thickness and device output was analysed in greater detail.

Finally, a sensor array was integrated into a smart glove to assess its suitability for use in wearable devices. The PAC pressure sensing units were mounted on the glove to monitor pressure changes during interactions with objects. Under dynamic loading, the sensors were able to generate electrical signals without an external bias voltage being applied across the

piezoelectric film. However, the wireless readout unit still required an independent power supply to perform signal acquisition, digitisation and Bluetooth transmission. The overall concept of the wireless, real-time health-monitoring system based on the flexible PAC sensors is illustrated in **Figure 7.1**.

7.2 Method

7.2.1 Preparation of PAC Films

The large area, uniform, and pinhole free PAC film was prepared at different thicknesses using the chemical vapour deposition technique, using a SCS coating system as shown in **Figure 7.2**. In this study, deposition conditions were set to a vacuum pressure ranging from 1.7 to 6.2 Pa with a substrate temperature of 10 °C. Multiple thin PET (Polyethylene Terephthalate) sheets (15 cm x 15 cm) were placed inside the chamber and used as a carrier substrate. The substrate is cleaned using Isopropyl Alcohol (IPA) and ultra-pure deionised (DI) water to remove any unwanted residues. Next, 90 g, 50 g and 20 g of PAC dimer powder

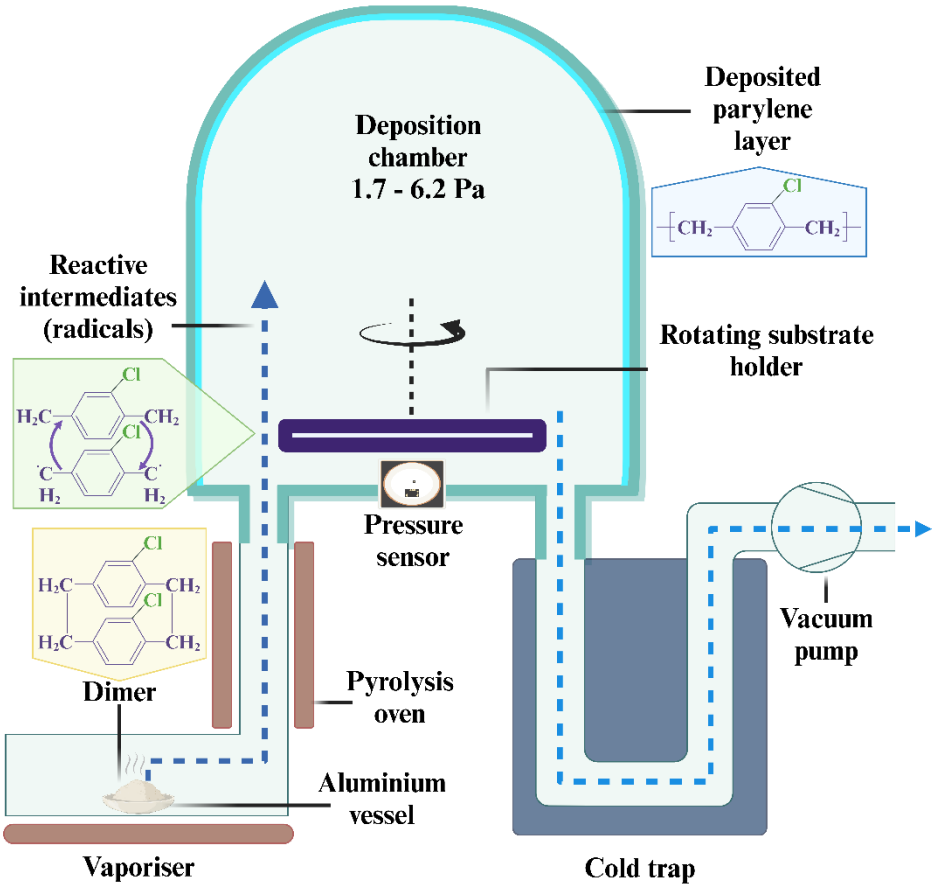


Figure 7.2 Schematic of the Chemical Vapor Deposition (CVD) process for PAC coating, showing vaporization, pyrolysis, and deposition onto a rotating substrate under low pressure (1.7 - 6.2 Pa).

was loaded inside the chamber (vaporiser) to obtain thicknesses of 45 µm, 25 µm and 10 µm films respectively. The deposition occurs in three phases, encompassing vaporisation, pyrolysis, and deposition. Initially, the dimer is added in the vaporiser and then heated up to a temperature of approximately 200 °C where the dimer slowly turns from powder into the vapor with the rise in temperature, thus the vaporisation phase. Next, in the pyrolysis stage, the temperature is increased up to around 680-700°C where it transforms into a monomer. Finally, in the deposition phase a transparent film is uniformly coated on the desired substrate.

7.2.2 Fabrication of Pressure Sensors

The flexible piezoelectric pressure sensor was fabricated using copper as the top and bottom electrodes, with the PAC as the active piezoelectric layer with an active area of the device being 2 cm x 2 cm. A simple insulator based capacitive structure was adopted for the piezoelectric based pressure sensor. A polyimide tape of thickness of 25 µm was used as an encapsulation layer. An ultra-thin and long copper wire was soldered using an adhesive silver paste to use as an external contact on both top and bottom electrode. PAC films of different thicknesses of 10 µm, 25 µm, and 45 µm were used as the piezoelectric layers for the fabrication of the pressure sensor. Finally, a flexible pressure sensor was fabricated and explored in the manufacture of a smart glove for touch sensor applications as shown in **Figure 7.3**.

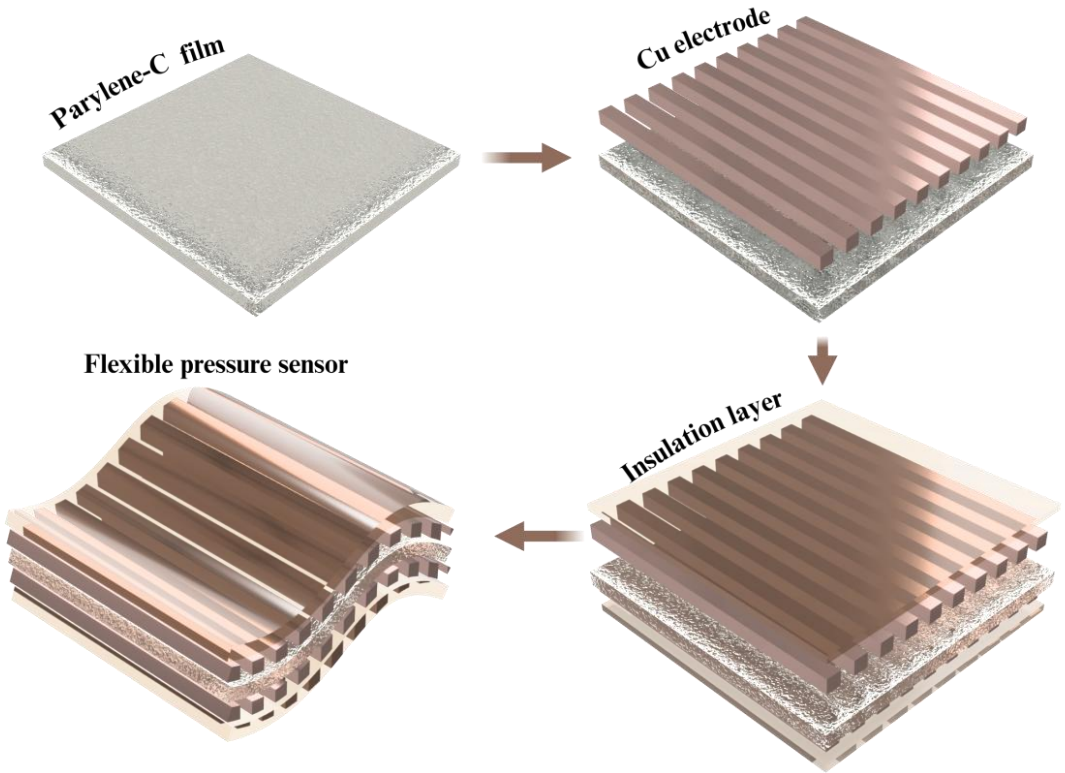


Figure 7.3 Stepwise of the flexible PAC pressure sensor fabrication.

7.3 Results and Discussion of PAC Sensor

7.3.1 Material Characterisation

To investigate the structural, chemical and morphological characteristics of the PAC films, SEM, AFM, XRD, FTIR and Raman spectroscopy were performed.

- **Morphology of PAC films using SEM**

SEM was utilised to examine the surface morphology of the PAC films, providing detailed insights into their microstructural features. As shown in **Figure 7.4(a)-(c)**, the SEM images of the 10, 25 and 45 µm films exhibited a mild surface texture and slight morphological variations, rather than a completely smooth surface. All films, deposited under similar CVD conditions, revealed incremental changes in surface texture with increasing thickness, and gradually developed more pronounced features indicative of increasing crystallinity. No

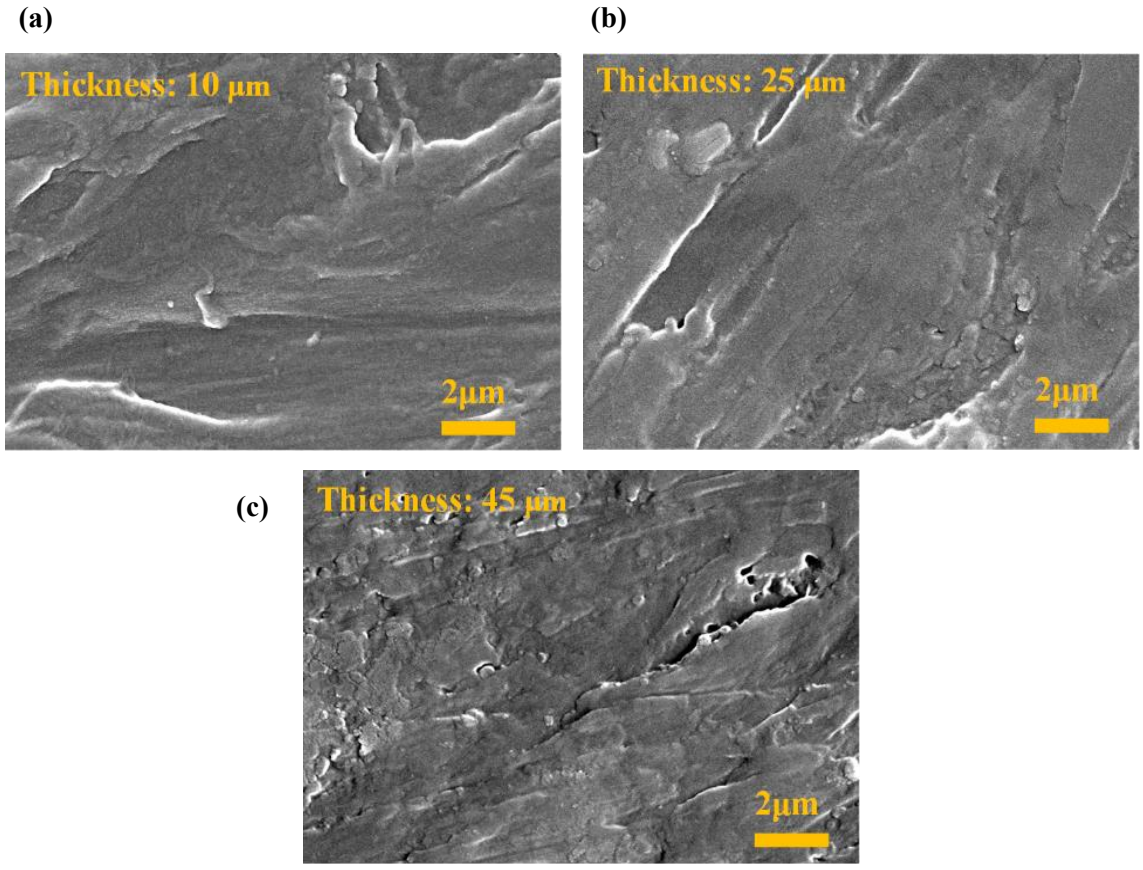


Figure 7.4 SEM images of PAC film surfaces with thicknesses of (a) 10 µm, (b) 25 µm, and (c) 45 µm (scale bar: 2 µm).

significant defects, such as cracks or pinholes, were observed, indicating consistent structural integrity across the three thicknesses and confirming the conformal nature of the

CVD coating. Particularly, no clearly defined grain boundaries were displayed in the 10 µm film, as shown in **Figure 7.4(a),** which is consistent with a predominantly amorphous character at lower thickness. In contrast, features suggestive of crystalline order appeared in the 45 µm film, as shown in **Figure 7.4(c),** indicating a gradual increase in crystallinity with film thickness. Consequently, these morphological observations provide a qualitative basis for the increase in crystalline order subsequently quantified by XRD.

- **Surface roughness of PAC films using AFM**

To further clarify the nanoscale surface features, AFM was performed on the PAC films over a 5 µm × 5 µm area, as shown in **Figure 7.5(a)-(c)**. The topographies revealed clear nanoscale features, with arithmetic roughness (Ra) values of approximately 11.95, 10.72 and 11.09 nm for the 10, 25 and 45 µm films, respectively. The roughness therefore remained within a narrow band of about 10 to 12 nm across all thicknesses, and a separate

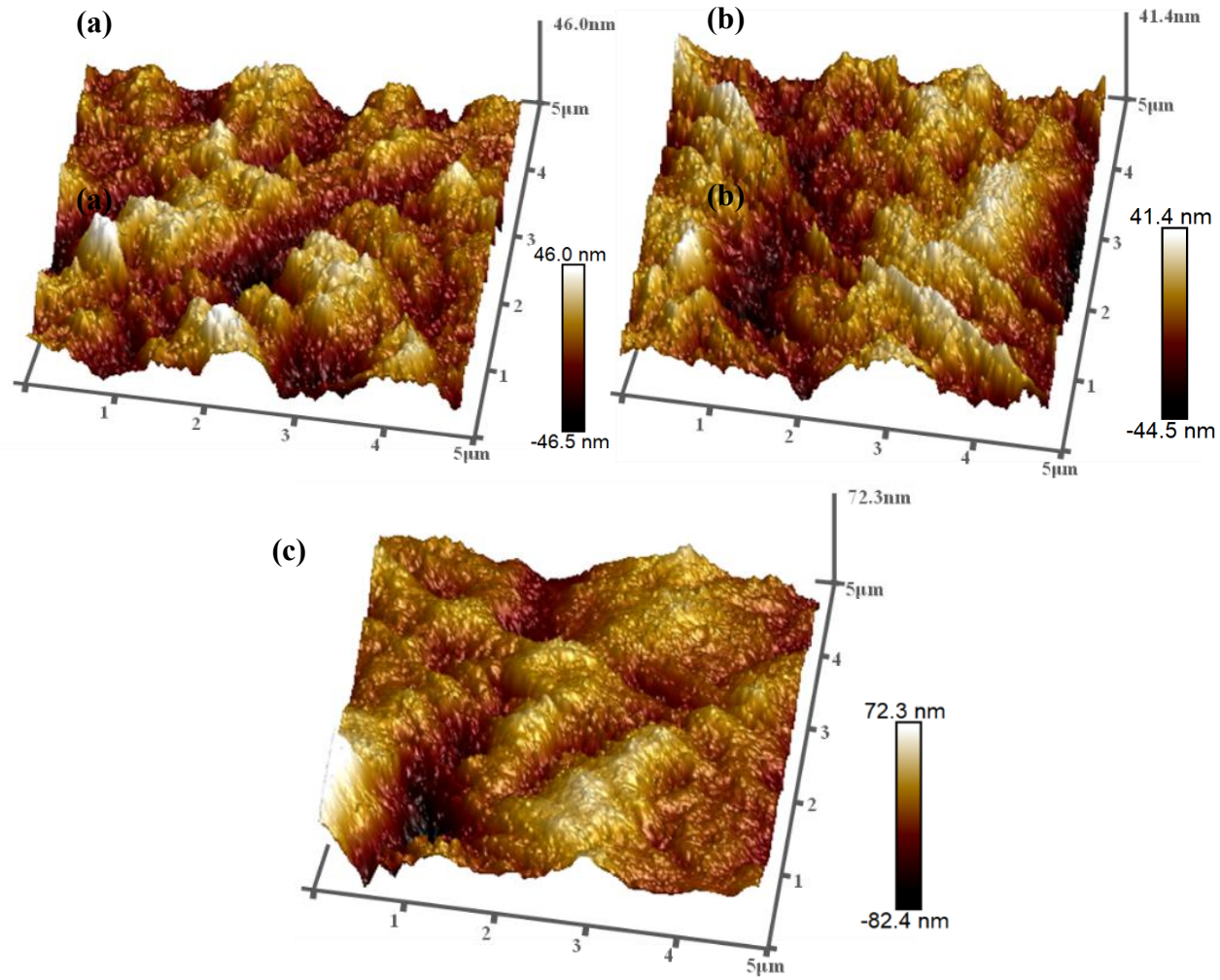


Figure 7.5 Corresponding AFM phase images (scan area: 5 µm × 5 µm) with thicknesses of (d) 10 µm, (e) 25 µm, and (f) 45 µm.

measurement using an optical 3D profilometer gave an average roughness of approximately 0.01 μm, which matches well with these values. The minor variations in Ra between the films may be attributed to internal stresses introduced during CVD and to changes in the alignment of the molecular chains, which is consistent with previous studies on PAC films deposited under comparable conditions [160]. Consequently, this quantitative AFM analysis strongly supports the SEM observations, confirming the nanoscale surface uniformity of the films across the three thicknesses.

- **Structural characterisation of PAC films using XRD**

XRD was used to provide insights into the crystalline structure of the PAC films and its dependence on thickness. The patterns of the 10 and 45 μm films, recorded over a 2θ range of 5 to 70°, are presented in **Figure 7.6(a).** Each film gave a single sharp reflection near 2θ = 15°, assigned to the (020) plane of the monoclinic unit cell and characteristic of a semicrystalline structure [161]. The reflection was more intense for the thicker film. Diffraction intensity is also influenced by the amount of material contributing to the measurement. The patterns were normalised to the maximum intensity of the (020) reflection for comparison, as shown in **Figure 7.6(b)**. The normalised patterns showed similar profiles, with relative amorphous peak intensities of approximately 0.34 and 0.32 for the 10 and 45 μm films, respectively. The overlapping crystalline reflection and amorphous peak were fitted with two Gaussian components using the Fit Peaks (Pro) function in Origin software. This provided the integrated peak areas and the FWHM of the crystalline reflection. The fits gave R^2 values of 0.990 and 0.992 for the 10 and 45 μm films, respectively. The degree of crystallinity was obtained from the crystalline and amorphous contributions using **Equation 7.1**:

$$X_c = \frac{A_c}{A_c + A_A} \times 100\ (\%) \tag{7.1}$$

where A_C is the integrated area of the crystalline peaks and A_A is the area under the curve of the amorphous peak. The crystallinity was 30.05% for the 10 μm film and 31.81% for the 45 μm film. The crystallite size was evaluated using the Scherrer equation, **Equation 7.2**:

$$D = \frac{K\lambda}{\beta \cos\theta} \tag{7.2}$$

where K is the shape factor, λ the X-ray wavelength, β the full width at half maximum in radians(2θ) and θ the Bragg angle. The fitted (020) peak positions were 14.43° and 14.20° with FWHM values of 2.26° and 2.18° for the 10 and 45 μm films and corresponding to an

increase in crystallite size from 3.55 to 3.68 nm. The rise in both crystallinity and crystallite size with thickness is consistent with denser molecular packing and greater chain alignment in the thicker films, promoted by van der Waals forces and hydrogen bonding [160].

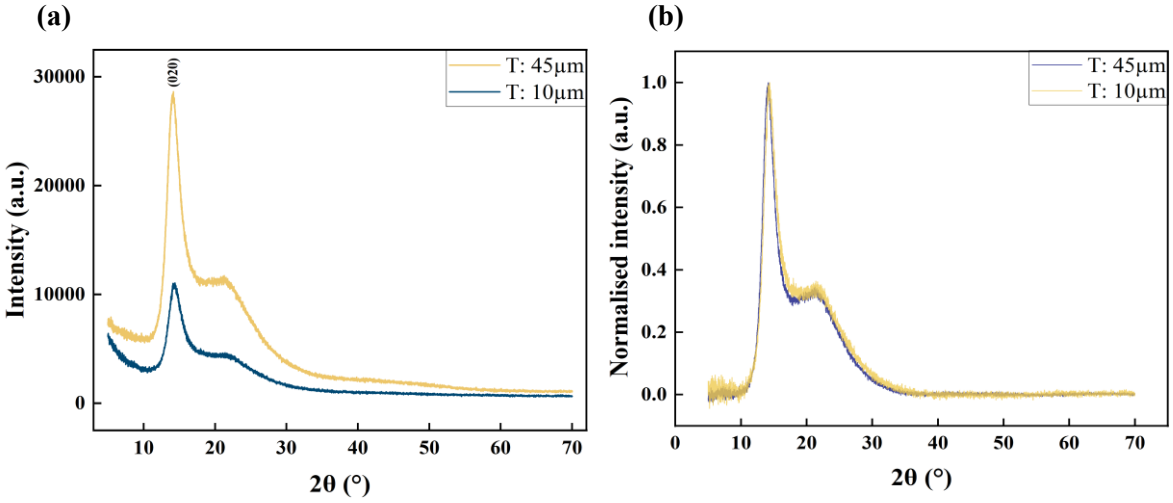


Figure 7.6 XRD patterns for PAC films (a) intensity and (b) normalised intensity.

- **Chemical characterisation of PAC films using FTIR**

To gain deeper insights into the chemical composition and functional groups within the PAC, FTIR analysis was performed on both 10 µm and 45 µm thickness films. The results in **Figure 7.7** show the transmittance spectrum for both PAC films across a spectral range of 100 cm^{-1} to 4000 cm^{-1}. The FTIR typically exhibits the spectral peaks for 10 µm thickness PAC films at wave numbers of (835, 1056, 1409, 1501, 1614, 1982, 2162,2359, 2867, 2949, and 3025) cm^{-1} respectively, where these were observed at (824, 1049, 1401, 1490, 1609, 1901, 2330, 2598, 2860, 2924, and 3027) cm^{-1} for 45 µm thickness PAC films respectively. The shifts of spectral peaks could be due to alterations in intermolecular forces such as van der Waals interactions or hydrogen bonding. Furthermore, strain or stress within the thicker PAC film during the fabrication process such as drying might slightly modify bond lengths or angles, thereby leading to minor shifts in the observed peak positions. The spectral peaks from 1409 to 1614 cm^{-1} relate to the in-plane vibrations of the benzene ring, as well as the stretching vibrations of the C-C and C=C present in the para-xylene monomer. The peak at 1056 cm^{-1} corresponds to the C-Cl bond which indicates the presence of the chlorine in the monomer. Similarly, the peaks in between 2800 cm^{-1} and 3025 cm^{-1} correspond to the C-H bond on the atomic ring which matches well with the literature[162].

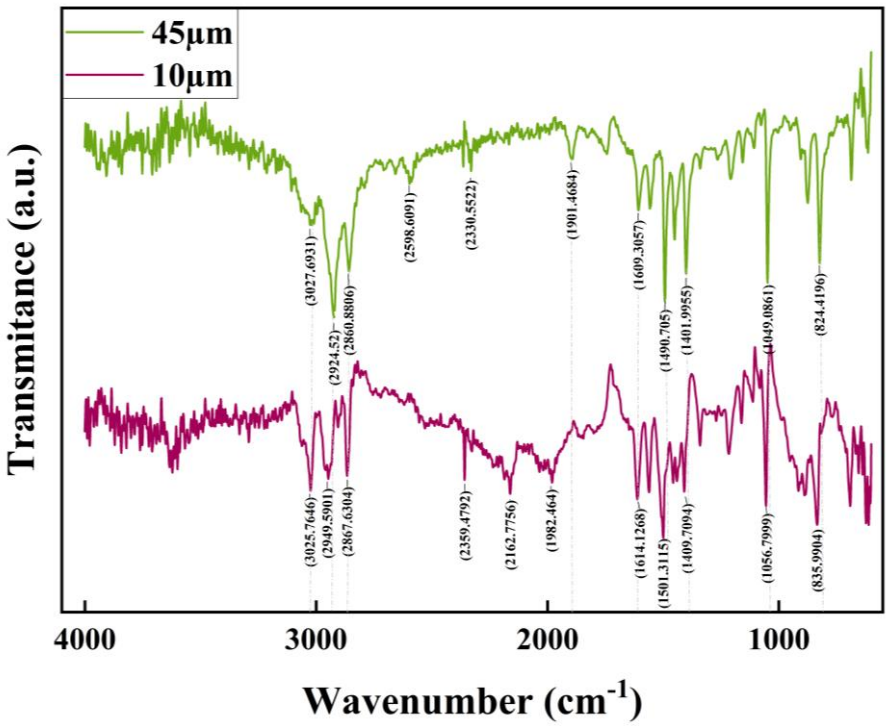
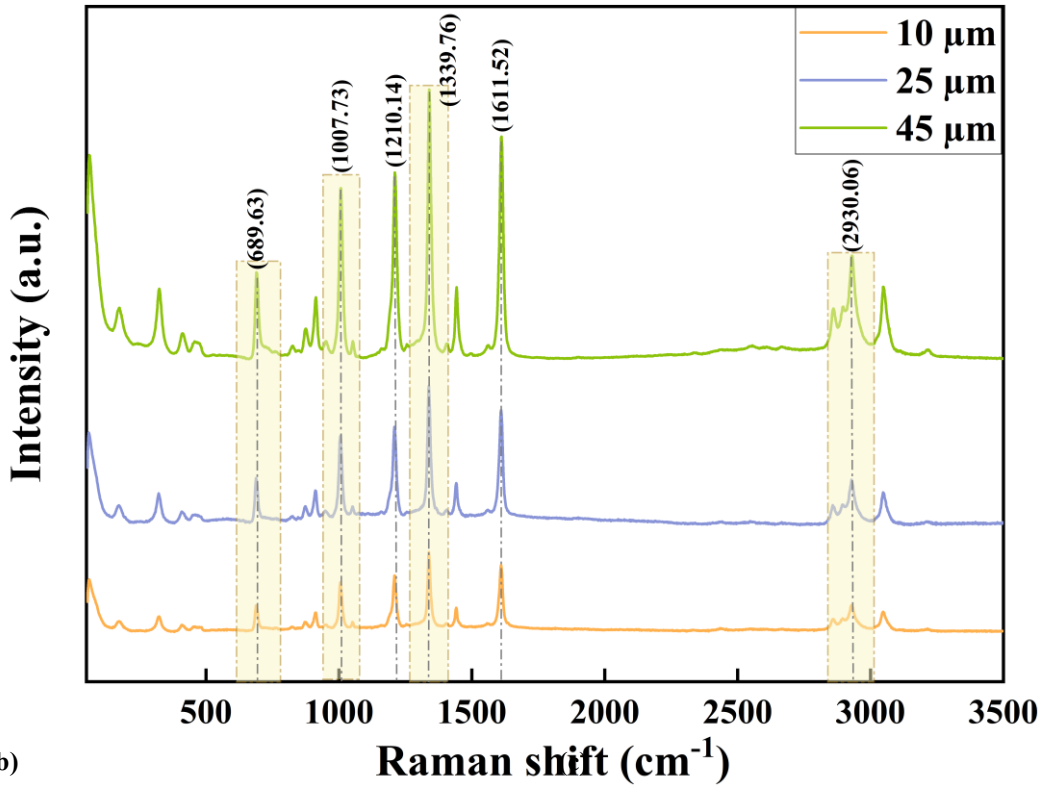


Figure 7.7 FTIR spectra of the 10 and 45 µm PAC films.

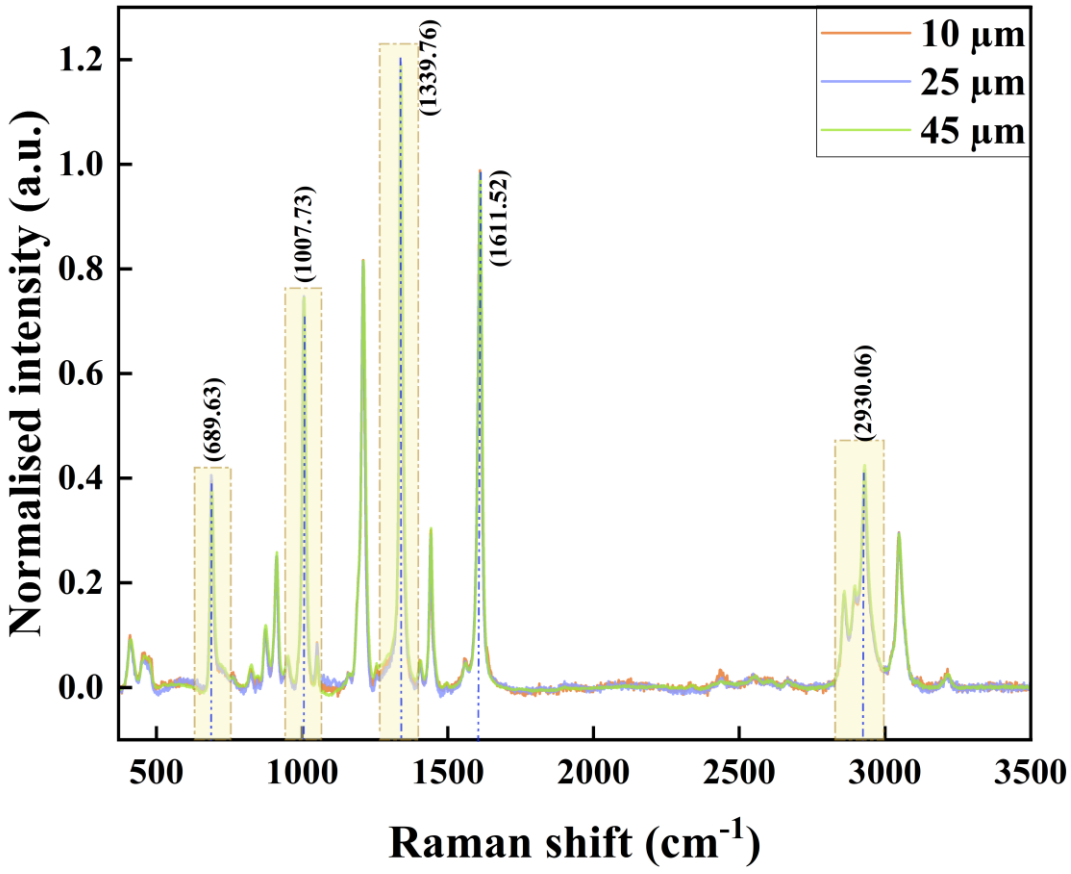
- **Molecular structure of PAC films using Raman spectroscopy**

To further clarify the vibrational structure and crystallinity of the PAC films, Raman spectroscopy was performed, as shown in **Figure 7.8**. The spectra of all three films displayed the characteristic bands of PAC at approximately 689, 1007, 1339 and 2930 cm^{-1}, assigned to C-Cl stretching, the symmetric breathing of the benzene ring, C-H bending, aromatic ring C=C stretch and C-H stretching, respectively. Particularly, the intensity of the 1339 cm^{-1} band increased markedly with thickness. To compare the relative band intensities, the spectra were normalised to the aromatic ring stretching band at 1611 cm^{-1} as a common intensity reference. The normalised spectra showed similar profiles for all three film thicknesses, as shown in **Figure 7.8(b)**. The relative intensity of the 1339 cm^{-1} band was 1.21, 1.22 and 1.21 for the 10, 25 and 45 µm films, respectively, corresponding to a variation of less than 1%. The relative intensities of the other principal bands varied by less than approximately 7%. The minor shifts in band position between the included an approximately 1.5 cm^{-1} shift towards higher wavenumbers for the 45 µm film, comparable to the spectral sampling interval. Collectively, these Raman results clearly demonstrate that the similar relative band intensities are consistent with the small difference in fitted crystalline fraction obtained from XRD analysis.

(a)


10 µm
25 µm
45 µm
(689.63)
(1007.73)
(1210.14)
(1339.76)
(1611.52)
(2930.06)
Intensity (a.u.)
500
1000
1500
2000
2500
3000
3500
Raman shift (cm-1)

(b)


10 µm
25 µm
45 µm
(689.63)
(1007.73)
(1339.76)
(1611.52)
(2930.06)
Normalised intensity (a.u.)
0.0
0.2
0.4
0.6
0.8
1.0
1.2
500
1000
1500
2000
2500
3000
3500
Raman shift (cm-1)

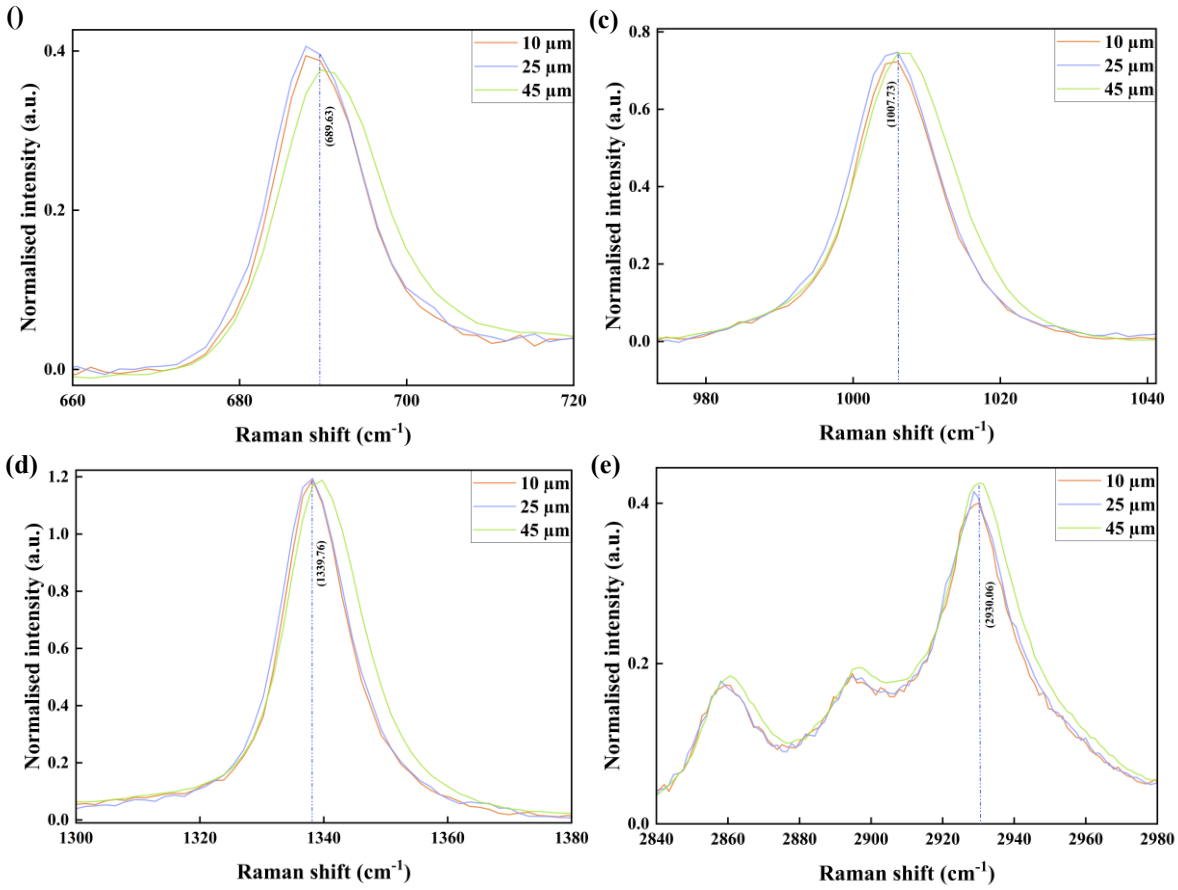


Figure 7.8 Raman spectra of the PAC films. (a) full spectra of the 10, 25 and 45 µm films, and (b)-(e) enlarged views of the bands at approximately 690, 1007, 1339 and 2930 cm^{-1}.

7.3.2 Dielectric and Piezoelectric Properties

The dielectric behaviour of the films was characterised by impedance spectroscopy, with the impedance recorded over 1 to 70 MHz in **Figure 7.9(a)**. For this measurement the films were placed between gold electrodes deposited by electron beam evaporation, which formed a separate test capacitor of area 2.5 cm² rather than the 2 cm × 2 cm sensor of Section 7.2.2. The 10 and 45 µm PAC films exhibit different impedance responses, with minima at 14.26 and 29.45 MHz and maxima at 54.96 and 53.75 MHz, respectively. As the electrode material and area of 2.5 cm² were the same for both measurements, the difference in film thickness affects the geometrical capacitance and the capacitive contribution to impedance. At a given frequency, the capacitance of a parallel plate structure decreases as the dielectric thickness increases, resulting in a higher capacitive impedance. Coelho et al. reported the same thickness dependence of capacitance in PAC capacitors, whilst Kahouli investigated changes in the dielectric response and morphology of PAC films with thickness[163], [160]. The differences in the positions of the impedance minima and in the spectral shapes also indicate

contributions other than geometrical capacitance that vary with frequency. At MHz frequencies, parasitic inductance and capacitance associated with the measurement connections and fixtures can influence the measured impedance and spectral features, as reported by Edwards et al. [164].

Treating the film between the electrodes as a parallel-plate capacitor, the capacitance and relative permittivity were obtained from the impedance data using **Equation 7.3**:

$$\varepsilon_r = \frac{\varepsilon_c}{\varepsilon_0} = \frac{Cd}{\varepsilon_0 A} \tag{7.3}$$

where C is the capacitance, d the film thickness, ε_0 the vacuum permittivity and A the electrode area, taken as 2.5 cm². The capacitance fell from 5 nF for the 10 μm film to 1.5 nF for the 45 μm film (**Figure 7.9(b)),** in line with its inverse dependence on thickness, while the relative permittivity rose from 27.89 to 31.76 as shown in **Figure 7.9(c**). The higher permittivity of the thicker film points to a greater population of dipolar groups within it, in agreement with reports on PAC films of comparable thickness [160]. Only the two extreme thicknesses were measured, as the 25 μm film lies within this range and would not change the trend. The measured voltage output of the sensor is, however, governed not by the dielectric response alone but also by the piezoelectric coefficient, the film thickness, the effective electrode area and the degree of deformation.

The piezoelectric response was quantified by the piezoelectric charge coefficient d_{33}, obtained from the charge generated per unit applied force using **Equation 7.4**:

$$d_{33} = \frac{Q}{F} \tag{7.4}$$

where Q is the generated charge and F the applied force. The coefficient rose with film thickness, from 0.7 pC/N at 10 μm to 0.8 pC/N at 25 μm and 1.8 pC/N at 45 μm as shown in **Figure 7.9(d)**. PAC has previously been established as a piezoelectric material, with a reported d_{33} of approximately −3.5 pC/N [165], and the values measured here confirm a measurable piezoelectric response in the deposited PAC films. This increase reflects the higher crystallinity and chain alignment found for the thicker films, where a more ordered

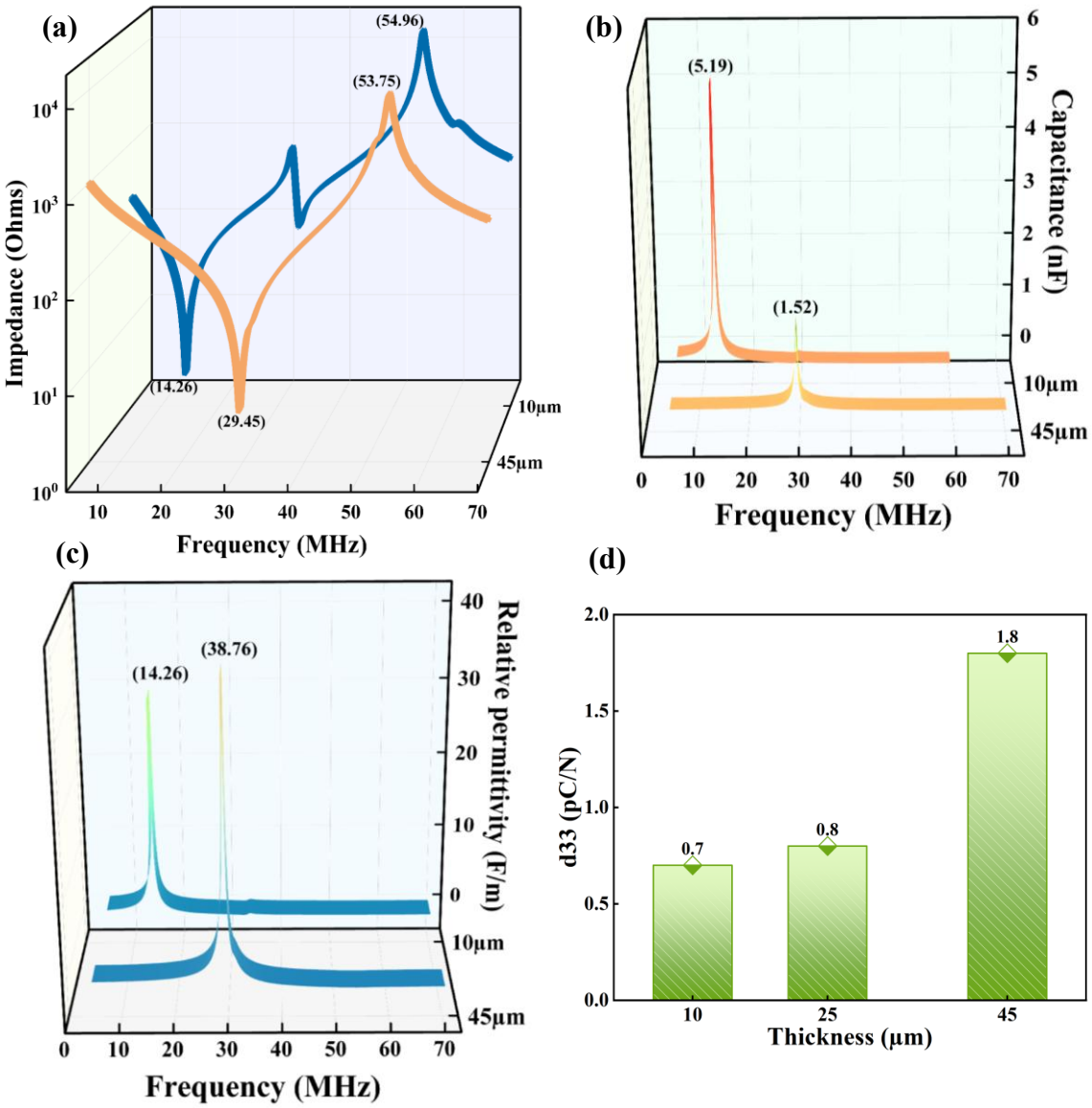


Figure 7.9 Dielectric and piezoelectric characterisation of the PAC films. (a) electrical impedance against frequency, (b) capacitance against frequency and (c) relative permittivity against frequency for the 10 and 45 µm films, and (d) piezoelectric charge coefficient d_{33} for the 10, 25 and 45 µm films.

structure allows the dipoles to respond more coherently to an applied stress. Consequently, the dielectric and piezoelectric measurements together demonstrate that the PAC films combine a stable dielectric response with a measurable, thickness-dependent piezoelectric coefficient, which provides the basis for their use as the active layer in a self-powered pressure sensor.

7.3.3 Pressure Sensor Characterisation

The sensor response was characterised with a custom dynamic loading system built around a mechanical vibration stage, a linear motor, a source-meter and a force calibration sensor,

following the arrangement used in the preceding chapters. Copper leads connected the device to a mixed-signal oscilloscope that recorded the output waveforms, and a secure ground was maintained to limit electromagnetic interference. The stage delivered controlled vibrations with an amplitude of 0.25 to 32 N and a frequency of 1 to 10 Hz at low distortion, while the linear motor moved vertically to apply periodic loading and unloading. Under an applied load, the film developed a piezoelectric potential that accumulated charge on the electrodes, and this charge was released through the external circuit once the load was removed.

The devices assembled from the 10, 25 and 45 μm films were tested under a range of forces and frequencies. In a pressure-increment test at a fixed frequency of 8 Hz, the pressure was raised in 10 kPa steps from 20 to 90 kPa, and the output of every device rose steadily with pressure, as shown in **Figure 7.10(a)**. Over this range, the output increased from 0.09 to 2.65 V for the 10 μm film, from 0.12 to 4.22 V for the 25 μm film and from 3.1 to 9.6 V for the 45 μm film. A frequency-increment test at a fixed pressure of 90 kPa, with the frequency raised in 1 Hz steps from 2 to 8 Hz, produced a similar trend illustrated in **Figure 7.10(b),** the output rising from 0.24 to 2.57 V, from 0.016 to 4.1 V and from 6.4 to 10.9 V for the 10, 25 and 45 μm films, respectively.

The thicker film gave the larger response, and the gap between films widened as the load increased, as **Figure 7.10(c)**. Raising the thickness from 10 to 25 μm increased the output only slightly, from 0.09 to 0.12 V, at 20 kPa, whereas at 90 kPa the same change raised it from 2.65 to 4.22 V. A comparable pattern appeared with frequency in **Figure 7.10(d).** At 2 Hz, the outputs of the 10, 25 and 45 μm films were 0.24, 0.016 and 6.4 V, so that the two thinner films barely responded while the 45 μm film already produced a large signal, whereas at 8 Hz, the outputs reached 2.57, 4.1 and 10.9 V. The rise in output with pressure follows from the larger deformation of the film, which displaces more charge across the electrodes, and the rise with frequency follows from the faster rate of deformation, which leaves less time for the generated charge to dissipate between cycles. The weak low-frequency response of the thinner films reflects the smaller deformation they undergo, whereas the thicker film deforms enough to generate a substantial signal even at low frequency. The time-domain output traces recorded during the pressure and frequency increment tests are shown in **Figure 7.11**.

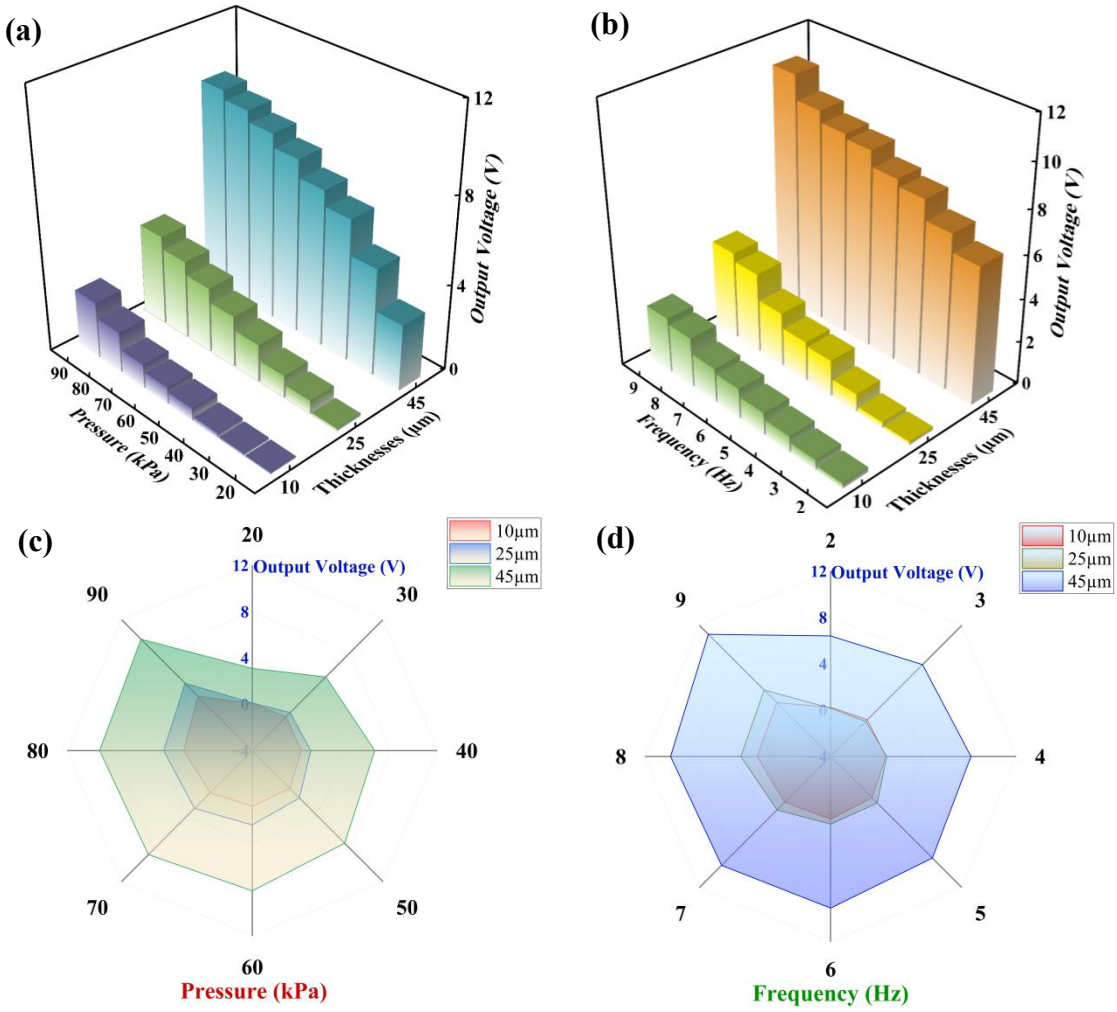


Figure 7.10 Changes in output voltage for PAC films under varying conditions, where (a) and (b) show the output voltage variations with respect to applied pressure and frequency, respectively for PAC films with different thicknesses; and output response voltages with increased (c) pressure and (d) frequency for PAC films with thicknesses of 10, 25, and 45 μm.

The transient behaviour of the 45 μm device was also measured. The response time, taken as the interval for the output to rise from baseline to its maximum under load, was approximately 12 ms, and the recovery time, the interval for the output to return to baseline after the load was removed, was approximately 10 ms.

The pressure sensitivity and the frequency sensitivity were obtained as the slopes of the output voltage against the applied pressure and against the loading frequency, as defined in **Equation 7.5** and **Equation 7.6**:

$$S_P = \frac{\Delta V}{\Delta P \text{ at a constant } frequency} \tag{7.5}$$

$$S_f = \frac{\Delta V}{\Delta f \ at \ a \ constant \ pressure} \tag{7.6}$$

where ΔV is the change in output voltage, ΔP the change in applied pressure at a constant frequency and Δf the change in applied frequency at a constant pressure. The quality of each least-squares fit was quantified by the coefficient of determination R^2 given by **Equation 7.7**:

$$R^2 = 1 - \frac{\sum_i (y_i - \hat{y}_i)^2}{\sum_i (y_i - \bar{y})^2} \tag{7.7}$$

where y_i are the measured values, $\hat{y}_i$ the fitted values, and $\bar{y}$ the mean value of y_i. The pressure and frequency sensitivities are shown in **Figure 7.12(a) and (b)**. The pressure sensitivity increased with thickness, reaching 35.52, 60.08 and 87.62 mV/kPa for the 10, 25 and 45 μm films (**Figure 7.12(c)**). The frequency sensitivity rose steeply and then fell slightly, giving 338.93, 596.55 and 580.95 mV/Hz for the same films, so that it peaked at the intermediate 25 μm thickness rather than at the largest thickness. The pressure sensitivity of the 45 μm device is comparable to or higher than values reported for common piezoelectric films, although such comparisons should be treated with caution because the reported figures depend on the film geometry, the electrode area and the testing conditions [166]. Across the full range of pressures and frequencies the device produced a stable, low-noise and repeatable output with a fast response, which supports its use in wearable and potential implantable pressure sensors.

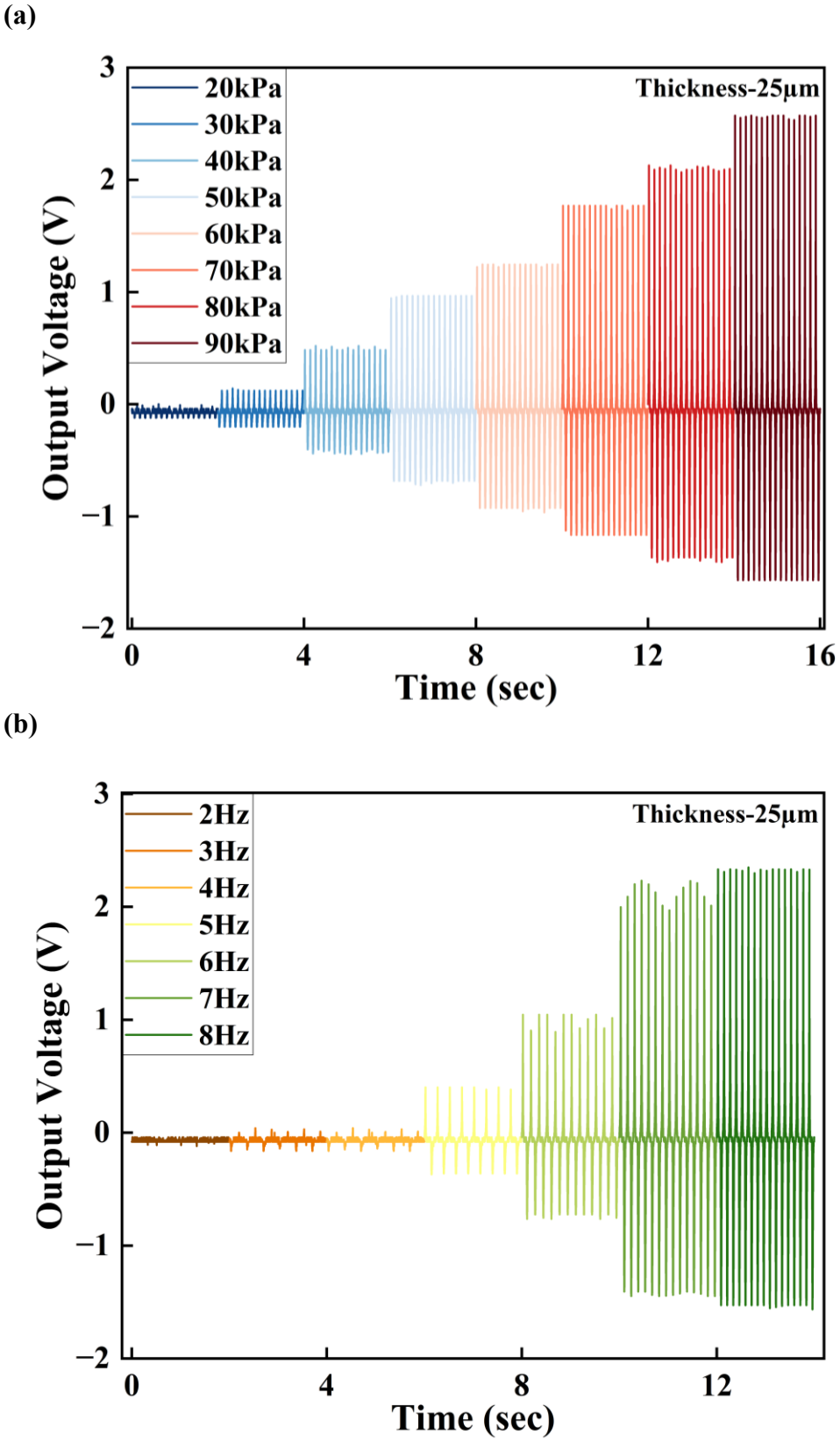


Figure 7.11 Stepwise output voltage of the 25 µm PAC sensor. (a) response to applied pressure increased in steps from 20 to 90 kPa at a fixed frequency, and (b) response to loading frequency increased in steps from 2 to 8 Hz at a fixed pressure.

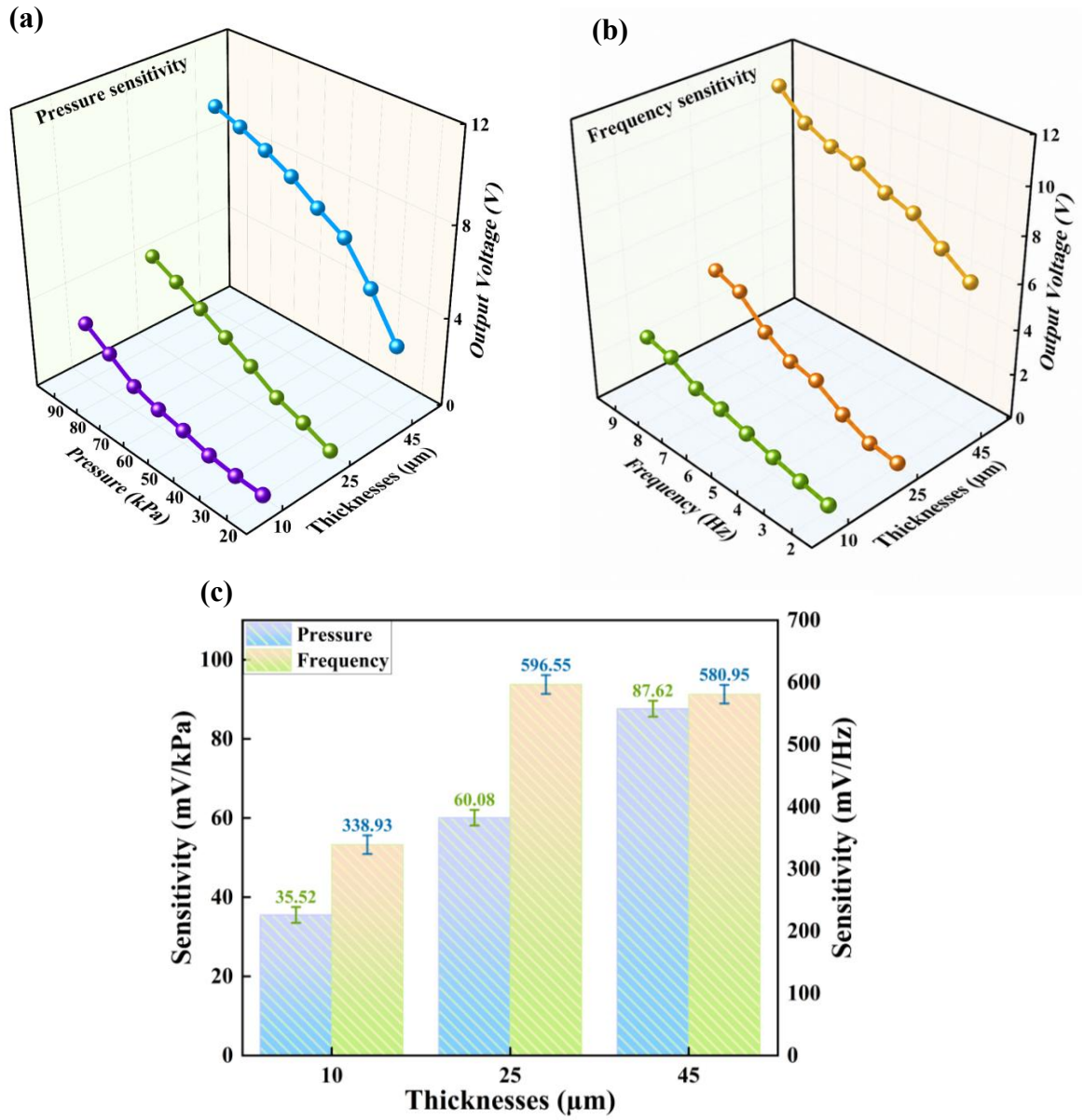
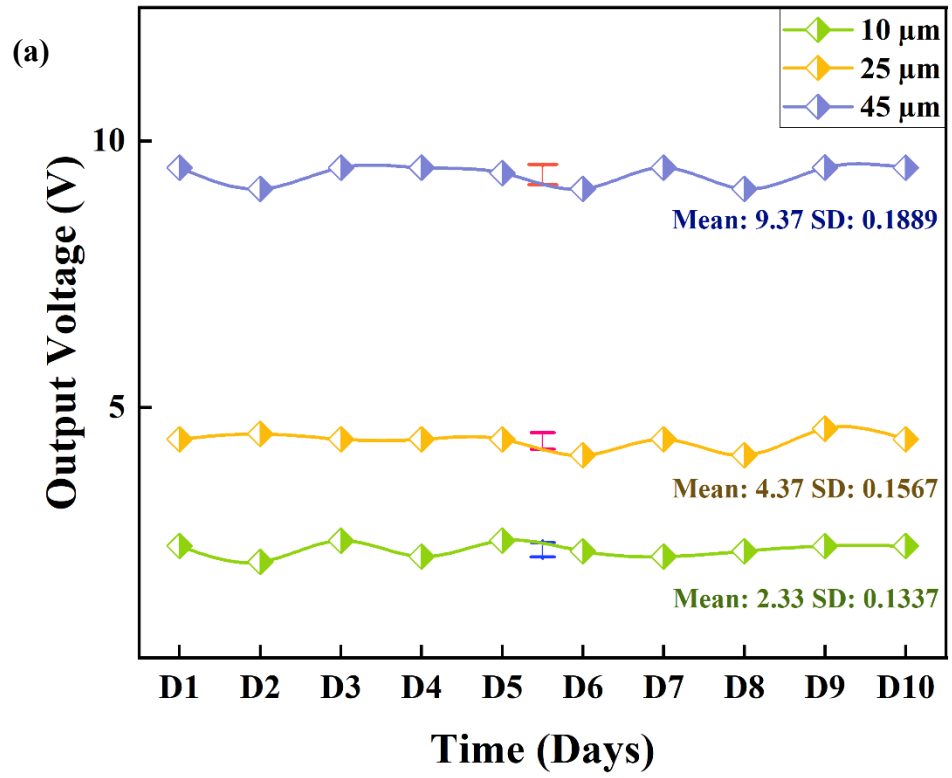


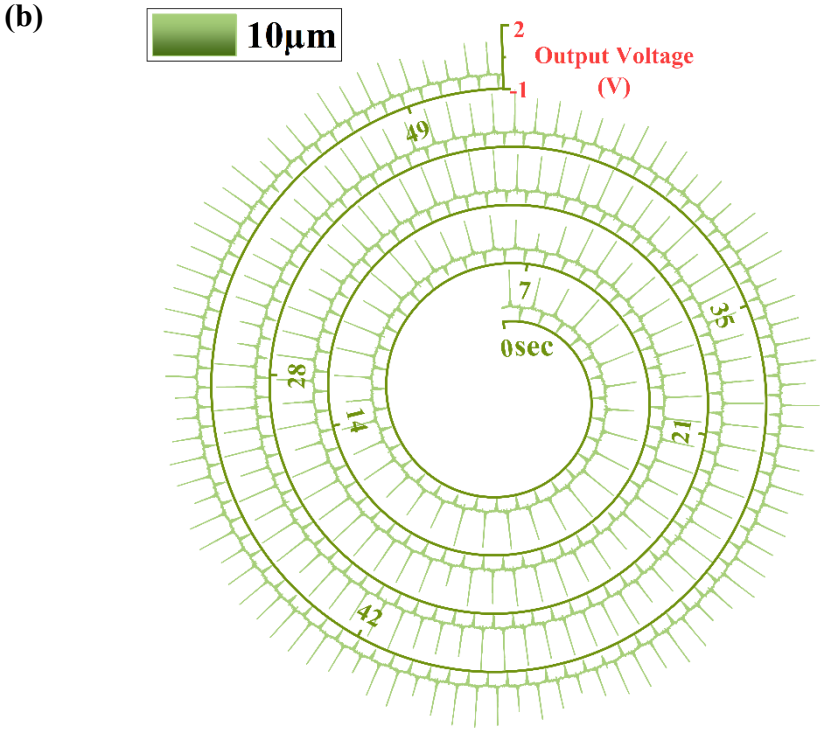
Figure 7.12 Sensitivity plot for (a) pressure and (b) frequency with output voltage changes, showing linear increases in pressure and frequency respectively for PAC films with different thicknesses; (c) Comparison of pressure and frequency sensitivities for PAC sensors with different thicknesses.

7.3.4 Stability

The stability and durability of the sensor were assessed by cyclic and long-term fatigue testing. In a continuous cyclic test, the 45 μm device was operated for more than 1,200 cycles with no measurable change in output, which indicates good cyclic stability. Long-term behaviour was then examined over 10 days at 20 to 25 °C and 30 to 35% relative humidity, with the sensor loaded at 90 kPa and 5 Hz for 4 hours each day and the output recorded throughout in **Figure 7.13(a).** The devices held a consistent output with only a small standard deviation over this period. For the 45 μm sensor the output varied between 9.1 and 9.5 V,

with a mean of 9.37 V and a standard deviation of 0.1889 V, which confirms the stable piezoelectric response and durability of the PAC film. This level of stability meets the requirements of practical use and supports continuous and accurate monitoring over prolonged periods.





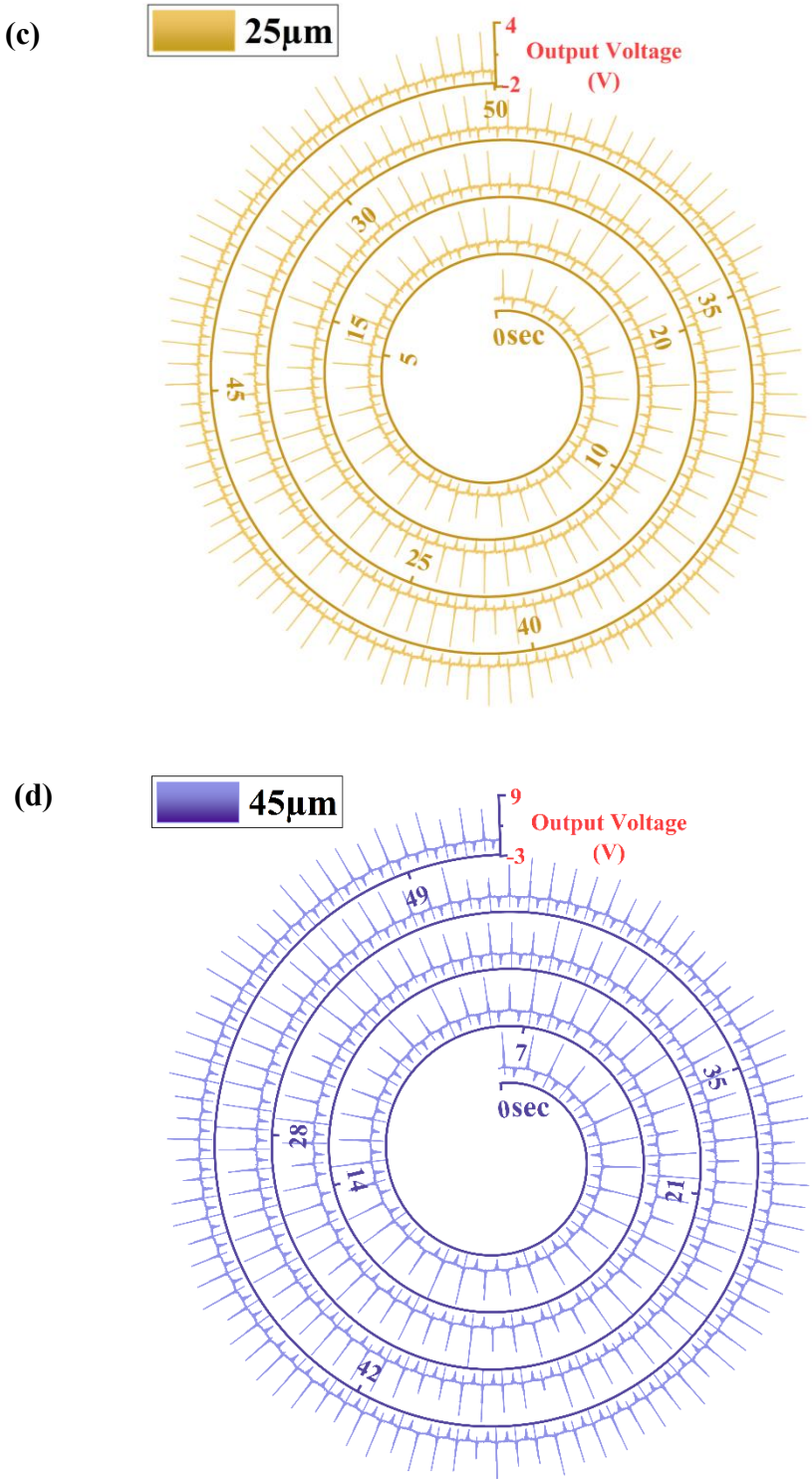


Figure 7.13. Long-term stability tests of PAC piezoelectric pressure sensors with various thicknesses (10 µm, 25 µm, and 45 µm). (a) Daily average output voltage values recorded over a 10-day period under continuous fatigue tests (pressure: 90 kPa, frequency: 5 Hz, temperature: 20-25 °C, humidity: 30-35%). Corresponding detailed spiral plots illustrating real-time output voltage stability for sensors with thicknesses of (b) 10 µm, (c) 25 µm, and (d) 45 µm, respectively.

The response time, another important performance indicator, was also evaluated, as shown in **Figure 7.14**. The response time is defined as the duration for which the output voltage increases from the baseline to the maximum value when pressure is applied to the sensor and was approximately 12 ms for the 45 μm PAC sensor. Conversely, the recovery time is the duration for the output voltage to revert from the maximum value to the baseline value upon the removal of the force, with an approximate value of 10 ms. These short response and recovery times indicate that the sensor can accurately detect dynamic pressure changes.

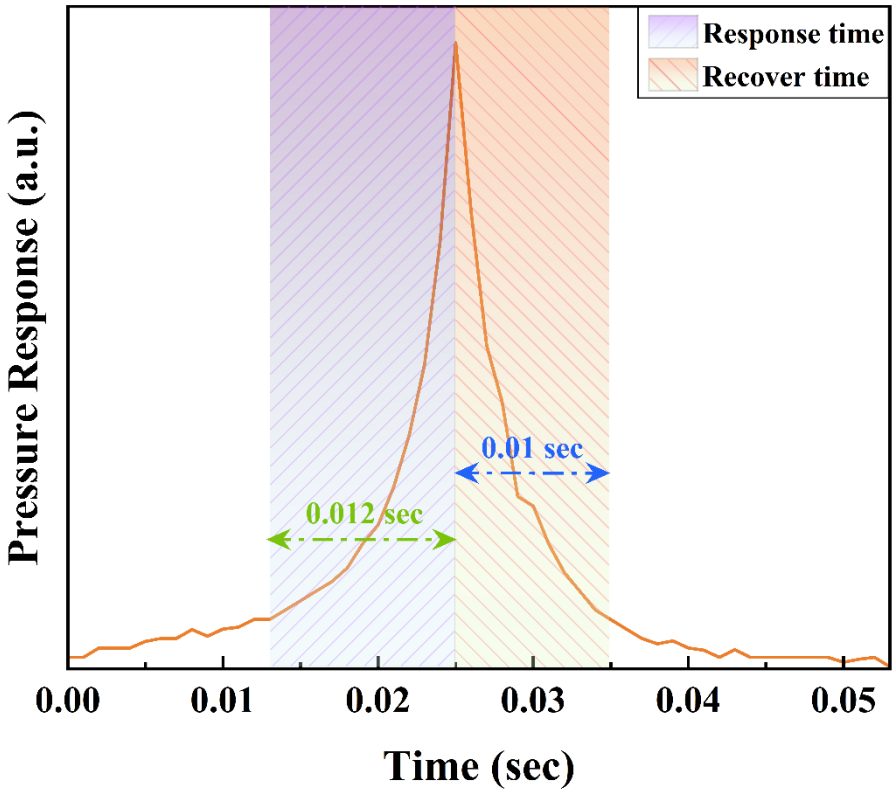


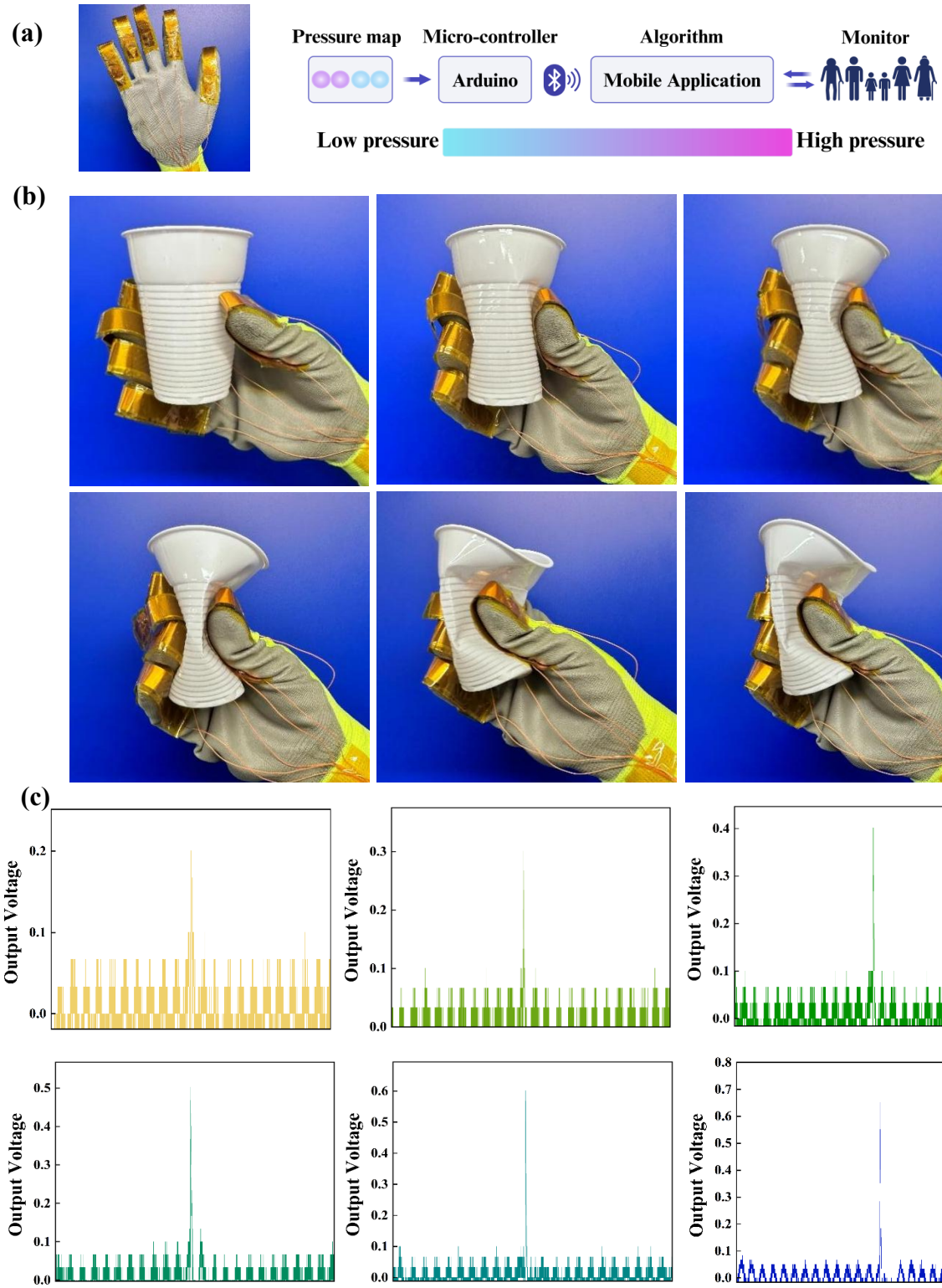
Figure 7.14. Response and recovery times of the PAC-based piezoelectric pressure sensor under instantaneous pressure loading and unloading conditions.

7.4 Applications

Human-machine interaction is receiving increasing attention as the Internet of Things, soft robotics, medical devices and machine learning continue to advance. Realising these applications relies on sensors that combine a reliable response with mechanical flexibility, among which flexible pressure sensors are particularly important. To illustrate such use, the PAC pressure sensor array developed in this work was integrated into a textile smart glove for real-time monitoring of hand-object interactions, using the 45 μm device, which gave the highest output, with the sensors placed at the fingertips so that the pressure applied during gripping could be recorded, as shown in **Figure 7.15(a)**.

The ability of the glove to monitor real-time interaction with an object was examined by using it to grasp a plastic cup, with the applied force increased from a light grip to a level that fully deformed the cup, as shown in **Figure 7.15(b).** The output voltage tracked the applied pressure in real time, increasing from 0.2 V to 0.7 V as the grip tightened and returning towards the baseline as it was released, so that the successive stages of the interaction were clearly distinguished in the recorded signal, as shown in **Figure 7.15(c)**. This indicates that the sensor can detect and quantify the varying pressure exerted by the fingers during a natural grasping task.

A wireless and real-time acquisition of the five-channel sensor array was implemented with a Nordic nRF52840 SoC, selected for its low power consumption and integrated BLE, as shown in **Figure 7.15(d)**. The SoC incorporates a 12-bit ADC that digitises the analogue voltage outputs of the array and supports BLE data rates of up to 2 Mbps, which is suited to applications requiring rapid data exchange. Firmware development and data transmission were carried out in the Arduino integrated development environment, with the digitised outputs transferred over the Serial Peripheral Interface (SPI) and displayed through a mobile application. The self-powered sensor requires no external bias to generate its signal, although the microcontroller and wireless module are externally powered, so that the combination of a flexible, biocompatible sensor with wireless readout provides a complete wearable monitoring chain from the mechanical stimulus to a remotely displayed signal, suited to wearable technology, healthcare, robotics and human-computer interaction.


(a)
Pressure map
Micro-controller
Algorithm
Monitor
Arduino
Mobile Application
Low pressure
High pressure
(b)
(c)
Output Voltage

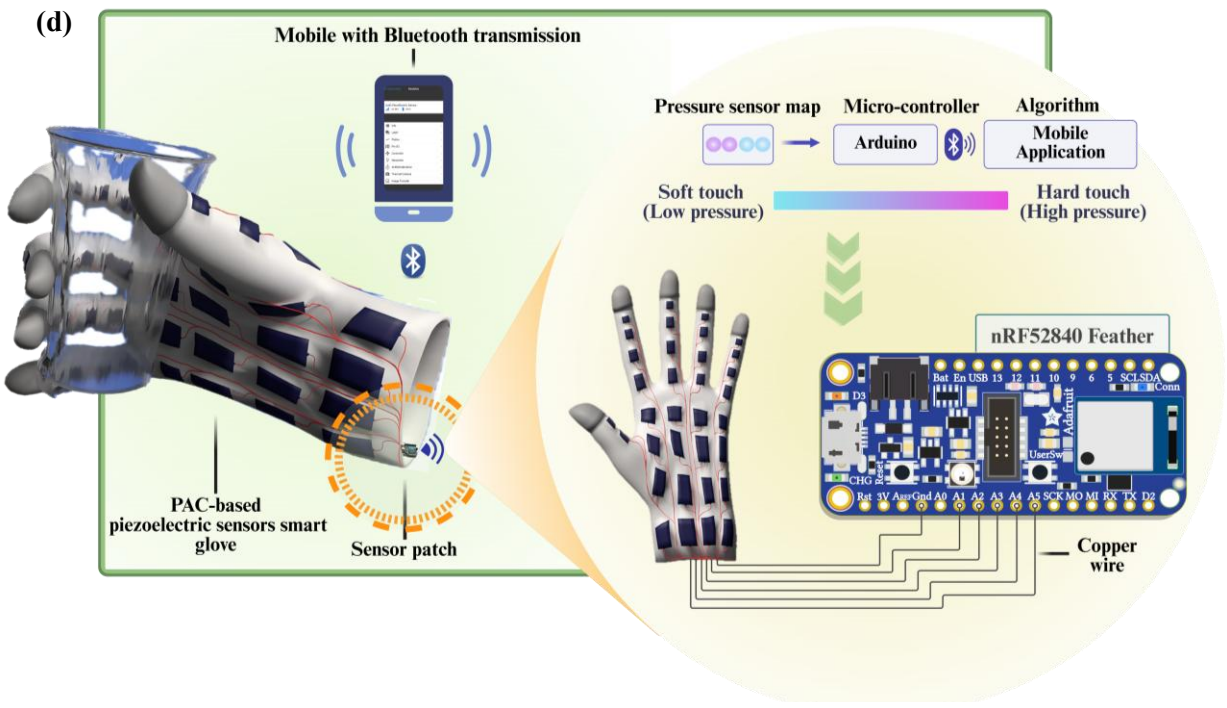


Figure 7.15 Smart glove demonstration with the PAC pressure sensor array. (a) the sensor array integrated into a textile glove, (b) the glove grasping a plastic cup at increasing grip pressure, (c) the corresponding real-time output voltage, increasing from 0.2 V to 0.7 V as the grip tightened, and (d) schematic of the wireless system, in which the sensor signals are digitised and processed by a Nordic nRF52840 System-on-Chip and transmitted over Bluetooth Low Energy to a mobile application.

7.5 Summary

In this chapter, the proposed dynamic piezoelectric based pressure sensor array using PAC film provides excellent pressure and frequency sensitivities with mechanical flexibility and biocompatibility. Various material characterisation processes like SEM, AFM, XRD, Raman, FTIR, and d_{33} measurements were performed to analyse the morphological and structural properties of PAC. Various optimisation studies of different PAC film thicknesses were used to enhance the piezoelectric coefficient, thereby improving the output voltage performance, resulting in the higher sensitivities that were successfully validated in this study. Furthermore, the sensors exhibit fast response and recovery times, with a level of cyclic stability demonstrating its suitability for high-speed flexible and wearable electronic applications including human healthcare monitoring systems, human-machine interfaces, and E-skin. Finally, an intelligent and smart glove with wireless data transfer capability using Bluetooth technology was successfully demonstrated by integrating a PAC based pressure sensor array for real-time pressure monitoring, postulated for use in applications such as knee replacement surgeries or physiological monitoring of human motions. This work will lay a

strong foundation for the development next generation wearable and implantable sensing technologies that bridge the gap between the human and machines, empowering advanced networking, communication and monitoring systems.

Chapter 8: Conclusions and Future Work

8.1 Conclusions

Based on the electromechanical conversion mechanism of piezoelectric materials and the self-powered sensing principle of piezoelectric nanogenerators, this thesis investigates the piezoelectric behaviour, device construction and application validation of chitosan and related composite materials. The work focuses on their potential for wearable pressure sensing and biomedical sensing, particularly in scenarios where mechanical compliance, low-power operation and material compatibility are required. To this end, pure chitosan, CS-ZnO, CS-BTO, PAC and its hybrid structures were developed and evaluated in terms of material characteristics, electromechanical response, stability and application-level performance.

The first stage of this thesis demonstrated the feasibility of using pure chitosan as a bio-sourced active piezoelectric layer for flexible self-powered pressure sensing. Pure chitosan was selected owing to its natural abundance, solution processability, flexibility, biocompatibility and solubility. The fabricated chitosan pressure sensor exhibited pressure- and frequency-dependent voltage outputs under dynamic mechanical stimulation, confirming that chitosan can serve not only as a flexible supporting substrate but also as an active piezoelectric transduction layer. This study established the baseline material platform for subsequent chitosan-based composite sensors.

The second stage focused on improving the piezoelectric response of chitosan by incorporating ZnO nanoparticles into the polymer matrix. The CS-ZnO composite sensor retained the flexibility and biodegradability of chitosan while introducing an additional inorganic piezoelectric phase to enhance electromechanical coupling. Among the investigated compositions, the 15 wt.% CS-ZnO sensors showed the most favourable sensing performance, with a pressure sensitivity of 70.71 mV/kPa and a frequency sensitivity of 471.43 mV/Hz over the tested dynamic range. In addition, the composite film degraded by approximately 50% within 30 min and almost completely after 2 h in mildly acidic deionised water, indicating that ZnO incorporation did not prevent the dissolution behaviour of the chitosan matrix. These results show that CS-ZnO composites can balance enhanced dynamic voltage output with rapid aqueous disintegration of the active film, complete-device sustainability was not assessed.

Furthermore, the CS-ZnO sensor was extended from a single sensing element to an array-level pressure mapping platform. A pressure sensor array was fabricated using the 15 wt.% CS-ZnO composites, enabling voltage mapping, object identification, gesture detection and wireless data transmission. This proof-of-concept demonstration showed that the developed piezoelectric composite film, which exhibited aqueous dissolution under the tested conditions, could be integrated into a distributed sensing architecture. The CS-ZnO system therefore linked material-level electromechanical enhancement to preliminary artificial tactile and e-skin demonstrations.

The next stage developed CS-BTO composite pressure sensors for high-sensitivity wearable healthcare applications. BTO was introduced as a lead-free inorganic piezoelectric filler to further improve the electromechanical coupling of the chitosan matrix. The 15 wt.% CS-BTO sensors exhibited the highest sensitivity among the chitosan-based composite sensors developed in this thesis, with a pressure sensitivity of 276.07 mV/kPa and a frequency sensitivity of 2564.29 mV/Hz. The corresponding output voltages reached 24.9 V under pressure variation and 23.3 V under frequency variation, while the d_{33} value increased from approximately 7 pC/N for pure chitosan to 13 pC/N for the 15 wt.% composite. In addition, the sensor showed a rapid dynamic response, with response and recovery times of 0.24 ms and 0.64 ms, respectively. Under the stated device and test conditions, these results support BTO incorporation as an effective strategy for increasing the electromechanical response and dynamic sensing capability of chitosan-based pressure sensors.

Compared with the CS-ZnO sensor, the CS-BTO sensor provided a much stronger electrical output and was therefore more suitable for applications requiring higher signal amplitude, such as smart insoles, gait monitoring, wearable healthcare and e-skin. Nevertheless, the results also indicate a material design trade-off. Increasing the inorganic filler concentration can enhance the piezoelectric output, but it may also increase stiffness and affect flexibility. Therefore, the design of CS-BTO sensors should consider not only sensitivity, but also nanoparticle dispersion, interfacial coupling, mechanical compliance and long-term stability.

In addition, PAC were investigated as related polymeric pressure sensing platforms. PAC exhibited advantages in chemical inertness, electrical insulation, flexibility, biocompatibility and biostability. The 45 μm PAC sensor achieved a pressure sensitivity of 87.62 mV/kPa and a frequency sensitivity of 580.95 mV/Hz, with response and recovery times of approximately 12 ms and 10 ms, respectively. The device was further integrated into a smart glove system

Table 8.1 Performance comparison of representative pressure sensors

Representative Sensor	Pressure sensitivity (mV/kPa)	Output voltage (V)	Response / recovery (ms)	d_{33}	Biocompatibility	REF
Gly/CS	2.82 ± 0.20	0.190	<100	/	Yes	[19]
PAN/PVDF	42	49	43	/	No	[167]
PLLA/Gly	13.2	≈0.42 Vpp	10	≈8 pC/N	YES	[168]
PZT@PDA/PVDF -TrFE	1380	44	2.6	/	No	[169]
β-Gly/gelatin	41.3 ± 1.3	2.1 ± 0.1	1.0 ± 0.1	22.5 pm/V	YES	[170]
Pure Chitosan	32.25	2.61	Not reported	7 pC/N	YES	Chapter 4
15 wt.% CS-ZnO	70.71	6.7	≈12 / ≈12	16 pC/N	YES	Chapter 5
15 wt.% CS-BTO	276.07	24.9	0.24 / 0.64	13 pC/N	YES	Chapter 6
PAC (45 μm)	87.62	9.6	≈12 / ≈10	1.8 pC/N	YES	Chapter 7

for real-time grip monitoring and wireless data transmission, demonstrating its potential for human-machine interfaces and wearable healthcare systems. The performance of these sensor systems is further compared in **Table 8.1**, alongside representative flexible piezoelectric pressure sensors reported in the literature. The comparison includes pressure sensitivity, output voltage, response and recovery times, and reported biocompatibility. The results show that incorporating ZnO and BTO into the CS matrix improved both pressure sensitivity and output voltage. Under dynamic loading from 20 to 80 kPa at 8 Hz, the pressure sensitivity increased from 32.25 mV/kPa for pure CS to 70.71 and 276.07 mV/kPa for the nominal 15 wt.% CS-ZnO and CS-BTO sensors, respectively. At 80 kPa, the corresponding output voltages were 2.61, 6.7 and 24.9 V. The 45 μm PAC sensor achieved a pressure sensitivity of 87.62 mV/kPa and an output voltage of 9.6 V at 90 kPa. The measured effective d_{33} values increased from approximately 7 pC/N for pure CS to 16 and 13 pC/N for

CS-ZnO and CS-BTO, respectively. Despite its lower effective d_{33} compared with CS-ZnO, CS-BTO exhibited a higher-pressure sensitivity. This indicates that the measured voltage sensitivity depends not only on the piezoelectric coefficient but also on the dielectric properties, device configuration and electrical measurement conditions.Compared with previously reported sensors, both CS composites exhibited higher pressure sensitivities than PAN/PVDF (42 mV/kPa) [167], while PZT@PDA/PVDF-TrFE achieved 1380 mV/kPa [169]. Differences in loading conditions, device structures and readout methods also influence the comparison of reported performance. The established biocompatibility of CS further supports its use as a flexible polymer matrix for wearable pressure sensors.

Overall, this thesis establishes a material-device-application pathway for flexible and self-powered piezoelectric pressure sensors based on chitosan and related composite materials. The work demonstrates that bio-sourced polymers can act as active piezoelectric sensing layers rather than merely passive flexible substrates. Through inorganic nanoparticle incorporation and polymer hybridisation, the sensing performance, solubility, biocompatibility and application scope of chitosan-based pressure sensors were progressively improved. The developed devices were validated in artificial mechanoreceptor emulation, array-level pressure mapping, object identification, gesture sensing, wireless transmission, smart glove monitoring and smart insole applications. These results provide a foundation for future sustainable e-skin, wearable healthcare devices, prosthetic interfaces and neurostimulation-oriented sensing systems.

8.2 Future Work

8.2.1 Further Investigation of Chitosan-Parylene C Hybrid Films

As my future work, a CS-PAC composite will be explored as a good alternative piezoelectric material. While CS offers good flexibility, biocompatibility and solubility, its hydrophilic nature and relatively limited mechanical stability may restrict its use in long-term wearable applications. In addition to the piezoelectric response investigated in this thesis, PAC can form coatings with good conformality, electrical insulation and chemical stability. Given the distinct characteristics of the two materials, future work will investigate whether depositing a PAC layer onto the surface of a CS film can improve its environmental stability and structural integrity, as well as the potential application of this layered structure in flexible piezoelectric pressure sensing.

The CS-PAC films were fabricated by depositing PAC onto the surface of pre-prepared CS films, as illustrated in **Figure 8.1**. First, the repapered CS film was mounted on a cooled, rotating substrate within the chemical vapour deposition (CVD) chamber. Using the CVD process described in Section 7.2.1, a PAC layer with a nominal thickness of approximately 5 μm was subsequently deposited onto the surface of the CS film. This process produced a layered CS-PAC film in which the PAC layer covered the surface of the CS film, rather than a composite film formed through solution blending.

Six CS-PAC samples with different CS-layer thicknesses have currently been prepared and were denoted S1-S6 in order of increasing CS-layer thickness. The PAC layer was deposited under the same CVD conditions for all samples, allowing the effect of CS-layer thickness to be examined in subsequent investigations. Preliminary material characterisation of SEM, XRD, and FTIR has been completed, and the corresponding results are presented in **Figures 8.2-8.4**, respectively.

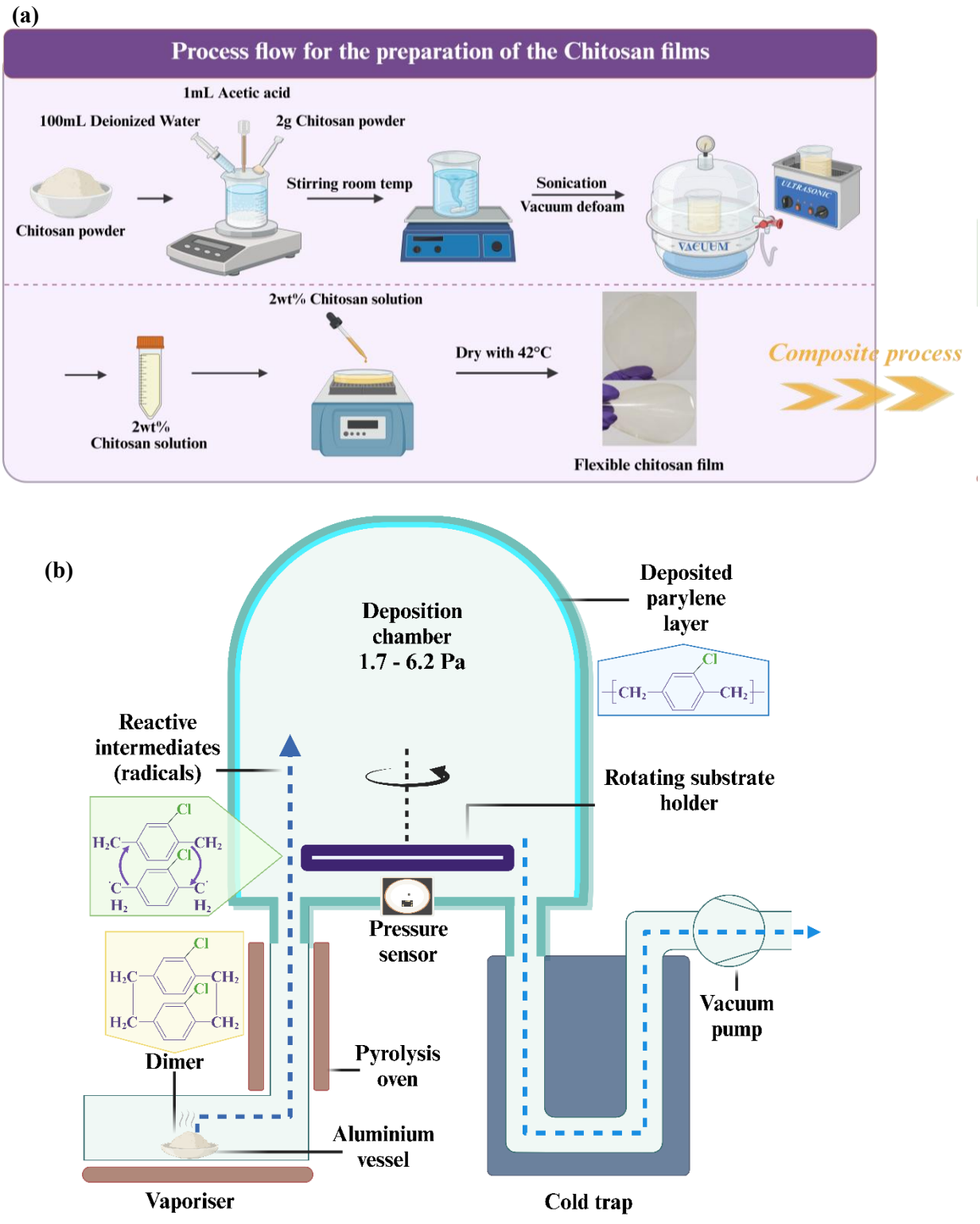


Figure 8.1 Schematic of the CS-PAC film preparation. (a) Preparation of the chitosan film, and (b) deposition of Parylene C onto the chitosan film by chemical vapour deposition to form the CS-PAC composite film.

These preliminary results provide initial information on the surface morphology, crystalline structure and chemical structure of the samples. My future work mainly focusses on the independent batch replication, statistical analysis and quantitative comparison under consistent testing conditions. Material characterisation and electromechanical measurements will be performed to investigate the piezoelectric pressure-sensing mechanism of the layered CS-PAC films. A major focus is on the interlayer stress transfer, interfacial interactions, and the processes of charge generation and transport, with the aim of clarifying the relationships among CS-layer thickness, layered structure and pressure-sensing performance.

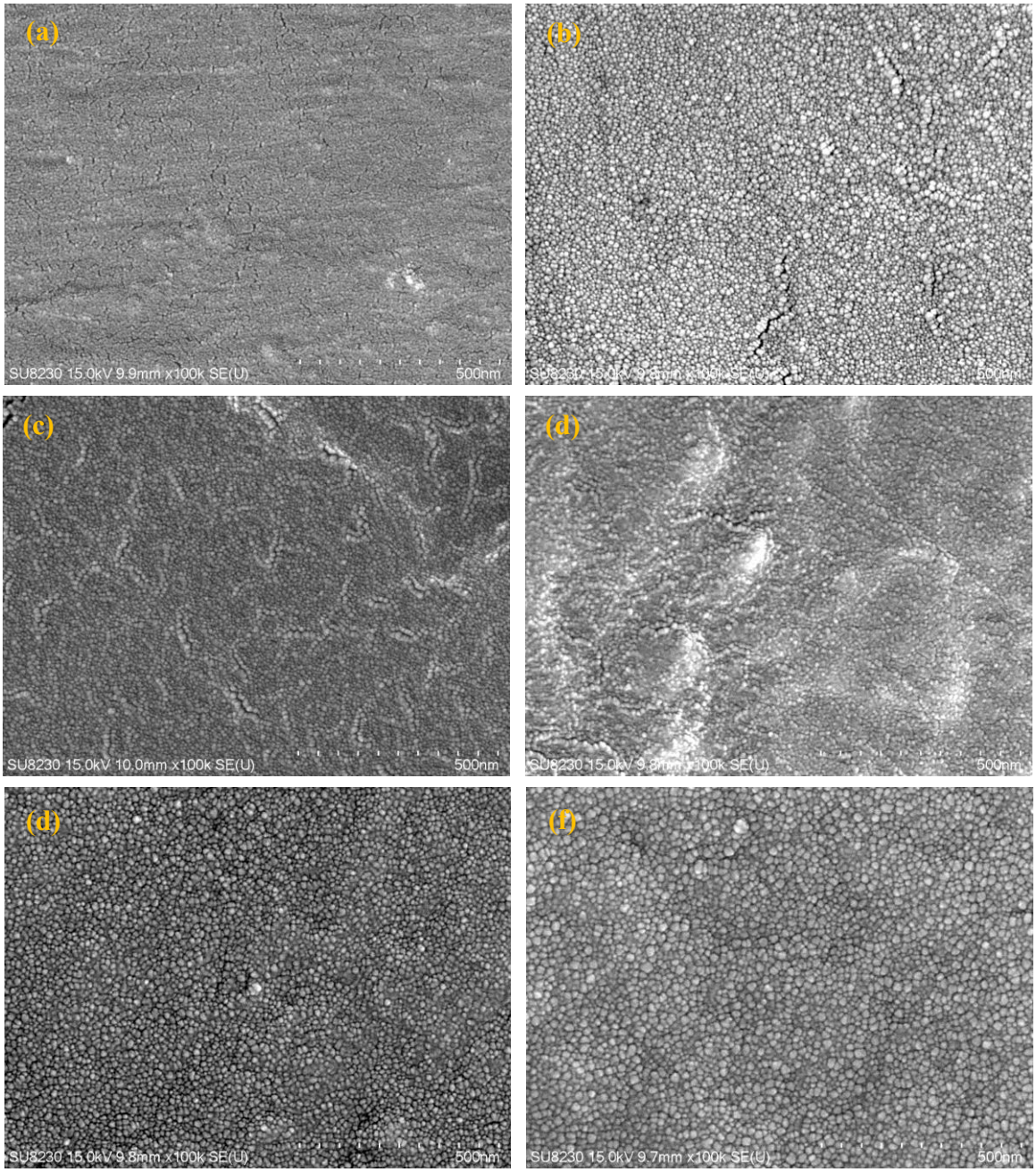


Figure 8.2 SEM images of the CS-PAC films. (a)-(f) surface morphology of samples S1 to S6, showing an increasingly granular texture with increasing chitosan film thickness.

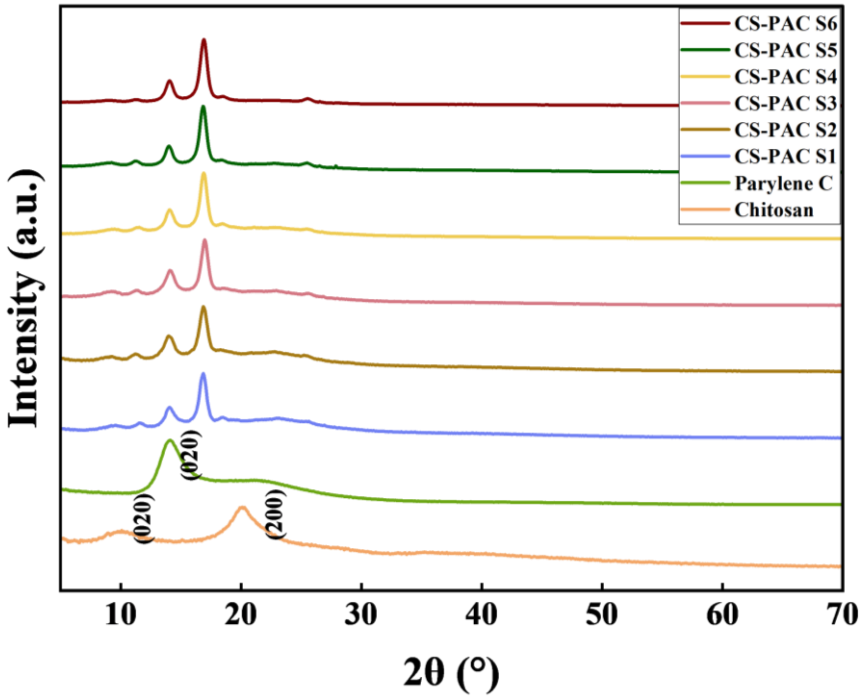


Figure 8.3 XRD patterns of the CS-PAC films, samples S1 to S6, with pristine chitosan and Parylene C included for reference.

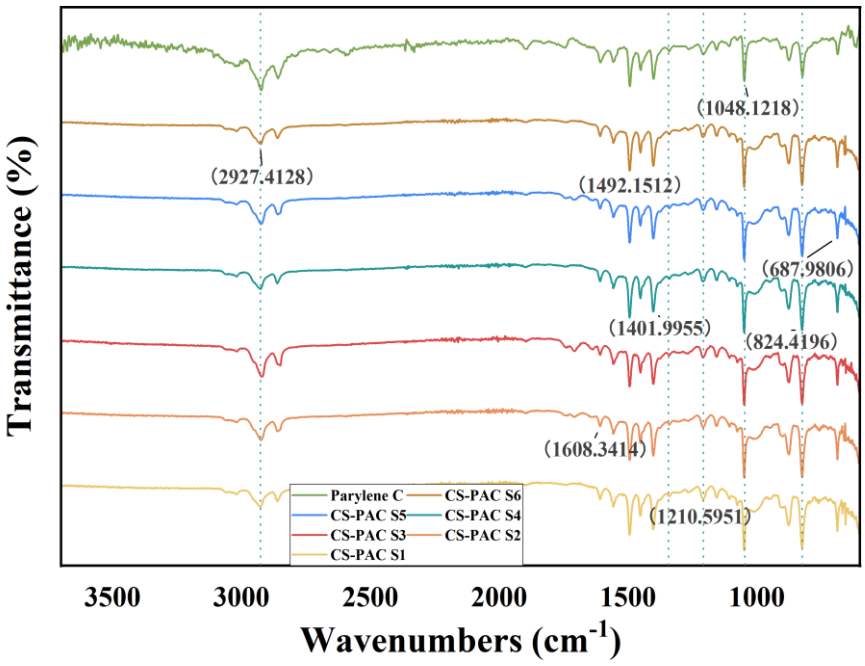


Figure 8.4 FTIR spectra of the CS-PAC films, samples S1 to S6, with pristine chitosan and Parylene C included for reference.

8.2.2 Further Development of the Chitosan-Based Sensor Systems

Although the developed sensors demonstrate promising performance, several issues remain to be addressed before they can be translated into practical wearable or biomedical systems. The future development of this work should focus on material optimisation, structural design,

device reliability, biological validation, system integration and neurostimulation-oriented application.

First, material composition and microstructure should be further optimised. In this thesis, ZnO and BTO nanoparticles were introduced into chitosan to enhance piezoelectric output. However, the relationship between filler concentration, nanoparticle dispersion, agglomeration, interfacial coupling and mechanical flexibility still requires more systematic investigation. Future work should explore a wider range of filler concentrations, particle sizes and surface functionalisation strategies. Improved nanoparticle-polymer interfacial bonding may enhance stress transfer and charge generation while reducing local aggregation and brittleness. This is particularly important for CS-BTO composites, where increased filler concentration improves sensitivity but may also reduce flexibility.

Second, the fabrication process and device structure should be improved to enhance reproducibility, flexibility and long-term mechanical robustness. The current devices mainly rely on solution-based film formation and sandwich-type structures. Although these methods are simple and cost-effective, further control of film thickness, surface morphology and microstructure is needed. Advanced fabrication methods such as electrospinning, multilayer stacking, microstructure films and patterned electrodes could be investigated to improve pressure sensitivity and mechanical compliance.

Third, device reliability and array-level consistency require further investigation under realistic operating conditions. Although cyclic stability was demonstrated in this thesis, practical wearable environments involve repeated bending, twisting, sweat exposure, humidity variation, temperature changes and irregular mechanical loading. These conditions may induce signal drift, hysteresis, electrode degradation and encapsulation failure. For sensor arrays, pixel-to-pixel variation, mechanical crosstalk, electrode resistance and calibration stability should be systematically evaluated. Future studies should therefore establish standardised calibration and testing protocols for large-area arrays, especially for smart gloves, smart insoles and e-skin systems.

Fourth, biological validation should be strengthened before implantable or bioresorbable applications are considered. Although chitosan and Parylene C are known for their favourable biocompatibility, the biological response of the complete composite devices should be examined in more detail. Future work should include cytotoxicity tests, cell viability assays, inflammatory response assessment, leachate analysis and degradation

product evaluation. CS-ZnO and CS-BTO composites should be tested in simulated body fluids, enzymatic media and controlled pH environments to better understand their degradation behaviour under physiological conditions.

Fifth, system-level integration should be further developed. Although the piezoelectric sensors are self-powered at the sensing element level, practical wearable systems still require signal conditioning, filtering, rectification, data acquisition, wireless communication and power management circuits. Future work should integrate the developed sensors with low-power electronics and wireless transmission modules to enable stable real-time monitoring. For smart glove and smart insole applications, signal processing and machine learning methods could be introduced to classify grip patterns, gestures, plantar pressure distributions and gait phases. This would allow the sensing system to move from simple voltage detection towards intelligent tactile and motion perception.

Finally, future work could move towards closed-loop neurostimulation-oriented systems. The sensors developed in this thesis can convert mechanical stimuli into electrical signals, suggesting their potential as mechanical input units for future sensory feedback systems. However, the present work has not experimentally demonstrated direct neural stimulation, in vivo implantation, safe charge injection, electrode-tissue interfaces or closed-loop feedback control. Future studies should therefore integrate the pressure sensors with stimulation circuits, define safe charge delivery limits, design suitable electrodes and investigate how pressure-derived signals can be transformed into biologically meaningful stimulation patterns. In vitro and in vivo validation will be necessary before these devices can be considered for implantable neurostimulation applications.

Reference

[1] F. Xu *et al.*, 'Recent Developments for Flexible Pressure Sensors: A Review', *Micromachines*, vol. 9, no. 11, p. 580, Nov. 2018, doi: 10.3390/mi9110580.

[2] X. Cui *et al.*, 'Flexible pressure sensors via engineering microstructures for wearable human-machine interaction and health monitoring applications', *iScience*, vol. 25, no. 4, p. 104148, Apr. 2022, doi: 10.1016/j.isci.2022.104148.

[3] H. Niu *et al.*, 'Advances in flexible sensors for intelligent perception system enhanced by artificial intelligence', *InfoMat*, vol. 5, no. 5, p. e12412, 2023, doi: 10.1002/inf2.12412.

[4] X. Zeng, R. Peng, Z. Fan, and Y. Lin, 'Self-powered and wearable biosensors for healthcare', *Mater. Today Energy*, vol. 23, p. 100900, Jan. 2022, doi: 10.1016/j.mtener.2021.100900.

[5] J. Li, Z. Fang, D. Wei, and Y. Liu, 'Flexible Pressure, Humidity, and Temperature Sensors for Human Health Monitoring', *Adv. Healthc. Mater.*, vol. 13, no. 31, p. e2401532, 2024, doi: 10.1002/adhm.202401532.

[6] Y. Song, D. Mukasa, H. Zhang, and W. Gao, 'Self-powered wearable biosensors', *Acc. Mater. Res.*, vol. 2, no. 3, pp. 184–197, Mar. 2021, doi: 10.1021/accountsmr.1c00002.

[7] R. Liu, Z. L. Wang, K. Fukuda, and T. Someya, 'Flexible self-charging power sources', *Nat. Rev. Mater.*, pp. 1–17, May 2022, doi: 10.1038/s41578-022-00441-0.

[8] S. D. Mahapatra, 'Piezoelectric materials for energy harvesting and sensing applications: roadmap for future smart materials', *Adv Sci*, vol. 8, p. 2100864, 2021.

[9] D. Hu, M. Yao, Y. Fan, C. Ma, M. Fan, and M. Liu, 'Strategies to achieve high performance piezoelectric nanogenerators', *Nano Energy*, vol. 55, pp. 288–304, Jan. 2019, doi: 10.1016/j.nanoen.2018.10.053.

[10] K. Park *et al.*, 'Highly-Efficient, Flexible Piezoelectric PZT Thin Film Nanogenerator on Plastic Substrates', *Adv. Mater.*, vol. 26, no. 16, pp. 2514–2520, Apr. 2014, doi: 10.1002/adma.201305659.

[11] Z. L. Wang and J. Song, 'Piezoelectric Nanogenerators Based on Zinc Oxide Nanowire Arrays', *Science*, vol. 312, no. 5771, pp. 242–246, Apr. 2006, doi: 10.1126/science.1124005.

[12] L. Persano *et al.*, 'High performance piezoelectric devices based on aligned arrays of nanofibers of poly(vinylidenefluoride-co-trifluoroethylene)', *Nat. Commun.*, vol. 4, no. 1, p. 1633, Mar. 2013, doi: 10.1038/ncomms2639.

[13] S. Anwar, M. Hassanpour Amiri, S. Jiang, M. M. Abolhasani, P. R. F. Rocha, and K. Asadi, 'Piezoelectric nylon-11 fibers for electronic textiles, energy harvesting and sensing', *Adv. Funct. Mater.*, vol. 31, no. 4, p. 2004326, 2021, doi: 10.1002/adfm.202004326.

[14] X. Ma, Q. Hu, Y. Dai, P. He, and X. Zhang, 'Disposable Sensors Based on Biodegradable Polylactic Acid Piezoelectret Films and Their Application in Wearable Electronics', *Sens. Actuators Phys.*, vol. 346, p. 113834, 2022, doi: 10.1016/j.sna.2022.113834.

[15] K. K. Sappati and S. Bhadra, 'Piezoelectric polymer and paper substrates: A review', *Sensors*, vol. 18, no. 11, p. 3605, Oct. 2018, doi: 10.3390/s18113605.

[16] M. Ali, S. M. Hoseyni, R. Das, M. Awais, I. Basdogan, and L. Beker, 'A flexible and biodegradable piezoelectric-based wearable sensor for non-invasive monitoring of dynamic human motions and physiological signals', *Adv Mater Technol*, vol. 8, p. 2300347, 2023.

[17] F. Yang *et al.*, 'Wafer-scale heterostructured piezoelectric bio-organic thin films', *Science*, vol. 373, no. 6552, pp. 337–342, Jul. 2021, doi: 10.1126/science.abf2155.

[18] P. J. VandeVord, H. W. T. Matthew, S. P. DeSilva, L. Mayton, B. Wu, and P. H. Wooley, 'Evaluation of the biocompatibility of a chitosan scaffold in mice'.

[19] E. S. Hosseini, L. Manjakkal, D. Shakthivel, and R. Dahiya, 'Glycine–Chitosan-Based Flexible Biodegradable Piezoelectric Pressure Sensor', *ACS Appl. Mater. Interfaces*, vol. 12, no. 8, pp. 9008–9016, Feb. 2020, doi: 10.1021/acsami.9b21052.

[20] Z. Wang, B. P. Yalagala, M. Hafezi, H. Heidari, and A. Feeney, 'A bioprotein-based flexible and self-powered pressure sensor towards a biomimic of an artificial Pacinian corpuscle', in *2023 30th IEEE International Conference on Electronics, Circuits and Systems (ICECS)*, Dec. 2023, pp. 1–4. doi: 10.1109/ICECS58634.2023.10382948.

[21] Z. Wang, B. P. Yalagala, J. Zhang, M. Hafezi, H. Heidari, and A. Feeney, 'Wireless and self-powered wearable pressure sensors based on chitosan for artificial mechanoreceptors', *Adv. Mater. Technol.*, vol. 10, no. 11, p. 2401858, 2025, doi: 10.1002/admt.202401858.

[22] Z. Wang, B. P. Yalagala, J. Zhang, Z. He, H. Heidari, and A. Feeney, 'A Hybrid Chitosan–BaTiO3 Composite-Based Flexible and Self-Powered Pressure Sensor for Wearable Healthcare Applications', *ACS Appl. Eng. Mater.*, vol. 4, no. 7, pp. 3620–3630, 2026, doi: 10.1021/acsaenm.6c00330.

[23] Z. Wang, B. P. Yalagala, H. Heidari, and A. Feeney, 'A flexible and self-powered chitosan-BaTiO3Composite pressure sensor for E-skin applications', in *2024 IEEE SENSORS*, Oct. 2024, pp. 1–4. doi: 10.1109/SENSORS60989.2024.10785172.

[24] J. Hu, G. Dun, X. Geng, J. Chen, X. Wu, and T.-L. Ren, 'Recent Progress in Flexible Micro-Pressure Sensors for Wearable Health Monitoring', *Nanoscale Adv.*, vol. 5, no. 12, pp. 3131–3145, 2023, doi: 10.1039/D2NA00866A.

[25] C. Xu *et al.*, 'Flexible Pressure Sensors in Human-Machine Interface Applications', *Small*, vol. 20, no. 15, p. e2306655, 2024, doi: 10.1002/smll.202306655.

[26] S. Mishra, S. Mohanty, and A. Ramadoss, 'Functionality of Flexible Pressure Sensors in Cardiovascular Health Monitoring: A Review', *ACS Sens.*, vol. 7, no. 9, pp. 2495–2520, 2022, doi: 10.1021/acssensors.2c00942.

[27] Y. Yang, G. Zhou, D. Ye, Z. Bai, Z. Deng, and J. Xu, 'A Self-Powered Laminated Fabric Sensor for Human Motion Detection and Heart-Rate Monitoring Based on PPy/Al Schottky Contact', *J. Sandw. Struct. Mater.*, vol. 24, no. 1, pp. 503–516, 2022, doi: 10.1177/10996362211021889.

[28] Z. Hu *et al.*, 'Flexible pressure sensing systems empowered by artificial intelligence: Materials, devices and emerging applications', *Mater. Horiz.*, vol. 13, no. 7, pp. 3178–3221, 2026, doi: 10.1039/d5mh02286j.

[29] R. Qin *et al.*, 'Recent advances in flexible pressure sensors based on MXene materials', *Adv. Mater.*, vol. 36, no. 24, Jun. 2024, doi: 10.1002/adma.202312761.

[30] H. Park, G. S. Gbadam, S. Niu, H. Ryu, and J.-H. Lee, 'Manufacturing strategies for highly sensitive and self-powered piezoelectric and triboelectric tactile sensors', *Int. J. Extreme Manuf.*, vol. 7, no. 1, p. 012006, Feb. 2025, doi: 10.1088/2631-7990/ad88be.

[31] Y. Zhou *et al.*, 'Recent advances in flexible self-powered sensors in piezoelectric, triboelectric, and pyroelectric fields', *Nanoenergy Adv.*, vol. 4, no. 3, pp. 235–257, Aug. 2024, doi: 10.3390/nanoenergyadv4030015.

[32] Y. Chen, X. Zhang, and C. Lu, 'Flexible piezoelectric materials and strain sensors for wearable electronics and artificial intelligence applications', *Chem. Sci.*, vol. 15, no. 40, pp. 16436–16466, 2024, doi: 10.1039/d4sc05166a.

[33] G. Sun, P. Wang, Y. Jiang, H. Sun, C. Meng, and S. Guo, 'Recent advances in flexible and soft gel-based pressure sensors', *Soft Sci.*, vol. 2, no. 4, p. 17, 2022, doi: 10.20517/ss.2022.16.

[34] K. Uchino, 'Fundamentals of piezoelectrics', in *Encyclopedia of Smart Materials*, 2022, pp. 1–21. doi: 10.1016/b978-0-12-803581-8.12129-0.

[35] B. Chen *et al.*, 'Flexible Piezoelectrics: Integration of Sensing, Actuating and Energy Harvesting'.

[36] Y. Luo *et al.*, 'Technology roadmap for flexible sensors', *ACS Nano*, vol. 17, no. 6, pp. 5211–5295, Mar. 2023, doi: 10.1021/acsnano.2c12606.

[37] X. Wang, J. Song, J. Liu, and Z. L. Wang, 'Direct-current nanogenerator driven by ultrasonic waves', *Science*, vol. 316, no. 5821, pp. 102–105, Apr. 2007, doi: 10.1126/science.1139366.

[38] Y. Hu, L. Lin, Y. Zhang, and Z. L. Wang, 'Replacing a battery by a nanogenerator with 20 V output', *Adv. Mater.*, vol. 24, no. 1, pp. 110–114, Jan. 2012, doi: 10.1002/adma.201103727.

[39] Z. Zhang, Z. Wang, X. Li, Y. Zheng, and Z. Yang, 'Design and Manufacturing of Piezoelectric Biomaterials for Bioelectronics and Biomedical Applications', *Chem. Rev.*, vol. 125, no. 20, pp. 9875–9929, 2025, doi: 10.1021/acs.chemrev.5c00399.

[40] Z. Wang *et al.*, 'Biodegradable piezoelectric materials: Powering the future of bioelectronic medicine', *Adv. Funct. Mater.*, vol. 36, no. 22, Mar. 2026, doi: 10.1002/adfm.202519501.

[41] J. Zhang, C. Boyer, and Y. X. Zhang, 'Enhancing the humidity resistance of triboelectric nanogenerators: A review', *Small*, Apr. 2024, doi: 10.1002/smll.202401846.

[42] S. R. Begum and A. Chandrasekhar, 'Opportunities and challenges in power management systems for triboelectric nanogenerators', *ACS Appl. Electron. Mater.*, vol. 5, no. 3, pp. 1347–1375, Mar. 2023, doi: 10.1021/acsaelm.2c01505.

[43] F. Dai, Q. Geng, T. Hua, X. Sheng, and L. Yin, 'Organic biodegradable piezoelectric materials and their potential applications as bioelectronics', *Soft Sci.*, vol. 3, no. 1, p. N/A-N/A, Feb. 2023, doi: 10.20517/ss.2022.30.

[44] N. Setter *et al.*, 'Ferroelectric thin films: Review of materials, properties, and applications', *J. Appl. Phys.*, vol. 100, no. 5, p. 051606, 2006, doi: 10.1063/1.2336999.

[45] Z. L. Wang, 'ZnO nanowire and nanobelt arrays for nanoscale energy and sensor systems', *Mater. Sci. Eng. R Rep.*, vol. 64, no. 3–4, pp. 33–71, 2009, doi: 10.1016/j.mser.2008.12.002.

[46] W. Wu *et al.*, 'Piezoelectricity of single-atomic-layer MoS2 for energy conversion and piezotronics', *Nature*, vol. 514, no. 7523, pp. 470–474, 2014, doi: 10.1038/nature13792.

[47] Ü. Özgür *et al.*, 'A comprehensive review of ZnO materials and devices', *J. Appl. Phys.*, vol. 98, no. 4, p. 041301, 2005, doi: 10.1063/1.1992666.

[48] N. Bhadwal, R. Ben Mrad, and K. Behdinan, 'Review of Zinc Oxide Piezoelectric Nanogenerators: Piezoelectric Properties, Composite Structures and Power Output', *Sensors*, vol. 23, no. 8, p. 3859, 2023, doi: 10.3390/s23083859.

[49] J. Yin *et al.*, 'Self-Powered Rapid Response Flexible Pressure Sensor for Wearable Application', *Adv. Eng. Mater.*, vol. 25, 2023, doi: 10.1002/adem.202201678.

[50] M. K. Singh, P. K. Iyer, and D. K. Singh, 'Piezoresistive/Piezoelectric Pressure Sensor Based on CVD-Grown ZnO Nanowires on Polyethylene Terephthalate Substrate', *ACS Appl. Electron. Mater.*, vol. 6, no. 8, pp. 6165–6173, 2024, doi: 10.1021/acsaelm.4c00991.

[51] Y. Qi, J. Kim, T. D. Nguyen, B. Lisko, P. K. Purohit, and M. C. McAlpine, 'Enhanced piezoelectricity and stretchability in energy harvesting devices fabricated from buckled PZT ribbons', *Nano Lett.*, vol. 11, no. 3, pp. 1331–1336, Mar. 2011, doi: 10.1021/nl104412b.

[52] T. Dufay, B. Guiffard, R. Seveno, S. Ginestar, and J.-C. Thomas, 'Flexible PZT thin film transferred on polymer substrate', *Surf. Coat. Technol.*, vol. 343, pp. 148–152, Jun. 2018, doi: 10.1016/j.surfcoat.2017.09.080.

[53] S. Liu, D. Zou, X. Yu, Z. Wang, and Z. Yang, 'Transfer-free PZT thin films for flexible nanogenerators derived from a single-step modified sol–gel process on 2D mica', *ACS Appl. Mater. Amp Interfaces*, vol. 12, no. 49, pp. 54991–54999, Dec. 2020, doi: 10.1021/acsami.0c16973.

[54] D. Berlincourt and H. Jaffe, 'Elastic and piezoelectric coefficients of single-crystal barium titanate', *Phys. Rev.*, vol. 111, no. 1, pp. 143–148, Jul. 1958, doi: 10.1103/physrev.111.143.

[55] W. Liu and X. Ren, 'Large piezoelectric effect in pb-free ceramics', *Phys. Rev. Lett.*, vol. 103, no. 25, Dec. 2009, doi: 10.1103/physrevlett.103.257602.

[56] S. Ippili *et al.*, 'Halide double perovskite-based efficient mechanical energy harvester and storage devices for self-charging power unit', *Nano Energy*, vol. 107, p. 108148, Mar. 2023, doi: 10.1016/j.nanoen.2022.108148.

[57] K. S. Novoselov *et al.*, 'Electric field effect in atomically thin carbon films', *Science*, vol. 306, no. 5696, pp. 666–669, Oct. 2004, doi: 10.1126/science.1102896.

[58] C. Di Giorgio, E. Blundo, G. Pettinari, M. Felici, F. Bobba, and A. Polimeni, 'Mechanical, elastic, and adhesive properties of two-dimensional materials: From straining techniques to state-of-the-art local probe measurements', *Adv. Mater. Interfaces*, vol. 9, no. 13, May 2022, doi: 10.1002/admi.202102220.

[59] R. Hinchet, U. Khan, C. Falconi, and S.-W. Kim, 'Piezoelectric properties in two-dimensional materials: Simulations and experiments', *Mater. Today*, vol. 21, no. 6, pp. 611–630, Jul. 2018, doi: 10.1016/j.mattod.2018.01.031.

[60] J. Kou, Y. Liu, Y. Zhu, and J. Zhai, 'Progress in piezotronics of transition-metal dichalcogenides', *J. Phys. Appl. Phys.*, vol. 51, no. 49, p. 493002, Dec. 2018, doi: 10.1088/1361-6463/aadb15.

[61] W. Choi, J. Kim, E. Lee, G. Mehta, and V. Prasad, 'Asymmetric 2D MoS2 for Scalable and High-Performance Piezoelectric Sensors', *ACS Appl. Mater. Interfaces*, vol. 13, no. 11, pp. 13596–13603, 2021, doi: 10.1021/acsami.1c00650.

[62] M. Dai *et al.*, 'Two-Dimensional van der Waals Materials with Aligned In-Plane Polarization and Large Piezoelectric Effect for Self-Powered Piezoelectric Sensors', *Nano Lett.*, vol. 19, no. 8, pp. 5410–5416, 2019, doi: 10.1021/acs.nanolett.9b01907.

[63] S. Mirjalali *et al.*, 'A Review on Wearable Electrospun Polymeric Piezoelectric Sensors and Energy Harvesters', *Macromol. Mater. Eng.*, vol. 308, no. 1, pp. 1–27, 2023, doi: 10.1002/mame.202200442.

[64] M. T. Chorsi *et al.*, 'Piezoelectric biomaterials for sensors and actuators', *Adv. Mater.*, vol. 31, no. 1, Jan. 2019, doi: 10.1002/adma.201802084.

[65] A. Chatterjee, A. Das, K. Saha, and U. Jeong, 'Nanofiller-Induced Enhancement of PVDF Electroactivity for Improved Sensing Performance', *Adv. Sens. Res.*, vol. 2, 2023, doi: 10.1002/adsr.202200080.

[66] D. R. Dillon, K. K. Tenneti, C. Y. Li, F. K. Ko, I. Sics, and B. S. Hsiao, 'On the structure and morphology of polyvinylidene fluoride–nanoclay nanocomposites', *Polymer*, vol. 47, no. 5, pp. 1678–1688, Feb. 2006, doi: 10.1016/j.polymer.2006.01.015.

[67] J. E. Lee, Y. Guo, R. E. Lee, and S. N. Leung, 'Fabrication of electroactive poly(vinylidene fluoride) through non-isothermal crystallization and supercritical CO_2 processing', *RSC Adv*, vol. 7, no. 77, pp. 48712–48722, 2017, doi: 10.1039/c7ra09162a.

[68] C. Chang, Y.-K. Fuh, and L. Lin, 'A direct-write piezoelectric PVDF nanogenerator', in *TRANSDUCERS 2009 - 2009 International Solid-State Sensors, Actuators and Microsystems Conference*, Jun. 2009, pp. 1485–1488. doi: 10.1109/sensor.2009.5285796.

[69] C.-T. Pan *et al.*, 'Near-field electrospinning enhances the energy harvesting of hollow PVDF piezoelectric fibers', *RSC Adv.*, vol. 5, no. 103, pp. 85073–85081, Nov. 2015, doi: 10.1039/c5ra16604g.

[70] Y. Mao, P. Zhao, G. McConohy, H. Yang, Y. Tong, and X. Wang, 'Sponge-like piezoelectric polymer films for scalable and integratable nanogenerators and self-powered electronic systems', *Adv. Energy Mater.*, vol. 4, no. 7, May 2014, doi: 10.1002/aenm.201301624.

[71] S. Chen, X. Li, K. Yao, F. E. H. Tay, A. Kumar, and K. Zeng, 'Self-polarized ferroelectric PVDF homopolymer ultra-thin films derived from langmuir–blodgett

deposition', *Polymer*, vol. 53, no. 6, pp. 1404–1408, Mar. 2012, doi: 10.1016/j.polymer.2012.01.058.

[72] J.-M. Hsu, L. Rieth, S. Kammer, M. Orthner, and F. Solzbacher, 'Effect of Thermal and Deposition Processes on Surface Morphology, Crystallinity, and Adhesion of Parylene-C', *Sens. Mater.*, vol. 20, no. 2, pp. 87–102, 2008, doi: 10.18494/SAM.2008.515.

[73] J. Y.-H. Kim, A. Cheng, and Y.-C. Tai, 'Parylene-C as a piezoelectric material', in *2011 IEEE 24th International Conference on Micro Electro Mechanical Systems*, Jan. 2011, pp. 473–476. doi: 10.1109/MEMSYS.2011.5734464.

[74] K. Batra, N. Sinha, S. Goel, H. Yadav, A. J. Joseph, and B. Kumar, 'Enhanced dielectric, ferroelectric and piezoelectric performance of nd-ZnO nanorods and their application in flexible piezoelectric nanogenerator', *J. Alloys Compd.*, vol. 767, pp. 1003–1011, Oct. 2018, doi: 10.1016/j.jallcom.2018.07.187.

[75] M. Habib, I. Lantgios, and K. Hornbostel, 'A review of ceramic, polymer and composite piezoelectric materials', *J. Phys. Appl. Phys.*, vol. 55, no. 42, p. 423002, Oct. 2022, doi: 10.1088/1361-6463/ac8687.

[76] M. Kim, Y. S. Wu, E. C. Kan, and J. Fan, 'Breathable and flexible piezoelectric ZnO@PVDF fibrous nanogenerator for wearable applications', *Polymers*, vol. 10, no. 7, p. 745, Jul. 2018, doi: 10.3390/polym10070745.

[77] R. Wang, J. Sui, and X. Wang, 'Natural piezoelectric biomaterials: A biocompatible and sustainable building block for biomedical devices', *ACS Nano*, vol. 16, no. 11, pp. 17708–17728, Nov. 2022, doi: 10.1021/acsnano.2c08164.

[78] M. Yadav, P. Goswami, K. Paritosh, M. Kumar, N. Pareek, and V. Vivekanand, 'Seafood waste: A source for preparation of commercially employable chitin/chitosan materials', *Bioresour. Bioprocess.*, vol. 6, no. 1, Dec. 2019, doi: 10.1186/s40643-019-0243-y.

[79] G. de Marzo *et al.*, 'Sustainable, flexible, and biocompatible enhanced piezoelectric chitosan thin film for compliant piezosensors for human health', *Adv. Electron. Mater.*, vol. 9, no. 9, Sep. 2023, doi: 10.1002/aelm.202200069.

[80] F. B. Ahmad, M. H. Maziati Akmal, A. Amran, and M. H. Hasni, 'Characterization of chitosan from extracted fungal biomass for piezoelectric application', *IOP Conf. Ser.*

Mater. Sci. Eng., vol. 778, no. 1, p. 012034, Apr. 2020, doi: 10.1088/1757-899x/778/1/012034.

[81] J. D. Giraldo *et al.*, 'Alternative processes to produce chitin, chitosan, and their oligomers', *Carbohydr. Polym.*, vol. 332, p. 121924, May 2024, doi: 10.1016/j.carbpol.2024.121924.

[82] T. Jin, T. Liu, E. Lam, and A. Moores, 'Chitin and Chitosan on the Nanoscale', *Nanoscale Horiz.*, vol. 6, no. 7, pp. 505–542, 2021, doi: 10.1039/D0NH00696C.

[83] F. Hisham, M. H. Maziati Akmal, F. Ahmad, K. Ahmad, and N. Samat, 'Biopolymer chitosan: Potential sources, extraction methods, and emerging applications', *Ain Shams Eng. J.*, vol. 15, no. 2, p. 102424, Feb. 2024, doi: 10.1016/j.asej.2023.102424.

[84] A. T. Hazmi, F. B. Ahmad, M. H. Maziati Akmal, and A. A. M. Ralib, 'Microbial chitosan for the fabrication of piezoelectric thin film', *IOP Conf. Ser. Mater. Sci. Eng.*, vol. 1173, no. 1, p. 012043, Aug. 2021, doi: 10.1088/1757-899X/1173/1/012043.

[85] A. T. Hazmi, F. B. Ahmad, M. H. Maziati Akmal, A. A. Md Ralib, and F. Binti Ali, 'Fungal chitosan for potential application in piezoelectric energy harvesting: Review on experimental procedure of chitosan extraction', *Alex. Eng. J.*, vol. 67, pp. 105–116, Mar. 2023, doi: 10.1016/j.aej.2022.08.020.

[86] A. Amran, F. B. Ahmad, M. H. M. Akmal, A. A. M. Ralib, and M. I. Bin Suhaimi, 'Biosynthesis of thin film derived from microbial chitosan for piezoelectric application', *Mater. Today Commun.*, vol. 29, p. 102919, Dec. 2021, doi: 10.1016/j.mtcomm.2021.102919.

[87] S. Papa *et al.*, 'A Comprehensive Study of Piezoelectricity in Chitosan Films', *Small Sci.*, vol. 6, no. 3, p. e202500593, Mar. 2026, doi: 10.1002/smsc.202500593.

[88] E. Prokhorov, G. Luna-Bárcenas, J. M. Yáñez Limón, A. Gómez Sánchez, and Y. Kovalenko, 'Chitosan-ZnO Nanocomposites Assessed by Dielectric, Mechanical, and Piezoelectric Properties', *Polymers*, vol. 12, no. 9, Art. no. 9, Sep. 2020, doi: 10.3390/polym12091991.

[89] E. Prokhorov *et al.*, 'Chitosan-BaTiO3 nanostructured piezopolymer for tissue engineering', *Colloids Surf. B Biointerfaces*, vol. 196, p. 111296, Dec. 2020, doi: 10.1016/j.colsurfb.2020.111296.

[90] J. Nicoletti *et al.*, 'Enhanced piezoelectricity in sustainable-by-design chitosan nanocomposite soft thin films for green sensors', *ACS Nano*, vol. 19, no. 40, pp. 35322–35332, Oct. 2025, doi: 10.1021/acsnano.4c12855.

[91] V. Antonaci *et al.*, 'Biodegradable chitosan-cellulose and sub-spherical nanocrystals composite piezoelectric thin film', *Npj Flex. Electron.*, vol. 10, no. 1, p. 55, Mar. 2026, doi: 10.1038/s41528-026-00550-8.

[92] P. Fan, H. Fan, and S. Wang, 'From emerging modalities to advanced applications of hydrogel piezoelectrics based on chitosan, gelatin and related biological macromolecules: A review', *Int. J. Biol. Macromol.*, vol. 262, p. 129691, Mar. 2024, doi: 10.1016/j.ijbiomac.2024.129691.

[93] Z. Xiong *et al.*, 'Biocompatible and stretchable chitosan piezoelectric gel with antibacterial capability and motion monitoring function for Achilles tendon rupture treatment', *Carbohydr. Polym.*, vol. 352, p. 123149, Mar. 2025, doi: 10.1016/j.carbpol.2024.123149.

[94] J. Liang, X. Liu, J. Du, G. Wallace, D. Wang, and S. Zhang, 'Advances in flexible piezoelectrics for wearable and implantable medical devices', *Npj Flex. Electron.*, vol. 10, no. 1, Mar. 2026, doi: 10.1038/s41528-026-00559-z.

[95] M. Fu, J. Zhang, Y. Jin, Y. Zhao, S. Huang, and C. F. Guo, 'A Highly Sensitive, Reliable, and High-Temperature-Resistant Flexible Pressure Sensor Based on Ceramic Nanofibers', *Adv. Sci.*, vol. 7, no. 17, p. 2000258, 2020, doi: 10.1002/advs.202000258.

[96] S. Wu *et al.*, 'Normal-Direction Graded Hemispheres for Ionic Flexible Sensors with a Record-High Linearity in a Wide Working Range', *ACS Appl. Mater. Interfaces*, vol. 15, no. 40, pp. 47733–47744, Oct. 2023, doi: 10.1021/acsami.3c09580.

[97] Z. Xu *et al.*, 'A flexible pressure sensor with highly customizable sensitivity and linearity via positive design of microhierarchical structures with a hyperelastic model', *Microsyst. Nanoeng.*, vol. 9, no. 1, p. 5, Jan. 2023, doi: 10.1038/s41378-022-00477-w.

[98] S. Sharma, A. Chhetry, M. Sharifuzzaman, H. Yoon, and J. Y. Park, 'Wearable Capacitive Pressure Sensor Based on MXene Composite Nanofibrous Scaffolds for Reliable Human Physiological Signal Acquisition', *ACS Appl. Mater. Interfaces*, vol. 12, no. 19, pp. 22212–22224, May 2020, doi: 10.1021/acsami.0c05819.

[99] M. A. Signore, G. Rescio, L. Francioso, F. Casino, and A. Leone, 'Aluminum Nitride Thin Film Piezoelectric Pressure Sensor for Respiratory Rate Detection', *Sensors*, vol. 24, no. 7, p. 2071, Apr. 2024, doi: 10.3390/s24072071.

[100] N. Wrońska, N. Katir, M. Nowak-Lange, A. El Kadib, and K. Lisowska, 'Biodegradable Chitosan-Based Films as an Alternative to Plastic Packaging', *Foods*, vol. 12, no. 18, p. 3519, Sep. 2023, doi: 10.3390/foods12183519.

[101] K. Kario *et al.*, 'Systemic hemodynamic atherothrombotic syndrome (SHATS) – coupling vascular disease and blood pressure variability: Proposed concept from pulse of asia', *Prog. Cardiovasc. Dis.*, vol. 63, no. 1, pp. 22–32, Jan. 2020, doi: 10.1016/j.pcad.2019.11.002.

[102] G. Chen, C. Au, and J. Chen, 'Textile triboelectric nanogenerators for wearable pulse wave monitoring', *Trends Biotechnol.*, vol. 39, no. 10, pp. 1078–1092, Oct. 2021, doi: 10.1016/j.tibtech.2020.12.011.

[103] B. Chong *et al.*, 'Global burden of cardiovascular diseases: Projections from 2025 to 2050', *Eur. J. Prev. Cardiol.*, vol. 32, no. 11, pp. 1001–1015, 2024, doi: 10.1093/eurjpc/zwae281.

[104] S. Min *et al.*, 'Clinical validation of a wearable piezoelectric blood-pressure sensor for continuous health monitoring', *Adv. Mater.*, vol. 35, no. 26, Jun. 2023, doi: 10.1002/adma.202301627.

[105] X. Wu *et al.*, 'Machine learning-augmented piezoelectric-ferroelectret nanogenerators for highly sensitive respiration monitoring in wearable healthcare', *Adv. Funct. Mater.*, vol. 36, no. 32, Apr. 2026, doi: 10.1002/adfm.202522897.

[106] C. Wang *et al.*, 'Tissue-adhesive piezoelectric soft sensor for in vivo blood pressure monitoring during surgical operation', *Adv. Funct. Mater.*, vol. 33, no. 38, Sep. 2023, doi: 10.1002/adfm.202303696.

[107] H. Xia *et al.*, 'MXene/PPy@PDMS sponge-based flexible pressure sensor for human posture recognition with the assistance of a convolutional neural network in deep learning', *Microsyst. Amp Nanoeng.*, vol. 9, no. 1, Dec. 2023, doi: 10.1038/s41378-023-00605-0.

[108] Y. Guo *et al.*, 'A self-powered flexible piezoelectric sensor patch for deep learning-assisted motion identification and rehabilitation training system', *Nano Energy*, vol. 123, p. 109427, May 2024, doi: 10.1016/j.nanoen.2024.109427.

[109] A. Nauman *et al.*, 'Stretchable anisotropic piezoelectric sensors with modulus engineering for monitoring multiaxial joint motion', *Mater. Amp Des.*, vol. 254, p. 114120, Jun. 2025, doi: 10.1016/j.matdes.2025.114120.

[110] C. Bouyam and Y. Punsawad, 'Human–machine interface-based wheelchair control using piezoelectric sensors based on face and tongue movements', *Heliyon*, vol. 8, no. 11, p. e11679, Nov. 2022, doi: 10.1016/j.heliyon.2022.e11679.

[111] Y. Qiu *et al.*, 'Nondestructive identification of softness via bioinspired multisensory electronic skins integrated on a robotic hand', *Npj Flex. Electron.*, vol. 6, no. 1, Jun. 2022, doi: 10.1038/s41528-022-00181-9.

[112] A. Šutka, P. C. Sherrell, N. A. Shepelin, L. Lapčinskis, K. Mālnieks, and A. V. Ellis, 'Measuring Piezoelectric Output—Fact or Friction?', *Adv. Mater.*, vol. 32, no. 32, p. 2002979, 2020, doi: 10.1002/adma.202002979.

[113] E. Podgorbunskikh, T. Kuskov, D. Rychkov, O. Lomovskii, and A. Bychkov, 'Mechanical amorphization of chitosan with different molecular weights', *Polymers*, vol. 14, no. 20, p. 4438, Oct. 2022, doi: 10.3390/polym14204438.

[114] A. Monshi, M. R. Foroughi, and M. R. Monshi, 'Modified scherrer equation to estimate more accurately nano-crystallite size using XRD', *World J. Nano Sci. Eng.*, vol. 2, no. 3, pp. 154–160, Sep. 2012, doi: 10.4236/wjnse.2012.23020.

[115] E. Gdoutos and M. Konsta-Gdoutos, 'Tensile testing', 2024. doi: 10.1007/978-3-031-45990-0_1.

[116] K. Uchino, 'Fundamentals of Piezoelectrics', in *Encyclopedia of Smart Materials*, Elsevier, 2022, pp. 1–21. doi: 10.1016/B978-0-12-803581-8.12129-0.

[117] D. Deflorio, M. Di Luca, and A. M. Wing, 'Skin and Mechanoreceptor Contribution to Tactile Input for Perception: A Review of Simulation Models', *Front. Hum. Neurosci.*, vol. 16, Jun. 2022, doi: 10.3389/fnhum.2022.862344.

[118] Y. H. Jung, B. Park, J. U. Kim, and T. Kim, 'Bioinspired Electronics for Artificial Sensory Systems', *Adv. Mater.*, vol. 31, no. 34, p. 1803637, 2019, doi: 10.1002/adma.201803637.

[119] J. Li, L. Fang, B. Sun, X. Li, and S. H. Kang, 'Review—Recent Progress in Flexible and Stretchable Piezoresistive Sensors and Their Applications', *J. Electrochem. Soc.*, vol. 167, no. 3, p. 037561, Feb. 2020, doi: 10.1149/1945-7111/ab6828.

[120] S. Chen, Z. Yang, Q. Huang, K. Li, and S. Ge, 'Vibrotactile Sensation: A Systematic Review of the Artificial Pacinian Corpuscle', *J. Bionic Eng.*, Feb. 2023, doi: 10.1007/s42235-023-00348-8.

[121] J.-K. Han, I.-W. Tcho, S.-B. Jeon, J.-M. Yu, W.-G. Kim, and Y.-K. Choi, 'Self-Powered Artificial Mechanoreceptor Based on Triboelectrification for a Neuromorphic Tactile System', *Adv. Sci.*, vol. 9, no. 9, p. 2105076, 2022, doi: 10.1002/advs.202105076.

[122] L.-H. Li, J.-C. Deng, H.-R. Deng, Z.-L. Liu, and L. Xin, 'Synthesis and characterization of chitosan/ZnO nanoparticle composite membranes', *Carbohydr. Res.*, vol. 345, no. 8, pp. 994–998, May 2010, doi: 10.1016/j.carres.2010.03.019.

[123] T. Winie and A. K. Arof, 'FT-IR studies on interactions among components in hexanoyl chitosan-based polymer electrolytes', *Spectrochim. Acta. A. Mol. Biomol. Spectrosc.*, vol. 63, no. 3, pp. 677–684, Mar. 2006, doi: 10.1016/j.saa.2005.06.018.

[124] Q. Li, J. Xing, D. Shang, and Y. Wang, 'A Flow Velocity Measurement Method Based on a PVDF Piezoelectric Sensor', *Sensors*, vol. 19, no. 7, p. 1657, Apr. 2019, doi: 10.3390/s19071657.

[125] Y. Li *et al.*, 'High-performance piezoelectric nanogenerators based on hierarchical ZnO@CF/PVDF composite film for self-powered meteorological sensor', *J. Mater. Chem. A*, vol. 11, no. 25, pp. 13708–13719, Jul. 2023, doi: 10.1039/d3ta01886e.

[126] M. Ahmad, D. Shukla, Y. Zhu, and O. D. Velev, 'Biodegradable Chitosan-Based Stretchable Electronics with Recyclable Silver Nanowires', *ACS Appl. Mater. Interfaces*, vol. 17, no. 11, pp. 17316–17329, Mar. 2025, doi: 10.1021/acsami.4c20193.

[127] Y. Liu, 'Piezoelectric energy harvesting for self-powered wearable upper limb applications', *Nano Sel*, vol. 2, pp. 1459–1479, 2021.

[128] P. Mujeeb Rahman, V. M. Abdul Mujeeb, K. Muraleedharan, and S. K. Thomas, 'Chitosan/nano ZnO composite films: enhanced mechanical, antimicrobial and dielectric properties', *Arab J Chem*, vol. 11, pp. 120–127, 2018.

[129] A. C. Jayasuriya, A. Aryaei, and A. H. Jayatissa, 'ZnO nanoparticles induced effects on nanomechanical behavior and cell viability of chitosan films', *Mater Sci Eng C*, vol. 33, pp. 3688–3696, 2013.

[130] M. Malekkiani, A. Heshmati Jannat Magham, F. Ravari, and M. Dadmehr, 'Facile fabrication of ternary MWCNTs/ZnO/chitosan nanocomposite for enhanced photocatalytic degradation of methylene blue and antibacterial activity', *Sci Rep*, vol. 12, p. 5927, 2022.

[131] E. Prokhorov, G. Luna-Bárcenas, J. M. Yáñez Limón, A. Gómez Sánchez, and Y. Kovalenko, 'Chitosan-ZnO nanocomposites assessed by dielectric, mechanical, and piezoelectric properties', *Polymers*, vol. 12, p. 1991, 2020.

[132] R. Salehi, M. Arami, N. M. Mahmoodi, H. Bahrami, and S. Khorramfar, 'Novel biocompatible composite (chitosan–zinc oxide nanoparticle): preparation, characterization and dye adsorption properties', *Colloids Surf B Biointerfaces*, vol. 80, pp. 86–93, 2010.

[133] K. T. Nguyen, 'The chitosan/ZnO bio-nanocomposites with selective antibacterial efficiency', *J Mater Res*, vol. 36, pp. 508–517, 2021.

[134] T. Yang, 'Hierarchically structured PVDF/ZnO core-shell nanofibers for self-powered physiological monitoring electronics', *Nano Energy*, vol. 72, p. 104706, 2020.

[135] Z. Chen, 'Flexible piezoelectric-induced pressure sensors for static measurements based on nanowires/graphene heterostructures', *ACS Nano*, vol. 11, pp. 4507–4513, 2017.

[136] K.-B. Kim, 'Transparent and flexible piezoelectric sensor for detecting human movement with a boron nitride nanosheet (BNNS)', *Nano Energy*, vol. 54, pp. 91–98, 2018.

[137] T. Sharma, S.-S. Je, B. Gill, and J. X. J. Zhang, 'Patterning piezoelectric thin film PVDF–TrFE based pressure sensor for catheter application', *Sens Actuators Phys*, vol. 177, pp. 87–92, 2012.

[138] Md. N. Islam, 'Boosting piezoelectricity by 3D printing PVDF-MoS_2 composite as a conformal and high-sensitivity piezoelectric sensor', *Adv Funct Mater*, vol. 33, p. 2302946, 2023.

[139] I. A. Mudunkotuwa, T. Rupasinghe, C.-M. Wu, and V. H. Grassian, 'Dissolution of ZnO Nanoparticles at Circumneutral pH: A Study of Size Effects in the Presence and Absence of Citric Acid', *Langmuir*, vol. 28, no. 1, pp. 396–403, Jan. 2012, doi: 10.1021/la203542x.

[140] Q. He *et al.*, 'A wearable and highly sensitive PVDF–TrFE–BaTiO3 piezoelectric sensor for wireless monitoring of arterial signal', *ACS Appl. Electron. Mater.*, Jul. 2025, doi: 10.1021/acsaelm.5c00548.

[141] A. D. Astin, 'Finger force capability: measurement and prediction using anthropometric and myoelectric measures', Virginia Tech, 1999. Accessed: Jan. 13, 2025. [Online]. Available: http://hdl.handle.net/10919/30923

[142] X. Lin, 'Piezotronic neuromorphic devices: principle, manufacture, and applications', *Int J Extreme Manuf*, vol. 6, p. 032011, 2024.

[143] A. D. Astin, 'Finger force capability: measurement and prediction using anthropometric and myoelectric measures', 1999.

[144] J. Gao, D. Xue, W. Liu, C. Zhou, and X. Ren, 'Recent progress on BaTiO3-based piezoelectric ceramics for actuator applications', *Actuators*, vol. 6, no. 3, p. 24, 2017.

[145] S. Murugan, D. Karthikesan, S. Sellathurai, E. Praveen, and K. Jayakumar, 'Design of mechanical sensing system based on nano BaTiO3 embedded in biopolymer electret', presented at the 2014 Fifth International Symposium on Electronic System Design, 2014, pp. 199–202.

[146] S. Pongampai, 'Triboelectric-piezoelectric hybrid nanogenerator based on BaTiO3-nanorods/chitosan enhanced output performance with self-charge-pumping system', *Compos. Part B Eng.*, vol. 208, p. 108602, 2021.

[147] Y. Huang, S. Chen, Y. Li, Q. Lin, Y. Wu, and Q. Shi, 'Flexible piezoelectric sensor based on PAN/MXene/PDA@ZnO composite film for human health and motion detection with fast response and high sensitivity', *Chem. Eng. J.*, vol. 488, p. 150997, 2024.

[148] M. D. Marsico and A. Mecca, 'A survey on gait recognition via wearable sensors', *ACM Comput. Surv.*, vol. 52, no. 4, pp. 1–39, 2019.

[149] Y. Yang, 'Flexible piezoelectric pressure sensor based on polydopamine-modified BaTiO3/PVDF composite film for human motion monitoring', *Sens. Actuators Phys.*, vol. 301, p. 111789, 2020, doi: 10.1016/j.sna.2019.111789.

[150] S.-H. Shin, Y.-H. Kim, J.-Y. Jung, M. Hyung Lee, and J. Nah, 'Solvent-assisted optimal BaTiO3 nanoparticles-polymer composite cluster formation for high performance piezoelectric nanogenerators', *Nanotechnology*, vol. 25, no. 48, p. 485401, Nov. 2014, doi: 10.1088/0957-4484/25/48/485401.

[151] C. Baek, 'Enhanced output performance of a lead-free nanocomposite generator using BaTiO3 nanoparticles and nanowires filler', *Appl. Surf. Sci.*, vol. 429, pp. 164–170, 2018, doi: 10.1016/j.apsusc.2017.06.109.

[152] K. Kakimoto, K. Fukata, and H. Ogawa, 'Fabrication of fibrous BaTiO3-reinforced PVDF composite sheet for transducer application', *Sens. Actuators Phys.*, vol. 200, pp. 21–25, 2013, doi: 10.1016/j.sna.2013.03.007.

[153] C.-R. Yang, M.-F. Lin, C.-K. Huang, W.-C. Huang, S.-F. Tseng, and H.-H. Chiang, 'Highly sensitive and wearable capacitive pressure sensors based on PVDF/BaTiO3 composite fibers on PDMS microcylindrical structures', *Measurement*, vol. 202, p. 111817, Oct. 2022, doi: 10.1016/j.measurement.2022.111817.

[154] C. E. Ciomaga *et al.*, 'BaTiO3 nanocubes-gelatin composites for piezoelectric harvesting: Modeling and experimental study', *Ceram. Int.*, vol. 48, no. 18, pp. 25880–25893, Sep. 2022, doi: 10.1016/j.ceramint.2022.05.264.

[155] H. Yao, 'Near-hysteresis-free soft tactile electronic skins for wearables and reliable machine learning', *Proc. Natl. Acad. Sci.*, vol. 117, no. 41, pp. 25352–25359, 2020.

[156] E. Gdoutos and M. Konsta-Gdoutos, 'Tensile testing', in *Mechanical Testing of Materials*, 2024.

[157] Z. Wang, B. P. Yalagala, J. Zhang, M. Hafezi, H. Heidari, and A. Feeney, 'Wireless and self-powered wearable pressure sensors based on chitosan for artificial mechanoreceptors', *Adv. Mater. Technol.*, vol. 10, no. 11, p. 2401858, 2025.

[158] M. Golda-Cepa, K. Engvall, M. Hakkarainen, and A. Kotarba, 'Recent progress on parylene C polymer for biomedical applications: A review', *Prog. Org. Coat.*, vol. 140, p. 105493, Mar. 2020, doi: 10.1016/j.porgcoat.2019.105493.

[159] S. Kurnaz, Ö. Öztürk, N. Yılmaz, and O. Çiçek, 'The Parylene C as a Flexible Substrate and Passivation Layer: A Promising Candidate for a Piezoelectric, Piezoresistive, and Capacitive Pressure Sensor in Low-Pressure Range', *IEEE Sens. J.*, vol. 23, no. 19, pp. 22277–22284, Oct. 2023, doi: 10.1109/JSEN.2023.3305058.

[160] A. Kahouli, 'Effect of film thickness on structural, morphology, dielectric and electrical properties of parylene C films', *J. Appl. Phys.*, vol. 112, no. 6, p. 064103, Sep. 2012, doi: 10.1063/1.4752022.

[161] N. Jackson, F. Stam, J. O'Brien, L. Kailas, A. Mathewson, and C. O'Murchu, 'Crystallinity and mechanical effects from annealing parylene thin films', *Thin Solid Films*, vol. 603, pp. 371–376, Mar. 2016, doi: 10.1016/j.tsf.2016.02.047.

[162] M. J. Herman and M. W. Blair, 'Determination of chemical decay mechanisms of Parylene-C during X-ray irradiation using two-dimensional correlation FTIR', *Polym. Degrad. Stab.*, vol. 171, p. 109024, Jan. 2020, doi: 10.1016/j.polymdegradstab.2019.109024.

[163] B. J. Coelho *et al.*, 'Parylene C as a Multipurpose Material for Electronics and Microfluidics', *Polymers*, vol. 15, no. 10, p. 2277, May 2023, doi: 10.3390/polym15102277.

[164] D. D. Edwards, J.-H. Hwang, S. J. Ford, and T. O. Mason, 'Experimental limitations in impedance spectroscopy:: Part V. Apparatus contributions and corrections', *Solid State Ion.*, vol. 99, no. 1, pp. 85–93, Aug. 1997, doi: 10.1016/S0167-2738(97)00206-3.

[165] J. Y.-H. Kim, 'Parylene-C as a New Piezoelectric Material', phd, California Institute of Technology, 2013. doi: 10.7907/1VEH-EP90.

[166] M. C. Sekhar, E. Veena, N. S. Kumar, K. C. B. Naidu, A. Mallikarjuna, and D. B. Basha, 'A review on piezoelectric materials and their applications', *Cryst. Res. Technol.*, vol. 58, no. 2, p. 2200130, 2023, doi: 10.1002/crat.202200130.

[167] J. Mu *et al.*, 'Synergistic Enhancement Properties of a Flexible Integrated PAN/PVDF Piezoelectric Sensor for Human Posture Recognition', *Nanomaterials*, vol. 12, no. 7, p. 1155, Apr. 2022, doi: 10.3390/nano12071155.

[168] M. Ali, S. M. Hoseyni, R. Das, M. Awais, I. Basdogan, and L. Beker, 'A Flexible and Biodegradable Piezoelectric-Based Wearable Sensor for Non-Invasive Monitoring of Dynamic Human Motions and Physiological Signals', *Adv. Mater. Technol.*, vol. 8, no. 15, p. 2300347, 2023, doi: 10.1002/admt.202300347.

[169] J. Wang *et al.*, 'Enhanced self-polarization effect by tuning interfacial binding energy for self-powered flexible piezoelectric pressure sensors', *Sens. Actuators Phys.*, vol. 374, p. 115473, Aug. 2024, doi: 10.1016/j.sna.2024.115473.

[170] S. Maity, R. K. Singh, M. Gadhewal, and S. P. Tiwari, 'Highly biodegradable piezoelectric flexible wearable tactile sensors with amino acid crystals: a paradigm shift towards smart transient electronics', *Chem. Eng. J.*, vol. 512, p. 162531, May 2025, doi: 10.1016/j.cej.2025.162531.